UNIVERSITÀ DEGLI STUDI DI MILANO

Department of Chemistry

PhD Course in Chemistry – XXXV Cycle

Titanium Dioxide Photoactivity: Effects of combined Structural, Surface and Morphological Modifications

Tutor: Prof. Maria Vittoria DOZZI

Co-Tutor: Prof. Elena SELLI

Marco MONTALBANO
Matriculation n°: R12763

Academic Year 2021/2022

[This page intentionally left blank]

Abstract

Titanium dioxide is the most widely used and studied photocatalyst for a variety of applications. However, its performance as a photocatalyst is limited by two main drawbacks: i) the fast recombination of photogenerated charge carriers and ii) a high band gap energy, requiring UV light irradiation to promote its electronic excitation.

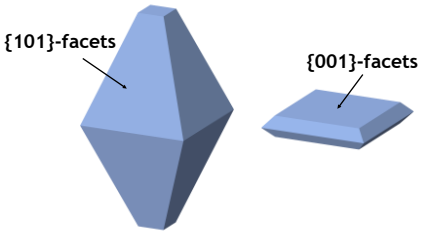

Several strategies have been investigated to overcome these limitations, such as surface modification with noble metal (NM) nanoparticles (NPs), Au, Pt, Pd, and doping with transition metals or *p*-block elements. The fine tuning of TiO_2 crystal morphology represents another modification strategy that recently gained a lot of attention. By using suitable shape-controlling agents it is possible to modify the crystal habit of anatase, favoring the transition from its typical truncated bipyramidal structure, characterized by approximately 90% surface exposure of {101} facets, to the nanosheet-like morphology, mainly exposing the thermodynamically less stable (but potentially more reactive) {001} surfaces. At the same time, recent studies demonstrated that *in-situ* adsorption of fluoride ions has specific effects on the photocatalytic activity of TiO_2, depending on the TiO_2 crystal phase composition and on the mechanism of the photocatalytic reaction. A systematic evaluation of the combined effects produced on photoactivity by NM NPs deposition and *in-situ* TiO_2 fluorination, as a function of the adopted deposition technique, the chosen NM and/or the semiconductor morphology, was still lacking.

In the present PhD thesis, the photocatalytic properties of doped and/or morphology-controlled anatase TiO_2 samples modified by surface deposition of Au NPs was firstly investigated in both photocatalytic oxidation and reduction reactions. In particular, the effects induced by Au NPs deposited on the TiO_2 surface by different techniques were investigated, as well as those of the *in-situ* addition of fluoride ions, to highlight possible synergistic effects on TiO_2 photoactivity induced by coupling surface fluorination, specific morphology, and deposited NM NPs.

A systematic study was thus undertaken by studying at first the effects deriving from the use of two different Au NPs deposition methods, *i.e.*, deposition-precipitation (DP) and photoreduction (P), on the photocatalytic activity of sol-gel prepared titanium dioxide samples bulk co-doped with different amounts of N and F. The photoactivity of the prepared composite Au/TiO_2 materials was monitored in two different photocatalytic test reactions, *i.e.*, formic acid oxidation and Cr(VI) reduction, each proceeding through completely different reaction paths. In

particular, whereas in the case of formic acid oxidation no significant differences in the materials photoactivity was induced by the use of different Au NPs deposition techniques, regardless of the dopant content introduced in the TiO_2 bulk structure, an outstanding photoactivity was instead attained in Cr(VI) to Cr(III) photoreduction upon coupling an optimal amount of bulk dopant in TiO_2 with the photodeposition of NM NPS. The origin of such synergy between the use of a selective Au NPs deposition method (*i.e.*, photodeposition) and the use of an optimal amount of dopant was then studied via Time-Resolved Photoluminescence Spectroscopy.

Next, the effects induced upon using the above-mentioned Au NPs deposition techniques on the photocatalytic activity of differently shaped anatase powders, eventually also coupled with *in-situ* surface fluorination, were evaluated mainly in three different photocatalytic test reactions, *i.e.*, formic acid (FA) oxidation, rhodamine B (RhB) bleaching and Cr(VI) to Cr(III) reduction. In particular, the deposition of Au NPs on TiO_2 was beneficial in FA degradation only in the case of {101} facet-dominated materials, whereas coupling Au NPs photodeposition with a nanosheet-like morphology of TiO_2 did not lead to better performing photocatalytic materials.

Similar results were also obtained in the case of rhodamine B photobleaching. In particular, whereas in the case of metal-free titanium dioxide a positive synergy was observed upon coupling a nanosheet morphology (*i.e.*, materials mainly exposing {001} facets) with *in-situ* surface fluorination, a positive effect on photoactivity induced by coupling the deposition of Au NPs and *in-situ* surface fluorination was obtained only when the materials were mainly dominated by the exposure of {101} facets (thus bearing a pseudo-spherical shape).

Differently, the photoactivity of morphology controlled Au/TiO_2 materials in Cr(VI) photoreduction was found to be only slightly affected by the deposition of NM NPs. Instead, the photoefficiency of anatase was largely improved upon shifting from a pseudo-spherical morphology towards nanosheet-shaped crystallites, producing materials which also significantly outperformed reference benchmark P25 TiO_2. This is possibly due to an improved oxidative power of {001} facets which help to overcome the kinetically rate-determining anodic half-reaction in Cr(VI) reduction, *i.e.*, water oxidation. Furthermore, an enhanced oxidative power of {001} surfaces in comparison to {101} facets was demonstrated by a higher production of $HO^{\bullet}$ radicals in solution during the hydroxylation of terephthalic acid in the aqueous media. This effect was observed when the morphology of TiO_2 was shifted from a pseudo-spherical shape to a nanosheet-like structure, providing further confirmation of the mentioned findings.

Lastly, the performance of the materials was assessed in hydrogen production via methanol photo steam reforming. Our results revealed significant enhancements in the photoactivity of the

powders upon deposition of NM NPs and, notably, the utilization of pseudo-spherically shaped TiO_2 materials. It is possible that the increased exposure of {101} facets, which act as reduction sites, facilitates a greater availability of reduction centres, thereby promoting H_2 evolution.

The obtained photoactivity results in the investigated test reactions allowed us to hypothesize a reaction mechanism based on charge migration in differently shaped Au/TiO_2 composite materials able to rationalize the effects on photoactivity induced upon coupling Au deposition with differently shaped TiO_2 materials, also under *in-situ* fluorinated conditions.

[This page intentionally left blank]

Table of Contents

List of Abbreviations

The following table describes the significance of various abbreviations and acronyms used throughout the thesis.

Abbreviation	Definition
2-TaOH	2-hydroxyterephthalic acid
AOP	Advanced oxidation process
BET	Brunauer-Emmett-Teller
CB	Conduction band
CCD	Charge-coupled device
CEM	Controlled evaporation and mixing unit
COUM	Coumarin
DFT	Density functional theory
DOS	Density of states
DP	Deposition-precipitation
DR	Diffuse reflectance
DRS	Diffuse reflectance spectroscopy
DSC	Differential scanning calorimetry
DSSC	Dye-sensitized solar cell
E_F	Fermi energy
E_g	Energy gap
EPR	Electron paramagnetic resonance spectroscopy
FT-IR	Fourier transform – infrared spectroscopy
FWHM	Full width at half maximum
GGA	Generalized gradient approximation
HR-TEM	High resolution transmission electron microscopy
HT	Hydrothermal
ICP-OES	Inductively coupled plasma – optical emission spectroscopy
IUPAC	International Union of Pure and Applied Chemistry
LSPR	Localized surface plasmon resonance
MFC	Mass flow meter and controller
NM	Noble metal

Abbreviation	Definition
NP	Nanoparticle
P	Photodeposition
PID	Proportional-integral-derivative controller
PL	Photoluminescence
PTFE	Polytetrafluoroethylene
QD	Quenching degree
RhB	Rhodamine B
ROS	Reactive oxygen species
SPR	Surface plasmon resonance
SSA	Specific surface area
TA	Terephthalic acid
TC	Temperature controlling unit
TCSPC	Time-correlated single photon counting
TEM	Transmission Electron Microscopy
TEOS	Tetraethylorthosilicate
TGA	Thermogravimetric analysis
Tl	Thermocouple
TRPL	Time-resolved photoluminescence
UHV	Ultra-high vacuum
VB	Valence band
XPS	X-Ray photoelectron spectroscopy

Chapter 1: Backgrounds

1.1 Introduction

The transition towards a sustainable and environmentally friendly economy and society represents one of the main challenges of the 21st century worldwide. In fact, environmental pollution has been poisoning the earth because of anthropogenic activities since the earliest civilization up to the present days,[1] threatening the health of human beings with a number of seriously harmful effects such as, for example, malignancies, cardiovascular disorders, mental health disorders, and many others.[2] Consequently, the preservation of the environment and human health has led to the current socio-political scenario in which the increased awareness and need for a sustainable way of life for humanity paved the way for several governmental and intergovernmental associations to take act with a number of plans and policies aimed at setting goals and initiatives, with the purpose of establishing an environmentally respectful and sustainable society. Among these, the two most relevant are represented by the 2030 Agenda for Sustainable Development adopted by all United Nations Member States in 2015 and the European Green Deal approved in 2020 by the European Union.

Among the various points discussed in such regulations, a lot of focus is posed on water remediation, prevention of its pollution, and increasing the availability of clean, safe water worldwide. As a matter of fact, water pollution, occurring when an unwanted substance results in severely degrading its quality, represents a widespread issue jeopardizing the health of millions of people around the world, killing more humans each year than any form of violence combined.[3] More worrying, only the 3% out of the billion and a half cube meters of water present on earth is constituted of fresh, ready to be consumed water. With the demand for human-consumable water expected to be increased by one-third by 2050,[4] prevention of water pollution and remediation of wastewaters from agricultural and industrial activities represent points of primary importance in achieving the goals of sustainability and safety at the centre of modern-day society.

In this scenario, a contribution from the scientific community in developing newly efficient and environmentally friendly wastewater treatment technologies becomes mandatory. Among these, heterogeneous photocatalysis represents an emerging advanced oxidation process (AOP) with the very advantageous characteristics of potentially completely mineralize pollutants into innocuous substances (ideally CO_2), requiring only mild reaction conditions and oxygen as a

reactant, no production of sludge, relatively rapid degradation and very high efficiency at degrading recalcitrant compounds such as drugs or dyes, with the only requirement being the activation of a catalyst material with light of appropriate wavelength.[5] Considering that photons can be provided with radiation coming from sunlight, the potential applications of heterogeneous photocatalysis as an environmentally friendly and energetically efficient wastewater remediation technology appears clear.

Potential heterogeneous photocatalysis-based environmental applications, however, are far from limited to wastewater treatment (Figure 1.1.1), with some of the most notable ones represented by air remediation and production of clean solar fuels such as hydrogen.[6] In fact, through the use of a suitable semiconductor photocatalyst, irradiation of an aqueous solution (more commonly in the presence of a hole scavenging species) in contact with a photo(electro)catalyst results in the evolution of H_2, a clean energy vector which can be burnt as a fuel without releasing any noxious chemical. Therefore, semiconductor photocatalysis also poses as a potential technology able to help in the ecological transition from the present day commonly used fossil fuels towards environmentally clean solar fuels, representing one of the pillars of the 2020 European Green Deal.

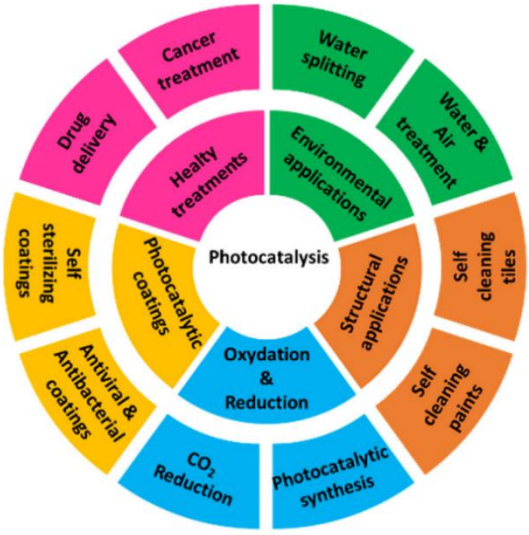

Figure 1.1.1: Graphic representation illustrating some potential applications of photocatalysis.[7]

Within this general framework, this PhD thesis aims at investigating some possible strategies focused at improving the performances in photocatalysis of the most widely employed and studied heterogeneous semiconductor photocatalyst, *i.e.*, titanium dioxide, exploring the effects deriving from different modification strategies, such as metal nanoparticles surface deposition, bulk doping, and crystal facets engineering. Final purpose is shedding light on the effects of the combination of

the mentioned modification strategies on the photocatalytic properties of the metal oxide material in a plethora of environmentally relevant photocatalytic applications, occurring through both oxidative and reductive processes.

1.2 Fundamental Aspects of Semiconductor Photocatalysis

According to IUPAC, photocatalysis is defined as "a change in the rate of a chemical reaction or its initiation under the action of ultraviolet, visible or infrared radiation in the presence of a substance – the photocatalyst – that absorbs light and is involved in the chemical transformation of the reaction partners". Thus, oppositely to a photochemical reaction, in a photocatalytic process the substance being transformed is not directly involved in the absorption of photons, whereas instead the light-photocatalyst interaction is responsible for photocatalysis. If a semiconductor solid material is used as a photocatalyst, as it happens most frequently, the terminology heterogeneous or semiconductor photocatalysis is preferred. On a basic principle, semiconductor photocatalysis can be summarized through a simple system in which a semiconductor material, named photocatalyst, is in contact with species that are either oxidized or reduced once an electronic excitation of the semiconductor via light absorption is provided. More realistically, semiconductor photocatalysis represents a wide field of science and technology characterized by a huge complexity of the physico-chemical processes occurring underneath an only apparently simple light-induced redox process.

To understand the basic principles of heterogeneous photocatalysis, a description of the structure of semiconductor materials is necessary. A semiconductor is a material whose electronic structure is characterized by a void energy region in between its valence and conduction band, named band gap. The mobility of the charge carriers in a semiconductor material is thus much more limited compared to metals, in which the absence of the void energy region allows the valence band and conduction band to overlap within each other, allowing electrons to freely move from one to the other, leading to the characteristic highly efficient transport properties in metals. However, in semiconductors, unlike insulators, the energy gap (E_g) is narrow enough (2-3 eV, Figure 1.2.1a) so that by providing enough energy it is possible to promote an electron from the conduction band to the valence band, with the parallel generation of a hole in the valence band. By this way the number of free charge carriers available within the semiconductor increases. Semiconductors, in fact, represent a class of materials of huge interest in many fields of science, because they allow to modulate the availability of their charge carriers.

In semiconductor photocatalysis, the energy required to induce the promotion of an electron from the valence band to the conduction band is provided by irradiation with light source whose photons are more energetic than the band gap energy, leading to electronic excitation of the semiconductor material. The produced species, i.e., electrons and holes, can be exploited to perform some sort of redox chemistry by transferring them from the photocatalyst surface to the species adsorbed there (Figure 1.2.1b).

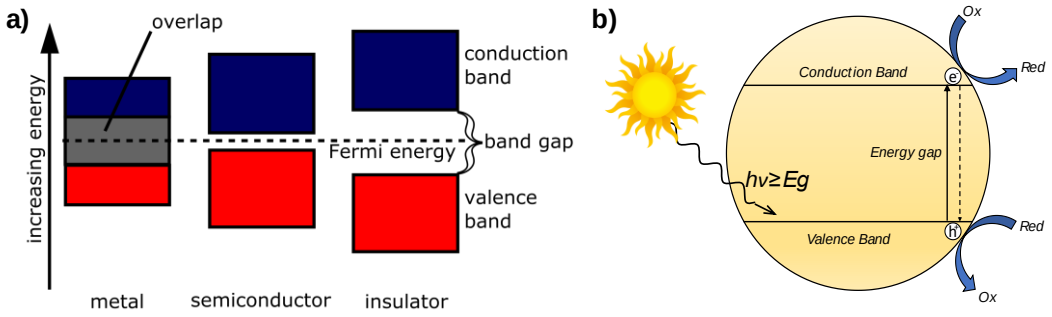

Figure 1.2.1: A band diagram showing the different sizes of band gaps for conductors, semiconductors, and insulators (a); schematic diagram illustrating the photo-induced semiconductor activation in photocatalysis (b).

A fundamental entity in describing the properties of semiconductor materials is the Fermi level and the corresponding Fermi energy (E_F), which represents a measure of the free energy of the electrons in the semiconductor and is defined as the energy level at which the probability of occupation of that state by an electron at the absolute zero temperature is equal to 50%. In the case of an *intrinsic* semiconductor, i.e., one free of impurities and defects, the Fermi level is positioned in the middle of the energy gap. However, as intrinsic semiconductors are unlikely to exist (and very little of interest to photocatalysis), the presence of specific defects or impurities can alter the position of the Fermi level from that of an intrinsic semiconductor. In particular, if the structure of the semiconductor is altered with oxygen vacancies or impurities of atoms carrying a higher number of electrons than those of semiconductor lattice (e.g., substitution of Si with P), a so-called *n-type* (negative) semiconductor is obtained, whereas if an atom with a lower number of electrons is introduced (e.g., substitution of Si with B), a so-called *p-type (*positive*)* semiconductor is obtained. The electronic structure of an n-type semiconductor differs from that of an intrinsic semiconductor since, as a consequence of the presence of impurities, an occupied intra-band gap energy level, located close to the valence band redox potential, is now introduced in the band structure. Such energy state favors the promotion of electrons to the conduction band, resulting in a shift of the semiconductor Fermi level towards more negative potentials. In a n-type semiconductor, thus, electrons represent the *majority carriers*, whereas holes are the *minority carriers*. Analogue considerations can be made for *p*-type semiconductors, although an empty state closer

to the valence band and a shift of the Fermi energy towards more positive potentials is rather obtained (Figure 1.2.2).

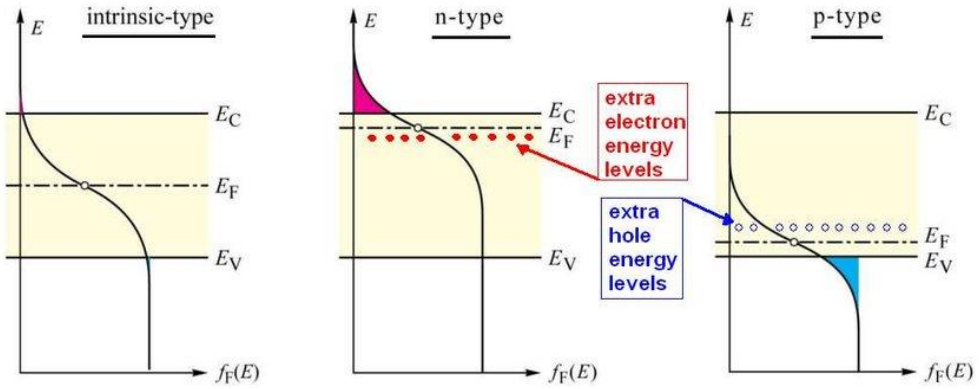

Figure 1.2.2: Diagram illustrating the changes in the electronic structure and positioning of the Fermi level of n-type and p-type semiconductors compared to the intrinsic case.

Semiconductor photocatalysis occurs in a heterogeneous medium, i.e., for a photocatalytic process to occur contact between the semiconductor and another phase, for example an electrolyte solution, is required. The contact of the semiconductor surface with a different phase induces charge reorganization and transfer phenomena between the semiconductor and the electrolyte. In fact, under equilibrium conditions, the electrochemical potential of the electrons in the two phases must be the same. Within the solution, the electrochemical potential is represented by the redox potential of the electrolyte solution, whereas for the semiconductor by its Fermi energy. The relative position of the Fermi level of the semiconductor and the potential of the redox couple determines what happens when the two phases are brought in contact under equilibrium conditions. If the Fermi level is more negative than the redox couple potential in solution, electrons will be transferred from the semiconductor to the electrolyte until an equilibrium of the electrochemical potential of electrons is established. In an n-type semiconductor, this charge transfer process results in the formation of a positively charged region within the semiconductor structure known as *depletion layer,* facing a layer of negatively charged ions at the electrolyte side. The whole interfacial region is also known as *space charge region*, whose width w_{sc} can be mathematically expressed as:

$$w_{sc} = \left(\frac{2\Delta\phi_{sc}\varepsilon\varepsilon_0}{qN_d}\right)^{\frac{1}{2}} \qquad (1.2.1)$$

where N_d is the doping density, $\Delta\phi_{sc}$ is the potential drop across the space charge region, ε is the absolute permittivity, ε_0 is the vacuum permittivity and q is the electron charge. In fact, the presence of a positively charged layer results in the generation of a quadratic electric potential

across the semiconductor surface extending from w_{sc} to the semiconductor-electrolyte interface, causing an upward bending of the band structure of the material as we approach the electrolyte solution from the bulk of the material (Figure 1.2.3).

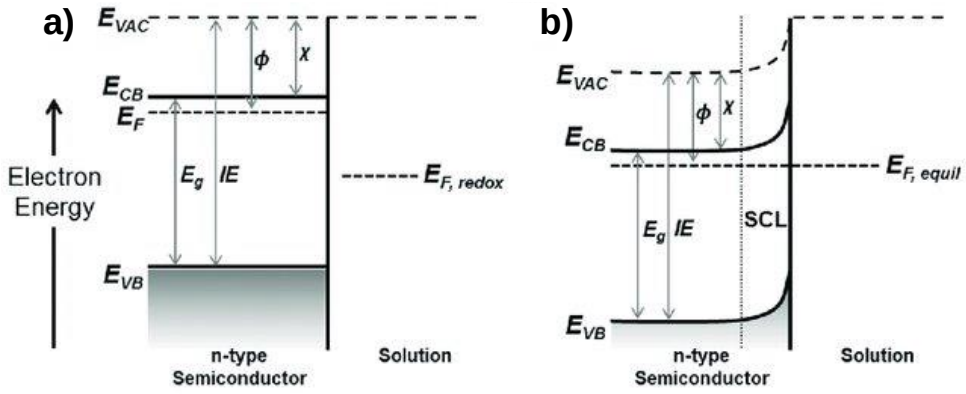

Figure 1.2.3: Energy levels of the semiconductor/electrolyte interface before (a) and after (b) contact of the two phases for an n-type semiconductor. After contact, equilibrium of the electrochemical potential of the electrons among the two phases is established, and as a result a space charge region and upward bending of the bands of the semiconductor is formed. Under Creative Common License CC BY 3.0.

The band bending at the semiconductor-electrolyte interface has a profound impact on the physical chemistry of a semiconductor photocatalyst, and its presence is of fundamental importance in photocatalysis. In fact, photogenerated holes in an n-type semiconductor are metastable species which tend to recombine at very high rates with conduction band electrons. Therefore, photogenerated and photopromoted charge carriers are characterized by a finite lifetime τ, which is generally in the order of nanoseconds for commonly employed semiconductor photocatalysts. The finite lifetime of the minority charge carriers in a semiconductor represents the main factor limiting the efficiency of photocatalysts in promoting redox processes and constitutes their major deactivation path, since recombination of the charge carriers competes with the desired transfer of the charged species towards adsorbed substrates, resulting in a net energy loss in the form of heat. The faster is the recombination rate compared to the charge transfer kinetics, the lower is the efficiency of the photocatalyst. In the bulk of the material, recombination processes are very efficient and occur at a very high rate. However, due to the presence of the electric field causing band bending, the majority charge carrier concentration $n(x)$ at the photocatalyst surface exponentially falls with increasing band bending $q\Delta\phi_{sc}$:

$$n(x) = n_{bulk} \exp -\left(\frac{q\Delta\phi_{sc}}{k_B T}\right) \qquad (1.2.2)$$

where n_{bulk} is the bulk charge carrier concentration, k_B is the Boltzmann constant and T is the temperature. Thus, in the space charge region, the separation between the charge carriers is much

more efficient than in the bulk, allowing the lifetime of the minority carriers at the semiconductor surface to be increased enough so that they can be efficiently transferred towards adsorbed species. However, if the charge transfer from the photocatalyst surface towards the substrates is slow, under illumination the majority charge carriers will accumulate in the space charge region changing the profile of the potential at the interface, i.e., band bending will be reduced, and recombination processes will be efficient also at the semiconductor surface. It is important to note, moreover, that in the case the photocatalyst material is in the form of small nanoparticles, to obtain a sufficient band bending it is necessary that the size of the particles is larger than the Debye length (L_D), defined as:

$$L_D = \left(\frac{\varepsilon\varepsilon_0 k_B T}{2q^2 N}\right)^{\frac{1}{2}} \quad (1.2.3)$$

where N is the dopant concentration. If the nanoparticles are smaller than the characteristic Debye length, a sufficient band bending cannot be established.

The absolute position of the valence (VB) and conduction band (CB) redox potentials determine the thermodynamic constraints for the range of attainable reduction and oxidation half reactions which can be promoted at the surface of a given semiconductor photocatalyst. In this respect, since different semiconductor materials are characterized by a different electronic structure, and consequently a different positioning of the VB and CB redox potentials, for a given photocatalyst to be able to promote a redox reaction it is essential that the oxidation potential of the electron donor couple (i.e., the one being oxidized) and the reduction potential of the electron donor couple are more positive (lower in the graph, Figure 1.2.4) and more negative (upper in the graph, Figure 1.2.4) than the valence and conduction band redox potentials, respectively, under the given experimental conditions. If the thermodynamic requirements are not met for both half-reactions, the reaction cannot be promoted by the photocatalyst. Consequently, materials characterized by a wider band gap are also capable of promoting a wider range of photocatalytic processes. However, this increased versatility comes at the expense of requiring irradiation with more energetic photons, thus limiting the possibility of exploiting visible light (and, therefore, to utilize sunlight) to perform photocatalysis.

It is important to note that the experimental conditions, especially regarding pH, play a fundamental role in photocatalysis, and can profoundly also impact the thermodynamic feasibility of a photocatalytic half reaction, as the potential of a lot of redox couples heavily depend on pH. Moreover, the absolute position of the band edges of metal oxide photocatalysts also exhibit a

Nernstian shift with the pH change. A change in pH, thus, can alter the relative position of a redox couple with respect to the position of a band edge potential, possibly completely changing the thermodynamic feasibility of the whole photocatalytic process.

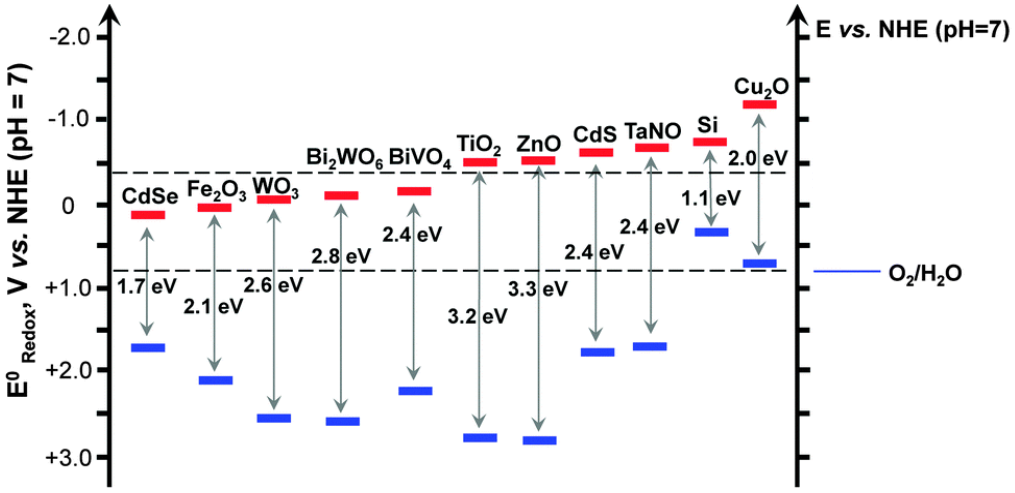

Figure 1.2.4: Position of the band edges of some commonly used semiconductor photocatalyst vs NHE at pH = 7.[7]

1.3 Titanium dioxide in photocatalysis

Titanium dioxide represents the prototypical semiconductor photocatalyst material since the earliest days of photocatalysis. By these means, the physical phenomenon of photocatalysis was first discovered in 1972 by Fujishima and Honda, when they observed that water could be split in gaseous H_2 and O_2 using titanium dioxide electrodes under UV-light irradiation.[8] Since then, titanium dioxide posed himself as a very powerful semiconductor for photocatalytic applications due to its many advantageous properties, some of the most notable of which being its chemical stability (i.e., the material does not undergo photoanodic corrosion under a huge range of experimental conditions such as strong alkaline and acidic solutions), cheapness, non-toxicity, and environmental friendliness. Moreover, titanium dioxide still represents nowadays the centrepiece semiconductor photocatalyst due to its most appealing characteristic, i.e., the extremely favourable positioning of its valence and conduction band potentials, allowing to efficiently promote a wide range of photocatalytic processes. Indeed, photogenerated holes in the VB of titanium dioxide, lying at E^0 = 3.0 V vs NHE at pH = 0 (thus characterized by a high oxidative power, superior to most photocatalysts), are capable of easily oxidize most organic compounds of environmental interest. On top of that, the bottom of the conduction band electrons is always located at negative potentials, thus making titanium dioxide also suitable to photocatalyse technologically relevant reduction reactions such as H_2 evolution, thus extending the TiO_2 application range also to the solar fuel production field.

The exact positioning of the VB reduction potential in titanium dioxide, as well as many other properties influencing its efficiency as a photocatalyst, is strictly dependent on its specific crystal phase. Titanium dioxide, in fact, is a solid inorganic compound present in nature mainly in three different crystalline forms, i.e., rutile, anatase, and brookite. Rutile is of relatively high abundance in nature, whereas both anatase and brookite are extremely rare. Moreover, oppositely to anatase, brookite is also quite difficult to synthesize even at laboratory scale, and thus represents a much less interesting phase for applications in photocatalysis and material sciences more in general. For such reason, the properties of brookite will be only briefly discussed herein.

As illustrated by the phase diagram of titanium dioxide, anatase represents a metastable phase formed at lower temperatures than rutile (Figure 1.3.1). Application of a thermal treatment to anatase induces an anatase to rutile phase transition, for which the specific transition temperature has been found to dependent on several parameters. However, for fine powder materials of relatively high purity, it can be stated that the phase transition in air is generally located in the 600-700 °C range. The rutile phase is more stable than anatase at all temperatures and pressures: once performed, the phase transition is irreversible.[9]

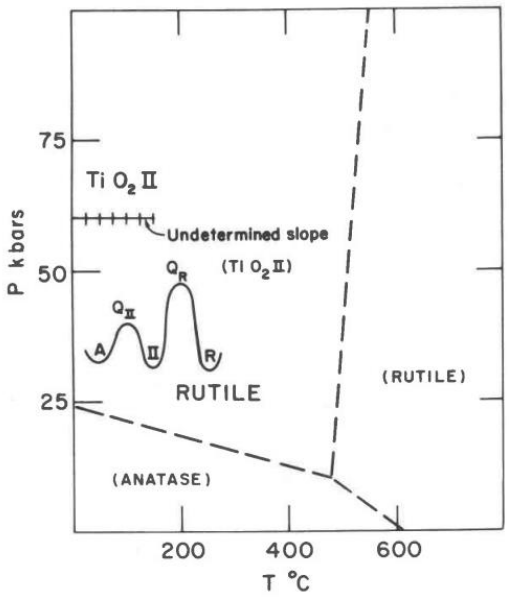

Figure 1.3.1: Phase diagram of titanium dioxide, illustrating that anatase represents a metastable phase formed at lower temperatures than rutile. The diagram also shows the domain in which the α-PbO_2 structured TiO_2 II polymorph is formed, although such polymorph is very rarely formed and has very low interest in photocatalytic applications.[9]

Anatase and rutile crystallise in a tetragonal unit cell, whereas the brookite structure is represented through an orthorhombic cell. The lattice parameters and space groups for the three crystalline phases are reported in Table 1.3.1.

The basic building block composing the structures of anatase and rutile is constituted by a titanium atom coordinated by six oxygens in a distorted octahedron configuration, although the distortion is much more pronounced in anatase. In each structure, the two titanium-oxygen bonds orthogonal to the octahedron plane are slightly longer than those in-plane, and in anatase a strong deviation from the theoretical 90° angle of the bonds is observed because of distortion. The main difference between the structure of anatase and that of rutile consists in how these building blocks are chained together. In rutile, each building block is linked with his neighbouring ones by sharing oxygen ions with other adjacent titanium atoms. Polyhedron constructed at the vertices of the elementary cell, moreover, also share one edge of the polyhedron (Figure 1.3.2 c). Instead, in the case of anatase, every polyhedron is linked with its neighbouring by sharing four edges. The unit cells of anatase and rutile also differs in the number of building block included within the elementary cell, equal to four and two, respectively. In both cases, oxygen ions are always coordinated with three neighbouring titanium ions (Figure 1.3.2).

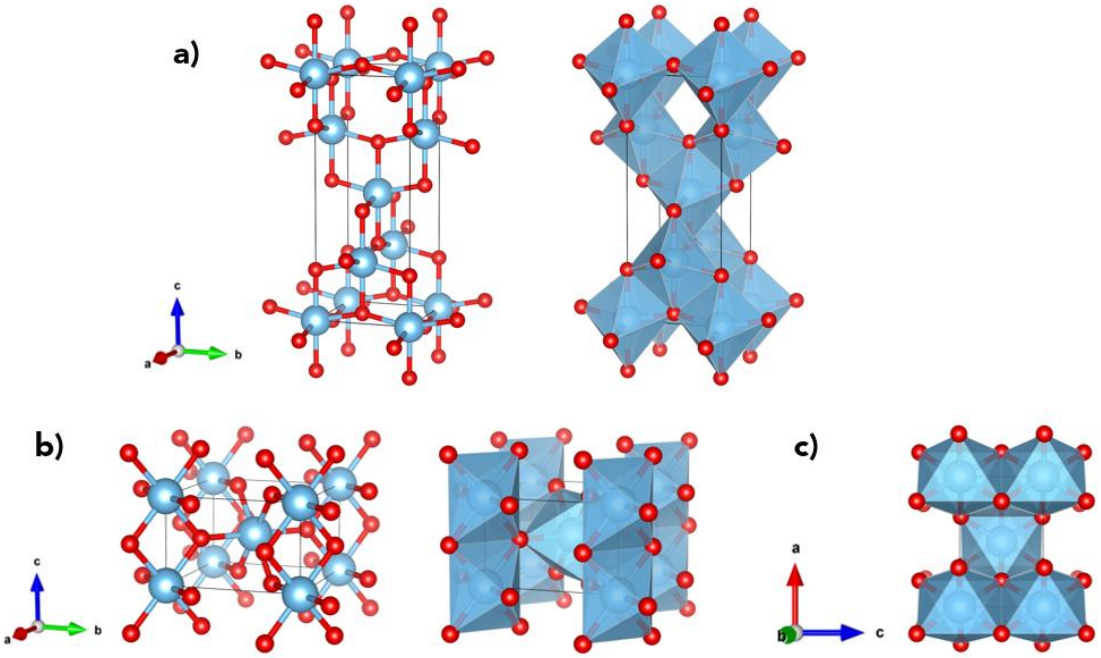

Figure 1.3.2: Balls & sticks and polyhedron representation of the unit cell of anatase (a) and rutile (b). Orienting the crystal structure of rutile along the b axis allows to observe that each octahedron located at the vertices of the unit cell also share one common edge (c).

Indeed, the structural differences in anatase and rutile are reflected in both their mass density and, more importantly, their electronic structure. The electronic band structures and density of states (DOS) of the different titanium dioxide crystal phases, calculated at the DFT GGA level of theory, are reported in Figure 1.3.3. In all three cases the DOS is quite similar, with the valence band DOS being mainly composed of O 2p states and few Ti 3d states, whose hybridization contributes to the formation of bonding states in the VB. The hybridization between the O 2p

and Ti 3d, moreover, broadens the valence band and promotes photogenerated hole transfer.[10] Instead, the conduction bands are mainly composed of Ti 3d states and few O 2p states, where hybridization leads this time to the formation of anti-bonding states. Most importantly, from the electronic band structure, we note that whereas rutile and brookite are direct band gap semiconductors, i.e., the top of the valence band and the bottom of the conduction band are vertically aligned in wave momentum in the first Brillouin zone, anatase is an indirect band gap semiconductor. Since electronic transitions in semiconductors must respect the selection rule of momentum conservation, electronic excitations from the top of the valence band to the bottom of the conduction band in anatase must be assisted by a phonon, differently from the other two phases. The requirement of the assistance of a phonon becomes particularly interesting when considering that, differently from the other two phases, also the recombination of electrons photopromoted to the conduction band with photogenerated holes at the top of the valence band requires the assistance of a phonon, and since phonon-assisted transitions are much slower that direct electronic transitions, this results in a net increase of the photogenerated electron-hole lifetime with respect to that of rutile and brookite.[11] The better charge separation in anatase improves its performance in photocatalysis compared to rutile and brookite, making anatase the most photocatalitically active and appealing titanium dioxide crystal phase in photocatalysis regardless of its more limited solar light absorption ability or possibly lower crystallinity due to the limited range of thermic stability not allowing calcination at temperatures as high as those of rutile (Table 1.3.1).

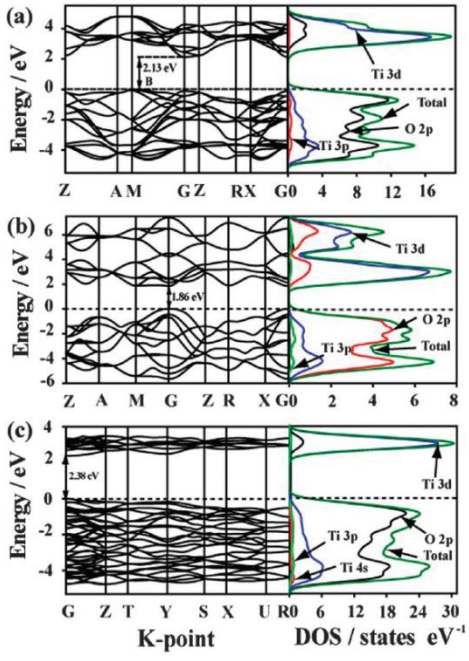

Figure 1.3.3: Electronic band structure and density of states of anatase (a), rutile (b) and brookite (c) calculated at the DFT GGA level of theory.[11]

Table 1.3.1: Structural parameters, density, and band-gap energy of different TiO_2 polymorphs.[12,13]

Phase	Crystal Structure	Space Group	a (Å)	b (Å)	c (Å)	Density (g cm^{-3})	Band Gap (eV)
Rutile	Tetragonal	$I4_1/amd$	4.584	4.584	2.953	4.24	3.00
Anatase	Tetragonal	$P4_2/mnm$	3.782	3.782	9.502	3.83	3.20
Brookite	Orthorhombic	$Pbca$	5.436	9.166	5.135	3.17	3.26

As for most metal oxide semiconductors used as photocatalyst, titania is thermodynamically stable as a non-stoichiometric compound characterized by the presence of anionic defects in the form of oxygen deficiencies, and it is thus better represented through the formula TiO_{2-x}. In titanium dioxide, the presence of oxygen vacancies is reflected in the formation of localized paramagnetic Ti^{3+} centres, in the same amount as oxygen vacancies. These Ti^{3+} ions can operate as electron donor species by forming an intra-band gap energy level localized close to the conduction band, effectively acting as a dopant specie intrinsic to the titanium dioxide structure itself. This phenomenon is at the basis of the observed n-type character of titanium dioxide even in its pristine, undoped form.

Titanium dioxide, however, is also affected by a number of shortcomings, the most notable being the poor visible light absorption due to the wide band gap, with the consequent need of exciting titanium dioxide with highly energetic UV radiation, the high recombination rate of the photoproduced charge carriers (which is a problem affecting all semiconductor materials employed in photocatalysis) and the difficulty of anchoring titanium dioxide over a supporting material making its recovery quite difficult, since titanium dioxide is commonly used in the form of suspended powders.

1.3.1 Crystal Facets Engineered Anatase

As heterogeneous photocatalysis consists of a physico-chemical process occurring at the interface between a semiconductor solid material and a different phase, the surface composition and structure of the semiconductor photocatalyst primarily affects the properties and the performance of the material in each reaction. More generally, the surface of titanium dioxide is involved as a protagonist in nearly all applications of the metal oxide material in science, from photocatalysis,[14–16] to DSSCs,[17,18] to lithium-ion batteries,[19,20] in which an interaction between molecules and/or ions is essentially required. In photocatalysis, particularly, the adsorption of the

reactants on the surface of the photocatalyst is a necessary requirement for photogenerated charge carriers to be transferred from the surface of the photocatalyst to the substrates.

The specific crystal habit of anatase, the most active TiO_2 polymorph in photocatalysis, is of particular interest when designing titanium dioxide-based materials for photocatalytic applications since different facets exposure in its crystallites has been found to deeply affect both the adsorption of substrates and the charge carrier dynamics of the metal oxide. The importance of the adsorption modes on different titanium dioxide crystal facets can be appreciated by comparing the adsorption of dyes or water molecules on anatase (001) and (101) surfaces. For instance, whereas anatase (101) facets allow only the adsorption of water in its molecular form, (001) facets predominantly adsorb water in a dissociative manner.[21–23] Moreover, several studies evidenced that different titanium dioxide crystal facets adsorb dyes and organics (such as, for example, the important model molecule formic acid) differently on different crystal facets, affecting both the electron injection and transfer dynamics at the semiconductor-substrate interface.[24–28]

In this sense, rarer (001) facets in anatase are generally considered as more reactive than the thermodynamically more stable (101) surfaces. In fact, according to the Wulff construction, which allows to predict the equilibrium habit of a crystal based on the minimization of the surface tension of exposed facets (and confirmed by the habit showcased by natural anatase minerals),[29] the equilibrium anatase shape of minimum Gibbs energy is obtained in the form of a slightly truncated tetragonal bipyramid, exposing eight trapezoidal isosceles (101) facets as well as two top squared (001) facets (Figure 1.3.4 a). In the predicted construction in vacuo, 94% of the surface exposure is composed of (101) surfaces, whereas (001) account only for the 6% of the total exposure. The strikingly marked difference in exposure represents a direct reflection of the different surface tension between the two crystal facets, being equal to 0.43 J m^{-2} and 0.90 J m^{-2} for (101) and (001), respectively.[30] This wide discrepancy in surface tension originates from the different composition and arrangement of atoms in the two crystal facets. In fact, anatase (001) surfaces, differently from (101), are exclusively composed of fivefold undercoordinated Ti centres, in which surface atoms are configured in such a way so that very large Ti-O-Ti bond angles are formed, generating very destabilized 2p states on surface oxygen atoms.[31] The peculiar structure and thermodynamic instability of (001) surfaces are at the basis of their higher reactivity compared to (101) surfaces, which is evidenced by their tendency to reconstruct under UHV conditions or by their ability to dissociatively adsorb water, methanol, or formic acid, contrarily to (101) surfaces, for which the opposite behaviour is observed.[32]

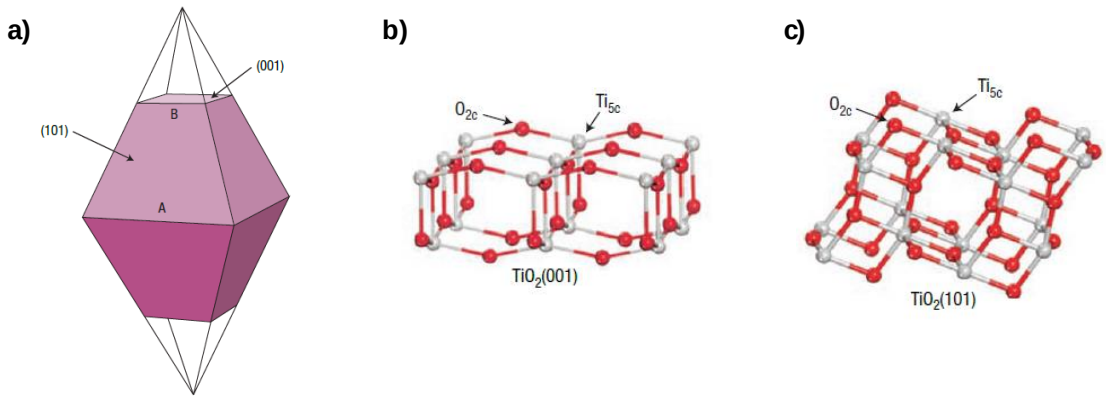

Figure 1.3.4: Equilibrium shape of anatase according to the Wulff construction (a); atomic arrangement on anatase (101) and (001) surfaces (b and c).[31]

The expected higher reactivity of (001) facets has attracted a lot of attention in the field of photocatalysis as a possible way to improve the photocatalytic activity of titanium dioxide by preparing materials with increased (001) facets exposure with respect to the equilibrium Wulff construction. Despite the reactivity of (001)-anatase had been predicted and theorized many years ago,[33] the outbreak in synthesizing anatase crystals with high exposed (001) facets had only started in 2008 after the pioneer work of Yang et al.,[34] who firstly successfully synthesized anatase crystals enclosed by 47% (001) and 53% (101) facets. In fact, starting from theoretical studies which proved that the shape of titanium dioxide crystals could be controlled by using different species adsorbed at surface terminations,[35] Yang and his co-workers found, through theoretically screening a series of 12 non-metallic atoms as adsorbates that fluorine atoms adsorbed at the anatase surface could invert the relative stability of (101) and (001) facets compared to clean ones, possibly allowing to synthesize titanium dioxide crystals with high exposed (001) facets. Their theoretical calculation was confirmed by the experimental preparation of highly truncated anatase crystals through a hydrothermal route using TiF_4 as Ti source and hydrofluoric acid as selective capping agent (Figure 1.3.5). Since then, the hydrothermal route using fluorine as selective capping agent has become the gold standard for preparing highly truncated anatase materials.

Indeed, materials bearing a higher percentage of exposed (001) facets generally confirmed the hypothesized improved photoactivity compared to materials mainly exposing (101) facets. However, as the number of studies on the subject started increasing, the correlation between photoactivity and increased exposure of (001) facets became more and more complex.[30] In particular, many researchers figured out that the photoactivity of crystal facets engineered (001)-anatase did not scale linearly with increasing (001) percentage facets exposure, but rather materials benefitted from an optimal (001)/(101) facets ratio range whose specific value depended on both the chosen test reaction and the synthetic conditions, indicating that the higher reactivity of (001)

facets was not the only factor contributing to the improved photoactivity of crystal facets engineered (001)-anatase, but others were also contributing.[36–38] Light on such effects was shed by the studies of Ohno et al., who observed that Pt and PbO_2 nanoparticles deposited through photodeposition (a metal nanoparticles deposition method based on the oxidation or reduction of precursors in solution by means of electron or holes photogenerated through the electronic excitation of the semiconductor, in-depth discussion provided at page 54), were selectively deposited on (101) and (001) facets, respectively.[39,40] Thus, in the case of crystal facets engineered anatase (101) facets acted as reductive sites, whereas (001) acted as oxidation sites. More importantly, this implied that electrons were preferentially migrating towards (101) facets, whereas holes preferentially migrated towards (001) surfaces, in a synergistic mechanism which resulted in a spatial separation of the photogenerated charge carriers with a consequently hindered recombination and improved photocatalytic activity. This behaviour, observed and confirmed in a plethora of subsequent studies,[41,42] has been rationalized in terms of a so called "surface heterojunction" originating from the different alignment of the redox potentials of (001) and (101) surfaces, causing the preferential migration of holes and electrons towards such facets (Figure 1.3.6b).[43,44]

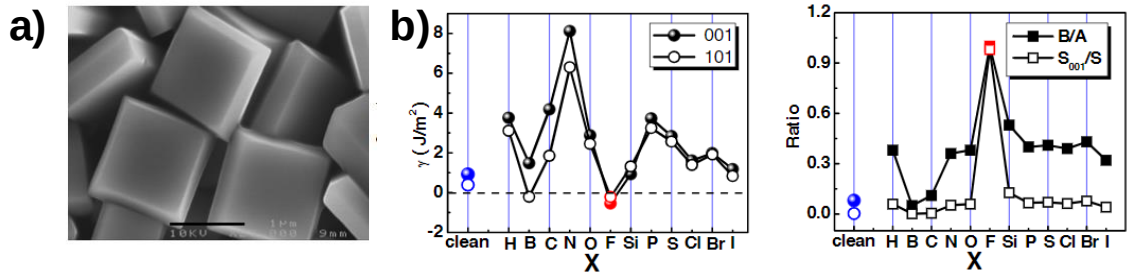

Figure 1.3.5: Highly truncated titanium dioxide crystals synthesized by Yang et al. in 2008 (a); Theoretical screening of the surface capping agent illustrating that fluorine could promote the growth of titanium dioxide with high exposed (001) facets (b).[34]

Since then, crystal facets engineering titanium dioxide anatase with increasing amounts of exposed (001) facets has attracted a lot of attention in the field of science and technology due to the possibly increased reactivity of highly-strained (001) surfaces and improved charge separation offered by an optimized (001)/(101) ratio, allowing to exploit the surface heterojunction formed between (001) and (101) surfaces and improving the charge separation within the metal oxide semiconductor material.

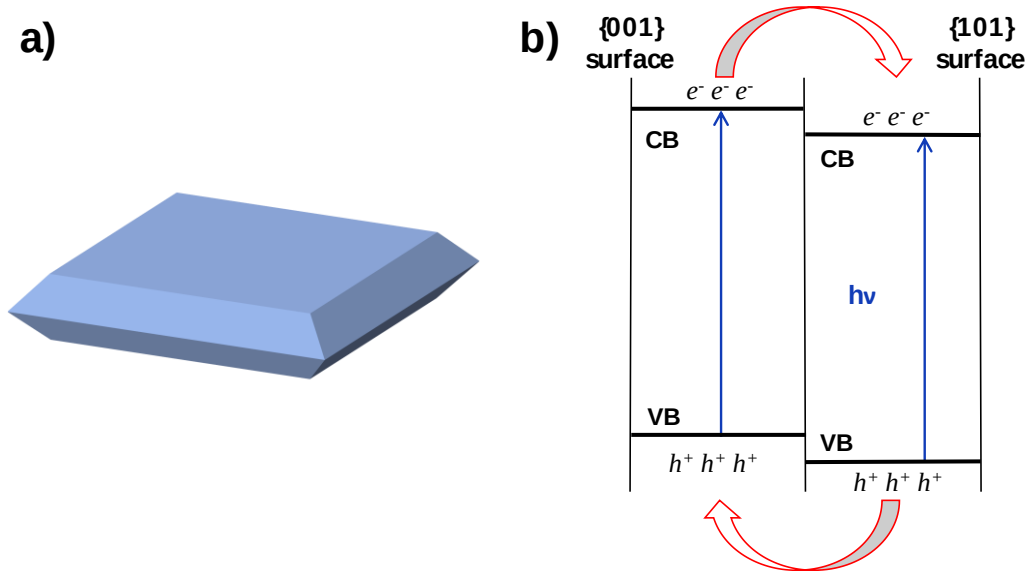

Figure 1.3.6: Scheme of a highly truncated titanium dioxide "nanosheet" with high exposed (001) facets (a); band diagram of the surface heterojunction causing the preferential migration of electrons towards (101) facets and holes towards (001) facets (b).

Nanosheet-shaped titanium dioxide is typically synthesized in environments containing concentrated F^- anions. This synthesis results in producing materials with surfaces covered by chemisorbed fluoride anions (≡Ti-F surface moieties).[32] However, several literature studies have shown that these F species may significantly alter the interfacial properties of titanium dioxide (section 1.3.3), leading to modifications in the photoactivity of the metal oxide semiconductor. The effects of surface fluorination on photoactivity are not yet fully understood, and the literature reports both beneficial and detrimental effects.[45-50] Furthermore, the presence of different amounts of surface fluorine among differently shaped titanium dioxide materials makes it challenging to determine whether photoactivity differences are induced by morphological variations or the extent of surface fluorination.[45,51] As a result, removing surface F impurities through post-synthetic treatments has become a standard procedure in literature studies investigating the properties of (001)-facets enriched anatase in photocatalysis.

Typically, residual surface F species are removed either through milder treatment involving washing cycles with aqueous alkali hydroxide solutions (often NaOH) or through harsher annealing at high temperatures (400-500 °C). Both methods have been reported to be effective.[48,52,53] However, it is important to note that thermal treatments can cause significant changes in the structure of anatase, such as surface reconstructions[48,54] and/or nanoparticles sintering,[55,56] which are not observed (or are greatly limited) when surface F species are removed via washing procedures.[57,58]

Due to their high surface energy, in fact, clean anatase (1 × 1)-(001) surfaces usually restructure to a (1 × 4)-(001) surface,[59] representing the surface reconstruction allowing to best minimize the surface stress of clean anatase (001) surfaces.[60] The structure of the reconstructed anatase (1 × 4)-(001) surface has been object of a conspicuous number of investigations throughout the years involving the combination of DFT calculations with experimental surface characterization techniques including low-energy electron diffraction (LEED), XPS and STM.[59] Nowadays, the structural model most widely accepted to describe the structure of (1 × 4)-(001) facets of anatase consists of the "ad-molecule" (ADM) model, originally theorized and reported by Lazzeri and Selloni.[60] In their DFT-based model, they proposed that surface bridging oxygens of (1 × 1)-(001) surfaces were replaced by TiO_3 rows periodically with a (1 × 4) periodicity, such model allowing to describe both the surface stress relief upon reconstruction while being highly consistent with experimental images (Figure 1.3.7 c,d). The most convincing evidence of the ADM model, however, was provided by Yuan et al. in 2017,[58] where they performed an in-situ atomic-scale side-view observation of the reconstruction using an aberration-corrected STEM and a heating holder system (Figure 1.3.7 a,b). Through their study, moreover, they confirmed that the reconstruction was triggered by the thermal treatment, as the surface of anatase (001) showed the typical (1 × 1)-(001) structure obtainable through terminating the bulk structure of anatase (001) until the sample was heated up to 750 °C. The unreconstructed (1 × 1)-(001) surface, moreover, was reported to have been observed in F-free nanosheet-shaped titanium dioxide whose surface was cleaned via NaOH washing by the same research group, its (1 × 4)-(001) reconstruction being observed only upon thermally annealing the sample, further confirming the thermal treatment as the trigger for the reconstruction.[57]

The effects of the (1 × 4)-(001) reconstruction on the physico-chemical properties of the resulting materials should be carefully considered when choosing the most appropriate F-species removal post-synthesis treatment for fluorine-free titanium dioxide materials, especially for nanosheet-shaped anatase that mainly exposes (001) facets. In fact, a recent study by Mino et al.[61] highlighted significant differences in surface/interfacial features of F-free nanosheet-shaped anatase, such as hydroxylation and hydrophilicity, depending on whether surface F species were removed via washing procedures or thermal annealing. In particular, thermal annealing resulted in a more complete removal of F species but led to a significant decrease in surface hydroxylation and hydration induced by the (1 × 4)-(001) surface reconstruction, negatively affecting the performance of nanosheet-shaped anatase in phenol photodegradation, even compared to the starting F-containing anatase nanosheets. Conversely, platelet-like anatase cleaned via NaOH washing showed significantly improved photoactivity compared to the starting F-containing

nanosheets, as the surface hydroxylation and hydration properties of (1 × 1)-(001) anatase were improved upon washing. These results are consistent with the theoretical prediction of Selloni et al.[54] that (1 × 4) reconstructed surfaces exhibit depressed reactivity compared to anatase (1 × 1)-(001) facets. Therefore, to avoid undesired (1 × 4)-(001) reconstructed surfaces, all the materials prepared in this PhD thesis were cleaned from surface residual F species by applying washing cycles with NaOH aqueous solutions rather than thermal annealing treatments.

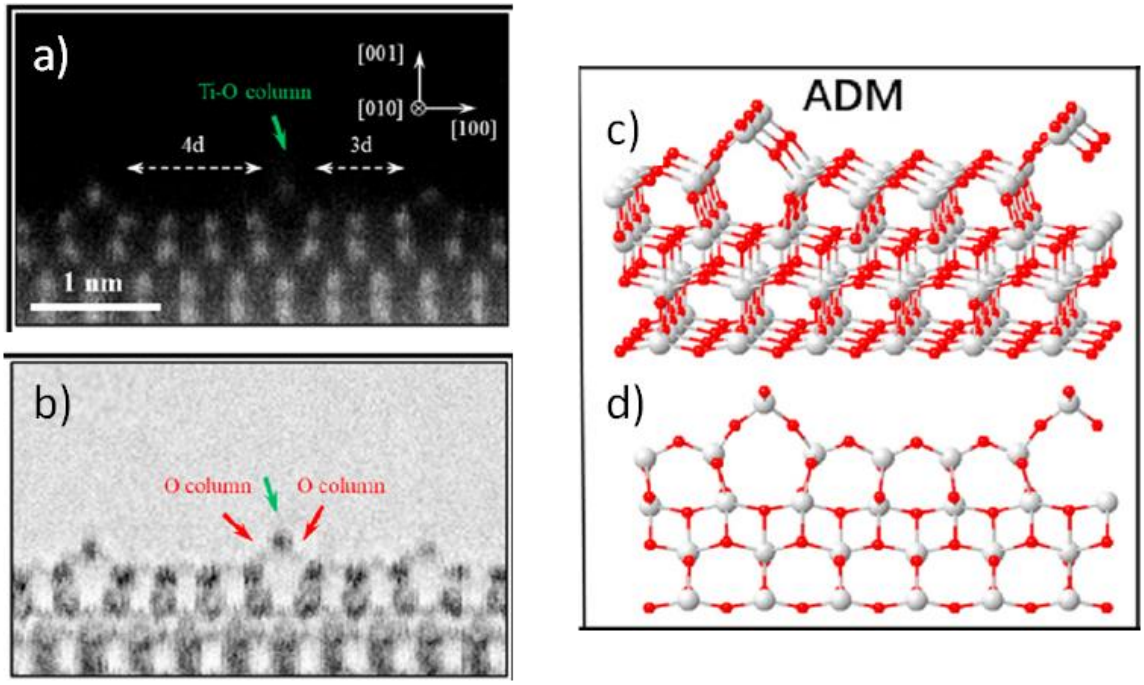

Figure 1.3.7: Atomic resolution HAADF-STEM and the corresponding BF-STEM images of the (1 × 4) reconstructed (001) surface viewed along the [010] axis (a,b);[58] ad-molecule model (ADM) (c) and its corresponding view along the [100] axis (d).[60]

1.3.2 F-doped Titanium Dioxide

Despite its wide range of advantageous properties, two main drawbacks limit the performance of titanium dioxide in photocatalysis, i.e., the fast recombination of the photoexcited charge carriers and its wide band gap (~2.9-3.2 eV depending on the polymorph), which demands the use of highly energetic UV radiation to promote its electronic activation, making it poorly capable of harvesting the solar spectrum. Various methods of titania modification have been proposed to improve its photocatalytic performance, including (but not limited to) doping with metal and/or non-metal (*p*-block or transition metal) elements and coupling with different metal oxides.[62–68]

For this purpose, bulk doping has attracted a lot of interest as a strategy to possibly overcome the main limits of titanium dioxide due to its capability of delaying the recombination of photogenerated charge carriers, as well as extending the absorption spectrum of TiO_2 towards visible light.[69] In fact, doping the bulk structure of a semiconductor with impurities results in the

insertion of intra-band gap states close to the valence or the conduction band of titanium dioxide (a more detailed description of *n* and *p*-type doping is provided at page 17). Such states, in fact, are capable of both trapping photopromoted CB electrons, thus delaying their recombination with VB holes, and allow new electronic transitions requiring the absorption of lower energetic photons, thus effectively extending the absorption spectra of titanium dioxide towards visible light.[70]

The bulk structure of titanium dioxide can be doped either with cations, especially transition metal ions, as well as *p*-block anions. The effects on photoactivity of cation doping has been widely investigated in the past years. Among these, the ability of trapping both types of charge carriers proved Fe, Cu and Mn to be better dopants compared to Cr, Ni and Co, which are only capable of trapping either holes or electrons.[71,72] More generally, a trend for which cations with higher valence (e.g., Nb^{6+} or Ta^{5+}) resulted to be beneficial dopants for the photocatalytic activity of titanium dioxide has been reported, whereas an opposite behavior was instead observed for lower valence cations.[73] A very in-depth investigation on the effect of cation doping has been performed by Choi et al., who systematically studied the doping of TiO_2 with 21 different metal ions.[74] In their study, they discovered that the photocatalytic activity of metal oxide semiconductors was significantly improved in both oxidation and reduction processes by doping with Fe^{3+}, Mo^{5+}, Os^{3+}, Ru^{3+}, V^{4+} and Rh^{3+}. However, these materials absorbed visible light only in rare cases and, moreover, were characterized by high thermal instability.

A second generation of doped TiO_2 photocatalysts, characterized by the introduction of *p*-block elements such as sulfur, carbon or nitrogen in the structure of the metal oxide semiconductor *in lieu* of transition metal ions, was then explored.[75] With anion doping, the DOS structure of the valence band of the semiconductor is modified, since anion doping usually results in the substitution of oxygen ions with dopant atoms. Due to this modification, a general upwards shift of the valence band potential is obtained, with a consequent narrowing of the band gap of the semiconductor material, thus also extending the absorption of the semiconductor towards visible light. Possible anions commonly employed to dope TiO_2 include C, N, F, P, O, S.[69]

Among these, fluorine represents a particularly interesting anionic *p*-block dopant.[76–78] In fact, the introduction of F^- anions in the bulk structure of titania results in highly improving its photocatalytic activity in the mineralization of various organic compounds, also under visible irradiation.[78] In fact, bulk doping the lattice of titanium dioxide with fluorine results in the substitution of oxygen atoms with F^- anions, causing the generation of Ti^{3+} centers, since the substitution of O^{2-} with fluoride results in the introduction of an additional electron in the structure because of charge compensation. Therefore, F-doped TiO_2 can be considered as a non-

stoichiometric oxide of general formula $Ti^{4+}_{(1-x)}Ti^{3+}_{x}O^{2-}_{(2-x)}F^{-}_{x}$, in which fluorine and Ti^{3+} centers are located far from each other, as evidenced by EPR measurements (Figure 1.3.8).[79] The formation of such Ti^{3+} states in the bulk of titania has been widely reported as one of the main factors at the origin of the improved photoactivity of F-doped TiO_2.[78,80] In fact, the high localization of electrons in Ti 3d orbitals causes the formation of an acceptor level whose localization energy localization is close to that of the CB of titania: as photoexcited electrons can be captured by these states, they promote the separation of photogenerated charge carriers, thus resulting in an improved photoactivity of the materials. Moreover, fluorine doping increases the thermal stability range of the anatase phase, shifting the anatase to rutile phase transition to higher temperatures. Thus, F-doped anatase can be calcined at higher temperatures with respect to pristine anatase, allowing to obtain materials with improved bulk charge transport properties due to their higher crystallinity.[32,76–78,81–83]

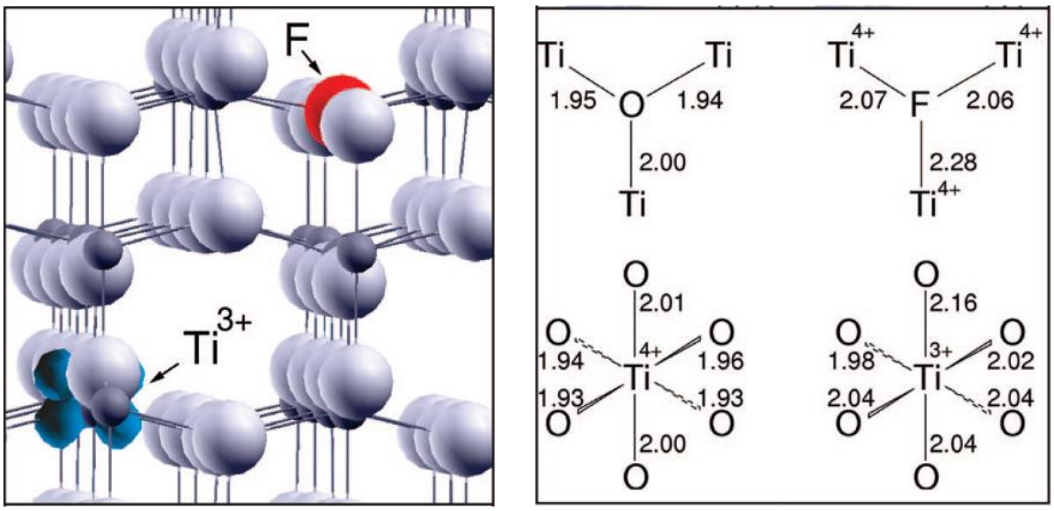

Figure 1.3.8: Ball and stick models for F-doped anatase TiO_2 reporting the spin density of the Ti^{3+} excess electron (a); Bond lengths in angstrom (b).[79]

1.3.3 Titanium dioxide surface fluorination

Parallelly to its use as a bulk dopant specie, fluorine can be also employed as a capping agent at the surface of titanium dioxide in a possible strategy aimed at improving its performances as a photocatalyst, especially in radical-mediated oxidation paths.[51,84,85] In fact, the presence of fluorine at the surface of titanium dioxide results in strongly modifying its overall surface chemistry.[86–88]

Fluorination of the surface of titanium dioxide occurs as a consequence of a fast adsorption of fluoride anions on the semiconductor surface, decreasing the amount of surface hydroxyl groups, i.e., the typical termination of TiO_2, in favor of ≡Ti-F species.[89] This process occurs via a ligand exchange reaction which is very favored at acidic pH: in fact, an almost complete displacement of surface -OH groups is observed at pH 3.7.[90,91]

This modification strongly impacts the adsorption properties at the water-semiconductor interface, especially that of organic species, and significantly modifies the photocatalytic behavior of the semiconductor metal oxide. In particular, ≡Ti-F groups prevent the trapping of holes at the semiconductor surface in the form of surface titanium hydroxy-radical groups ≡Ti-O$^{\bullet}$, formed via direct oxidation of surface -OH groups by means of valence band holes, h_{VB}^{+}. In fact, contrarily to hydroxyl groups, the reduction potential of photogenerated holes at the semiconductor surface is not positive enough (c.ca +3.0 V) to oxidize surface F^{-} anions to their corresponding radical anion ($E^{0}_{F^{\bullet}/F^{-}}$ = +3.6 V). Instead, photogenerated holes at the F-TiO_2 surface can only directly react with water molecules there adsorbed or recombine, resulting in an increased net production of $^{\bullet}$OH radicals in solution, one of the main oxygen reactive specie responsible for many photocatalytic processes in aqueous media, by means of the here reported mechanism:[83,84,92,93]

$$\equiv Ti - OH + h_{VB}^{+} \rightarrow \equiv Ti - O^{\bullet} + H^{+} \qquad (1.3.1)$$

$$\equiv Ti - F + h_{VB}^{+} + H_2O \rightarrow \equiv Ti - F + HO^{\bullet} + H^{+} \qquad (1.3.2)$$

Due to their protagonist role in oxidative photocatalytic chemistry in the aqueous media, an improved production of hydroxy-radicals on the surface of F-TiO_2 may definitely improve the overall performance of titanium dioxide, especially in the photocatalytic oxidation of organic molecules.

Crystal facets engineered anatase with high exposed (001) surfaces, moreover, can interact with surface fluoride anions in a very peculiar and interesting way. In fact, as shown in the brilliant work of Chen et al. on the photocatalytic oxidation of ammonia in the gas phase,[94] the presence of fluorine on the surface of crystal facets engineered titanium dioxide can deeply influence the charge carrier migration over different crystal facets due to the interaction of fluorination with the surface heterojunction present in the metal oxide support. In their work, in particular, they showed that F^{-} ions, due to their high electronegativity, generate a negative electric field on the surface of titanium dioxide,[95] promoting a more marked drawing of the photogenerated holes towards fluorinated surfaces due to electrostatic effects.

In particular, as (001) facets tend to intrinsically act as effective hole-trapping sites, the presence of F^{-} ions adsorbed on such facets further promote the diffusion of positively charged holes towards (001) facets, resulting in a synergistic beneficial effect on the overall electron-hole separation. In contrast, when surface F^{-} ions are present on (101) facets, the interaction between the preferential migration of electrons towards such crystalline facets and fluoride anions there

adsorbed work rather in opposite directions. In fact, while photogenerated electrons tend to migrate on (101) facets, the surface F^- anion electrostatic effect may simultaneously promote the attraction of the photogenerated holes on the same facets, with a consequent enhancement of the undesired electron-hole recombination process. Therefore, crystal facets engineered anatase with high exposed (001) facets may be used not only to improve the charge separation in titanium dioxide due to an optimized (001)/(101) ratio, which favors charge separation, but also as a support to further exploit the possible beneficial effects on photoactivity induced by surface fluorination.[83]

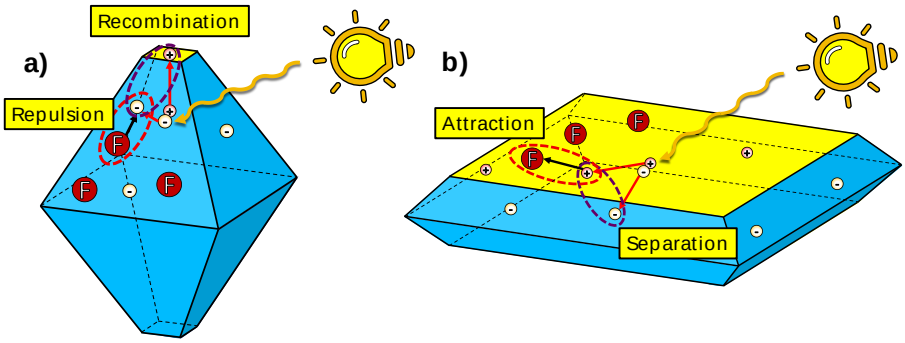

Figure 1.3.9: Schematic illustration of the likelihood of charges migration on fluorinated (101) facets (a) and (001) facets (b).

1.3.4 Noble metal nanoparticles deposition

One of the most widely employed strategies to overcome the limitations of TiO_2 is represented by its surface modification with noble metal nanoparticles which, by virtue of their high work function (i.e., the energy required to remove an electron from a solid, calculated with respect to the vacuum level), are capable to efficiently promote the separation of photogenerated charge carriers in a semiconductor material. The enhancement in reactivity was first observed by Sato et al. in 1980 for the photoconversion of water to H_2 and O_2 using Pt/TiO_2.[96]

The surface properties of a semiconductor drastically change whether they are isolated or in contact with another phase such as a noble metal or an electrolyte solution. In fact, when a semiconductor comes in contact with a metal, a spontaneous electron transfer between the metal and the semiconductor occurs due to the equilibration of the electrochemical potential of the electron in the two different phases at thermodynamic equilibrium. In particular, if the work function of the metal (Φ_m) is higher than that of the semiconductor (Φ_s), the electrons flow from the latter to the former until equilibration of their Fermi levels is attained (Figure 1.3.10).

Due to the low concentration of free charge carriers in the semiconductor, the electric field between the metal and semiconductor interfaces cannot be effectively screened. This results in the semiconductor surface to be positively charged forming the so-called depletion layer, while the

metal surface acquires a net negative charge. By this way, a space charge region is formed. Due to the generation of an electrostatic potential, the bands of the semiconductor bend upward toward the surface. This results in the formation of an energy barrier named Schottky barrier. The height of the barrier is Φ_b given by:

$$\Phi_b = \Phi_m - E_x \qquad (1.3.1)$$

where E_x is the electron affinity, measured from the conduction band edge to the vacuum level of the semiconductor.

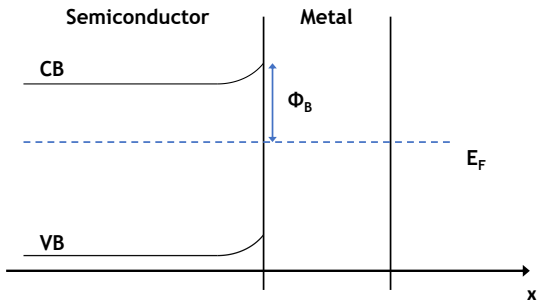

Figure 1.3.10: Schematic representation of a metal-semiconductor interphase.

Figure 1.3.11 illustrates the dynamics of photoexcited electrons in metal-modified TiO_2 powders.

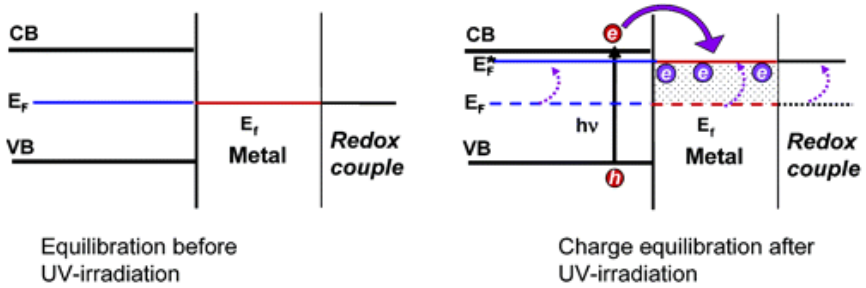

Figure 1.3.11: Fermi level re-equilibration upon photoexcitation in noble-metal surface modified TiO_2 nanoparticles.[97]

Under illumination conditions, when a photon of ultra-band gap energy is absorbed by the metal oxide, photopromoted electrons tend to be distributed between TiO_2 and the noble metal nanoparticles, until the two systems attain equilibration. This storage of photogenerated carriers within the noble metal nanoparticles results in greatly suppressing the recombination rate of the charge carriers due to the spatial separation of the photogenerated electrons. Moreover, since the accumulation of electrons increases the Fermi level of the metal towards more negative potentials, the overall reductive power of the composite materials is increased with respect of the bare TiO_2.[97] Therefore, the effect of the Schottky barrier generation is that of creating an efficient electron trap preventing electron – hole recombination. This results in a greater probability of electron transfers

from the photocatalyst surface to the reactants, thus possibly improving the photocatalytic activity of the materials.[98]

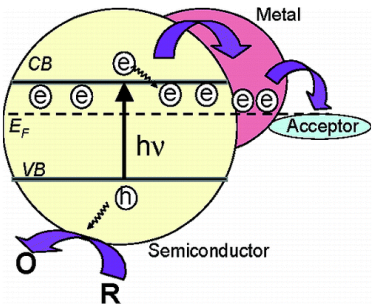

Figure 1.3.12: Scheme of electron transfers in metal modified TiO_2.

1.4 References

1. Caradonna, J. L. *Sustainability: A History*. (Oxford University Press, 2014).
2. Kampa, M. & Castanas, E. *Environ. Pollut.* **151**, 362–367 (2008).
3. *Lancet (London, England)* **392**, 1923–1994 (2018).
4. WWAP. *The United Nations world water development report 2018: Nature-Based Solutions for Water. Unesco* (2018).
5. Crini, G. & Lichtfouse, E. *Environ. Chem. Lett.* **17**, 145–155 (2019).
6. Kisch, H. *Semiconductor photocatalysis: principles and applications*. (John Wiley & Sons, 2015).
7. Xie, S., Zhang, Q., Liu, G. & Wang, Y. *Chem. Commun.* **52**, 35–59 (2016).
8. Fujishima, A. & Honda, K. *Nature* **238**, 37–38 (1972).
9. Hanaor, D. A. H. & Sorrell, C. C. *J. Mater. Sci.* **46**, 855–874 (2011).
10. Liu, J. J., Fu, X. L., Chen, S. F. & Zhu, Y. F. *Appl. Phys. Lett.* **99**, 191903 (2011).
11. Zhang, J., Zhou, P., Liu, J. & Yu, J. *Phys. Chem. Chem. Phys.* **16**, 20382–20386 (2014).
12. Ma, Y., Wang, X., Jia, Y., Chen, X., Han, H. & Li, C. *Chem. Rev.* **114**, 9987–10043 (2014).
13. Rahimi, N., Pax, R. A. & Gray, E. M. *Prog. Solid State Chem.* **44**, 86–105 (2016).
14. Xie, H., Li, N., Chen, X., Jiang, J. & Zhao, X. *Appl. Surf. Sci.* **511**, 145597 (2020).
15. Guo, Q., Zhou, C., Ma, Z. & Yang, X. *Adv. Mater.* **31**, 1901997 (2019).
16. Walenta, C. A., Courtois, C., Kollmannsberger, S. L., Eder, M., Tschurl, M. & Heiz, U. *ACS*

Catal. **10**, 4080–4091 (2020).

17. Rodríguez-Martínez, C., García-Domínguez, Á. E., Guerrero-Robles, F., Saavedra-Díaz, R. O., Torres-Torres, G., Felipe, C., Ojeda-López, R., Silahua-Pavón, A. & Cervantes-Uribe, A. *J. Compos. Sci.* **4**, 89 (2020).

18. Liu, Q. & Wang, J. *Sol. Energy* **184**, 454–465 (2019).

19. Paul, S., Rahman, M. A., Sharif, S. B., Kim, J.-H., Siddiqui, S.-E.-T. & Hossain, M. A. *Nanomaterials* vol. 12 2034 at (2022).

20. Opra, D. P., Gnedenkov, S. V & Sinebryukhov, S. L. *J. Power Sources* **442**, 227225 (2019).

21. Sumita, M., Hu, C. & Tateyama, Y. *J. Phys. Chem. C* **114**, 18529–18537 (2010).

22. Smith, P. B. & Bernasek, S. L. *Surf. Sci.* **188**, 241–254 (1987).

23. Kenmoe, S., Lisovski, O., Piskunov, S., Bocharov, D., Zhukovskii, Y. F. & Spohr, E. *J. Phys. Chem. B* **122**, 5432–5440 (2018).

24. De Angelis, F., Vitillaro, G., Kavan, L., Nazeeruddin, M. K. & Grätzel, M. *J. Phys. Chem. C* **116**, 18124–18131 (2012).

25. Laskova, B., Zukalova, M., Kavan, L., Chou, A., Liska, P., Wei, Z., Bin, L., Kubat, P., Ghadiri, E., Moser, J. E. & Grätzel, M. *J. Solid State Electrochem.* **16**, 2993–3001 (2012).

26. Gong, X. Q., Selloni, A. & Vittadini, A. *J. Phys. Chem. B* **110**, 2804–2811 (2006).

27. Li, W. K., Gong, X. Q., Lu, G. & Selloni, A. *J. Phys. Chem. C* **112**, 6594–6596 (2008).

28. Ma, S., Song, W., Liu, B., Zhong, W., Deng, J., Zheng, H., Liu, J., Gong, X.-Q. & Zhao, Z. *Appl. Catal. B Environ.* **198**, 1–8 (2016).

29. Gamboa, J. A. & Pasquevich, D. M. *J. Am. Ceram. Soc.* **75**, 2934–2938 (1992).

30. Liu, G., Yang, H. G., Pan, J., Yang, Y. Q., Lu, G. Q. M. & Cheng, H. M. *Chem. Rev.* **114**, 9559–9612 (2014).

31. Selloni, A. *Nat. Mater.* **7**, 613–615 (2008).

32. Dozzi, M. V. & Selli, E. *Catalysts* **3**, 455–485 (2013).

33. Chen, X. & Mao, S. S. *Chem. Rev.* **107**, 2891–2959 (2007).

34. Yang, H. G., Sun, C. H., Qiao, S. Z., Zou, J., Liu, G., Smith, S. C., Cheng, H. M. & Lu, G.

Q. *Nature* **453**, 638–641 (2008).

35. Barnard, A. S. & Curtiss, L. A. *Nano Lett.* **5**, 1261–1266 (2005).

36. Zhao, X., Jin, W., Cai, J., Ye, J., Li, Z., Ma, Y., Xie, J. & Qi, L. *Adv. Funct. Mater.* **21**, 3554–3563 (2011).

37. Pan, J., Liu, G., Lu, G. Q. (Max) & Cheng, H.-M. *Angew. Chemie Int. Ed.* **50**, 2133–2137 (2011).

38. Gordon, T. R., Cargnello, M., Paik, T., Mangolini, F., Weber, R. T., Fornasiero, P. & Murray, C. B. *J. Am. Chem. Soc.* **134**, 6751–6761 (2012).

39. Bae, E., Murakami, N. & Ohno, T. *J. Mol. Catal. A Chem.* **300**, 72–79 (2009).

40. Murakami, N., Katayama, S., Nakamura, M., Tsubota, T. & Ohno, T. *J. Phys. Chem. C* **115**, 419–424 (2011).

41. Liu, C., Han, X., Xie, S., Kuang, Q., Wang, X., Jin, M., Xie, Z. & Zheng, L. *Chem. – An Asian J.* **8**, 282–289 (2013).

42. Zheng, Z., Huang, B., Lu, J., Qin, X., Zhang, X. & Dai, Y. *Chem. – A Eur. J.* **17**, 15032–15038 (2011).

43. Yu, J., Low, J., Xiao, W., Zhou, P. & Jaroniec, M. *J. Am. Chem. Soc.* **136**, 8839–8842 (2014).

44. Di Liberto, G., Tosoni, S. & Pacchioni, G. *J. Phys. Chem. Lett.* **10**, 2372–2377 (2019).

45. Maisano, M., Dozzi, M. V. & Selli, E. *J. Photochem. Photobiol. C Photochem. Rev.* **28**, 29–43 (2016).

46. Yang, Y., Hong, A., Liang, Y., Xu, K., Yu, T., Shi, J., Zeng, F., Qu, Y., Liu, Y., Ding, M., Zhang, W. & Yuan, C. *Appl. Surf. Sci.* **423**, 602–610 (2017).

47. Kus, M., Altantzis, T., Vercauteren, S., Caretti, I., Leenaerts, O., Batenburg, K.J., Mertens, M., Meynen, V., Partoens, B., Van Doorslaer, S., Bals, S. & Cool, P. *J. Phys. Chem. C* **121**, 26275–26286 (2017).

48. Peng, Y.-K., Hu, Y., Chou, H.-L., Fu, Y., Teixeira, I.F., Zhang, L., He, H. & Tsang, S.C.E. *Nat. Commun.* **8**, 675 (2017).

49. Peng, Y.-K., Keeling, B., Li, Y., Zheng, J., Chen, T., Chou, H.-L., Puchtler, T.J., Taylor, R. A. & Tsang, S.C.E. *Chem. Commun.* **55**, 4415–4418 (2019).

50. Luan, Y., Jing, L., Xie, Y., Sun, X., Feng, Y. & Fu, H. *ACS Catal.* **3** 1378–1385 (2013).

51. Dozzi, M. V, Montalbano, M., Marra, G., Mino, L. & Selli, E. *Mater. Today Chem.* **22**, 100624 (2021).

52. Yuan, W., Wang, Y., Li, H., Wu, H., Zhang, Z., Selloni, A. & Sun, C. *Nano Lett.* **16**, 132–137 (2016).

53. Yang, H.G., Sun, C.H., Qiao, S.Z., Zou, J., Liu, G., Smith, S.C., Cheng, H.M. & Lu, G.Q. *Nature* **453**, 638–641 (2008).

54. Selçuk, S. & Selloni, A. *J. Phys. Chem. C* **117**, 6358–6362 (2013).

55. Maisano, M., Dozzi, M. V., Coduri, M., Artiglia, L., Granozzi, G. & Selli, E. *ACS Appl. Mater. Interfaces* **8**, 9745–9754 (2016).

56. Pellegrino, F., Sordello, F., Mino, L., Minero, C., Hodoroaba, V. D., Martra, G. & Maurino, V. *ACS Catal.* **9**, 6692–6697 (2019).

57. Yuan, W., Yong, W., Li, H., Wu, H., Zhang, Z., Selloni, A. & Sun C. *Nano Lett.* **16**, 132-137 (2016).

58. Yuan, W., Wu, H., Li, H., Dai, Z., Zhang, Z., Sun, C. & Wang, Y. *Chem. Mater.* **29**, 3189–3194 (2017).

59. Li, G., Fang, K., Ou, Y., Yuan, W., Yang, H., Zhang, Z. & Wang, Y. *Progress in Natural Science: Materials International* **31**, 1-13 (2021).

60. Lazzeri, M. & Selloni, A. *Phys. Rev. Lett.* **87**, 266105 (2001).

61. Mino, L., Pellegrino, F., Rades, S., Radnik, J., Hodoaraba, V.-D., Spoto, G., Maurino, V., Martra, G., *ACS Appl. Nano Mater.* **9**, 5355-5365 (2018).

62. Zhang, P., Wang, Y., Yao, J., Wang, C., Yan, C., Antonietti, M. & Li, H. *Adv. Synth. Catal.* **353**, 1447–1451 (2011).

63. Shifu, C., Lei, C., Shen, G. & Gengyu, C. *Mater. Chem. Phys.* **98**, 116–120 (2006).

64. Ku, Y., Lin, C.-N. & Hou, W.-M. *J. Mol. Catal. A Chem.* **349**, 20–27 (2011).

65. Shifu, C., Lei, C., Shen, G. & Gengyu, C. *Powder Technol.* **160**, 198–202 (2005).

66. Yalçın, Y., Kılıç, M. & Çınar, Z. **13**, 281–296 (2010).

67. Zaleska, A. *Recent patents Eng.* **2**, 157–164 (2008).

68. Basavarajappa, P. S., Patil, S. B., Ganganagappa, N., Reddy, K. R., Raghu, A. V & Reddy,

C. V. *Int. J. Hydrogen Energy* **45**, 7764–7778 (2020).

69. Dozzi, M. V. & Selli, E. *J. Photochem. Photobiol. C Photochem. Rev.* **14**, 13–28 (2013).

70. Chen, X. & Mao, S. S. *Chem. Rev.* **107**, 2891–2959 (2007).

71. Litter, M. I. & Navío, J. A. *J. Photochem. Photobiol. A Chem.* **98**, 171–181 (1996).

72. Dholam, R., Patel, N., Adami, M. & Miotello, A. *Int. J. Hydrogen Energy* **34**, 5337–5346 (2009).

73. Karakitsou, K. E. & Verykios, X. E. *J. Phys. Chem.* **97**, 1184–1189 (1993).

74. Choi, W., Termin, A. & Hoffmann, M. R. *J. Phys. Chem.* **98**, 13669–13679 (1994).

75. Dozzi, M. V. & Selli, E. *J. Photochem. Photobiol. C Photochem. Rev.* **14**, 13–28 (2013).

76. Dozzi, M. V., D'Andrea, C., Ohtani, B., Valentini, G. & Selli, E. *J. Phys. Chem. C* **117**, 25586–25595 (2013).

77. Dozzi, M. V., Candeo, A., Marra, G., D'Andrea, C., Valentini, G. & Selli, E. *J. Phys. Chem. C* **122**, 14326–14335 (2018).

78. Dozzi, M. V., Ohtani, B. & Selli, E. *Phys. Chem. Chem. Phys.* **13**, 18217–18227 (2011).

79. Czoska, A. M., Livraghi, S., Chiesa, M., Giamello, E., Agnoli, S., Granozzi, G., Finazzi, E., Di Valentiny, C. & Pacchioni, G. *J. Phys. Chem. C* **112**, 8951–8956 (2008).

80. Dozzi, M. V., Prati, L., Canton, P. & Selli, E. *Phys. Chem. Chem. Phys.* **11**, 7171–7180 (2009).

81. Dozzi, M. V., Livraghi, S., Giamello, E. & Selli, E. *Photochem. Photobiol. Sci.* **10**, 343 (2011).

82. Chiarello, G. L., Dozzi, M. V., Scavini, M., Grunwaldt, J. D. & Selli, E. *Appl. Catal. B Environ.* **160–161**, 144–151 (2014).

83. Dozzi, M. V., Zuliani, A., Grigioni, I., Chiarello, G. L., Meda, L. & Selli, E. *Appl. Catal. A Gen.* **521**, 220–226 (2016).

84. Mrowetz, M. & Selli, E. *Phys. Chem. Chem. Phys.* **7**, 1100–1102 (2005).

85. Dozzi, M. V., Chiarello, G. L. & Selli, E. *J. Adv. Oxid. Technol.* **13**, 305–312 (2010).

86. Park, H., Park, Y., Kim, W. & Choi, W. *J. Photochem. Photobiol. C Photochem. Rev.* **15**, 1–20 (2013).

87. Henderson, M. A. *Surf. Sci. Rep.* **66**, 185–297 (2011).

88. Pellegrino, F., Morra, E., Mino, L., Martra, G., Chiesa, M. & Maurino, V. *J. Phys. Chem. C* **124**, 3141–3149 (2020).

89. Herrmann, M., Kaluza, U. & Boehm, H. P. *Zeitschrift für Anorg. und Allg. Chemie* **372**, 308–313 (1970).

90. Minero, C., Mariella, G., Maurino, V., Vione, D. & Pelizzetti, E. *Langmuir* **16**, 8964–8972 (2000).

91. Minero, C., Mariella, G., Maurino, V. & Pelizzetti, E. *Langmuir* **16**, 2632–2641 (2000).

92. Mrowetz, M. & Selli, E. *New J. Chem.* **30**, 108–114 (2006).

93. Dozzi, M. V. & Selli, E. *Catal. Today* **206**, 26–31 (2013).

94. Chen, M., Ma, J., Zhang, B., He, G., Li, Y., Zhang, C. & He, H. *Appl. Catal. B Environ.* **207**, 397–403 (2017).

95. Sheng, H., Li, Q., Ma, W., Ji, H., Chen, C. & Zhao, J. *Appl. Catal. B Environ.* **138–139**, 212–218 (2013).

96. Sato, S. & White, J. M. *Chem. Phys. Lett.* **72**, 83–86 (1980).

97. Subramanian, V., Wolf, E. E. & Kamat, P. *J. Am. Chem. Soc.* **126**, 4943–4950 (2004).

98. Bumajdad, A. & Madkour, M. *Phys. Chem. Chem. Phys.* **16**, 7146–7158 (2014).

[This page intentionally left blank]

Chapter 2: Material Synthesis and Characterization Techniques

2.1 Sol-Gel Synthesis

In the wide field of techniques for nanomaterials preparation, sol-gel synthesis represents one of the mainstay synthetic methods for preparing high quality, highly crystalline titanium dioxide nanoparticles.[1] In fact, several different methods have been proposed for the preparation of TiO_2-based materials over the course of the years, including (but not limited to) hydrothermal, solvothermal, direct oxidation, chemical vapor deposition, flame spray pyrolysis, and many others.[2] The aforementioned sol-gel methods have retained their primary role as metal oxide nanoparticles preparation techniques due to their simplicity, robustness, low cost and great flexibility, allowing to easily prepare metal oxide nanomaterials with different properties by simply adjusting easily tunable experimental parameters.[3–7]

The sol-gel method is a wet chemistry preparation technique based on the transformation of a liquid precursor solution into a sol, a colloidal suspension formed by very fine solid particles dispersed in a fluid (some examples of sols are commonly found in everyday life such as blood, milk, or pigmented inks) that evolves in a gel, an extended network structure including both a liquid and a solid phase, formed as a consequence of a manifold of condensation reactions.

The first reports of the sol-gel process appeared in the mid-1800s with the pioneering studies of Ebelman and Graham, which discovered the formation of silica (SiO_2) gels upon hydrolysis and condensation of tetraethylorthosilicate (TEOS) under acidic conditions.[8,9] Since then, the interest towards this type of synthetic process has started to increasingly grow with a number of scientific contributions, up to the first real showcase of the potency of the synthetic technique, highlighted by glass scientist Dislich in 1971 who, while working for the Schott glass company, showed the possibility of synthesizing Pyrex glass starting from a homogeneous solution containing a mixture of sodium alkoxides, boron, aluminum, and silicon on hot pressing at 630 °C, i.e., lower than the temperature above 1500 °C normally required to produce Pyrex glass via traditional glass-making techniques.[10] From the early 70s onwards, the sol-gel technique has been studied in depth and used to prepare a wide variety of materials such as nano powders[11–13] or coating films.[14,15]

A typical sol-gel process can be divided in four/five sequential elementary steps: hydrolysis, condensation, aging, drying and crystallization.[16] In the first step, a metal precursor, usually in the form of inorganic metal salts or metal-organic compounds such as metal alkoxides or oxoalkoxides, is added to a suitable solvent, necessary to guarantee the reaction between water and the precursor since water and metal alkoxides are usually immiscible, thus making mandatory the use of a mutual solvent.[17] In the case of titanium dioxide, the material prepared during this PhD thesis work, the most commonly used titanium precursors are titanium tetraisopropoxide or titanium tetraisobutoxide, whereas typical solvents are aliphatic alcohols such as ethanol or isopropanol.[18] Addition of water to the dissolved homogeneous solution results in the rapid nucleophilic attack of the water molecules to the positively charged metallic center of the metal alkoxide precursor, causing the rapid hydrolysis of the precursor with the consequent substitution of the metal alkoxide functional group with metal hydroxide functionalities:

$$\mathrm{M(OR)_n + H_2O \rightarrow HO - M(OR)_{n-1} + ROH} \qquad (2.1.1)$$

Depending on the metal/water ratio and/or the presence of a catalyst, hydrolysis can go to completion to give metal hydroxides $\mathrm{M(OH)_n}$ or stop to give partially hydrolyzed alkoxides $\mathrm{M(OH)_m(OR)_{n-m}}$. Then, formed hydrolized species in solution can be linked together by means of condensation reactions

$$\mathrm{(OR)_{n-1}M - OH + HO - M(OR)_{n-1} \rightarrow (OR)_{n-1}M - O - M(OR)_{n-1} + H_2O} \qquad (2.1.2)$$

$$\mathrm{(OR)_{n-1}M - OR + HO - M(OR)_{n-1} \rightarrow (OR)_{n-1}M - O - M(OR)_{n-1} + ROH} \qquad (2.1.3)$$

The condensation step results in the polymerization of the metal-hydroxide species via metal-oxide linkages, allowing to build larger metal-containing molecular blocks which, once grown to a sufficient size, end up forming a *sol*. The solubility of the resulting solid phase in the solvent-water liquid medium is usually so low that the condensation reaction can be considered as practically irreversible. Moreover, condensation of the metal alkoxide species usually causes an increase in the viscosity of the suspension. Both herein described steps are strongly affected by experimental parameters, the most important being the nature of the R-group (in particular its steric hindrance), temperature, pH, specific solvent used, solvent/metal precursor ratio and, most importantly, the presence of a catalyst and its concentration.[19,20,29–31,21–28] All these parameters have a profound impact on the resulting synthesized materials affecting both particle size, shape, and crystallinity, thus making the control of synthetic conditions of primary importance to obtain reproducible materials. Among these parameters, the presence of either acidic or basic conditions result in generally favoring the hydrolysis of the metal oxide as both H^+ and OH^- species are capable of

speeding up the rate of S_N2-type reactions by acting as acid/base catalysts for the nucleophile substitution reaction step.[32–35] A series of condensation reactions, then, allow sol particles to further grow into a three-dimensionally branched porous polymeric structure known as *gel*. Bonds and structure in the gel, however, are not static, but continuously change in a dynamic process which involves the interaction between the solid network and the locally present solvent, until the solvent is removed. This process is known as *aging*. The aging step has a profound impact on the produced materials as the redissolution and precipitation of the gel network occurring during aging causes a decrease in the porosity of the gel, an increase of the thickness of the colloidal particles and generally strengthen the linkages of the polymeric network.[36–38]

The successive step in the formation of the desired ceramic materials is the elimination of the solvent from the gel. In the sol-gel process, something as simple as *drying* can have enormous impact on the resulting final materials.[39–42] In fact, depending on the method chosen for the elimination of the solvent, the structure of the gel can be either retained, forming a highly porous solid polymeric structure known as aerogel (usually obtained by removing the solvent via reaching supercritical solvent conditions in an autoclave), or collapse to form a more dense, compact amorphous solid known as xerogel (obtained through evaporation by heating in an oven). If, instead, the solvent is removed at low temperature by freeze drying, a cryogel is rather obtained.

Regardless of the chosen solvent removal method, dried gels obtained are always amorphous polymers: if a crystalline material or a dense ceramic monolith is desired, a successive *calcination* step, consisting of heat treatment at high temperature causing the collapse, sintering and crystallization of the dried gels, is therefore required. The temperature at which the thermal treatment is applied also represents a fundamental parameter deeply affecting the properties of the resulting metal-oxide material: in particular, as the calcination temperature is increased, higher crystallinity degrees are expected to be obtained at the expenses of the specific surface area of the materials, as higher temperatures favor sintering of the nanoparticles, thus resulting in a collapse of the surface exposure of the materials in favor of a higher volume/surface ratio and larger crystallites, together with influencing the phase composition of the prepared oxide.[43–46] Moreover, thermally treating gels results in cleaning the surface of the material from both residual adsorbed water and (or) solvent and from the presence of organic species residual from the hydrolysis of the metal precursor, which may have adsorbed on the surface of the dried gel.

The sol-gel process has many advantages compared to other nanomaterials preparation techniques such as:

- Synthesizing materials with high levels of purity, homogeneity, and crystallinity.

- Possibility of synthesizing new materials with improved properties which may not exist in nature.
- The chemical reaction is simple and requires low temperatures.
- The reaction with an aqueous solution makes incorporation of a water-soluble guest species in trace concentration in the solid very easy, thus allowing to achieve a uniform, controlled doping of the material.
- Preparing various types of solid materials, even in special form, such as films or coatings, powders, or fibers.
- Control of the produced particles size and morphology.

The method, however, is affected by some drawbacks, for example represented by:

- Fairly high reactivity of metal alkoxides precursor to water makes the method susceptible to air moisture, sometimes requiring controlled atmospheric conditions depending on the chosen precursor.
- The process is slow and time consuming, several other processes can produce materials faster than sol-gel methods.
- Very effective for laboratory scale synthesis, very difficult to scale up for industrial production.
- High costs for most good purity metal alkoxides precursors can cause the materials production to be quite expensive.

Despite the herein reported drawbacks, we decided to adopt the sol-gel process as synthetic method for preparing N,F-doped titanium dioxide nanoparticles due to the simplicity of the sol-gel process in preparing homogeneously bulk-doped metal oxide nanoparticles.

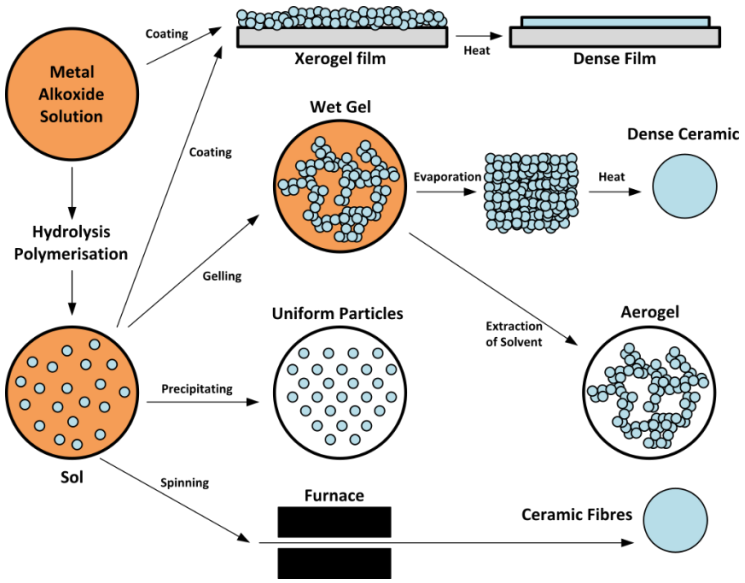

Figure 2.1.1: Schematic representation of the different stages and routes of the sol-gel process. Under Creative Common License CC BY-SA 3.0.

2.1.1 Experimental procedure

The syntheses of TiO_2 N,F-doped powders were carried out in a 500 cm^3 PYREX glass triple-neck round bottom flask containing 100 cm^3 of absolute pure ethanol, connected to an Allihn condenser immersed in a thermostatic ethylene glycol bath with temperature set to 35 °C. Then, 10 cm^3 of titanium(IV) isopropoxide (Sigma-Aldrich, 97% purity) were added to ethanol using a volumetric pipette, while keeping the solution under constant stirring. The hydrolysis of the metal organic-alkoxide precursor is very rapid and can take place even in the presence of traces of water. For this reason, it is of primary importance to use dried up lab glassware and to rinse the volumetric pipette with ethanol to prevent unwanted precursor hydrolysis. Moreover, all the reaction environment needs to be closed with appropriate plugs to also prevent the undesired presence of air moisture in it. By means of a dropping funnel, 34 cm^3 of ultrapure Milli-Q water containing the desired amount of NH_4F were added dropwise, observing an immediate hydrolysis of the precursor upon water addition, causing a change in the colour of the solution passing from transparent to brilliant white.

After 60 min stirring, the suspension was transferred to a pear-shaped evaporating flask and dried in a Heidolf rotary evaporator with a mechanical pump as vacuum system at 50 °C and 2 kPa pressure. The so-obtained materials were then put in a glass Petri dish and let dry overnight at 70 °C in an oven. Samples were then ground into fine powders with the use of an agate mortar.

A thermal treatment has been then applied to 3 g of each sample. The calcination cycles were performed in a Carbolite tubular furnace, equipped with an alumina tube, by placing the sample powders in a proper alumina holder. The samples were thus heated with a controlled temperature slope of 5 °C/min under air flux until the desired temperature was reached. Powders were then heated at constant temperature for 4 hours. Calcined samples were finally ground into fine powders with the use of the mortar once again.

All reagents were purchased from Sigma-Aldrich and employed as received. All solutions were prepared employing ultrapure water (18.2 MΩ cm at 25 °C), supplied by a Millipore Direct-Q 3 UV water purification system.

2.2 Hydrothermal synthesis

The increasing demand in the recent years for the development of newly improved materials has led to the consequential necessity of exploring different innovative synthetic routes able to provide materials with properties up to pace with current modern technologies. Among these, the hydrothermal method represents one of the most widely studied and employed methods for

producing nanostructured ceramics with various types of geometries such as nanowires, nanorods, nanospheres and nanosheets.[47–53] Due to the relative simplicity in producing high performing advanced materials, the hydrothermal method has been intensively improved during the years with a continuous process development that has led to its widespread use to prepare materials for different scientific branches and applications such as chemistry, physics, biology, *etc.* In fact, by simply adjusting the reactants concentration, the pH of the aqueous solution and the reaction temperature, it is possible to finely control the shape, size, and degree of aggregation of the resulting materials' crystallites.[54]

Hydrothermal methods are a series of preparation techniques in which solid materials are produced starting from a heterogeneous solid/liquid system containing a precursor inserted in a special closed reactor pressure vessel, usually included in an autoclave system, aimed at recreating high-pressure environmental conditions by heating the reaction environment around the critical point of the solution (thus increasing the vapor pressure of the liquid included in the reactor) or through additional external pressurization, if needed.[55] The application of high pressure allows to obtain materials with otherwise unachievable properties due to the ability of the method to dissolve and recrystallize substances which would likely be poorly soluble (or non-soluble at all) under normal atmospheric pressure conditions.[56,57] In fact, the application of high temperature and pressure allows to exploit the equilibrium between the solvent and the solid phase to obtain specific target products with desired characteristics.[58] Excellent examples of hydrothermal reactions are commonly found in nature, for which several different minerals have been naturally formed under hydrothermal conditions due to the temperature and pressure inside the Earth, allowing itself to behave as a planetary-scale hydrothermal vessel.

In fact, the first uses of the term "hydrothermal" go back to the mid-19th century, in which geologists were trying to recreate the conditions under which many minerals were naturally formed to deepen the knowledge about mineral formation processes. The first scientific paper known to report research on the hydrothermal synthesis appeared in 1845 by German geologist K. F. E. Schafthaul, who observed the formation of microcrystals of quartz from precipitated silicic acid in a steam digester system.[59] Since then, mainly in Europe by means of mineralogists and geochemists, hydrothermal processes started to be intensively studied, inspired by the pioneer work of Bunsen (1848) who prepared $BaCO_3$ and $SrCO_3$ using thick-walled glass tubes containing high-temperature high-pressure liquids.[60] Hydrothermal synthesis, then, started taking its modern form with the work of de Sénarmont in 1874,[61] who investigated and reported the first methodologies for synthesizing minerals in a laboratory using gun barrels as autoclaves. The method was later improved in 1914 by Morey, who developed hydrothermal vessels made of thermostable and

corrosion-resistant alloys, effectively representing the first prototypes of the nowadays used hydrothermal closed systems.[62] Moving on, hydrothermal processes have been then widely utilized to prepare a wide range of solid materials such as zeolites, single crystals, ceramics, and a wide variety of nanostructured materials,[63–66] settling as one of the most popularly used laboratory-scale preparation methods of inorganic materials.

In introducing the fundamental properties on which the hydrothermal synthesis is based on, we will discuss at first the properties of the most important solvent used in this type of synthesis, i.e., water. The properties herein discussed can be easily translated and applied for any non-water solvent. It is important to note that, up to now, the physical chemistry of hydrothermal synthesis represents the least understood step of the whole hydrothermal process, due to the intrinsic complexity in performing *in-situ* measurements in high-pressure closed reactor vessels.[67,68]

As illustrated by the phase diagram of water (Figure 2.2.1a), the equilibrium vapor pressure of water is a function of temperature and, if enclosed in a rection vessel, increasing the temperature results in increasing the pressure of the whole system. The existence of a gas phase in equilibrium with the liquid phase is at the basis of the hydrothermal synthesis: in fact, imposing high-temperature conditions (minimum above 100 °C) results in increasing the pressure inside the whole closed reactor. The operating vapor pressure can be thus easily obtained through the water-vapor equilibrium curve in the phase diagram. If the temperature is increased up to 374 °C (reaching the critical point of water), the boundaries of the vapor and liquid phase are not distinguishable anymore and, as a result, a supercritical fluid is obtained, reaching a pressure of 221 bar. If, however, higher pressures are required, it is possible to apply an external pressurization and work outside the equilibrium liquid-vapor water pressure curve. It is important to note that, for experimental purposes, the actual pressure under working conditions in a reaction vessel is determined by the filling degree of the reactor, i.e., the fraction of volume that was occupied by the solvent at the beginning of the whole synthesis (before heating the whole system), as the filling factor heavily influences the actual p-T diagram of the solvent (Figure 2.2.1b).[69,70] Fill factors lower than 32% are commonly used during hydrothermal syntheses, however increasing the fill factor allows to reach higher pressures and supercritical conditions at lower temperatures.

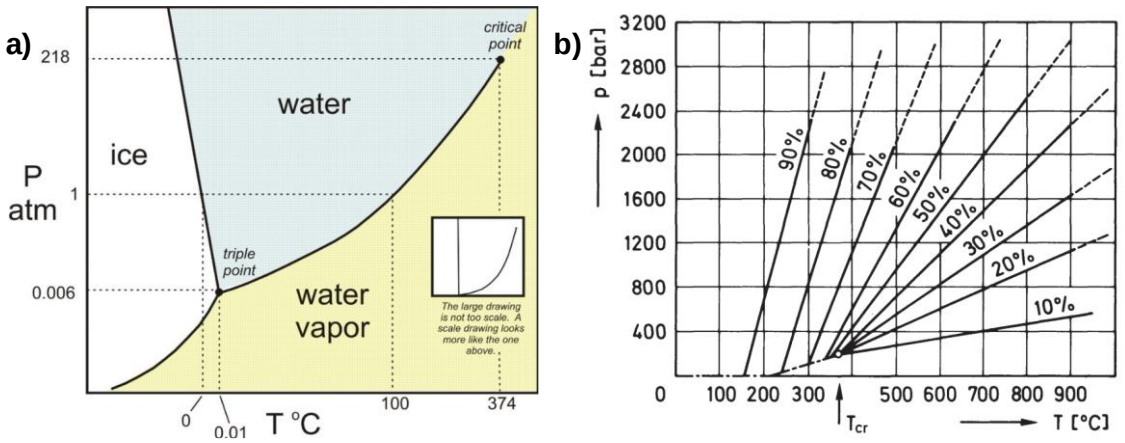

Figure 2.2.1: Phase diagram of water (a); p-T curves of water with differing percentage filling (fill factor) of the closed reactor vessel (b).[69]

The hydrothermal method bases its physico-chemical principles in the increased solubility of basically all inorganic species in a solvent with increasing temperature and pressure conditions, obtaining the desired products because of a successive crystallization of the solid materials starting from their dissolved species in solution. In fact, the solubilization of a solid substance in contact with a liquid phase can be expressed as a result of two different processes:

1. Melting of the solid substance
2. Mixing of the melted solid and the liquid in contact with it

If, for the sake of simplicity, we consider an ideal system, the heat for the second process is equal to zero and we can express the quantitative dependence of the composition variation of a solution in contact with a solid at equilibrium with pressure as:[71]

$$\frac{\mathrm{d}x_2}{\mathrm{d}p} = \frac{(v_2 - v_2^s)}{\left(\frac{\delta\mu_2}{\delta x_2}\right)_{p,T}} \qquad (2.2.1)$$

where:

- x_2 is the composition of the saturated solution (molar fraction)
- v_2 is the partial volume of the solute in the solution
- v_2^s is the specific volume of the solute in the solid phase
- $\left(\frac{\delta\mu_2}{\delta x_2}\right)_{p,T}$ is the rate of change in chemical potential of the solute in the solution with change of concentration at fixed temperature and pressure.

As $\left(\frac{\delta\mu_2}{\delta x_2}\right)_{p,T}$ must always be positive, it follows that the solubility of the solid in the solution depends on pressure whether is $(v_2 - v_2^s)$ is either positive or negative. Considering that most solids expand on melting, $(v_2 - v_2^s)$ is usually positive and increasing the pressure of the system

such as under hydrothermal conditions also causes an increase in the solubility of the solid inorganic substance. Solubilized solid materials under hydrothermal conditions, then, can either recrystallize or grow in an aging process via an Oswald ripening-type mechanism.[67] Thus, reaction time represents a fundamental parameter in ensuring the obtainment of the desired reaction product, along with setting the right pressure and temperature conditions. The application of high pressure and temperature, moreover, causes a decrease in the viscosity of the solvent,[69,70] with a consequent increase in the mobility of dissolved species and a general improvement of diffusion-limited processes in solution, thus improving the rate of Oswald ripening and crystal growth mechanisms.

The hydrothermal process, compared to other nanomaterials preparation techniques, has many advantages such as:[72]

- Synthesizing materials with high levels of purity and crystallinity
- Possibility of synthesizing high quality, large sized single crystals
- The process is usually environmentally friendly and versatile
- The morphology of the products can be easily tuned

The method, however, is affected by some drawbacks, for example, represented by:

- The use of expensive equipment such as costly autoclaves and liners
- Samples obtained can be polydispersed
- High-temperature high-pressure conditions of the reactor pose safety concerns
- The use of highly toxic chemicals can be necessary to produce the desired materials

Despite the herein reported drawbacks, we decided to adopt the hydrothermal process as chosen synthetic method for preparing differently shaped titanium dioxide nanoparticles due to the unique possibilities offered by the hydrothermal process in controlling the shape of metal oxide crystallites, allowing to tune their shape by simply adding a suitable capping agent and setting appropriate experimental parameters such as temperature, pressure, reaction time, type and concentration of both precursors and capping agent.[73–78]

2.2.1 Experimental procedure

Differently shaped TiO_2 samples, characterized by a pseudo-spherical shape or a nanosheet structure, were prepared through the hydrothermal route by employing titanium isopropoxide as Ti precursor and HF as capping agent. In particular, a fixed amount of titanium isopropoxide (10 mL) was mixed under stirring for 15 min in a Teflon liner with different volumes of a 48 wt% HF solution and different amounts of water (Table 2.2.1) up to a 11.2 mL final volume. A reference

sample was prepared under the same conditions by simply adding 1.2 mL of water (and no HF) to titanium isopropoxide.

The liner was then transferred into a closed stainless-steel autoclave to be heated at 180 °C for 24 h. The obtained precipitate was recovered after cooling the autoclave down to room temperature using a stream of compressed air. A series of washing cycles with ultrapure Milli-Q water followed, up to a fluoride ion concentration in the supernatant, detected by means of ionic chromatography (Methrohm 761 compact IC with conductivity detector), below 5 ppm. The solid was then collected, dried in an electric oven at 70 °C overnight, and grounded into the form of fine powders by means of an agate mortar. The so-obtained materials were labelled as HT_X, where HT refers to the employed preparation method (hydrothermal procedure) and X stands for the nominal F/Ti ratio employed during the synthesis, *i.e.,* 0.1 or 1.0. The reference sample was labelled as HT_0, as no fluorine was used during its synthesis.

In order to remove the residual fluorine on the materials' surface, a portion of each sample underwent washing cycles with an aqueous NaOH solution. During the washing procedure, a fixed amount of photocatalyst (1.0 g) was dispersed in 200 cm^3 of a 0.1 M NaOH aqueous solution by means of a 30 min ultrasonic treatment. The suspension was then left stirring in the dark for 1 h at 60 °C, followed by a 10 h-long stirring in the dark at room temperature. The powders were then recovered by centrifugation and washed several times (maximum six times) with Milli-Q water (200 cm^3) up to neutral pH of the suspension and finally dried at 70 °C overnight.

Table 2.2.1: Amounts of HF aqueous solution (48 wt%) and of ultrapure H_2O employed in the hydrothermal synthesis of the photocatalysts.

Sample	HF Volume / cm^3	H_2O Volume / cm^3
HT_0	-	1.200
HT_0.1	0.120	1.080
HT_1	1.200	-

All reagents were purchased from Sigma-Aldrich and employed as received. Water purified by a Milli-Q water system (Millipore) was used throughout.

2.3 Deposition-Precipitation

The deposition-precipitation (DP) represents one of the most performing methods for the modification of the surface of a metal oxide with point of zero charge (pzc) > 5 (such as TiO_2, MgO or Al_2O_3) due to its ability to quantitatively deposit very finely dispersed, very small nanoparticles on the surface of the material.[79–81] The deposition-precipitation is a wet-chemistry

technique which exploits the precipitation of metal hydroxides from an aqueous solution containing a dissolved metal salt precursor, usually because of alkalinization of the solution. In the classical variant of this method, most famously reported by Haruta in 1991,[82] alkalinization of the solution was achieved through addition of sodium hydroxide, which caused the precipitation of the metal hydroxides as

$$M^{X+} + X\,HO^{-} \rightarrow M(OH)_x \qquad (2.3.1)$$

If a metal oxide is finely suspended in the same solution, the produced metal hydroxides can interact with the surface of the metal oxide itself and anchor to it.[83]

The desired metal nanoparticles are obtained through a reductive step aimed at converting the metal ions to their zero-valent oxidation state, which can be performed either via calcination or through chemical reduction, although the properties of the resulting material are heavily dependent on the method chosen for the reductive step.[81,84–86]

In the modern variants of the deposition-precipitation method, the thermal decomposition of urea

$$CO(NH2)_2 + H_2O + \text{heat} \rightarrow 2\,NH_3 + CO_2 \qquad (2.3.2)$$

has replaced the addition of NaOH to increase the pH of the solution as it provides a milder, gradual pH increase compared to the abrupt alkalinization offered by the addition of NaOH.[87] With this variant, an actual quantitative deposition of the metal nanoparticles is obtained, whereas in the case of Haruta's method it is not infrequent to observe a non-quantitative deposition of the metal nanoparticles on the metal oxide surface. Moreover, the slow addition of the base ensures a more homogeneously distributed precipitation of the metal hydroxides, thus allowing to have better dispersed metal nanoparticles on the surface of the support.[80] The thermal decomposition of urea, thus, allows to better control not only the actual noble metal nanoparticles loading on the surface of the support, but also to deposit better distributed nanoparticles.

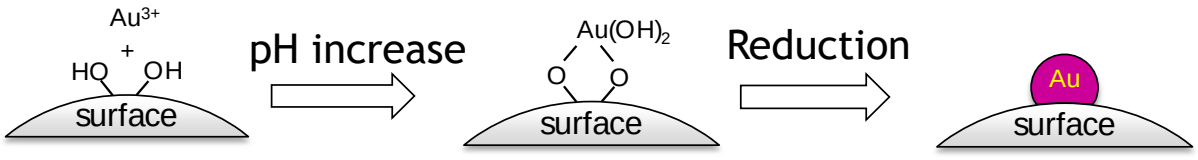

Figure 2.3.1: Schematic representation of the deposition-precipitation process.

The deposition-precipitation method was chosen during this PhD thesis to modify the surface of both N,F-doped and differently shaped titanium dioxide nanoparticles with Au noble metal

nanoparticles because it allows to deposit finely dispersed, very small Au NPs with a completely random way on the whole surface of the support. In fact, this method is not affected by preferential deposition of nanoparticles on any specific region of the metal oxide support.

2.3.1 Experimental procedure

In the DP method, 400 mg of TiO_2 powder were suspended in 10 cm^3 of ultrapure Milli-Q water in a round bottom flask. The powders were then finely dispersed by sonication with ultrasound radiation of 59 kHz frequency and 250 W for 30 min using a Falc Instruments Labsonic LBS2 ultrasonic bath. A gold precursor solution was then prepared by dissolving the proper amount of $HAuCl_4 \cdot xH_2O$ to obtain the deposition of the desired amount of metallic Au in 5 cm^3 of water. Reactants were recovered with additional 5 cm^3 of Milli-Q water, bringing the total volume of the suspension to 20 cm^3, setting up the final concentration of urea to 0.42 M and that of the photocatalyst in the suspension to 20 g dm^{-3}.

The flask was then immersed in an ethylene glycol thermostatic bath with temperature set to 80 °C and stirred at 1000 rpm for 4 hours. By applying these experimental conditions, the urea progressively decomposed, causing a mild, gradual alkalinization of the slurry, which resulted in the slow precipitation of Au hydroxides on the surface of titanium dioxide. TiO_2 powders were then separated from the liquid phase via centrifugation and recovered with milli-Q water, where a slight excess of $NaBH_4$ was added. Addition of the reducing agent causes an immediate reduction of the deposited Au(III) hydroxides to finely dispersed metallic Au NPs on the surface of TiO_2, as evidenced by the sudden chromatic change of the TiO_2 powders, passing from brilliant white to deep purple.

Au-modified powders were then washed several times (at least three) with ultrapure Milli-Q water until the concentration of chloride ions in the supernatant, detected by ionic chromatography, was reduced to less than 1 ppm. Each washing cycle consisted in suspending the samples in ultrapure Milli-Q water, stirring the suspension for 20 min and collecting the powders by centrifugation. The product was then transferred in a glass Petri dish and dried overnight in an oven at 70 °C. Fine powders were finally obtained by grinding in an agate mortar.

2.4 Photodeposition

Photodeposition, also often referred to as photoreduction and photochemical deposition, is a metal nanoparticles deposition method based on exploiting the photopromoted electrons of a photocatalyst under irradiation with light of ultra-band gap energy to reduce surface adsorbed

metal ions in an aqueous suspension, causing their deposition as metal nanoparticles on the semiconductor surface.[88] The interest towards this very peculiar metal nanoparticles deposition method started in 1978 with the work released by Kraeutler and Bard,[89] who showed the possibility of loading platinum nanoparticles on the TiO_2 surface by illuminating a slurry containing the photocatalyst itself, H_2PtCl_6, HCl, Na_2CO_3 and acetic acid, which acted as hole scavenging species. To observe the deposition of the Pt nanoparticles, removal of oxygen was necessary by purging the reaction environment with a steady stream of N_2.

For a metal cation in solution M^{X+}, a general mechanism for the photodeposition process can be expressed as the result of two different photochemical reactions, the first one being the photocatalytic reduction of the adsorbed metal ions:

$$M^{X+}(aq) + x\, e^-_{CB} \rightarrow M^0(s) \qquad (2.4.1)$$

and the second one being the oxidation of the hole scavenging species by photogenerated holes. Being a photocatalytic reaction, to photodeposit a given metal on the titanium dioxide surface it is necessary than the conduction band potential of the semiconductor is more negative that the reduction potential of the M^{X+}/M^0 couple, while the valence band potential must be more positive than the redox potential of the species being oxidized, either be water, as a hole scavenger, or any adsorbed species capable of undergoing oxidation.

The photodeposition method, in theory, could work even in the absence of a hole scavenger in solution. However, the presence of such species is practically a necessary requirement to guarantee a sufficiently fast oxidation kinetics for the oxidation half reaction which, if not fast enough (as in the case of water oxidation), may represent a kinetic bottleneck for the whole process causing the deposition of only partially reduced metal nanoparticles, rather than in their metallic state.[90,91] In fact, the use of a sacrificial agent increases the availability of photopromoted electrons by reducing the electron-hole recombination rate due to the hole-subtraction effect played by the hole scavenging species, causing a more effective reduction of the adsorbed metal ions at the photocatalyst surface.

The need to purge oxygen from the reaction environment originates from the super-efficient electron scavenging ability played by O_2^- to form $O_2^{-\bullet}$ radical anions, hindering metal ions from being reduced at the photocatalyst surface, slowing down the nucleation and growth of the noble metal nanoparticles which, in the presence of oxygen, are also characterized by incomplete reduction and high oxidation states, if ever deposited.[92]

Compared to other noble metal nanoparticles deposition methods such as electrodeposition, chemical reduction, or sputtering,[93–96] photoreduction places itself as a very appealing modification technique due to the ability of the method to deposit nanoparticles at low temperatures, without the need to apply any external bias and, most importantly, the peculiar possibility to deposit noble metal nanoparticles preferentially on certain areas of the metal oxide support such as specific crystal facets,[97–99] or closely interacting with specific surface defects present on the photocatalyst surface itself. In fact, as the growth of the nanoparticles is triggered by the intrinsic properties of the photocatalyst, the deposited nanoparticles' properties can be deeply intertwined with those of the photocatalyst support.[79]

The photochemical deposition method was chosen during this PhD thesis to modify the surface of both N,F-doped and differently shaped titanium dioxide nanoparticles with Au noble metal nanoparticles because of the ability offered by the modification method to deposit finely dispersed, small Au NPs closely interacting with the surface of the support, preferentially deposited on either specific crystal facets and/or surface defects, thus possibly synthesizing materials with differing properties compared to the deposition-precipitation method.

2.4.1 Experimental procedure

In the photodeposition method 600 mg of TiO_2 powder were suspended in 100 cm^3 of ultrapure Milli-Q water in a photoreactor consisting of a 250 cm^3 Schott DURAN glass laboratory bottle jar equipped with a GLS 80® connection system with four GL18 red screw caps, one of which is holed and connected to a gas resistant PTFE/silicone septum which allows gas bubbling by means of a syringe (Figure 2.4.1). The powders were then finely dispersed by sonication with ultrasound radiation of 59 kHz frequency and 250 W (corresponding to 100% power) for 30 min using a Falc Instruments Labsonic LBS2 ultrasonic bath.

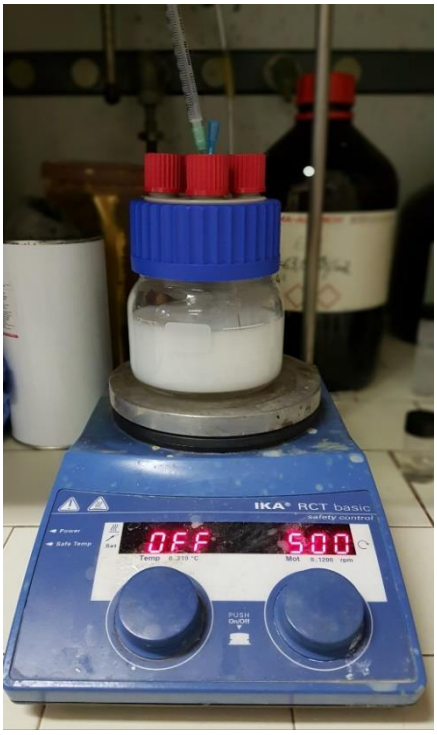

Figure 2.4.1: Glass jar photoreactor under N_2 bubbling.

Then, the proper amount of $HAuCl_4 \cdot xH_2O$ to obtain the deposition of the desired amount of metallic Au were dissolved in 7.5 cm^3 of Milli-Q water and added to the suspension, followed by addition of 72.5 cm^3 of ultrapure Milli-Q water and 20 cm^3 of CH_3OH, bringing up the total reaction volume to 200 cm^3. The reaction mixture was then bubbled with N_2 under constant stirring for 15 min.

The suspension was irradiated for 60 min under constant stirring using the experimental setup described in section 3.1.2 (page 95). A color change from white to deep purple was observed within few seconds after the beginning of irradiation, indicating that Au^{III} ions were almost immediately reduced to metallic gold.

Then, the powders were recovered from the reactor by centrifugation with a relative centrifugal force of 3661 x g corresponding to 5000 rpm in a Thermo Scientific CL 10 centrifuge with F-G1 Fixed Angle Rotor of 131 mm radius for 20 min. The supernatant was recovered from the test tubes and a slight excess of $NaBH_4$ was then added to check that no metal precursor remained in the solution and confirm the quantitative deposition of metallic Au on the surface of the samples.

Au-modified powders were then washed several times (at least three) with ultrapure Milli-Q water until the concentration of chloride ions in the supernatant, detected by ionic chromatography, was reduced to less than 1 ppm. Each washing cycle consisted in suspending the samples in ultrapure Milli-Q water, stirring the suspension for 20 min and collecting the powders by centrifugation. The product was then transferred in a glass Petri dish and dried overnight in an oven at 70 °C. Fine powders were thus obtained by grinding in an agate mortar.

2.5 X-Ray Diffraction

X-Ray diffraction (also known as X-Ray Powder Diffraction, XRPD) is a versatile non-destructive analytical technique for the characterization of solid crystalline materials. This technique represents one of the most powerful for gaining information on a plethora of properties of solid materials, such as:

- Structure of the material bulk
- Phase composition
- Presence of texture or preferred orientation of crystallites
- Crystallinity
- Grain size
- Crystal defects

Most commonly, the technique has been widespreadly used as a relatively cheap and easy to access analytical method for performing qualitative (i.e., identification) and quantitative analysis of the phase composition of solid specimens.

X-Ray diffraction poses its bases from the pioneer noble-prize awarded work of Von Laue et al. in 1912,[100] who discovered that crystalline substances could diffract X-Ray radiation with a wavelength close in magnitude to the spacing of the planes in a crystal lattice. The work of Laue

et al. is ground-breaking not only because they discovered the physical phenomenon of diffraction of X-Ray by crystalline solids, but also because it proved that the crystallinity of a solid depends on the regular arrangement in the three-dimensional space of atoms and molecules, and not by its external properties.[101] Afterwards, the independent works of Debye, Scherrer (Germany, 1916/1917)[102] and the Bragg brothers (England, 1913)[103] paved the way for this technique to become the nowadays most frequently used crystallographic method.

As the name implies, XRD is an analytical technique employing X-Rays, consisting of electromagnetic radiation of wavelength ranging from 0.01 to 10 nm, corresponding to an energy between 0.125 to 125 keV, thus relatively high in the electromagnetic spectrum, being second only to γ rays (Figure 2.5.1).

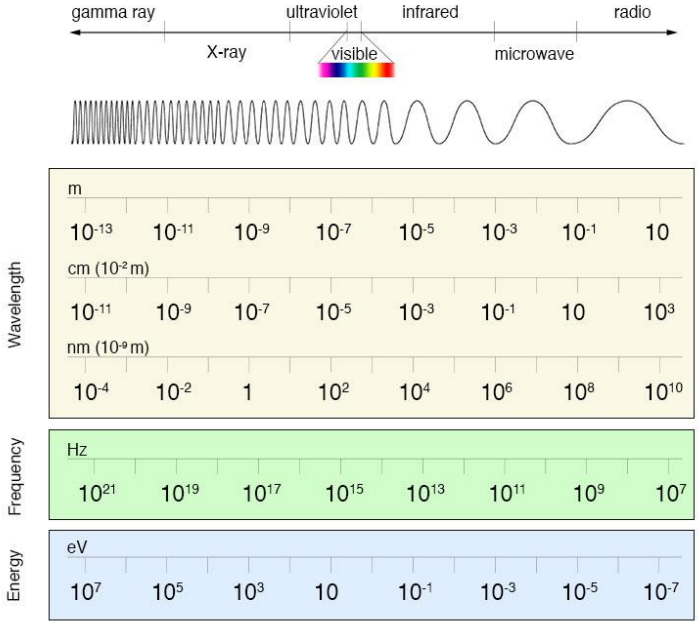

Figure 2.5.1: Spectrum of Electromagnetic radiation.

A quantitative description of the X-Ray diffraction phenomena has first been proposed by Von Laue and then by Bragg & Bragg. Despite Von Laue's description is more rigorous and physically accurate, Bragg's interpretation results to be the most commonly used and discussed as it enormously simplified the description of the results for a more practical use and easier understanding. For such reason, it will be used in this context for describing the diffraction phenomena in solids.

When a solid crystalline material is irradiated with X-Ray radiation, the electromagnetic beam is scattered in a specular fashion by crystal planes separated by a distance d_{hkl}, with (hkl) being a series of integer indexes identifying a specific family of lattice planes (Figure 2.5.2a). The

differences in optical path between X-Ray radiation scattered by different lattice planes generates phase differences in reflected beams, which give rise to a series of constructive and destructive interference phenomena, i.e., diffraction. The diffraction process is thus described in terms of incident and reflected focused beams, each approaching the different crystallographic planes with a fixed θ glancing angle.

The interference between the scattered beams results to be constructive only for those reflections which satisfy Bragg's Law:

$$n\lambda = 2\, d_{hkl} \sin\theta \qquad (2.5.1)$$

in which:

- n is a positive integer
- λ is the incident radiation wavelength
- d_{hkl} is the spacing between planes of the (hkl) family
- θ is the glancing angle

If Bragg's conditions are not met, a destructive interference is instead produced, obtaining no diffraction signal due to the repetition of the lattice planes in the crystal reinforcing the interference.

By looking at Bragg's Law for the diffraction of X-Rays, important conclusions can be obtained. If we rewrite Bragg's law as a function of $\sin\theta$, we obtain:

$$\sin\theta = \frac{n\lambda}{2d_{hkl}} \qquad (2.5.2)$$

that is, fixing a wavelength and excluding higher order of magnitude reflections, we can observe that Bragg's Law can be satisfied only for those glazing angles proportional to $\frac{1}{2d_{hkl}}$. Since the distance between lattice planes is specific for each substance, it follows that scanning a monochromatic X-Ray radiation as a function of the glazing angle gives rise to characteristic diffraction spots, in which a diffraction signal is obtained only in correspondence of those glazing angles able to satisfy the Bragg's condition. Since such angles are proportional to the distance between lattice planes, it follows that each specific crystal phase of a given substance produces unique diffraction spots. It is important to note that Bragg's law describes only the conditions at which a diffraction spot can be observed but doesn't give any information on the intensity of the diffracted beam. However, from the diffraction theory, the intensity of a diffracted beam is proportional to the product of the intensity of the incident beam and the concentration of

electrons in the reflecting plane. Therefore, for a pure substance, the relative intensity of the diffraction signals vs θ is also a property of the phase structure.

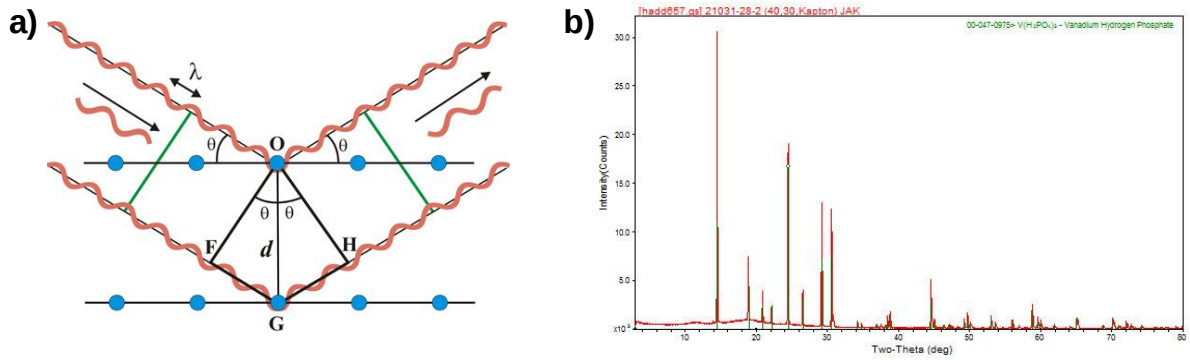

Figure 2.5.2: Bragg's Law for X-Ray Diffraction (a); Example of the diffraction pattern of an unknown substance and identification of its crystal phase ($V(H_2PO_4)_3$) via comparison with reference diffraction patterns in databases (b).

A typical X-Ray diffraction experiment is performed by varying the glazing angle of a monochromatic X-Ray beam, while recording the intensities of the diffracted beams as a function of 2θ (usually preferred to the glazing angle θ for experimental reasons), obtaining a so-called diffraction pattern (Figure 2.5.2b).

Analysis of the diffraction pattern is at the basis of the analytical applications of XRD. For example, recognition of the phases present in an unknown specimen can be performed by comparing the position and relative intensity of the diffraction spots with reference patterns contained in dedicated databases, in a procedure closely resembling the comparison of fingerprints in forensic studies.

In contrast to single crystal X-Ray Diffraction, XRPD makes use of powders as samples. A *powder* is defined as a collection of a huge number of small crystallites completely randomly oriented in space. When a powder is exposed to X-Ray radiation, some crystallites will be oriented in such a way so that the Bragg's law is satisfied. Each family of crystallographic planes generates then a collection of reflections distributed over a cone of 4θ angle. Therefore, the intensities monitored in a powder diffraction experiment are the result of the incoherent superposition of the beams diffracted by each crystallite. Therefore, it is extremely important to ensure that the crystallites are not preferentially oriented by any means, otherwise the relative intensities of the diffraction peaks will lose their physical meaning.

X-Ray Powder Diffraction can also be used to gather useful morphologic data on the samples, since the physical broadening of the diffraction pattern peaks shows a very strong dependence on

the dimension of the crystallites along a specific crystallographic direction. This phenomenon is quantitatively described by the Scherrer equation:[104]

$$d_{hkl} = \frac{0.9\lambda}{\beta_{hkl} \cos \theta_{hkl}} \quad (2.5.3)$$

in which d_{hkl} represents the size of crystallites in the direction vertical to the (hkl) lattice plane, λ is the X-ray incident wavelength, β is the line broadening at half maximum intensity (FWHM) expressed in rad and θ stands for the incident angle. Therefore, the FWHM of a diffraction peak allows one to calculate the size of the crystallite in the corresponding direction. Although the Scherrer formula is very powerful and widespread used, it should be noted that careful use is required when accurate absolute data on crystallite sizes are required. In fact, the Scherrer formula as here presented is affected by some approximations. First, the numerical value for the shape factor K, here chosen as 0.9, represents an approximation.[105] Second, the line broadening in the observed diffraction pattern is the result of two different broadening phenomena, i.e.,

1. Instrumental broadening
2. Physical broadening due to the finite dimension of the crystallites.

It follows that only the second broadening type carries information on the crystallite size along specific crystallographic directions, whereas the instrumental broadening represents an unwanted parameter which is a cause of error in the determination of the absolute value of the crystallite size. To minimize the instrumental broadening effect, Warren et al.[106,107] proposed that the square of the line broadening at half maximum intensity (FWHM) in a diffraction pattern (B) can be expressed as the sum of the square of instrumental broadening (b) with the square of the desired physical crystallite broadening (β):

$$B^2 = \beta^2 + b^2 \quad (2.5.4)$$

Accurate evaluation of the instrumental broadening at each 2θ, usually obtained by measuring the broadening produced by the diffraction pattern of reference standard materials which are not affected by physical broadening of its crystallites (e. g., pure crystalline Si), allows one to correct the observed broadening for the instrumental broadening, improving the quality of the calculated crystallite sizes. Moreover, the Scherrer equation neglects the effects on FWHM produced by lattice distortion effects. If the materials are expected to be characterized by strong lattice distortion, the Williamson-Hall equation,[108] which includes the description of such effect of by modeling a dedicated strain parameter ε, should be used instead. The Scherrer equation, therefore, should be used only for comparing the relative size of the crystallites of different materials rather

than for obtaining accurate data on the crystallite size. Moreover, comparison with other characterization techniques, such as electronic microscopies, should be carried out to confirm the validity of the calculated Scherrer crystallite size.

Quantitative phase determination of a heterogeneous polyphasic sample can be performed by applying a refinement method to the diffraction pattern. Among these, the most widely employed is the Rietveld refinement.[109–111] This method is based on the construction of a starting model for the entire diffractogram whose parameters are refined and optimized by minimizing the differences between the experimental pattern and the model calculated diffractogram. The expression of the minimized function in the Rietveld method is given by:

$$\Phi = \sum_{i=1}^{n} w_i \left(Y_i^{obs} - Y_i^{calc}\right)^2 \qquad (2.5.5)$$

where w_i is the weight assigned to the *i*th data point, Y_i^{obs} the integrated intensity of the observed *i*th peak and Y_i^{calc} the integrated intensity of the calculated *i*th peak. In the case of a polyphasic sample the function gets expanded as follows (for a dual wavelength experiment such as the dual K_α components of a Cu X-Ray emission):

$$\Phi = \sum_{i=1}^{n} w_i \left(Y_i^{obs} - \left[b_i + \sum_{l=1}^{p} K_l \sum_{j=1}^{m} I_{l,j} \{ y_{l,j}\left(x_{l,j}\right) + 0.5 y_{l,j}\left(x_{l,j} + \Delta x_{l,j}\right) \} \right] \right)^2 \qquad (2.5.6)$$

where b_i is the background contribution of the *i*th data point, K_l is the scale factor for *l*th phase, p is the number of phases present, m is the number of Bragg reflections contributing to the intensity of the *i*th point, $I_{l,j}$ is the integrated intensity of the *j*th Bragg reflection for the *l*th phase, $y_{l,j}\left(x_{l,j}\right)$ is the peak-shape function of the *j*th Bragg reflection for the *l*th phase and $\Delta x_{l,j}$ is the difference in position of the two wavelength components, where $x_{l,j} = 2\theta_{l,j}^{calc} - 2\theta_{l,i}$.

The common scale factors K_l are representative of the total number of unit cells of each phase present in the irradiated volume of the sample. It follows that the weight fraction of a given phase can be calculated from the scale factor as:

$$w \simeq K \cdot ZMV \qquad (2.5.7)$$

where Z is the number of formula units in the unit cell, M is the molecular mass of the formula unit, and V is the volume of the unit cell of the given phase. As individual weight fractions must be normalized so that the total weight fraction is unity, we get to the expression:

$$w_i = \frac{w_i'}{\sum_j w_j'} \tag{2.5.8}$$

2.5.1 Experimental procedure and data elaboration

During this PhD thesis, X-Ray Powder Diffraction (XRPD) patterns were acquired using a Panalytical X'Pert Pro diffractometer operating at 40 kV and 40 mA, using Ni-Filtered Cu K_α radiation (λ=1.54056 Å) at a scan rate of 0.05 degree s^{-1}. In the case of differently shaped titanium dioxide nanoparticles, the relative amount of exposed {001} facets of the full anatase samples was calculated by applying a Rietveld-based approach to diffraction data described in detail in a paper previously published by our research group.[112] Briefly, the method relies on calculating the width w and thickness t of anatase crystallites (Figure 2.5.3) via a least-square minimization procedure performed by refining structural parameters related to the crystallography of the unit cell, line profile parameters and two additional parameters denoted as p_1 and p_2, accounting for the description of anisotropy in crystallite size along perpendicular crystallographic directions, against an experimental powder diffraction pattern. The width and thickness of the crystallites can be thus calculated starting from the anisotropy descriptors as:

$$w = \frac{K \cdot \lambda}{p_1} \tag{2.5.9}$$

$$t = \frac{K \cdot \lambda}{p_2} \tag{2.5.10}$$

where λ is the incident X-Rays wavelength and K is a constant set to 0.94. Then, the percentage of exposed {001} facets ($\%\{001\}$) can be calculated using Equation 2.5.11:

$$\%\{001\} = \frac{v^2}{v^2 + t\frac{v+w}{\sin\varphi}} \cdot 100 \tag{2.5.11}$$

where v is the shorter base of the trapezoidal {101} facet (Figure 2.5.3), calculated as:

$$v = w - t \cdot \cot(\varphi) \tag{2.5.12}$$

with $\varphi = 68.3\,°$, being the theoretical angle between {001} and {101} facets (Figure 2.5.3).

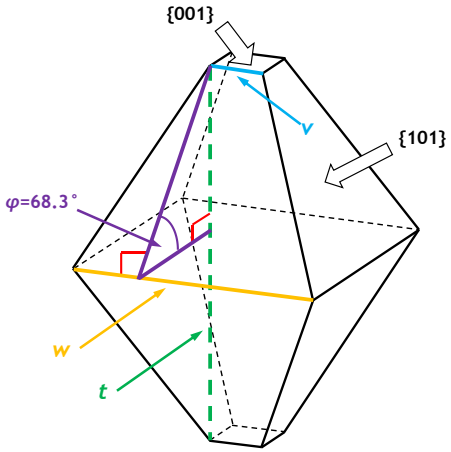

Figure 2.5.3: Scheme of an ideal anatase truncated bipyramidal octahedron illustrating the parameters calculated via Rietveld refinement.

Rietveld analyses were always performed using the GSAS II software.[113] The quality of the fits was defined according to the fit residual R_p, defined as:

$$R_p = \frac{\sum_{i=1}^{n} \left| Y_i^{obs} - Y_i^{calc} \right|}{\sum_{i=1}^{n} \left| Y_i^{obs} \right|} \times 100\% \qquad (2.5.13)$$

where Y_i^{obs} and Y_i^{calc} stand for the observed and calculated intensity of the ith data point, respectively.

In the case of N,F-doped anatase, the dimension of the crystallites was evaluated using the Scherrer formula from the FWHM of the most intense anatase reflection by fitting XRD peaks with suitable Pseudo-Voigt functions, consisting of a linear combination of a Lorentzian and a Gaussian function, by means of the WinPLOTR software.[114] Correction for the instrumental broadening was performed by measuring the FWHM of the diffraction pattern of a reference Si standard, for which the FWHM at each 2θ was obtained by fitting the FWHM as a function of 2θ across the whole diffraction pattern with a suitable polynomial function by means of the MATLAB software (Figure 2.5.4).

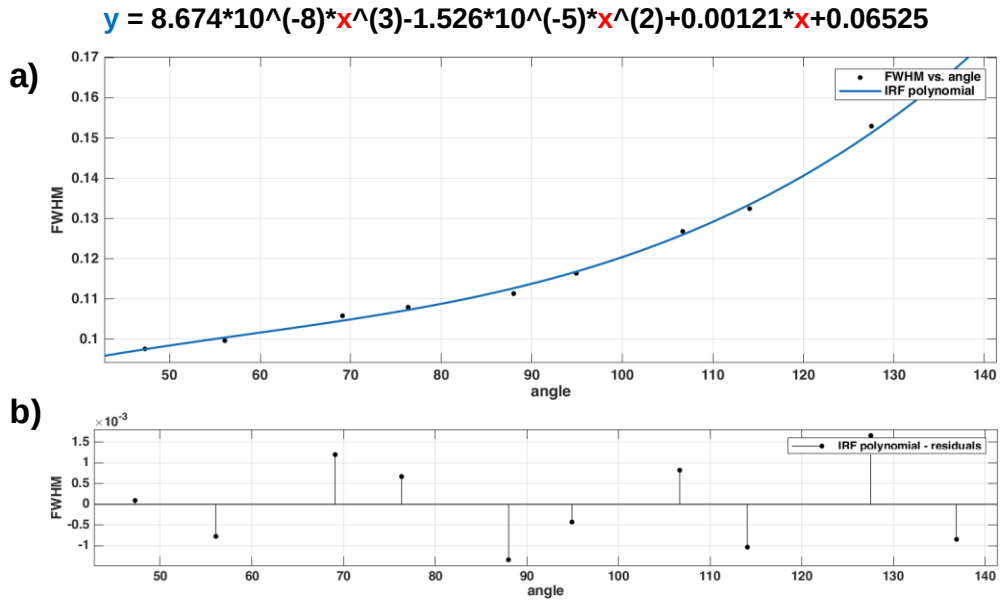

Figure 2.5.4: Polynomial fit of the FWHM vs 2ϑ function for the reference Si standard (a); residuals of the fits (b).

2.6 Surface Area evaluation (BET method)

The specific surface area (SSA) of a solid material represents one of its most important parameters deeply affecting both its physical and chemical properties. This property acquires fundamental importance when investigating materials for catalytic applications as the surface extent of the catalyst directly affects its ability to interact with substrate molecules, with materials bearing a higher surface area usually carrying a higher number of catalytic sites readily available for reaction. The technique acquires even more importance in designing material for remediation of pollutants via adsorption or for stocking gas molecules.

Assessing of the surface area of a material can be performed via different methodologies, among which the most employed are represented by permeability and gas adsorption methods.[115] Between the two, the latter is meant to measure an area represented by a surface covered with a monolayer of close-packed molecules and is usually the preferred method in characterizing powder materials for photocatalytic applications. Among the many models and methods proposed for the measurement of SSA via gas adsorption, the Brunauer-Emmet-Teller (BET) represents undoubtedly the main pillar and most applied method.[116]

The fundamental basis on which the BET theory is derived from stems on the adsorption of gases on solid surfaces, which occurs by means of two different types of interactions, i.e., physisorption and chemisorption. The main difference between the two is represented by the strength of the interaction itself, with physisorbed molecules interacting with the surface only via van der Waals-type forces, whereas chemisorption is characterized by a highly specific chemical interaction occurring via chemical reactions. Due to the energies involved, physisorption represents a reversible type of interaction, with the quantity of gas adsorbed at a given pressure increasing with decreasing temperature, whereas in the case of chemisorption the interaction between the solid and the adsorbed gas is irreversible, and due to the true chemical bonding of the gas on the surface, chemisorption occurs also at temperature higher than the critical temperature of the adsorbate. In addition, chemisorption is, by nature, only restricted to a monolayer of gas adsorption, whereas in the case of physisorption multilayer adsorption is usually observable. Among the two, physisorption is of most interest when determining the specific surface area of a material via the BET method.

The BET model is closely related to the Langmuir theory of monolayer adsorption. In a monolayer adsorption, all adsorbed molecules are in contact with the solid material surface, usually in a tight, close-packed configuration. Clearly, this is not the only configuration of adsorbed

molecules when interacting with a solid surface, with multilayer adsorption, via interaction of gas molecules with themselves through vapor-vapor interaction, being also possible. As the energies of gas-solid physisorption and gas-gas interactions are usually similar in magnitude, if the temperature of the solid is lower than the critical temperature of the gas, condensation of the gas to liquid phase occurs on the surface of the solid material.

In this juncture, the BET theory is derived through an extension of the Langmuir model for monolayer molecular adsorption by considering a multilayer adsorption of gas on the surface of a solid. Each layer is approximated as non-interacting with each other and in-equilibrium conditions, each one being described via the Langmuir equation, with each successive layer acting as adsorption site only for molecules in the layer above itself. With these conditions set, the well know BET equation can be formulated:

$$\frac{\frac{p}{p_0}}{V\left(1-\frac{p}{p_0}\right)} = \frac{1}{V_m C} + \frac{C-1}{C}\cdot\frac{\frac{p}{p_0}}{V_m} \qquad (2.6.1)$$

Where

- V is the volume of gas adsorbed at pressure p and absolute temperature T
- p_0 is the vapor pressure of the gas at temperature T
- V_m is the volume of gas adsorbed when the adsorbent surface is covered with a monolayer of gas
- C is a mathematical parameter related to heat of adsorption also known as *BET constant*

Volumes in the BET equation are expressed as volumes of gas at normal temperature and pressure (NPT). In its simplest form, the value of the C parameter, usually quite constant for a given class of materials, can be expressed as:

$$C \propto \exp\left(\frac{q_1 - q_L}{RT}\right) \qquad (2.6.2)$$

Where

- q_1 represents the heat of adsorption of the first layer
- q_L represents the heat of adsorption of multilayers, i.e., via vapor-vapor interaction
- R is the gas constant
- T is the absolute temperature

The C parameter is thus directly related to the affinity of the adsorbed gas for the adsorbent surface: in particular, materials characterized by a high C parameter are more likely to provoke a

monolayer adsorption of the gas on the solid surface before multilayer condensation occurs (i.e., the solid is easily wettable by the gas molecules), whereas for materials characterized by a small C value multilayer adsorption, maximizing vapor-vapor interactions rather than solid-vapor interactions, will prevail, thus preventing the formation of the monolayer adsorption at the surface of the adsorbent (Figure 2.6.1).

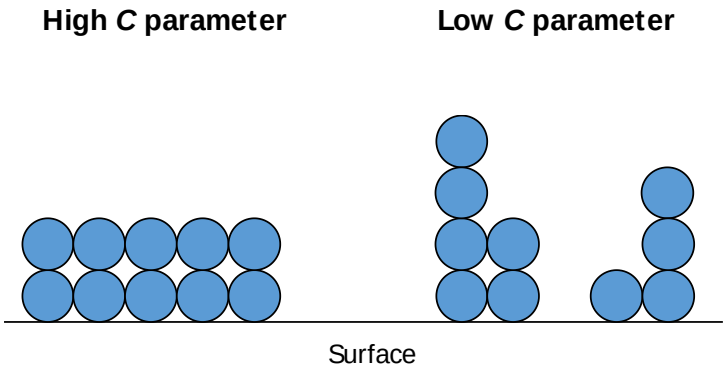

Figure 2.6.1: Examples of gas physical adsorption on a high (left) and low (right) wettable surface of a solid.

In a BET experiment for the study of specific surface area and pore structure of a solid material, gas adsorption/desorption isotherms of physically adsorbed probe gas molecules are recorded. An adsorption/desorption isotherm is a measure of the amount of gas adsorbed (usually expressed as volume or molar) or released by a clean solid surface at temperature T as a function of the p/p_0 relative pressure. To favour the condensation of the probe gas molecules, adsorption/desorption isotherms are usually recorded at the boiling temperature of the probe gas, therefore being cryogenic temperatures. The most employed probe gas molecule is molecular nitrogen, N_2, with the relative adsorption/desorption isotherm being recorded at liquid nitrogen temperature (77 K). The here reported BET equation can be rearranged in a straight-line form obtained by plotting $\frac{p/p_0}{V\left(1-\frac{p}{p_0}\right)}$ as a function of p/p_0, allowing to obtain the desired values of the volume of the monolayer gas adsorption and C parameter starting from the angular coefficient and intercept of the straight line, usually obtained via linear regression of the experimental data (Figure 2.6.2). Notably, the BET equation yields a straight line only for relative pressures between 0.05 and 0.35; thus, to obtain reliable parameters it is important to apply the linear regression only to experimental points within the indicated relative pressure range. The magnitude of the C parameter is of primary importance in determining if the employed probe molecule is suitable for measuring the specific surface area of the material. In fact, if the value of the C parameter is not large and positive enough, a monolayer at the surface of the solid material is not formed, and the specific surface area of the material cannot be obtained.

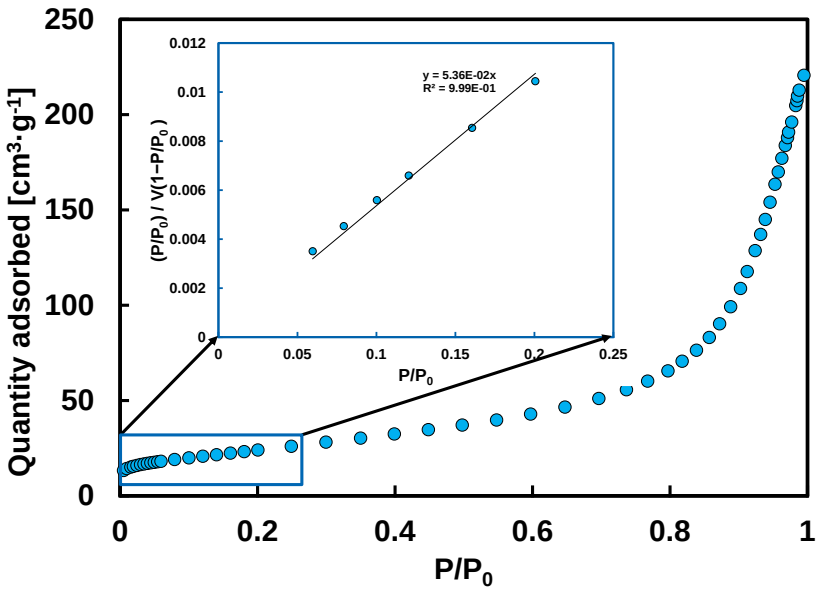

Figure 2.6.2: BET transform plot with a regression line through the linear region (inset).

Knowledge of the area occupied by the adsorbate (in the case of nitrogen A_{N_2} = 16.2 · 10^{-20} m^2) allows one to access the SSA of the material through the formula

$$SSA = \frac{V_m \, N_A \, A}{22.414 \times g} \tag{2.6.3}$$

where:

- N_A is Avogadro's number
- A is the area occupied by a probe molecule
- 22.414 is volume (dm^3) occupied by 1 mole of gas under standard conditions
- g is the mass of the sample used during the adsorption/desorption measurement expressed in grams

In addition to multilayer adsorption, as the pressure of the gas in contact with the solid increases, pore condensation might also be observed. In pore condensation, the gas condenses to a liquid phase in a pore at pressures p lower than the saturation pressure p_0. In this case, the adsorption and desorption isotherm presents a hysteresis which is rationalised in terms of the Kelvin equation:

$$r_k = \frac{2\gamma V_1}{RT} \ln\left(\frac{p}{p_0}\right) \tag{2.6.4}$$

where r_k is the radius of a hemispherical meniscus, γ is the surface tension of the liquid and V_1 represents its molar volume. Moreover, the shape of the hysteresis loop of BET isotherms carries a lot of information regarding the shape of the pore of the analysed materials, as different pore

geometries and sizes originate characteristic, peculiar hysteresis loops.[117,118] Analysis of the isotherm shape, thus, allows to access information regarding the morphology of the investigated specimen. The common stages of pore condensation over the surface of a solid material occurring in a BET experiment with increasing relative pressure are schematized and resumed in Figure 2.6.3. In brief, for a material with a sufficiently high C parameter for the probe gas used, increasing the relative pressure leads to the initial formation of a monolayer of gas adsorption. Subsequently, the adsorption extends to multiple layers, filling smaller pores, and eventually covering larger pores, thereby completely coating the entire surface of the sample.

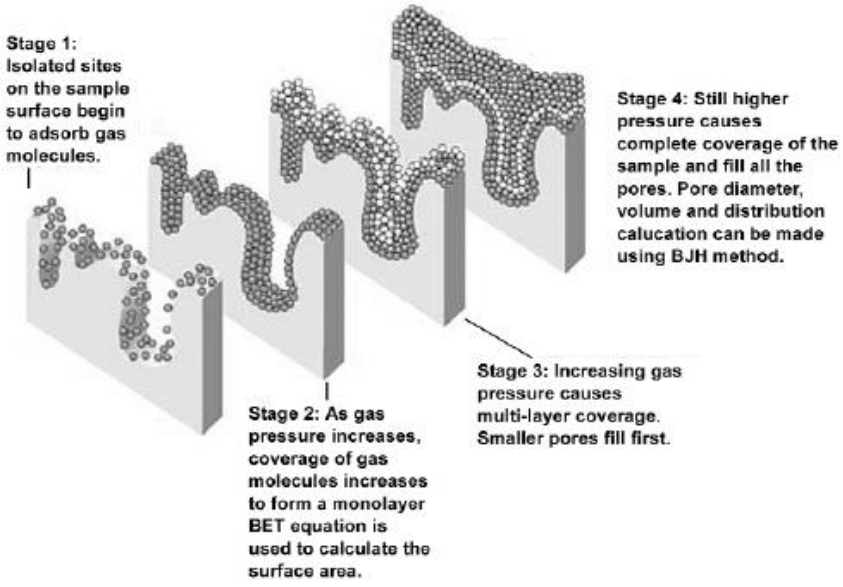

Figure 2.6.3: Scheme of the pore condensation of a gas as a function of pressure at the surface of a porous solid material.[119]

2.6.1 Experimental procedure

During this PhD thesis, Specific surface area (SSA) of the samples was obtained by measuring N_2 adsorption/desorption isotherms at liquid nitrogen temperature according to the Brunauer-Emmet-Teller (BET) method in a Micrometrics Tristar II 3020 V1.03 apparatus equipped with an ASAP 2020 surface area and porosity analyzer, after outgassing at 150 °C for 2 h under constant nitrogen flux. SSA data were calculated by the instrument provided software starting from the linear region of the BET isotherm, using the linearized form of the BET equation.

2.7 UV-Vis Diffuse Reflectance Spectroscopy

UV-Vis Diffuse Reflectance spectroscopy is a widely used, cheap and easily accessible non-destructive analytical technique aimed at the investigation of the spectroscopic features of samples in the form of powders, requiring minimal sample preparation. The technique is an optical

spectroscopy based on recording the electromagnetic radiation reflected by a mat or dull surface as a function of the incident light wavelength, which is commonly used in the case of samples opaque to UV-Vis electromagnetic radiation, which cannot to be analyzed via conventional transmission spectroscopy. Oppositely to smooth surfaces, on which incident electromagnetic radiation is reflected in a specular fashion with a mirror-like behavior, when a sample in powder form is irradiated with a collimated electromagnetic beam a series of complex optical phenomena including reflection, diffraction, refraction, and absorption, along with specular reflection, is produced in a process known as *diffused reflection*, causing the dispersion of the radiation in all spatial directions independently of the electromagnetic radiation incidence angle.

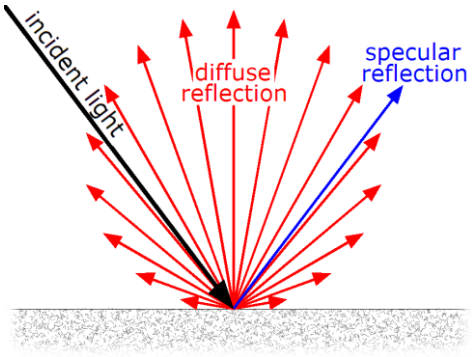

Figure 2.7.1: Specular and diffused reflection of electromagnetic radiation from a surface. Under Creative Common License CC BY-SA 3.0.

In the ideal case, the diffused radiation should behave according to Lambert's Cosine Law,[120] i.e., the light intensity observed from an ideal diffusely reflecting surface or ideal diffuse radiator is directly proportional to the cosine of the angle θ between the direction of the incident light and the surface normal, $I = I_0 \cos\theta$. Clearly, if part of the incident light radiation is be absorbed by the sample, the diffused radiation will carry spectroscopic information on it.[121] Most commonly, if the sizes of the particles are similar or smaller than the irradiation wavelength, multiple scattering and absorption processes occur, usually causing a far from isotropic distribution of the diffused radiation, if not for samples composed of multiple very dense and thick layers.[122]

Complete and rigorous quantitative descriptions of the diffuse reflectance phenomena are not possible due to the intrinsic complexity that characterizes multiple scattering and absorption processes occurring during diffuse reflection. Instead, theoreticians in the past have proposed several different phenomenological theories mostly based on two constants, i.e., the *absorption coefficient* and the *scattering coefficient*, which have proved to provide sufficiently accurate results to be qualitatively and quantitatively used to describe the diffuse reflection process, provided that the right experimental conditions are set. The most famous two-constant theory proposed is represented by the Kubelka-Munk theory[123] from which, under the assumption that the reflecting

sample is thick enough so that a further increase in its thickness won't produce a change in reflectance, the Kubelka-Munk function $\mathrm{F(R_\infty)}$ can be obtained:

$$\frac{K}{S} = \frac{(1 - R_\infty)^2}{2R_\infty} = F(R_\infty) \qquad (2.7.1)$$

where R_∞ is the absolute diffuse reflectance of an infinitely thick sample K, is the absorption coefficient and S is twice the scattering coefficient of the material. The diffuse reflectance R_∞ is defined, similarly to the transmission coefficient, as:

$$R_\infty = \frac{J}{I_0} \qquad (2.7.2)$$

where J is the intensity of the reflected radiation and I_0 is the intensity of the incident light. Since absolute reflectance is not practical to measure experimentally, the use of the relative reflectance R'_∞, defined as

$$R'_\infty = \frac{R_{\infty,sample}}{R_{\infty,standard}} \qquad (2.7.3)$$

is preferred.

Through the Kubelka-Munk function $F(R_\infty)$, a photoabsorption spectra of the investigated specimen in terms of Kubelka-Munk units can be obtained and represents the most commonly method used in the photocatalysts literature for investigating the photo absorption properties of semiconductor photocatalysts. As pointed out by Ohtani et al.,[124] however, Kubelka-Munk units are not appropriate as units to measure the intensity of absorbed light since they are mainly proportional to the concentration of a given material dispersed in a homogeneous medium, but not to the number of photons absorbed by a solid sample. For this reason, during the course of this PhD thesis, photoabsorption spectra were rather expressed in terms of the more appropriate absorption units, which can be easily calculated as $(1 - R_\infty)$.

Diffuse reflectance spectra are acquired using a UV-Vis spectrophotometer equipped with a special accessory named integrating sphere (Figure 2.7.2), capable of collecting the radiation diffused by the sample, usually easily adaptable in the sample holder compartment of most commercially available spectrophotometers. An integrating sphere is a hollow sphere whose walls are coated with a material whose reflectance is close to 1 at all wavelengths (usually MgO, $BaSO_4$ or the thermoplastic resin Spectralon®), with apertures allowing the incident beam to enter the sphere, loading the sample in its appropriate location and mounting the desired detector. The

sphere is constructed in such a way so that the incident beam impinges on the sample with a 0 degree angle, so that the unwanted specularly reflected light, being the least spectroscopically informative component of the reflected light, can be totally avoided from being collected, by placing the detector with a 90° angle with respect to the incident beam. With such geometry, through multiple reflection on the walls of the hollow cavity, the integrating sphere is able to finely collect all radiation diffused from the sample. Due to the presence of possible imperfections in the geometry of the sphere and to the inexistence of perfectly reflecting materials, to obtain a DR-spectrum, measurement of the reflectance of a standard material whose reflectance is close to 1 at each wavelength (usually composed of the same material with which the walls of the integrating sphere are coated with) is determined prior to any measurement. The desired spectra are obtained by measuring the relative reflectance of the analyzed sample with respect to that of the reference material at each wavelength.

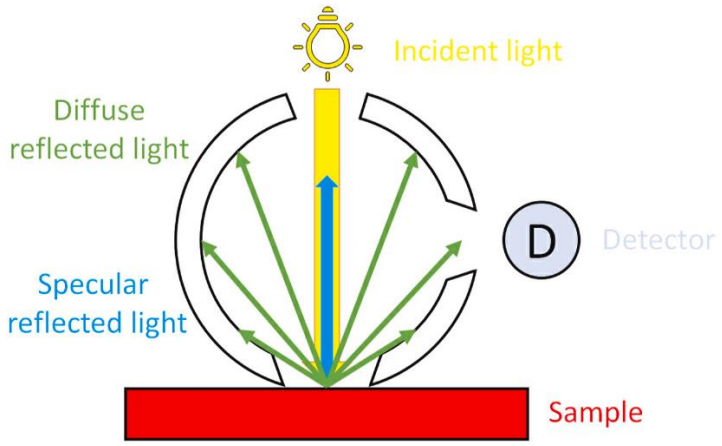

Figure 2.7.2: Scheme of a typical integrating sphere.[125]

2.7.1 Experimental procedure

During this PhD thesis, UV-Visible absorption spectra of the materials in powder form were acquired in diffuse reflectance mode (DR spectra) using a Jasco V-670 spectrophotometer equipped with a PIN-757 integrating sphere, using barium sulphate as a reference standard. Reflectance (R) spectra in the 200-800 nm region, with a 1 nm spectral resolution, were converted into absorption (A) spectra using the relation $A = 1 - R$.

2.8 Inductively Couple Plasma – Optical Emission Spectroscopy (ICP-OES)

Inductively Coupled Plasma Optical Emission Spectroscopy (ICP-OES), sometimes referred to as ICP-Atomic Emission Spectroscopy (ICP-AES), is an analytical technique aimed at the

quantitative detection of chemical elements in a sample. The technique is an emission spectroscopy based on the spontaneous emission of atoms and ions that have been excited through thermal excitation at high temperature by means of a radio frequency inductively coupled plasma. In fact, atoms and ions can absorb energy such as heat to promote electrons from their ground state to a higher energy excited state. The lifetime of an excited atom, however, is very brief, and its return to a lower energy level, usually the ground state, results in the emission of a photon whose wavelength is determined by the energy difference between the two levels involved in the electronic transition. Since the amount of light released at each wavelength is proportional to the number of atoms or ions involved in the electronic transition, the emission intensity at specific wavelengths can be used to quantitively determine the content of specific elements in a sample.[126]

In ICP-OES, the energy source used for the excitation process is heat from an argon plasma, a heavily ionized gas that can operate up to 10'000 K. The inductively coupled plasma is generated as follows: radio frequency power of usually 700-1500W is applied to a radiofrequency load coil, where the changing external magnetic field applied induces the flow of an alternate current oscillating at the same rate of the RF generator inside to load coil. For most ICP, the RF generator operates at either 27 or 40 MHz. Oscillation of high frequency current inside the coil (which is typically shaped as a cylindrical solenoid) causes the same high-frequency oscillation of electric and magnetic fields inside the top of the torch. With Ar gas flowing through the torch, a spark from a Tesla coil is used to produce 'seed' electrons and ions inside the load coil region. Using the electromagnetic field created in the torch tube by the high frequency current, the electrons are accelerated and collide with other argon atoms, causing further ionization in a chain-reaction manner. This process continues until a very intense, brilliant white, teardrop-shaped, high-temperature plasma is formed. Since plasma operates at much higher temperature than flames, it provides better atomization and a higher population of excited states compared to flame-AES.

In ICP-OES, the analytical information is obtained by introducing a liquid sample into a nebulizer, where it is converted into a fine aerosol of droplets in a process called nebulization. The aerosol then passes into a spray chamber, where larger droplets condense and are removed via the drain, while finer droplets move with the argon flow and enter the plasma, where atoms and ions undergo the excitation process, followed by the emission of characteristic radiation. The emitted electromagnetic radiation is detected typically through charge coupled devices (CCD) and converted into an electrical signal used to trace both the type and concentration of the analyte that emitted the radiation, provided that an appropriate calibration curve is constructed. To calibrate an ICP-OES, solutions containing known amounts of each element are measured. From these

data, a calibration curve is created, determining the relationship between the intensity of light emitted at a specific wavelength and the concentration of the element in solution.

Advantages of ICP-AES are its excellent limit of detection and linear dynamic range, multi-element analysis capability, low chemical interference, a stable and reproducible signal, high matrix tolerance, and enhanced speed of analysis. Its main drawbacks are represented by the presence of possible spectral interferences (especially if many emitting elements are present in a sample), high instrumentation and operating costs, and ability to analyse samples in solution only.[128]

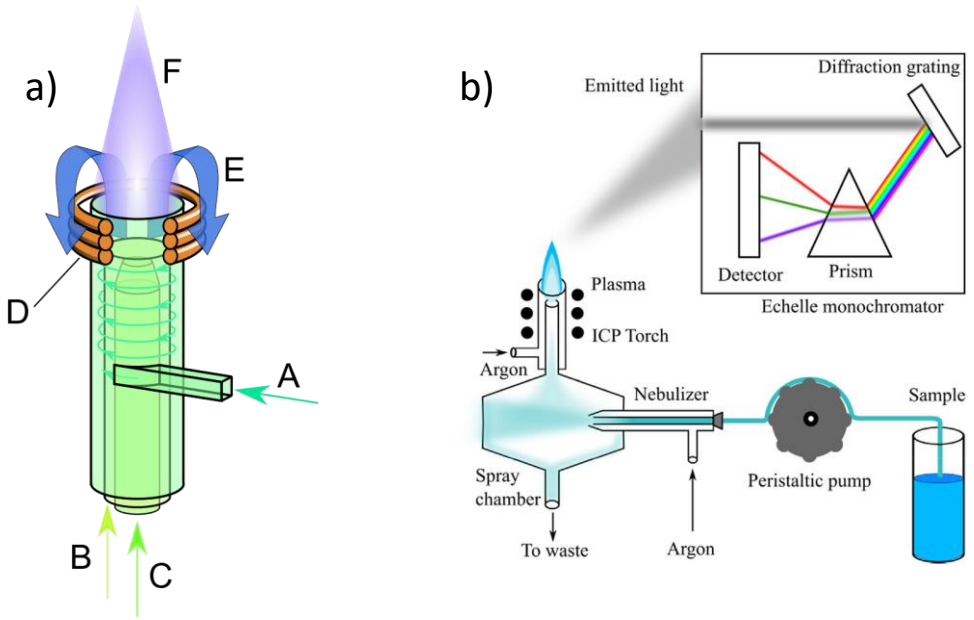

Figure 2.8.1: Scheme of an ICP torch (a). A: cooling gas tangential flow to the outer quartz tube; B: discharge gas flow (usually Ar); C: flow of carrier gas, containing nebulized sample; D: induction coil which forms the strong magnetic field inside the torch; E: force vectors of the magnetic field; F: plasma torch (discharge). Under Creative Common License CC BY-SA 3.0; simplified scheme of an ICP-OES instrument (b).[127]

2.8.1 Experimental procedure

During this PhD thesis, ICP analyses were carried out with a PerkinElmer® Optima™ 8000 ICP-OES, equipped with full-wavelength-range CCD array detector operating in a spectral range between 165-900 nm with resolution of 0.009 nm at 200 nm. ICP analyses were performed to determine the actual percent Au loading on the surface of gold-modified titanium dioxide materials. The samples were subjected to a digestion treatment in aqua regia aimed at dissolving and quantify the gold nanoparticles deposited on them.

The digestions were carried out as follows: a known amount of Au-modified titanium dioxide powder was suspended under constant stirring in an *in-situ* prepared aqua regia solution, obtained by mixing aqueous HCl (34 vol%) with HNO_3 (65 vol%) in a 3:1 molar ratio. Both employed acids were of analytical-grade purity. The obtained suspension was then heated on a stirring-heating

plate at the boiling temperature of aqua regia (108 °C) and stirred at 1000 rpm for 4 hours. Once the mixture had cooled down naturally to room temperature, the powders were separated from the suspension by centrifugation with a relative centrifugal force of 3661 x g using a Thermo Scientific CL 10 centrifuge with F-G1 Fixed Angle Rotor of 131 mm radius for 30 min. The supernatant was then quantitatively recovered from the Falcon tubes, transferred to a 25 or 50 cm^3 flask, and brought up to volume with ultrapure Milli-Q water. The obtained solutions were then injected in the ICP -OES system for the analytical detection of gold. Concentration of the noble metal was obtained via construction of appropriate calibration curves.

All reagents were purchased from Sigma Aldrich and employed as received. Water purified by a Millipore Direct-Q 3 UV water purification system was used throughout (18.2 MΩ cm at 25°C).

2.9 Transmission Electron Microscopy

Transmission Electron Microscopy (TEM) is a microscopy technique in which electrons are used to form an image, oppositely to optical microscopy which instead uses photon-matter interactions to produce magnification of an object. There are many advantages to use electrons to form an image rather than photons. First and foremost, electrons can provide very short wavelengths: for example, electrons with around 100 keV energy (a common electron energy employed in TEM images acquisition experiments) are characterized by a wavelength ~$4 \cdot 10^{-3}$ nm, whereas with optical microscopy photons with a wavelength around 400 nm represent the common wavelength lower limit, order of magnitudes larger than that of electron beams. The very short wavelength of the electron beam allows to magnify objects with a resolution unachievable through optical microscopy.

In fact, according to classical optics, a converged focused light beam passing through a lens originates a peculiar diffraction pattern known as the Airy disk, characterized by a bright central region accompanied by a series of concentric rings of decreasing intensity all around the central spot (Figure 2.9.1a). The formation of Airy disks is of primary importance in optics, as for systems in which the resolution is no longer limited by aberration the maximum resolution with which an object can be distinguished from another is determined by the diffraction limit, i.e., blurring of the images caused by diffraction phenomena occurring between two neighbouring Airy disks. The resolution of an optical system in diffraction limit can be easily obtained through the Rayleigh criterion, stating that the maximum resolution of a system of known angular resolution is obtained when the maximum of the Airy disk of one image coincides with the first minimum of the airy

disk of the other (Figure 2.9.1b). The Rayleigh criterion can be mathematically expressed in the form:

$$\delta = \frac{0.61\,\lambda}{\mu \sin \beta} \qquad (2.9.1)$$

where δ is the resolution, λ is the wavelength of the beam used to form the images, μ is the refracting index, and β is the semi-angle of collection, whose value is determined by the size of the optical aperture. The denominator of the expression is also known as numerical aperture (NA), a dimensionless number that characterizes the range of angles over which a lens can transmit light. From the expression above it is easy to understand that a much shorter wavelength such as that provided by accelerated electrons in TEM allows to obtain much better resolved images compared to optical microscopy. It is important to note, however, that the Rayleigh criterion represents the theoretical maximum resolution of an optical system, being practically unachievable for any real system as optics unaffected by any sort of aberration cannot exist.

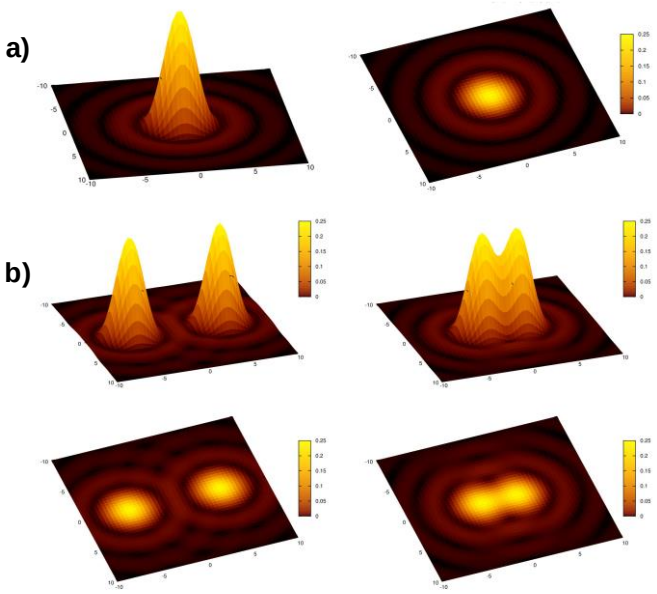

Figure 2.9.1: Airy disk diffraction pattern (a); graphical demonstration of the Rayleigh criterion for the diffraction limit of images (b). As the Airy disks in the picture on the left are well-separated, the resulting images are well resolved. On the right, instead, the images are blurred as the Rayleigh criterion is not respected, and interference phenomena disturb the acquired images causing blurring.

In a transmission electron microscope, highly accelerated electrons are produced through an electron gun, in its simplest form comprised of a tungsten wire with a very sharp tip, acting as a cathode, connected to a current generator (Figure 2.9.2b). As current is passed through the wire, its heating induces the expulsion of electrons from its sharp tip due to the thermionic effect. Once electrons are expelled, the presence of a potential difference around 100'000-300'000 V between

the cathodic wire and an anodic plate accelerates the electrons, increasing their energy in the above discussed order of magnitudes. Then, electrons pass through the column of the microscope to be collimated by an electromagnetic lens named condenser lens, which adjusts the magnification degree of the microscope by controlling the size the spot of the specimen being illuminated by the electron beam (Figure 2.9.2a). The condenser lens adjusts the size of the spot by collimating the electrons through generation of an electromagnetic field, thus modifying their trajectory according to Lorentz forces. Then, electrons are projected to the sample which, due to their high energy, are able to pass through. Samples in TEM are usually mounted on tiny copper grids and placed in a specific sample holder commonly located at the side of the column (Figure 2.9.2c). Then, the electron beam is collimated and magnified through a series of electromagnetic lenses to be finally focused to a fluorescent screen and/or to the image generation system, usually a CCD camera. Moreover, TEM instruments are always provided with an ultra-high vacuum system, as the whole instrument needs to be maintained under ultra-high vacuum conditions (10^{-7}-10^{-8} Pa) to avoid any possible collision between electrons and atoms, which could be present in the instrument and are not part of the investigated specimen.

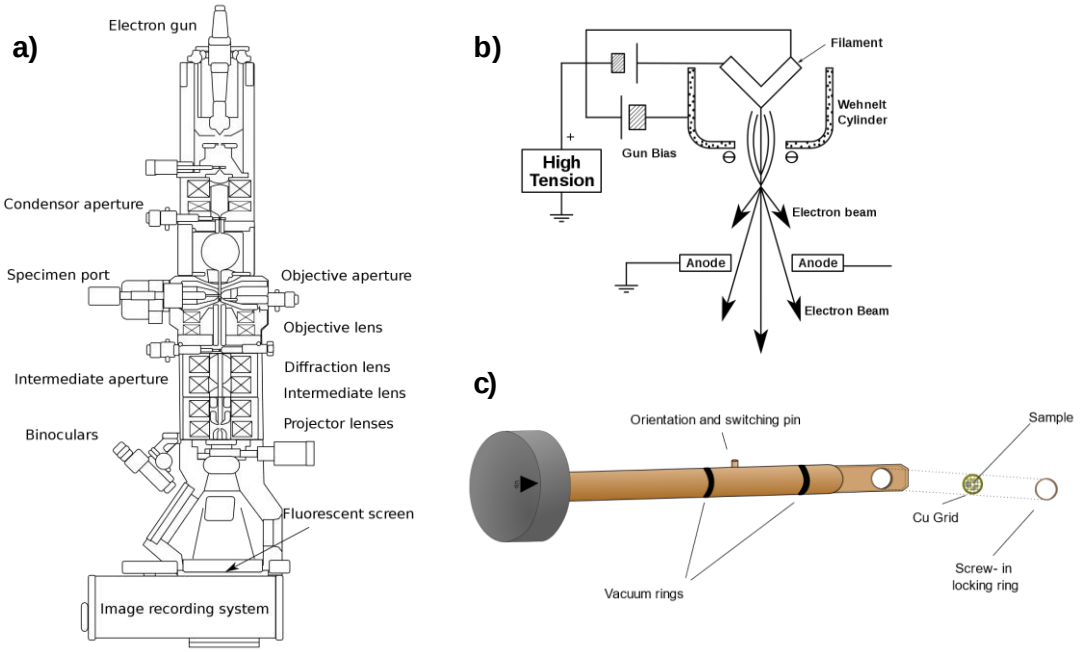

Figure 2.9.2: Schemes of Transmission Electron Microscope (a); Electron gun (b); Sample holder and copper grid (c). Under Creative Common license CC BY 4.0s.

Transmission Electron Microscopy allows to record images mainly in three different imaging modes. The most basic, ordinary method is named *bright field imaging*. In that, the aperture is set in such a way so that only electrons that pass straight through the sample arrive to the detector, whereas electrons which could be reflected and/or scattered are excluded (Figure 2.9.4). In bright

field imaging, contrast is formed because scattering and reflection processes reduce the number of electrons reaching the detector in that pixel, so that darker areas in the image correspond to parts of the specimen with higher atomic number or higher density, whereas bright spots correspond to areas where electrons encounter less obstacles within their path (Figure 2.9.3a). Images formed via bright field imaging consist of 2D projections of the sample. Oppositely, in *dark field imaging* mode, the aperture is set in such a way so that the electrons that pass directly through the sample are completely cut out the measurement, whereas only a fraction of the diffracted electrons are allowed to pass through the aperture (Figure 2.9.4). Since diffracted electrons interact strongly with the specimen, useful information on the sample can be gathered in dark field mode such as crystal structure, planar defects, phase composition, stacking faults, grain boundaries, and so on (Figure 2.9.3b).

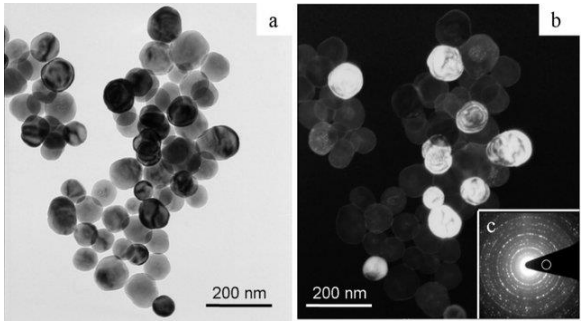

Figure 2.9.3: Examples of bright (a) and dark (b) field transmission electron microscopy images of hydrothermally synthesized $BaTiO_3$ nanoparticles. Bright sports in the dark field image highlight the presence of nanoparticles affected by high strain.[129]

In the third operating mode, both transmitted and diffracted electrons are selected to produce the image, provided that proper corrections for the spherical aberration of the optics are used. In such mode, TEM images with a resolution below 0.1 nm can be obtained; therefore the name *High-Resolution TEM* (HR-TEM). With such high resolution, it is possible to observe reticular planes and, in some cases, even the atomic structure of crystalline materials.

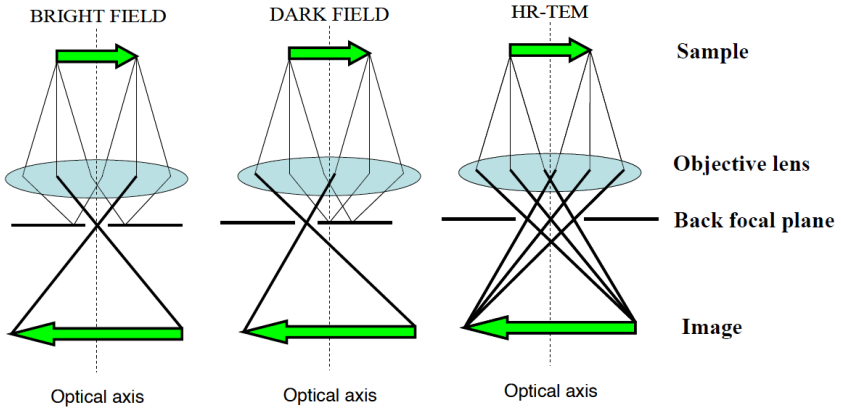

Figure 2.9.4: Diagram of the beam selection in the three main operating modes in transmission electron microscopy.

2.9.1 Experimental procedure

During this PhD thesis, HRTEM images were recorded in two separate acquisitions by using two different TEM instruments. A first set of images was acquired on a JEOL JEM 2010 electron microscope, equipped with a LaB_6 electron gun operating at 200 keV and a Gatan CCD camera allowing high-resolution imaging. Image acquisition was performed by Dr. Gianluigi Marra at Istituto Eni Donegani, Novara (NO). The second set was acquired on a FEI Tecnai F20 Field Emission Gun (FEG) microscope, working at accelerating voltage of 200 kV. A S-Twin system lens guarantees a point resolution of 0.24 nm, and an energy dispersive X-ray spectrometer (EDS) with ultrathin window allows for chemical characterization at the nanoscale. The imaging system is composed by one tv rate 626 Gatan and one slow scan 794 Gatan CCD cameras. All the detectors are embedded in the control unit of the microscope. The sample holder is double tilt. Image acquisition was performed by Dr. Nicola Rotiroti at Univesità degli Studi di Milano, Earth Sciences Department, Milano (MI). In both cases, specimens for TEM analysis were prepared by sonicating 4 mg of powder in 2 mL of 2-propanol for 30 min. 50 μL of the obtained suspension were thus transferred on a copper grid covered with a holey carbon film. Micrographs were taken after solvent evaporation, spanning over the whole region of the sample, to achieve a truly representative statistical mapping of the investigated materials.

2.10 Time-Resolved Photoluminescence Spectroscopy (TRPL)

Time-Resolved Photoluminescence Spectroscopy (TRPL) is an optical emission method allowing the investigation of a wealth of dynamic processes involving photoexcited charge carriers including charge and energy relaxation, recombination, and transfer.[130] Despite the origin and interpretation of photoluminescence is known since the mid nineteenth century, TRPL techniques started to be regularly used for the investigation of the photoluminescent properties of both liquid and solid samples only in the last decades, mostly due to the technological development of advanced devices such as ultrafast detectors and lasers, which made possible recording the temporal evolution of the emission spectra of a fluorophore up to the pico-to-femtosecond time scale.

In a photoluminescence experiment, as a sample is irradiated with a light source of sufficient energy, an electronic excitation of the absorber to a higher-energy state is induced. Due to the intrinsic instability of electronically excited states, rapid relaxation processes in the system occur, which can be broadly divided in two major categories, i.e., radiative and non-radiative processes. As the name implies, through radiative relaxation processes an electronically excited electron

returns to its ground state releasing energy via emission of a photon. Non-radiative decays, on the other hand, consist of all deactivation processes involving loss of energy without emission of a photon, most commonly in the form of heat. This simplified first approximation is usually depicted in more detail in terms of the so-called Jablonski diagram, a graphical representation of the possible deactivation paths of an electronically excited system (Figure 2.10.1).

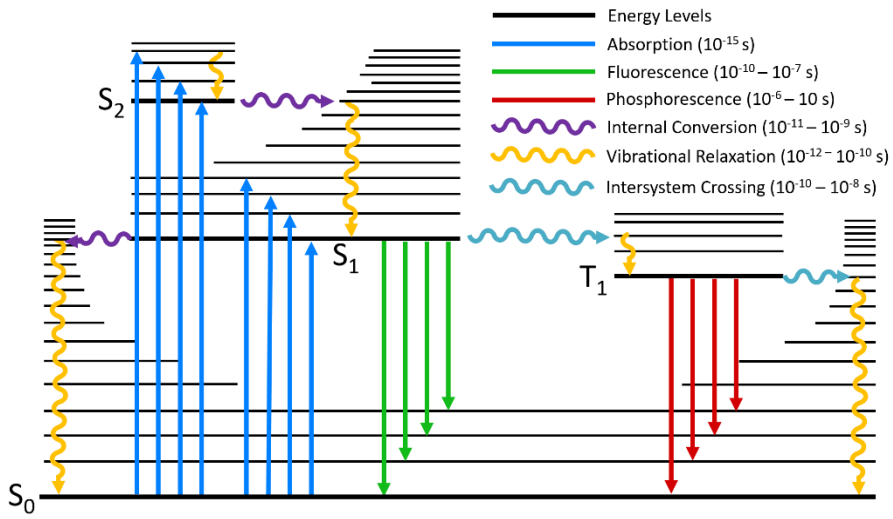

Figure 2.10.1: Example of a Jablonski diagram showing the possible radiative (straight lines) and non-radiative transitions (curved lines).

Recording the intensity of the photons emitted from a sample during its relaxation to the ground state as a function of the emission wavelength produces a so-called photoluminescence spectrum. If the light source irradiates the sample continuously while recording the spectrum, a so-call steady-state emission is produced. Oppositely, if excitation is provided through short bursts of light, as excited states have a finite lifetime it is possible to monitor the decay of the intensity of the photoluminescent emission within a certain wavelength range as a function of time. If we consider, for simplicity, an ideal case of a single fluorophore-containing molecule, the decay of the photoluminescence intensity as a function of time can be expressed through a single exponential decay function in the form:

$$\frac{I(t)}{I(0)} = \exp\left(-\frac{t}{\tau}\right) \qquad (2.10.1)$$

where $I(0)$ is the emission intensity at time zero, $I(t)$ is the emission intensity at time t and τ is the *lifetime* of the excited state, which can be expressed as

$$\tau = \frac{1}{k_r + k_{nr}} \qquad (2.10.2)$$

where k_r and k_{nr} are the rate constants for the radiative and non-radiative decay processes, respectively. Mathematically fitting an experimentally recorded photoluminescence decay curve for such molecule with the single exponential decay function above reported allows to calculate the lifetime of the excited state at the temperature of the experiment. Clearly, in a real case, for most fluorescent substances and especially for semiconductors, the photoluminescence decay curve is often represented by more complex multiexponential decay functions (Figure 2.10.2).

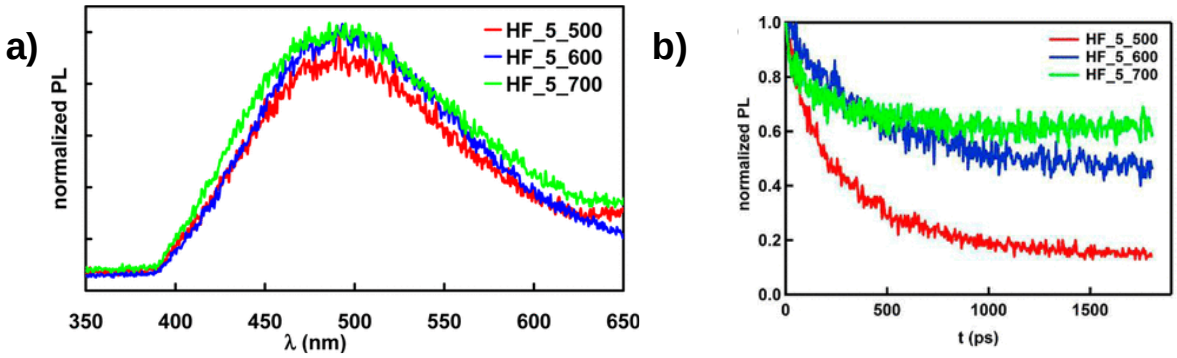

Figure 2.10.2: Example of the steady state photoluminescent emission (a) and PL decay curves (b) of N,F-doped titanium dioxide materials calcined at different temperatures.[131]

The basic concept on which all TRPL methods are based is the excitation of the investigated sample with a pulsed light followed by the recording of its emission spectrum during the time frame in which light is switched off. High repetition rates of the excitation pulses are a necessary requirement for obtaining TRPL analyses of sufficiently high quality since emission spectra of systems excited through a pulsed light are usually of low intensity and signal/noise ratio. The recording of multiple emission spectra in a very short frame allows to greatly improve both signal/noise ratio and intensity counts through an averaging procedure. The maximum repetition rate allowed for the analysis of the TRPL of a specimen is determined by the relaxation time of the fluorophores to their ground states, i.e., the delay between each pulse should be set so that only ground state → first excited states transitions occur within the sample. Avoiding higher order excitation is usually mandatory for obtaining experimental results simple enough to gather meaningful physical information out of them.[132]

Time-Resolved Photoluminescence can be performed by means of different experimental apparatuses and methods, mainly differing in their excitation and detection systems, each one allowing to observe radiative decay phenomena occurring at different time scales. The most basic method for recording TRPL spectra consists in simply relying on basic fast-detection electronic components to capture the emission spectra in between each pulse. In this type of configuration, the sample is irradiated through a light source, typically a pulsed laser, and detected via a fast-responding electronic system such as a CCD camera. The light source and the detector are

interconnected by means of a delay generator which precisely sets up the time difference between the light source and the detector, allowing to measure the decay of the photoluminescent emission intensity as a function of time. Usually, through such configuration, radiative decay phenomena occurring in the nanoseconds time scale can be observed.

However, different types of apparatuses and methods allow to bring the temporal resolution down to shorter time scales such as picoseconds. Among these, Time-Correlated Single Photon Counting (TCSPC) represents one of the most commonly employed techniques. In TCSPC, excitation of the investigated sample is provided through illumination with a very low intensity periodic laser pulse. After the excitation pulse is sent, the time delay between a single photon emitted from the sample and a reference trigger pulse is recorded. Through that, a histogram consisting of counts of the number of single photons arriving at the detector with a given temporal delay is obtained (Figure 2.10.3a). By this way, a sort of probabilistic lifetime of the excited states can be derived. The method requires a high number of repetitions of excitation and detection events to provide statistically meaningful experimental results, since the emission of single photons from the fluorophore is monitored, with PL traces being detected in each emission. In TCSPC the photons are detected either through a fast-responding photomultiplier or a single photon avalanche photodiode. Through this technique, shorter time resolutions can be achieved. However, this comes at the expenses of long data acquisition times, instrumentation with more complex electronics, more susceptibility to stray light interferences and the impossibility of monitoring radiative phenomena occurring within a time scale longer than 10 μs.

Another possibility to reduce the time resolution in TRPL measurements is represented by the use of streak cameras as detectors instead of CCD cameras. A streak camera is a device allowing to convert the temporal component of the optical signal coming from the emitted photons into a spatial profile. The way this conversion is made closely resembles the image formation process in an old cathodic ray tube television. In a streak camera, photons emitted from the sample are absorbed by a photocathode, which emits electrons through the photoelectric effect. Then, produced electrons are accelerated in a cathodic ray tube and projected towards a microchannel plate. Within their path, the electrons pass through a pair of electrode plates between which a potential difference is applied to, placed perpendicularly to their trajectory. The potential difference between the electrodes is set up so that it ramps up as a function of the time delay from the excitation pulse. The electrons emitted from the photocathode are deflected in their trajectory by the electric field generated by the electrode plates, with a magnitude depending on the potential difference applied between the plates. As a consequence, electrons generated by photons arriving at the photocathode at a longer delay time will reach the microchannel plate at a spatial position

different than those arrived earlier and, through a proper setup of the electronics, this spatial position difference can be back converted to the time delay value of the photons approaching the photocathode (Figure 2.10.3b). By this way, the average lifetime of the emitting excited state can be obtained with a temporal resolution close to 2 ps. The main drawbacks of the use of a streak camera, however, are represented by a high dependence on the stability of the employed light source, a very narrow range of time resolution (2-10 ps), the need of careful and frequent calibration and, last but not least, the high cost of the instrumentation.

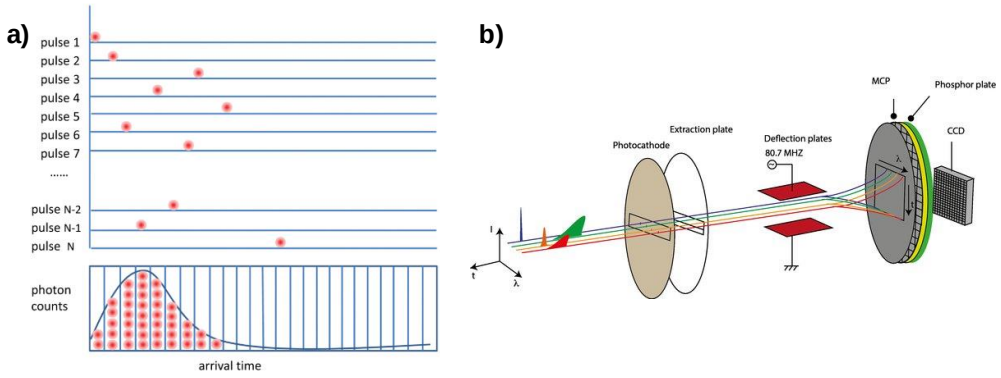

Figure 2.10.3: In time-correlated single photon counting, a statistical distribution of the delay time between photons emitted by single photons is obtained (a); Operational diagram of a streak camera (b).

2.10.1 Experimental procedure

During this PhD thesis, steady-state (acquired as time-gated spectrum in the 0-120 ns time scale) and time-resolved photoluminescence spectra have been acquired with a unique experimental setup located at the Politecnico of Milano in the photonics laboratory of Prof. Gianluca Valentini. The setup consists in a time-resolved spectroscopy system based on a pulsed laser and a fast-gated detector. The excitation light was provided by the third harmonic of a Nd:YAG laser, in Q-switch regime, emitting subns pulses at 355 nm (CryLas FTSS 355-50-779) with 100 Hz repetition rate. The measurements were performed directly on the powders. The fluorescence emission was collected and focused to the entrance slit of an imaging spectrometer (SP2300, Princeton Instruments, USA) that enabled us to record the emission spectrum from 400 to 720 nm, with a resolution of ca. 3 nm.

The exit port of the spectrometer was coupled to a time-gated image intensifier (C9546−03, Hamamatsu Photonics, Japan), featuring an acquisition gate adjustable from 3 ns to continuous mode. The light intensifier was optically coupled to a low noise, 1280 × 1024 pixel, CCD camera (Retiga R6, QImaging, Canada), which records the wavelength dispersed luminescent emission. The synchronization of the gated intensifier with the laser pulses was provided by a homemade circuit coupled to a precision delay generator (DG535, Stanford Research Systems, Sunnyvale,

CA). The jitter of the system, which sets the overall time resolution, is very small (<250 ps) and significantly lower than the rising edge of the acquisition gate.

For time-resolved measurements, the gate width was set to 10 ns and a sequence of delayed spectra was taken with uneven temporal spacing between delays. A first sequence of delayed spectra was acquired with 1 ns relative spacing, starting from a null delay (leading edge of the gate synchronous with the laser pulse) to a delay of 13 ns; then, a 5 ns spacing between delay was adopted up to 113 ns; finally, a sequence of delayed spectra was acquired with 40 ns relative spacing. The uneven temporal sampling was adopted in order to account for the different decay times of the emission components. A total of 60 spectra, including some background spectra taken at very long delays (milliseconds), were acquired for each sample. The whole measurement procedure took about 3 min per sample and was repeated in the same way for all of the investigated materials. Yet, for several samples, the long-delay spectra were dropped from the analysis due to lack of signal. A schematic representation of the experimental setup is reported in Figure 2.10.4.

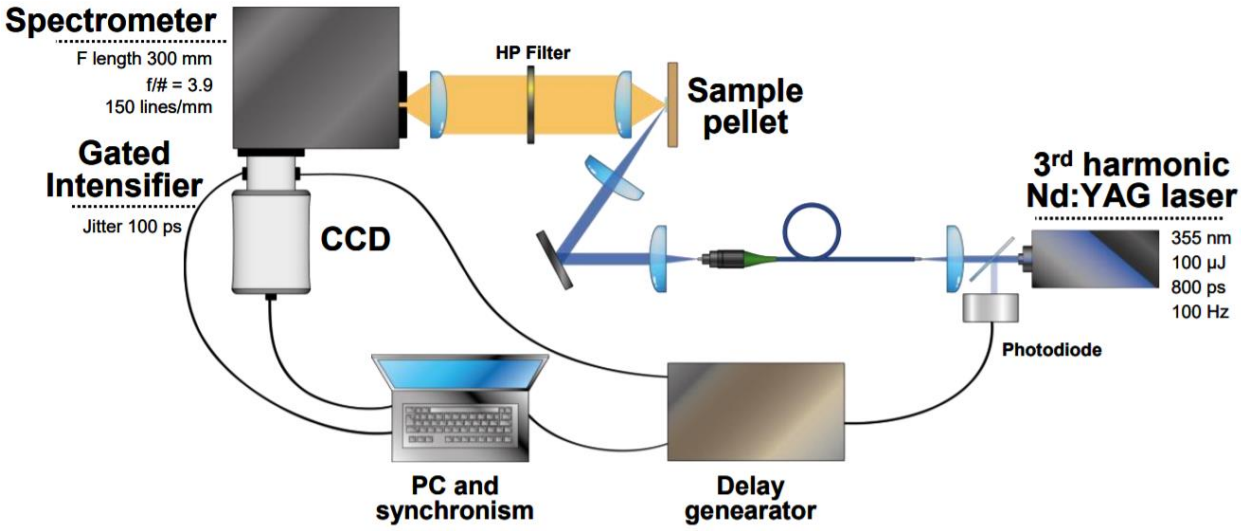

Figure 2.10.4: Main scheme of the employed gate intensifier-based time-resolved PL spectroscopy experimental setup.[79]

Emission decay curves were fitted according to the following tri-exponential decay model function:

$$F(d) = A_1\tau_1 \exp\left(-\frac{d}{\tau_1}\right)\left(1 - \exp\left(-\frac{W}{\tau_1}\right)\right) + A_2\tau_2 \exp\left(-\frac{d}{\tau_2}\right)\left(1 - \exp\left(-\frac{W}{\tau_2}\right)\right)$$
$$+ A_3\tau_3 \exp\left(-\frac{d}{\tau_3}\right)\left(1 - \exp\left(-\frac{W}{\tau_3}\right)\right) + W_{offset}$$

where F is the fluence, i.e., the integral of the emission intensity within the gate window, d is the acquisition delay for each data point of the sequence, while A_i and τ_i are the amplitude and lifetime

of each emission component. The terms $\left[1-\exp\left(-\frac{W}{\tau_i}\right)\right]$ are required to correct for the fixed time width W of the sampling window (10 ns). The fitting method is based on a standard least mean square algorithm employing the OriginLab® software.

Steady-state photoluminescence spectra were acquired as time-gated spectra in the same experimental conditions. Elaboration of steady-state photoluminescence data was performed using a MATLAB® script provided by Prof. Daniela Comelli, Politecnico of Milano.

Evaluation of the total photoluminescence intensity of the analyzed samples was performed by integrating the area underneath the curve of each spectrum in the 400-700 nm wavelength range, using a numerical integration algorithm based on trapezoidal integration provided by the OriginLab® software. Total photoluminescence intensity data are reported as the average value of multiple acquisitions performed in different points of each pellet to check the reproducibility of the recorded data and provide statistical uncertainty values.

2.11 References

1. MacWan, D. P., Dave, P. N. & Chaturvedi, S. *J. Mater. Sci.* **46**, 3669–3686 (2011).
2. Baig, N., Kammakakam, I., Falath, W. & Kammakakam, I. *Mater. Adv.* **2**, 1821–1871 (2021).
3. Eshtiagh-Hosseini, H., Housaindokht, M. R. & Chahkandi, M. *Mater. Chem. Phys.* **106**, 310–316 (2007).
4. Meixner, D. L. & Dyer, P. N. *J. Sol-Gel Sci. Technol.* **14**, 223–232 (1999).
5. Arya, S., Mahajan, P., Mahajan, S., Khosla, A., Datt, R., Gupta, V., Young, S.-J. & Oruganti, S. K. *ECS J. Solid State Sci. Technol.* **10**, 023002 (2021).
6. Akia, M., Alavi, S. M., Rezaei, M. & Yan, Z. F. *Microporous Mesoporous Mater.* **122**, 72–78 (2009).
7. Milea, C. A., Bogatu, C. & Duta, A. *Eng. Sci.* **4**, 59–66 (2011).
8. Ebelmen, M. *Ann. Chim. Phys.* **16**, 129–166 (1846).
9. Graham, T. *J. Chem. Soc.* **17**, 318–327 (1864).
10. Dislich, H. *Angew. Chemie Int. Ed. English* **10**, 363–370 (1971).
11. Purcar, V., Rădiţoiu, V., Dumitru, A., Nicolae, C. A., Frone, A. N., Anastasescu, M.,

Rădiţoiu, A., Raduly, M. F., Gabor, R. A. & Căprărescu, S. *Appl. Surf. Sci.* **487**, 819–824 (2019).

12. Purcar, V., Şomoghi, R., Niţu, S. G., Nicolae, C. A., Alexandrescu, E., Gîfu, I. C., Gabor, A. R., Stroescu, H., Ianchiş, R., Căprărescu, S. & Cinteză, L. O. *Nanomaterials* **7**, 439–452 (2017).

13. Fu, M., Li, Y., Wu, S., Lu, P., Liu, J. & Dong, F. *Appl. Surf. Sci.* **258**, 1587–1591 (2011).

14. Znaidi, L. *Mater. Sci. Eng. B Solid-State Mater. Adv. Technol.* **174**, 18–30 (2010).

15. Spataru, C. I., Purcar, V., Ghiurea, M., Radovici, C., Stanga, G. & Donescu, D. *J. Sol-Gel Sci. Technol.* **65**, 344–352 (2013).

16. Parashar, M., Shukla, V. K. & Singh, R. *J. Mater. Sci. Mater. Electron.* **31**, 3729–3749 (2020).

17. Brinker, C. J. & Scherer, G. W. *J. Non. Cryst. Solids* **70**, 301–322 (1985).

18. Su, C., Hong, B.-Y. & Tseng, C.-M. *Catal. Today* **96**, 119–126 (2004).

19. Gopal, R., Goyal, A., Saini, A., Nagar, M., Sharma, N., Gupta, D. K. & Dhayal, V. *Ceram. Int.* **44**, 19099–19105 (2018).

20. Lee, J.-E., Kim, J.-W., Jung, Y.-G., Jo, C.-Y. & Paik, U. *Ceram. Int.* **28**, 935–940 (2002).

21. Cassidy, D. J., Woolfrey, J. L., Bartlett, J. R. & Ben-Nissan, B. *J. Sol-Gel Sci. Technol.* **10**, 19–30 (1997).

22. Amari, R., Mahroug, A., Boukhari, A., Deghfel, B. & Selmi, N. *Chinese Phys. Lett.* **35**, 16801 (2018).

23. Kelly, J. A., Henderson, E. J. & Veinot, J. G. C. *Chem. Commun.* **46**, 8704–8718 (2010).

24. Biswas, S., Majumder, A., Hossain, M. F., Takahashi, T., Kubota, Y. & Fujishima, A. *J. Vac. Sci. Technol. A* **26**, 678–682 (2008).

25. Xiao, Z., Yu, S., Li, Y., Ruan, S., Kong, L. B., Huang, Q., Huang, Z., Zhou, K., Su, H., Yao, Z., Que, W., Liu, Y., Zhang, T., Wang, J., Liu, P., Shen, D., Allix, M., Zhang, J. & Tang, D. *Mater. Sci. Eng. R Reports* **139**, 100518 (2020).

26. Djaoued, Y., Badilescu, S., Ashrit, P. V, Bersani, D., Lottici, P. P. & Brüning, R. *J. Sol-Gel Sci. Technol.* **24**, 247–254 (2002).

27. Wetchakun, N. & Phanichphant, S. *Curr. Appl. Phys.* **8**, 343–346 (2008).

28. Omri, K., Najeh, I., Dhahri, R., El Ghoul, J. & El Mir, L. *Microelectron. Eng.* **128**, 53–58 (2014).

29. Vinogradov, A. V & Vinogradov, V. V. *RSC Adv.* **4**, 45903–45919 (2014).

30. Fardad, M. A. *J. Mater. Sci.* **35**, 1835–1841 (2000).

31. Pope, E. J. A. & Mackenzie, J. D. *J. Non. Cryst. Solids* **87**, 185–198 (1986).

32. Venkatachalam, N., Palanichamy, M. & Murugesan, V. *Mater. Chem. Phys.* **104**, 454–459 (2007).

33. Lim, C. S., Ryu, J. H., Kim, D.-H., Cho, S.-Y. & Oh, W.-C. *J. Ceram. Process. Res.* **11**, 736–741 (2010).

34. Yamane, M., Inoue, S. & Yasumori, A. *J. Non. Cryst. Solids* **63**, 13–21 (1984).

35. Lim, C. S., Ryu, J. H., Kim, D. H., Cho, S. Y. & Oh, W. C. *J. Ceram. Process. Res.* **11**, 736–741 (2010).

36. Li, Y., Xu, L., Li, X., Shen, X. & Wang, A. *Appl. Surf. Sci.* **256**, 4543–4547 (2010).

37. Yazıcı, M., Çomaklı, O., Yetim, T., Yetim, A. F. & Çelik, A. *Tribol. Int.* **104**, 175–182 (2016).

38. Feng, W., Mu-sen, L., Yu-peng, L. & Yong-xin, Q. *Mater. Lett.* **59**, 916–919 (2005).

39. Rahman, I. A., Vejayakumaran, P., Sipaut, C. S., Ismail, J. & Chee, C. K. *Ceram. Int.* **34**, 2059–2066 (2008).

40. Jafarzadeh, M., Rahman, I. A. & Sipaut, C. S. *J. Sol-Gel Sci. Technol.* **50**, 328–336 (2009).

41. Song, C., Feng, W., Shi, Z. & Wang, X. *Ionics (Kiel).* **25**, 4607–4614 (2019).

42. Dutoit, D. C. M., Schneider, M. & Baiker, A. *J. Catal.* **153**, 165–176 (1995).

43. Rida, K., Benabbas, A., Bouremmad, F., Peña, M. A., Sastre, E. & Martínez-Arias, A. *Appl. Catal. A Gen.* **327**, 173–179 (2007).

44. Kumar, S., Bhunia, S. & Ojha, A. K. *Phys. E Low-dimensional Syst. Nanostructures* **66**, 74–80 (2015).

45. Jung, K. Y., Park, S. Bin & Anpo, M. *J. Photochem. Photobiol. A Chem.* **170**, 247–252 (2005).

46. Ismail, A. M., Menazea, A. A., Kabary, H. A., El-Sherbiny, A. E. & Samy, A. *J. Mol. Struct.* **1196**, 332–337 (2019).

47. Wu, X., Lu, G. Q. (Max) & Wang, L. *Energy Environ. Sci.* **4**, 3565–3572 (2011).

48. Cao, J., Qin, C., Wang, Y., Zhang, H., Zhang, B., Gong, Y., Wang, X., Sun, G., Bala, H. & Zhang, Z. *RSC Adv.* **7**, 25504–25511 (2017).

49. Jia, T., Liu, M., Yu, D., Long, F., Mo, S., Deng, Z. & Wang, W. *Nanomaterials* **8**, (2018).

50. Livage, J. *Materials (Basel).* **3**, 4175–4195 (2010).

51. Li, X., Xue, F., Li, N., Wei, X., Liu, H., Zhou, J., Lyu, B. & Liu, M. *Front. Chem.* **8**, 1–10 (2020).

52. Baruah, S. & Dutta, J. *Sci. Technol. Adv. Mater.* **12**, (2011).

53. Shi, W., Song, S. & Zhang, H. *Chem. Soc. Rev.* **42**, 5714–5743 (2013).

54. Yang, G. & Park, S. J. *Materials (Basel).* **12**, (2019).

55. Kopp Alves, A., Bergmann, C. P. & Berutti, F. A. *Eng. Mater.* 61–76 (2013).

56. Morey, G. W. & Niggli, P. *J. Am. Chem. Soc.* **35**, 1086–1130 (1913).

57. Brown, P. W. & Constantz, B. *Hydroxyapatite and Related Materials*. (CRC Press, 1994).

58. Walters, L. N., Zhang, C., Dravid, V. P., Poeppelmeier, K. R. & Rondinelli, J. M. *Chem. Mater.* **33**, 2726–2741 (2021).

59. Schafthaul, K. F. E. *Bayer. Akad.* **20**, 569, 575, 592 (1845).

60. Debye, P., Scherrer, P. & K. Nac. *Ges. Wiss. Göttingen Math. Physik* 1–26 at (1916).

61. de Sénarmont, H. H. *Comptes rendus l'Académie des Sci. Paris* **32**, 762–763 (1851).

62. Morey, G. W. *J. Am. Chem. Soc.* **36**, 215–230 (1914).

63. Suchanek, W. L. & Riman, R. E. in *Advances in Science and Technology* vol. 45 184–193 (Trans Tech Publ, 2006).

64. Cundy, C. S. & Cox, P. A. *Microporous Mesoporous Mater.* **82**, 1–78 (2005).

65. Laudise, R. A. *Prog. Inorg. Chem. Vol. 3* **3**, 1 (2009).

66. Gan, Y. X., Jayatissa, A. H., Yu, Z., Chen, X. & Li, M. *Journal of Nanomaterials* vol. 2020 at (2020).

67. Ghobarkar, H., Schäf, O., Massiani, Y. & Knauth, P. *Reconstr. Nat. Zeolites* 19–33 (2003).

68. Byrappa, K. & Yoshimura, M. *Handb. Hydrothermal Technol.* 139–175 (2013).

69. Rabenau, A. *Adv. Ceram. III* 163–179 (1990).

70. Rabenau, A. *Angew. Chemie Int. Ed.* **24**, 1026–1040 (1985).

71. Gibson, R. E. *American Journal of Science* vol. 35 49–69 at (1938).

72. Movlaee, K., Ganjali, M. R., Norouzi, P. & Neri, G. *Nanomaterials* **7**, 1–33 (2017).

73. Ma, M. G. *Int. J. Nanomedicine* **7**, 1781–1791 (2012).

74. Wang, X., Fan, H., Ren, P. & Li, M. *Mater. Res. Bull.* **50**, 191–196 (2014).

75. Canu, G. & Buscaglia, V. *CrystEngComm* **19**, 3867–3891 (2017).

76. Dozzi, M. V. & Selli, E. *Catalysts* **3**, 455–485 (2013).

77. Dozzi, M. V., Montalbano, M., Marra, G., Mino, L. & Selli, E. *Mater. Today Chem.* **22**, 100624 (2021).

78. Maisano, M., Dozzi, M. V., Coduri, M., Artiglia, L., Granozzi, G. & Selli, E. *ACS Appl. Mater. Interfaces* **8**, 9745–9754 (2016).

79. Dozzi, M. V., Candeo, A., Marra, G., D'Andrea, C., Valentini, G. & Selli, E. *J. Phys. Chem. C* **122**, 14326–14335 (2018).

80. Prati, L. & Villa, A. *Catalysts* **2**, 24–37 (2011).

81. Dozzi, M. V., Prati, L., Canton, P. & Selli, E. *Phys. Chem. Chem. Phys.* **11**, 7171–7180 (2009).

82. Tsubota, S., Haruta, M., Kobayashi, T., Ueda, A. & Nakahara, Y. *Stud. Surf. Sci. Catal.* **63**, 695–704 (1991).

83. Qian, K., Fang, J., Huang, W., He, B., Jiang, Z., Ma, Y. & Wei, S. *J. Mol. Catal. A Chem.* **320**, 97–105 (2010).

84. Weerachawanasak, P., Mekasuwandumrong, O., Arai, M., Fujita, S.-I., Praserthdam, P. & Panpranot, J. *J. Catal.* **262**, 199–205 (2009).

85. Vannice, M. A. *Top. Catal.* **4**, 241–248 (1997).

86. Dimitratos, N., Villa, A., Bianchi, C. L., Prati, L. & Makkee, M. *Appl. Catal. A Gen.* **311**, 185–192 (2006).

87. Zanella, R., Giorgio, S., Henry, C. R. & Louis, C. *J. Phys. Chem. B* **106**, 7634–7642 (2002).

88. Wenderich, K. & Mul, G. *Chem. Rev.* **116**, 14587–14619 (2016).

89. Kraeutler, B. & Bard, A. J. *J. Am. Chem. Soc.* **100**, 4317–4318 (1978).

90. Lee, J. & Choi, W. *J. Phys. Chem. B* **109**, 7399–7406 (2005).

91. Nakamatsu, H., Kawai, T., Koreeda, A. & Kawai, S. *J. Chem. Soc. Faraday Trans. 1 Phys. Chem. Condens. Phases* **82**, 527–531 (1986).

92. Mahlamvana, F. & Kriek, R. J. *Appl. Catal. B Environ.* **148–149**, 387–393 (2014).

93. Sasaki, T., Koshizaki, N., Koinuma, M. & Matsumoto, Y. *Nanostructured Mater.* **12**, 511–514 (1999).

94. An, W.-J., Wang, W.-N., Ramalingam, B., Mukherjee, S., Daubayev, B., Gangopadhyay, S. & Biswas, P. *Langmuir* **28**, 7528–7534 (2012).

95. Rodríguez-Martínez, C., García-Domínguez, Á. E., Guerrero-Robles, F., Saavedra-Díaz, R. O., Torres-Torres, G., Felipe, C., Ojeda-López, R., Silahua-Pavón, A. & Cervantes-Uribe, A. *J. Compos. Sci.* **4**, 89 (2020).

96. Zhu, W., Wang, G., Hong, X., Shen, X., Li, D. & Xie, X. *Electrochim. Acta* **55**, 480–484 (2009).

97. Akple, M. S., Low, J., Liu, S., Cheng, B., Yu, J. & Ho, W. *J. CO_2 Util.* **16**, 442–449 (2016).

98. Hu, X., Lu, S., Tian, J., Wei, N., Song, X., Wang, X. & Cui, H. *Appl. Catal. B Environ.* **241**, 329–337 (2019).

99. Meng, A., Zhang, J., Xu, D., Cheng, B. & Yu, J. *Appl. Catal. B Environ.* **198**, 286–294 (2016).

100. Eckert, M. *Ann. Phys.* **524**, 83–85 (2012).

101. Chatterjee, S. K. *Crystallography and the World of Symmetry*. (Springer Berlin Heidelberg, 2008).

102. Mueller, E. *Open Phys.* **20**, 888–890 (2022).

103. Bragg, W. H. & Bragg, W. L. *Nature* **88**, 246–248 (1913).

104. Patterson, A. L. *Phys. Rev.* **56**, 978–82 (1939).

105. Jagodzinski, H. *Berichte der Bunsengesellschaft für Phys. Chemie* **79**, 553 (1975).

106. Warren, B. E. *J. Am. Ceram. Soc.* **24**, 256–261 (1941).

107. Warren, B. E. & Biscob, J. *J. Am. Ceram. Soc.* **21**, 259–265 (1938).

108. Williamson, G. K. & Hall, W. H. *Acta Metall.* **1**, 22–31 (1953).

109. Rietveld, H. M. *J. Appl. Crystallogr.* **2**, 65–71 (1969).

110. Hill, R. J. & Howard, C. J. *J. Appl. Crystallogr.* **20**, 467–474 (1987).

111. Scardi, P., Mccusker, L. B., Dreele, R. B. Von, Cox, D. E. & Loue, D. *J. Appl. Cryst.* **32**, 36–50 (1999).

112. Coduri, M., Maisano, M., Dozzi, M. V. & Selli, E. *Zeitschrift fur Phys. Chemie* **230**, 1233–1248 (2016).

113. Toby, B. H. & Von Dreele, R. B. *J. Appl. Crystallogr.* **46**, 544–549 (2013).

114. Roisnel, T. & Rodríguez-Carvajal, J. in *Materials Science Forum* (2001).

115. Dollimore, D., Spooner, P. & Turner, A. *Surf. Technol.* **4**, 121–160 (1976).

116. Brunauer, S., Emmett, P. H. & Teller, E. *J. Am. Chem. Soc.* **60**, 309–319 (1938).

117. Thommes, M. *Chemie-Ingenieur-Technik* **82**, 1059–1073 (2010).

118. Thommes, M., Kaneko, K., Neimark, A. V., Olivier, J. P., Rodriguez-Reinoso, F., Rouquerol, J. & Sing, K. S. W. *Pure Appl. Chem.* **87**, 1051–1069 (2015).

119. Orellana, M. F., Nelson, A., Carey, J., Heo, G., Boychuk, D. & Major, P. *J. Dent. Res.* **87**, 532–536 (2008).

120. Lambert, J. H. *Photometria sive de mensura et gradibus luminis, colorum et umbrae*. (W. Engelmann, 1892).

121. Frei, R. W. & Zeitlin, H. *Diffuse Reflectance Spectroscopy*. *C R C Critical Reviews in Analytical Chemistry* vol. 2 (1971).

122. Kortüm, G. *Reflectance Spectroscopy*. (Springer Berlin Heidelberg, 1969).

123. Kubelka, P. & Munk, F. *Z. Tech. Phys.* **12**, 593–601 (1931).

124. Ohtani, B. *J. Photochem. Photobiol. C Photochem. Rev.* **11**, 157–178 (2010).

125. Morozzi, P., Ballarin, B., Arcozzi, S., Brattich, E., Lucarelli, F., Nava, S., Gómez-Cascales, P. J., Orza, J. A. G. & Tositti, L. *Atmos. Environ.* **252**, (2021).

126. Fassel, V. A. & Knfseley, R. N. *Anal. Chem.* **46**, 1110A-1120a (1974).

127. Cherevko, S. & Mayrhofer, K. J. J. in *Encyclopedia of Interfacial Chemistry* 326–335 (Elsevier,

2018).

128. Nuttall, K. L., Gordon, W. H. & Ash, K. O. *Ann. Clin. Lab. Sci.* **25**, 264–271 (1995).

129. Wu, H. & Zhu, X. *Perovskite Mater. - Synth. Characterisation, Prop. Appl.* (2016).

130. Ahrenkiel, R. K. *Solid. State. Electron.* **35**, 239–250 (1992).

131. Dozzi, M. V., D'Andrea, C., Ohtani, B., Valentini, G. & Selli, E. *J. Phys. Chem. C* **117**, 25586–25595 (2013).

132. Prasankumar, R. P. & Taylor, A. J. *Optical Techniques for Solid-State Materials Characterization*. (CRC Press, 2012).

Chapter 3: Experimental Setups, Testing Procedures and Data Treatment

3.1 Photocatalytic Oxidation of Formic Acid

3.1.1 Introduction

Photocatalytic oxidation of formic acid (FA, HCOOH) is one of the simplest photocatalytic oxidation test reactions due to its complete conversion to CO_2 without forming any stable intermediate species possibly competing for adsorption on the photocatalyst surface.[1,2] Therefore, for this test reaction the interpretation of kinetic data is greatly simplified. Moreover, FA does not absorb light in the 320 – 400 nm range, which is often selected to test photocatalytic reactions, and does not evaporate from aqueous solutions at room temperature. Furthermore, FA represents a good model molecule since, aside from being dissolved in industrial effluents, is also a stable intermediate in the complete mineralization to CO_2 of many organic pollutants.[3-5]

The photocatalytic oxidation of FA in aqueous media occurs primarily through a degradation mechanism that involves the direct oxidation of the adsorbed anion molecules on the surface of the photocatalyst (Equation 3.1.3) rather than the indirect oxidation of the organic molecule by means of *in-situ* generated oxygen reactive species, with the formation of the highly unstable $CO_2^{-\bullet}$ specie, or $HCO_2^{-\bullet}$ depending on pH:[3,6,7]

$$h_{VB}^{+} + HCOO_{ads}^{-} \rightarrow CO_2^{-\bullet} + H^{+} \qquad (3.1.3)$$

Due to the strongly reductive nature of the $CO_2^{-\bullet}$ radical anion ($E^0_{CO_2/CO_2^{-\bullet}} = -1.8\ V$), the so-formed radical can either originate the current doubling effect by injecting electrons within the titanium dioxide CB,[8] or mediate the reduction of a variety of molecules and, in particular, that of dissolved O_2, as demonstrated in Equation 3.1.4:

$$CO_2^{-\bullet} + O_2 \rightarrow CO_2 + O_2^{-\bullet} \qquad (3.1.4)$$

Hydroperoxide radicals $HOO^{\bullet}$ are then formed by protonation of the produced superoxide radical anion $O_2^{-\bullet}$ (Equation 3.1.5). However, these hydroperoxide radicals are not reactive enough to oxidize formic acid in homogeneous phase. Instead, being highly unstable species, they rapidly

decay through disproportionation (Equation 3.1.6) or by reacting with superoxide radical anions (Equation 3.1.7), forming hydrogen peroxide and oxygen:[9]

$$O_2^{-\bullet} + H^+ \rightarrow HOO^\bullet \quad (3.1.5)$$

$$HOO^\bullet + HOO^\bullet \rightarrow H_2O_2 + O_2 \quad (3.1.6)$$

$$HOO^\bullet + O_2^{-\bullet} \rightarrow HOO^- + O_2 \xrightarrow{(H_2O)} H_2O_2 + O_2 + HO^- \quad (3.1.7)$$

Simultaneously, photopromoted electrons are transferred to adsorbed molecular oxygen in the cathodic half-reaction, which can either involve a mono-electronic (Equation 3.1.8) or a bi-electronic reduction (Equation 3.1.9):

$$O_2 + e_{CB}^- \rightarrow O_2^{-\bullet} \quad (3.1.8)$$

$$O_2 + 2\, e_{CB}^- + 2\, H^+ \rightarrow H_2O_2 \quad (3.1.9)$$

In both cases, hydrogen peroxide is produced during the cathodic processes, as the mono-electronic reduction leads to the rapid protonation of the superoxide radical $O_2^{-\bullet}$, converting it to H_2O_2 (Equations 3.1.5 to 3.1.7). However, it is well-established that the formation of H_2O_2 is difficult to detect during FA photomineralization on pristine, unmodified TiO_2.[10-12] In fact, H_2O_2 undergoes extremely fast decomposition by photogenerated species[11-13] (Equations 3.1.10 - 3.1.11) over the clean surface of titania during FA photodegradation, having a high affinity for the oxide surface and being able to complex Ti(IV) ions at the interface:[14]

$$H_2O_2 + 2\, e_{CB}^- + 2\, H^+ \rightarrow 2\, H_2O \quad (3.1.10)$$

$$H_2O_2 + 2\, h_{VB}^+ \rightarrow O_2 + 2\, H^+ \quad (3.1.11)$$

In contrast, when the surface of titanium dioxide is modified with *in-situ* surface fluorination and deposition of Au nanoparticles, an accumulation of H_2O_2 in solution during formic acid photocatalytic oxidation has been reported.[10,15] In particular, surface fluorination of the metal oxide semiconductor significantly inhibits the formation of surface peroxides species ($\equiv Ti^{IV} - OOH$),[16] which is a crucial step for their subsequent photodegradation over titanium dioxide. As a result, the decomposition rate of H_2O_2 is slowed down, leading to its accumulation in solution. Additionally, the deposition of Au metal nanoparticles during FA photodegradation enhances the production rate of H_2O_2 due to more efficient transfer of conduction band electrons to adsorbed molecular dioxygen (Equation 3.1.8) and a preferential adsorption of O_2 on Au nanoparticles.[17]

3.1.2 Experimental Setup

The test reaction was performed under atmospheric conditions in a quartz glass cylindric reactor, with 70 cm^3 volume capacity, 130 mm height and 30 mm base diameter. Powder suspensions were kept under constant stirring by means of a Topolino IKA magnetic stirrer. The reactor was inserted in a home-made housing consisting in a black box mounted on an optical bench, by maintaining an identical setup geometry in all photocatalytic runs, with the light source in a fixed in position and the reactor kept at a 10 cm constant distance from the lamp. The reaction environment was kept at ambient temperature by a continuous stream of compressed air as cooling system. A 285 nm cut off filter was usually mounted at the black box entrance to provide protection from the UV-C radiation and to ensure a 5x5 cm^2 square irradiated surface area.

Figure 3.1.1: Experimental setup for the photocatalytic degradation of formic acid. A) Light source, B) Black box, C) Compressed air, D) Glass quartz photoreactor, E) Cut-off filter, F) magnetic stirrer.

The irradiation source was an Osram Powerball HCI-T 150 W/942 NDL PB G12 neutral white lamp (color temperature: 4200 K) with emission wavelength $\lambda_{em} > 340$ nm mounted on a Twin Beam T 150 R reflector with an average full emission intensity on the reactor of 123 mW cm^{-2}, periodically monitored using a Thorlabs PM200 Power and Energy Meter Console equipped with a S130VC Slim Photodiode Power Sensor. The emission spectrum of the lamp, acquired using a Thorlabs CCS100 Compact Spectrometer equipped with a multimode optical linear output fiber, is reported in Figure 3.1.2.

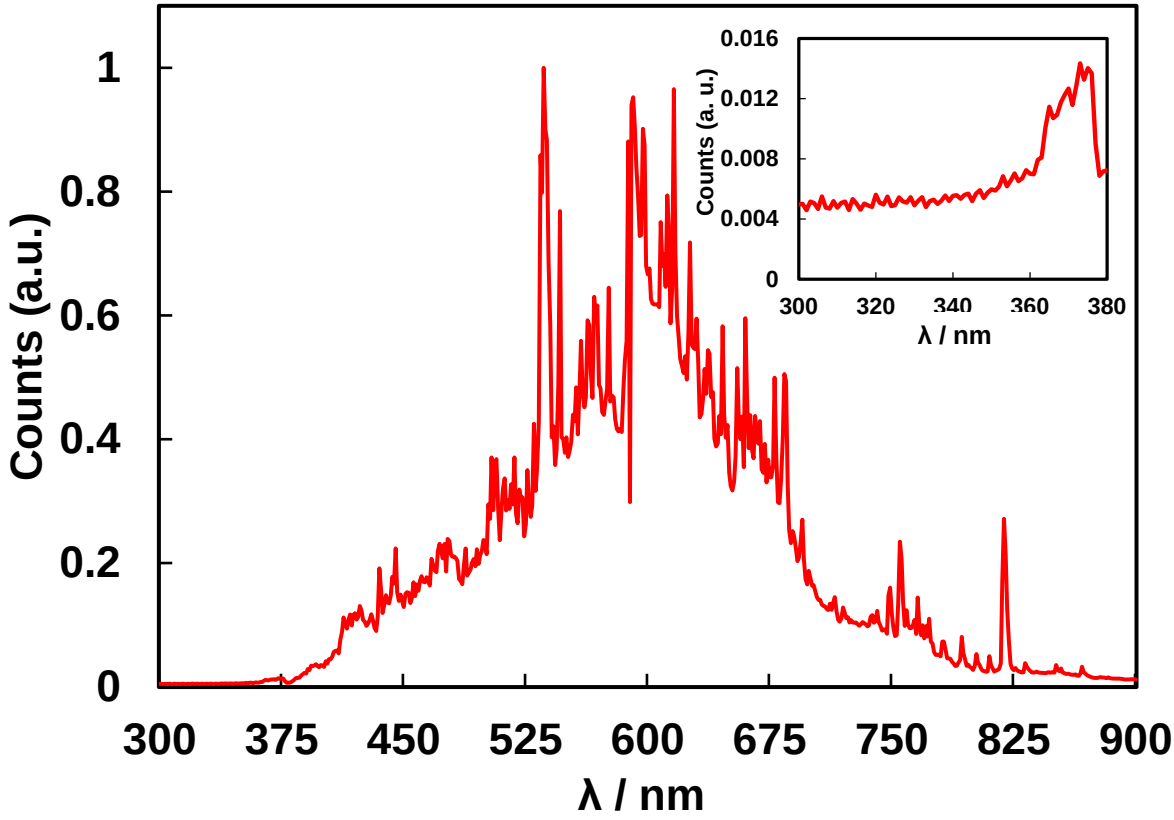

Figure 3.1.2: Emission spectrum of Osram Powerball HCI-T 150 W/942 NDL PB G12 neutral white lamp.

3.1.3 Experimental Procedure

Photocatalytic degradation tests were performed according to a well-established procedure, employing the above-mentioned experimental setup.[15,18,19] In each run, 6.3 mg of TiO_2 powder were suspended in 60 cm^3 of ultrapure Milli-Q water and finely dispersed by sonication with ultrasound radiation of 59 kHz frequency and 250 W (corresponding to 100% power) for 30 min using a Falc Instruments Labsonic LBS2 ultrasonic bath. Subsequently, 3.5 cm^3 of a HCOOH aqueous solution (0.0208 M) were added to the suspension, setting up the total volume of the suspension to 63.5 cm^3 and the photocatalyst amount to 0.1 g dm^{-3}. The suspension was then left stirring in the dark for 15 min to attain the adsorption equilibrium of the substrate on the photocatalyst surface, before starting irradiation. The lamp was always switched on at least 30 min before the beginning of the runs.

The equilibrated suspension was then transferred to the cylindric photoreactor and irradiation started, under stirring. At regular time intervals 2 cm^3 of the suspension were withdrawn from the reactor by means of a syringe and transferred to a 15 cm^3 conical glass centrifuge tube. The powders were then separated from the solution by centrifugation for 20-30 min with a relative centrifugal force of 986 x g corresponding to 3200 RPM in a Hettich EBA 20 centrifuge equipped

with an 8-place angle rotor with a radius of 86 mm. The supernatant was then analyzed through ion chromatography (Metrohm 761 Compact IC) to detect the residual concentration of formate anions.

All reactants were purchased from Sigma-Aldrich and used as received. Milli-Q water was used throughout.

3.1.4 Data Treatment

The photocatalytic degradation of formic acid in aqueous suspensions can be considered a heterogeneous solid-liquid reaction, and therefore its kinetics can be described on the basis on the Langmuir-Hinshelwood rate law for unimolecular reactions on surfaces:

$$r = k \cdot \frac{C_s \cdot K(s)}{1 + C_s \cdot K(s) + \sum_x C_x \cdot K(x)} \qquad (3.1.12)$$

where k is the reaction rate constant, C_s the substrate concentration in the bulk of the liquid phase, $K(s)$ is the adsorption constant of the substrate onto the photocatalyst surface, C_x and $K(x)$, respectively, represent the bulk concentration and adsorption constant of any species able to compete with the substrate for its active sites. Two main limit cases of the model allow to greatly simplify this expression. If $C_s \cdot K(s) \gg 1 + \sum_x C_x \cdot K(x)$, the reaction proceeds through a pseudo-zeroth order rate law, while if $C_s \cdot K(s) + \sum_x C_x \cdot K(x) \ll 1$ a pseudo-first order kinetics is observed.

Rate constant values were obtained by fitting experimental data of formate anions concentration in the solution as a function of time according to a zeroth-order rate law:

$$C_0 - C = kt \qquad (3.1.13)$$

Linear least square regression analysis was applied to the experimental data. Kinetic rate constants were obtained as the average value of at least two photocatalytic runs for each photocatalyst sample, to check the reproducibility of the data. Concentrations of formate anions lower than 30% of the initial FA concentration value were excluded from the regression model, as boundary conditions of the Langmuir-Hinshelwood pseudo zeroth-order limit case might not be respected anymore under such conditions.

All experimental data elaboration was performed using Microsoft® Excel® spreadsheets.

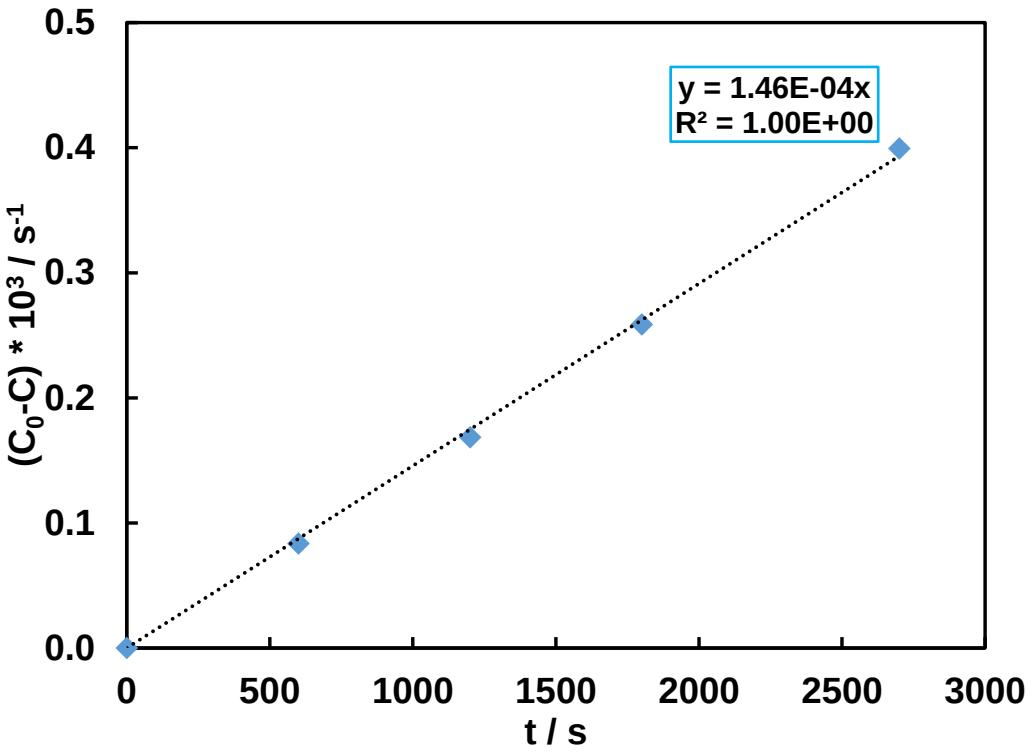

Figure 3.1.3: Example of a formic acid photocatalytic degradation run illustrating data elaboration according to zeroth-order plots.

3.2 Photocatalytic oxidation of Rhodamine B

3.2.1 Introduction

Advanced oxidation processes such as semiconductor photocatalysis represent powerful and efficient wastewater remediation methods from many non-biodegradable organic pollutants such as dyes and pharmaceutical products.[20-23] Dyes represent a good share of the large organic compounds released in industrial effluents since they are widely used for a plethora of large-scale applications. Among these, Rhodamine B (RhB) has emerged in recent years as a threatening water pollutant due the increased use of xanthene-based dyes in a wide variety of industrial activities such as leather tanning and paper production.[24,25] In fact, the presence of highly soluble xanthene dyes in water and food represents a serious worry as they are notoriously noxious to humans due to their ability to cause damage to skin, eyes, respiratory system, besides being potentially carcinogenic and neurotoxic chemicals.[26,27] Therefore, the development of photocatalytic systems able to efficiently degrade xanthene-based dyes to harmless chemicals for both humans and the environment represents a technological challenge aimed at the remediation of dye-polluted wastewaters as an environmentally friendly and energetically efficient solution.

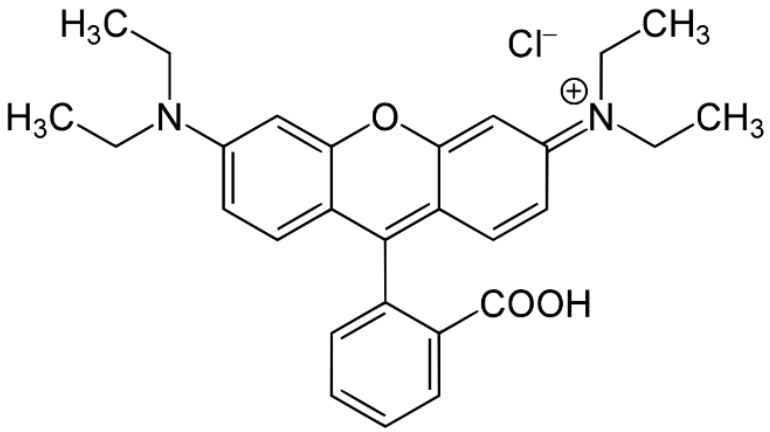

Figure 3.2.1: Chemical structure of the xanthene cationic dye Rhodamine B.

3.2.2 Experimental Procedure

The photocatalytic degradation experiments were conducted following a procedure that was recently described,[28] utilizing the same experimental setup described for formic acid photocatalytic degradation. The only difference is the use of a 100 cm^3 round-bottom glass flask as reactor instead of the cylindric reactor described for FA degradation.

In each photocatalytic test, 10 mg of photocatalyst were dispersed in 90 mL of ultrapure water under sonication treatment for 30 min. Then, 20 μL of a 1:10 solution of commercial $HClO_4$ were added under stirring to the obtained suspension for 5 min. Later, 10 mL of RhB solution (1.2 x 10^{-4} M) were added under stirring, so that the concentration of TiO_2 in solution was 0.1 $g{\cdot}L^{-1}$. Then, the suspension was magnetically stirred in dark for 15 min to attain the adsorption equilibrium of the substrate on the photocatalyst surface, before starting irradiation. Stirring was continued during the runs. The lamp was always switched on at least 30 min before the beginning of irradiation. At regular time intervals during the run, 4 mL of the suspensions were withdrawn from the reactor and centrifuged for minimum 25 min to ensure separation between catalyst and solution. Spectrophotometric measurements were carried out immediately after separation in order to monitor the progressive photobleaching of Rhodamine B.

For kinetic runs performed in the presence of fluoride ions, 10 mg of anatase TiO_2 were dispersed in 70 mL of ultrapure water under sonication treatment for 30 min. 40 μL of a 1:10 solution of commercial $HClO_4$ solution were added under stirring to the obtained suspension. After 5 min, 20 mL of NaF solution (1.2 x 10^{-2} M) were added and maintained under stirring for further 5 min. Later, 10 mL of RhB solution (1.2 x 10^{-4} M) were added under stirring, so that the concentration of TiO_2 in solution was 0.1 $g{\cdot}L^{-1}$ and with a F/Ti ratio corresponding to 2. Then, the suspension was magnetically stirred in dark for 15 min to attain the adsorption equilibrium of

the substrate on the photocatalyst surface, before starting irradiation. Stirring was continued during the runs. The lamp was always switched on at least 30 min before the beginning of irradiation. At regular time intervals during the run, 4 mL of the suspensions were withdrawn from the reactor by means of a syringe and centrifuged for minimum 25 min to ensure separation between the photocatalyst and the solution. Spectrophotometric measurements in transmittance mode were carried out immediately after separation using a Jasco V-670 spectrophotometer, in order to monitor the progressive photobleaching of Rhodamine B.

3.2.3 Data Treatment

Photocatalytic degradation of Rhodamine B occurred with a pseudo-first order decay of the absorbance of the dye at 553 nm. Therefore, photocatalytic activity results have been expressed in terms of pseudo-first order rate constants labeled as k_{ac} and k_F obtained under acidic and *in-situ* fluorinated conditions, respectively, by fitting the data to a first-order kinetic model (Equation 3.2.1):

$$\ln\left(\frac{C_0}{C}\right) = k_r \cdot t \qquad (3.2.1)$$

where k_r, with $r = ac$ or F, represents the first order rate constant for the photocatalytic process under the employed experimental conditions, C_0 the starting RhB concentration and C the concentration of the dye at time t. The concentration of the dye in solution was calculated by applying the Lambert-Beer law, using a molar extinction coefficient ε_{553} at 553 nm value equal to 9920 M^{-1} cm^{-1}, according to a calibration curve previously determined in our laboratories.[28]

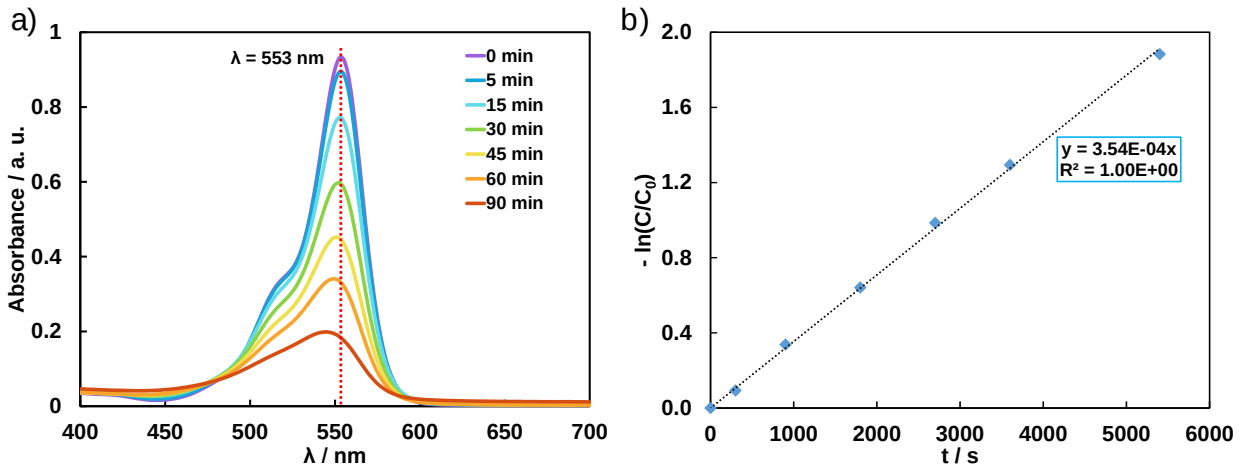

Figure 3.2.2: Example of a Rhodamine B photocatalytic degradation run illustrating the xanthene dye absorption spectra as a function of irradiation time (a) and data elaboration according to first-order plots (b).

3.3 Photocatalytic Reduction of Cr(VI) to Cr(III)

3.3.1 Introduction

Hexavalent chromium, a widely used metal ion in many industrial processes such as metal plating, leather tanning, pigment, and refractory production, represents one of the most dangerous pollutants due to its high toxicity to humans, animals, and plants.[29,30] Cr(VI), in fact, notoriously is a toxic, mutagenic and carcinogenic hazardous chemical.

In the aqueous media, chromium is mainly in the form of highly mobile, highly soluble Cr(VI) ions, and in the form of Cr(III), which is not only significantly less toxic than hexavalent chromium, but also an essential vital micronutrient.[31-34] Moreover, Cr(III) is easily precipitated in the form of $Cr(OH)_3$ due to its relatively low mobility, or readily separated using natural clays. This makes water remediation techniques significantly more effective than if the species to be removed were the much more mobile Cr(VI).

Photocatalytic reduction of Cr(VI) to Cr(III) using semiconductor photocatalysts has proven to be a valid modern technology for surpassing the main shortcomings of conventional Cr(VI) remediation techniques such as adsorption, ultrafiltration or chemical reduction, especially considering its cost-effectiveness ratio and minimization of the production of hazardous sub-products.[35-39] When performed on TiO_2, the photocatalytic reduction of Cr(VI) represents a thermodynamically feasible process due to the relative energetic positioning of the TiO_2 conduction band with respect to the reduction potential of the Cr(VI)/Cr(III) couple, with the process being more favored with decreasing pH.[38] In fact, since $Cr_2O_7^{2-}$ anions represent the predominant dichromate species at low pH, the overall photocatalytic reduction process of Cr(VI) on the TiO_2 surface can be represented as:

$$TiO_2 + h\nu \rightarrow h_{VB}^+ + e_{CB}^- \qquad (3.3.1)$$

$$Cr_2O_7^{2-} + 14\,H^+ + 6\,e_{CB}^- \rightarrow 2\,Cr^{3+} + 7\,H_2O \qquad (3.3.2)$$

$$2\,H_2O + 4\,h_{VB}^+ \rightarrow O_2 + 4\,H^+ \qquad (3.3.3)$$

Due to the three-electrons involved in the photocatalytic reduction of Cr(VI) to Cr(III), the redox potential of the Cr(VI)/Cr(III) couple shifts towards more positive values with decreasing pH with a steeper shape than the TiO_2 conduction band potential, thus making the reduction of the metallic cation at low pH more efficient than at higher pH.

3.3.2 Experimental Procedure

All photocatalytic runs were performed in aqueous suspensions under atmospheric conditions in a magnetically stirred 100 cm^3 round-bottom flask glass reactor, using the experimental setup described in detail in Section 3.2.2. The appropriate volume of a 0.001 N $K_2Cr_2O_7$ solution (prepared by dilution of a standardized 0.1 N $K_2Cr_2O_7$ solution) to obtain an initial potassium dichromate concentration equal to $3.3 \cdot 10^{-5}$ M were added to pre-sonicated aqueous suspensions containing 0.1 g dm^{-3} of photocatalyst.

At regular time intervals during the runs, 5 cm^3 of the suspension were withdrawn from the reactor by means of a syringe and transferred to a 15 cm^3 conical glass centrifuge tube. The powders were then separated from the solution by centrifugation for 20-30 min with a relative centrifuge force of 986 x g in a Hettich EBA 20 centrifuge equipped with an 8-place angle rotor with a radius of 86 mm. Then, 3.0 cm^3 of the separated supernatant were withdrawn by means of a syringe and analyzed via spectrophotometric analysis (using a JASCO V-670 spectrophotometer) for the residual Cr(VI) content, using the 1,5-diphenylcarbazide method.[40]

All kinetic runs were performed up to *ca.* 70% Cr(VI) removal and repeated at least twice to check their reproducibility. The initial pH of the suspension was fixed at pH 3.7 by addition of an appropriate volume of concentrated $HClO_4$. The acidified suspension was stirred for at least five min before adding the reaction substrate. Before irradiation, acidified suspensions containing the potassium dichromate substrate were stirred in the dark for 15 min to attain adsorption equilibrium.

3.3.3 Data Treatment

The kinetics of the photocatalytic reduction of Cr(VI) under the here employed experimental conditions generally follows a Langmuir-Hinshelwood mechanism in heterogeneous media, with the initial rate r being

$$r = k\frac{KC}{1+KC} \tag{3.3.4}$$

where K represents the Langmuir adsorption constant, k represents a "reactivity rate constant", providing a measure of the reactivity of the photocatalyst with the substrate, and C is the initial concentration of the substrate. In the case of dilute solutions, such as those employed under our experimental conditions, the reaction model can be reduced to a first order kinetics:

$$\ln\left(\frac{C_0}{C}\right) = k_r \cdot t \tag{3.3.5}$$

with $k_r = kK$ being the apparent macroscopic rate constant, C_0 the initial Cr(VI) concentration and C the concentration of dichromate anions at time t.

Throughout all experimental runs, the initial concentration of Cr(VI) in solution was determined based on the dichromate concentration after 5 min of irradiation. This approach was adopted to enhance the accuracy of the first-order linear fits of the obtained data.

All experimental data elaboration was performed using Microsoft® Excel® spreadsheets.

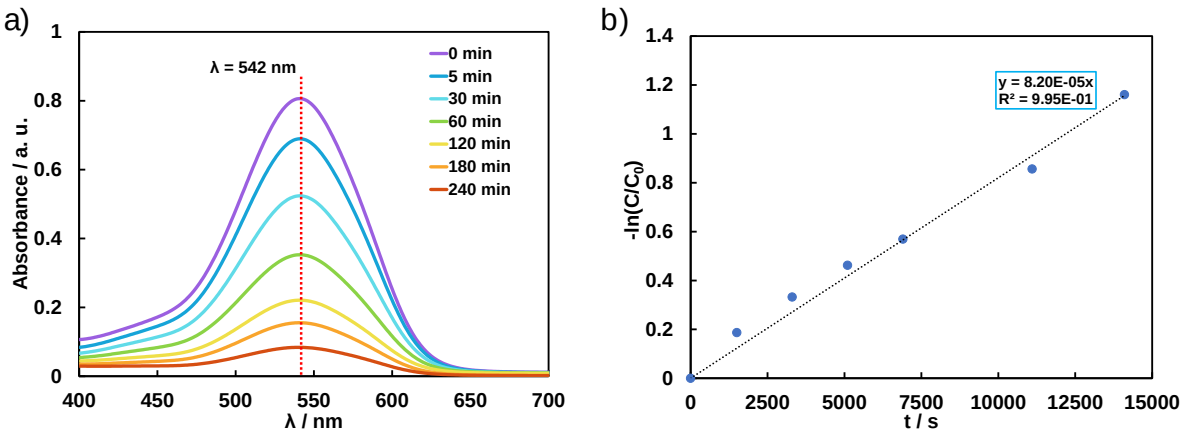

Figure 3.3.1: Example of a Cr(VI) photocatalytic reduction run illustrating the absorption spectra of the magenta-coloured complex formed via reaction of Cr(VI) with 1,5-diphenylcarbazide in acidic solutions[41] as a function of irradiation time (a) and data elaboration according to first-order plots (b).

3.4 Hydrogen production by photo-steam reforming of methanol

3.4.1 Introduction

Low temperature production of hydrogen through photocatalytic steam reforming of organics on metal oxide semiconductors is an up-hill reaction that provides a way to convert solar energy into chemical energy with a small CO_2 impact compared to the use of fossil fuels. In fact, contrarily to traditional steam reforming, photo-assisted processes occur at room temperature, atmospheric pressure and no feed stock needs to be burnt because the required energy is totally supplied by photons.[42-46]

Organic compounds also deriving from renewable sources, *i.e.,* biomasses, acting as hole scavengers, can play an essential role in increasing the overall rate of photocatalytic hydrogen evolution.[47-49] For instance, methanol is widely used as a sacrificial agent in the liquid–phase photocatalytic production of hydrogen, for which the overall reaction is represented by:

$$CH_3OH + H_2O \xrightarrow{h\nu} 3H_2O + CO_2 \qquad (3.4.1)$$

Photocatalytic methanol steam reforming is based on subsequent fundamental steps that occur on the semiconductor surface after electronically activating the photocatalyst. In fact, after light absorption and generation of $e^-_{CB} - h^+_{VB}$ pairs, electron acceptor (EA, represented in our case by protons) and electron donor (ED, represented by methanol and water) species adsorbed on the photocatalysts surface can react with electrons and holes:

$$EA_{ads} + e^-_{CB} \rightarrow P_{1;ads} \quad (3.4.2)$$

$$ED_{ads} + h^+_{VB} \rightarrow P_{2;ads} \quad (3.4.3)$$

As illustrated in Figure 3.4.1, the oxidation of competitively adsorbed methanol and water molecules (both molecularly and dissociatively adsorbed) results in starting a complex sequence of photoinduced oxidation reactions, resulting in the formation of a plethora of partially oxidized subproducts such as formaldehyde, formic acid, carbon monoxide, and finally to the maximum carbon oxidation state, carbon dioxide.[46] Once formed, products or intermediate species then desorb from the surface of the photocatalyst ($P_{1;ads} \leftrightarrows P_{1;g}$ and $P_{2;ads} \leftrightarrows P_{2;g}$).

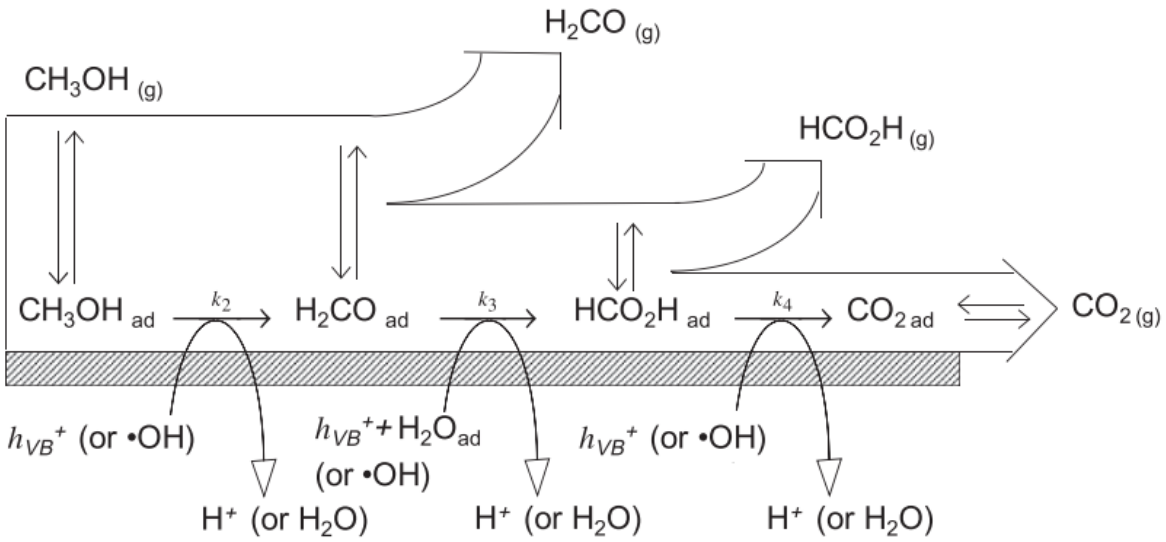

Figure 3.4.1: Reaction scheme of the photocatalytic oxidation of methanol on the TiO_2 surface under steady-state conditions.[50]

The recombination of the electron-hole pairs represents an unwanted process which results in a net energy loss in the form of released heat and represents the most important factor limiting the efficiency of the whole photocatalytic process. Modification of the TiO_2 surface with noble metal nanoparticles can significantly improve the photoefficiency of the photocatalysts for methanol photo-steam reforming due to the electron trapping effect played by the formed Schottky barrier, resulting in a possibly improved charge separation ability of the photocatalyst, accompanied by a more efficient electron transfer towards adsorbed protons, both limiting unwanted recombination processes.[46,49,51,52]

3.4.2 Experimental Procedure

Photocatalytic methanol steam reforming kinetic runs were performed using a bench scale gas-phase setup operating in continuous feeding mode of the gas mixture to the reactor. The setup consists of a stainless steel photoreactor in which the photocatalyst bed is loaded consisting in a stainless-steel body (A) with a front round hollow closed by a Pyrex glass window (C), allowing the illumination of the photocatalyst (B) (Figure 3.4.2).

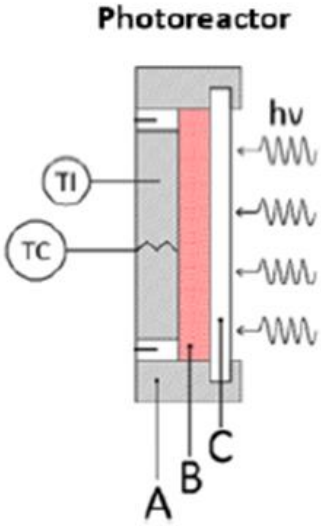

Figure 3.4.2: Schematics of the photoreactor used in the photocatalytic methanol steam reforming.

During each photocatalytic test, the reactor bed was prepared by mixing 14 mg of photocatalyst with 7.5 g of quartz sand. The photocatalyst was properly dispersed over the quartz beads by adding 2 cm^3 of milli-Q water to the mixture over a laboratory watch glass and carefully stirred with the help of a lab spoon. Photocatalyst-loaded quartz beads were then dried in an electric oven at 70 °C for 4 hours. This treatment is performed so that the photocatalyst is both highly dispersed and tightly adhered on the supporting quartz bed (Figure 3.4.3a). The temperature of the photocatalytic bed was managed by a PID controller connected with the photoreactor by means of a thermocouple (TI).

The irradiation source consists of a 300 W Xenon arc lamp placed 20 cm from the window (LSH302, LOT-Oriel), characterized by a broad emission spectrum ranging from 350 to 1000 nm and maximum emission intensity around 800 nm (Figure 3.4.3b).

The photoreactor is then connected to a stainless-steel gas insulated circuit operating in continuous feeding mode composed of three mass flow meters and relative control (MFC, Bronkhorst) for the supply and control of flow gases, one mass flow meter and control (Bronkhorst) for supplying and control the flow of the liquid feed mixture (composed by a water/methanol solution with a H_2O/CH_3OH molar ratio equal to 1.1) fed by a pressurized (3 bar) 500 cm^3 tank, a Controlled Evaporation and Mixing unit (CEM) used to evaporate the liquid feed solution and mix it with He (used as supplementary carrier gas), and a Hyden Analitical QGA Mass Spectrometer equipped with a SEM and Faraday detector, as illustrated in Figure 3.4.4.

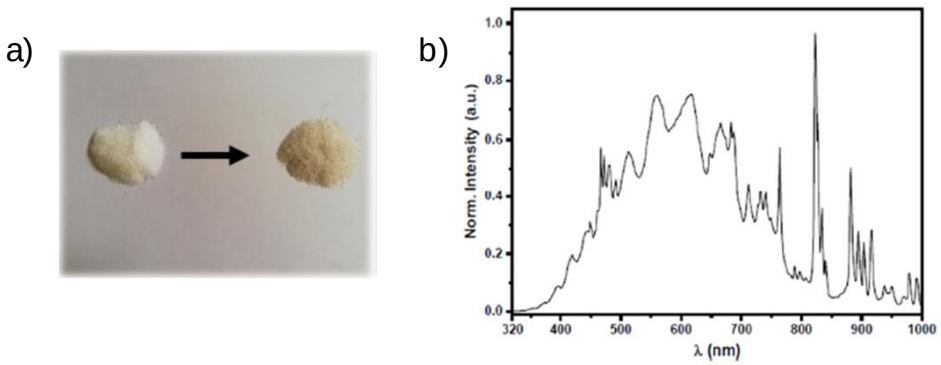

Figure 3.4.3: Quartz beads before and after deposition of the photocatalyst (a). Normalized emission spectrum of the 300 W Xe arc lamp used for methanol photo-steam reforming tests (b).

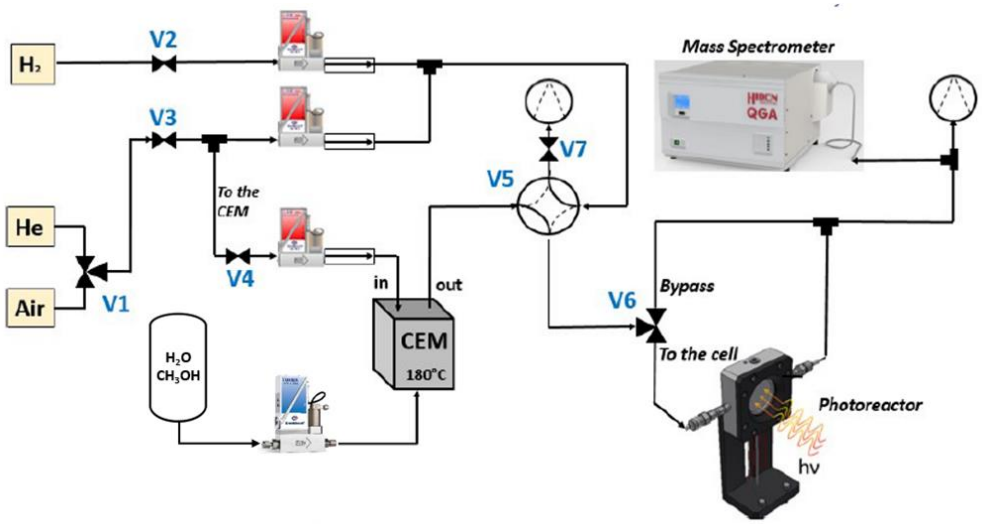

Figure 3.4.4: Schematic representation of the experimental set-up used for the photocatalytic methanol steam reforming kinetic runs.

Before the beginning of irradiation, a reductive pre-treatment was performed with all samples aimed at ensuring the complete reduction of the metal nanoparticles to their zero-valent form (M^0) and avoid any sintering or thermally induced morphological change of the photocatalyst during irradiation. The pre-treatment procedure consisted in flowing a 5 vol.% H_2/He mixture in the photoreactor with a flowrate of 50 cm^3 min^{-1} at 100 °C for 1 hour.

In each photocatalytic run, a stream of He containing *ca.* 2.0 vol.% and 2.2 vol.% H_2O with a flow rate of 50 cm^3 min^{-1} was fed to the photoreactor. The stream was maintained on for 15 min under dark conditions to ensure the attainment of the adsorption equilibrium of the reactant on the photocatalyst surface. During each run, samples were irradiated with multiple light/dark cycles consisting of 2 hours of irradiation followed by 15 min of dark conditions. During each run, temperature was kept fixed at 30 °C by means of the PID system. The composition of the gas mixture during the run was analysed by mass spectrometry, monitoring the exiting gas flow in continuous mode with 30 seconds sampling interval. This allowed us to obtain real time

information regarding both the H_2 production rate and the selectivity to each photocatalytic oxidation product (CO, H_2CO, HCOOH, CO_2).

3.4.3 Data treatment

The photocatalytic activity of the investigated materials in methanol photo-steam reforming was compared in terms of their H_2 production rate normalized by the amount of photocatalyst used during each photocatalytic run, expressed as $\mathrm{mmol_{H_2} \cdot h^{-1} \cdot g^{-1}}$. In all photocatalytic tests H_2, CO_2 and CO evolution occurred at constant rate under full lamp irradiation, as in previous studies;[45,46,48,49] no hydrogen production was observed under visible light irradiation ($\lambda_{irr} > 420$ nm). The rate of hydrogen production was calculated from the slope of the linear regression curve obtained through linearly fitting the amount of evolved $\mathrm{H_2}$, in $\mathrm{mmol_{H_2} \cdot g^{-1}}$ vs time data.

The percent selectivity to partially oxidated subproducts S_i, where $i = \mathrm{CO_2}$, $\mathrm{H_2CO}$, CO, HCOOH, $\mathrm{H_2}$, was calculated according to the following equations (3.4.4 - 3.4.7):

$$\mathrm{CH_3OH + H_2O \xrightarrow{h\nu,\ TiO_2} 3H_2 + CO_2} \qquad S_{CO_2} = \frac{3 \cdot r_{CO_2}}{r_{H_2}} \times 100 \qquad (3.4.4)$$

$$\mathrm{CH_3OH \xrightarrow{h\nu,\ TiO_2} H_2 + H_2CO} \qquad S_{H_2CO} = \frac{r_{H_2CO}}{r_{H_2}} \times 100 \qquad (3.4.5)$$

$$\mathrm{CH_3OH \xrightarrow{h\nu,\ TiO_2} 2H_2 + CO} \qquad S_{CO} = \frac{2 \cdot r_{CO}}{r_{H_2}} \times 100 \qquad (3.4.6)$$

$$\mathrm{CH_3OH + H_2O \xrightarrow{h\nu,\ TiO_2} 2H_2 + HCOOH} \qquad S_{HCOOH} = \frac{2 \cdot r_{HCOOH}}{r_{H_2}} \times 100 \qquad (3.4.7)$$

where r_{CO_2}, r_{H_2CO}, r_{CO}, r_{HCOOH} and r_{H_2} are the rates of formation of $\mathrm{CO_2}$, $\mathrm{H_2CO}$, CO, HCOOH and $\mathrm{H_2}$, respectively.

3.5 Photocatalytic hydroxylation of terephthalic acid

3.5.1 Introduction

In heterogeneous photocatalysis, illumination of a semiconductor with photons of sufficient energy results in the formation of electron-hole pairs capable of reacting with species adsorbed on the photocatalyst surface. Thus, unstable and highly reactive oxygen species known as ROS (reactive oxygen species) can be formed. Among these, hydroxyl radicals ($HO^{\bullet}$), usually formed through oxidation of water molecules adsorbed at the photocatalyst surface with photogenerated holes or via reaction with the $O_2^{-\bullet}$ species formed via adsorbed oxygen reduction by conduction band electrons, are considered the main reactive species responsible for the photocatalytic

processes in aqueous media.[55-58] Due to their primary actor role in photocatalytic oxidation reactions, quantification of the capability of photocatalyst materials to produce hydroxyl radicals upon electronic excitation represents a powerful tool to rationalize the oxidative capability of semiconductor materials, especially towards substrates the degradation of which mainly proceeds through a hydroxyl radicals-mediated oxidation path.[59]

Due to their unstable nature, all $HO^{\bullet}$ detection methods involve their reaction with a probe compound which forms a stable specie whose concentration can be monitored by means of traditional instrumental analytical techniques such as EPR,[60-63] UV-Vis spectroscopy or fluorescence spectroscopy.[58,64] Among these, coumarin (COUM) and terephthalic acid (TA) represent some of the most powerful probe compounds to easily determine the relative capability of photocatalytic materials to generate hydroxyl radicals. In fact, their reaction with $HO^{\bullet}$ forms stable products which can be easily selectively detected via fluorescence spectroscopy. Furthermore, they are suitable as substrates for photocatalytic runs as they do not absorb light at the excitation wavelength of the photocatalyst.[58,65-69]

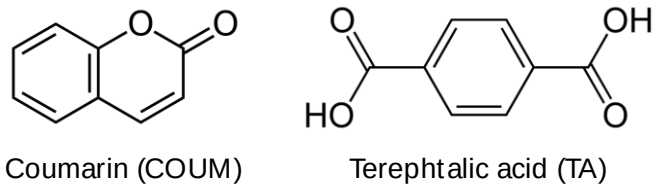

Figure 3.5.1: Molecular structure of $HO^{\bullet}$ radicals probe compounds coumarin (COUM) and terephthalic acid (TA).

Among the two compounds, terephthalic acid is a more robust and more reliable substrate for the detection of hydroxyl radicals since its indirect oxidation leads to the formation of the photoluminescent 2-hydroxyterephthalic acid (2-TaOH) as the only hydroxylation product.[70,71] In contrast, COUM reaction with $HO^{\bullet}$ brings to the formation of several different hydroxylation products, among which only 7-hydroxycoumarin is photoluminescent; this makes the COUM test less robust and more prone to experimental conditions variations compared to terephthalic acid.[72,73]

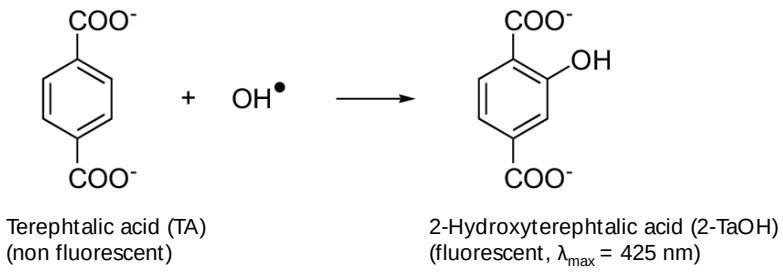

Figure 3.5.2: Photocatalytic hydroxylation of terephthalic acid

TA, however, is only soluble in highly alkaline solutions, making impossible to measure the relative ability of photocatalytic materials to produce HO• radicals under acidic pH conditions.[73] Despite this shortcoming, the terephthalic acid test was adopted here as a tool to investigate if and how a different titanium dioxide morphology and/or the presence of surface deposited Au nanoparticles may affect the relative ability of the prepared materials to produce highly reactive ROS species such as HO• radicals.

3.5.2 Experimental setup and procedure

Photocatalytic hydroxylation of terephthalic acid (TA) was performed in the experimental setup already described in detail for the photocatalytic oxidation of formic acid, following a slightly modified version of the procedure reported in literature.[74,75] In each photocatalytic run, 10 mg of photocatalyst was suspended in 45 cm^3 of ultrapure milli-Q water via ultrasound sonication for 30 min. Then, 5 cm^3 of a $5 \cdot 10^{-3}$ M terephthalic Acid solution in $2 \cdot 10^{-2}$ M NaOH was added to the suspension, obtaining a slurry composed of 0.5 g dm^{-3} titanium dioxide and $5 \cdot 10^{-4}$ M terephthalic acid at pH = 11. The suspension was then left under stirring in the dark for 30 min to attain the adsorption equilibrium of the substrate on the photocatalyst surface prior to irradiation.

The equilibrated suspension was then transferred to the cylindric photoreactor and irradiation started, under stirring. During the tests, samples were withdrawn from the suspension at regular time intervals by means of a syringe, separating the solid powders from the liquid portion by centrifugation for 20-30 min as described in section 3.1.3. The concentration of the fluorescent 2-hydroxyterephthalic acid produced during the photocatalytic runs was determined via fluorescence spectroscopy in an Edimburgh FLS980 spectrofluorimeter, using an excitation wavelength λ_{exc} = 315 nm and reading at the maximum emission intensity λ_{em} = 425 nm.

3.5.3 Data treatment

The concentration of fluorescent 2-hydroxyterephthalic acid (2-TaOH) in solution was determined using a calibration curve constructed by measuring the integrated area underneath the emission spectrum of standard solutions of known 2-TaOH concentration between 375 and 570 nm (Figure 3.5.3). Emission spectra were always obtained as the sum of three subsequent spectra to improve the signal/noise ratio. Calculation of the area underneath the emission spectrum was performed by means of a trapezoid integration algorithm using MathWorks® MATLAB®.

The photocatalytic hydroxylation of terephthalic acid in the presence of titanium dioxide always proceeded linearly as a function of irradiation time according to the following equation:

$$C - C_0 = k_{2-\mathrm{TaOH}} \cdot t \qquad (3.5.1)$$

where C is the 2-TaOH concentration at time t, C_0 is the 2-TaOH concentration at $t = 0$ s and $k_{2-\mathrm{TaOH}}$ is the pseudo-zeroth order rate constant for the photocatalytic hydroxylation of TA. Thus, the photoactivity of the investigated materials was studied by comparing their hydroxylation ability in terms of zeroth-order rate constants obtained by fitting experimental C vs time data.

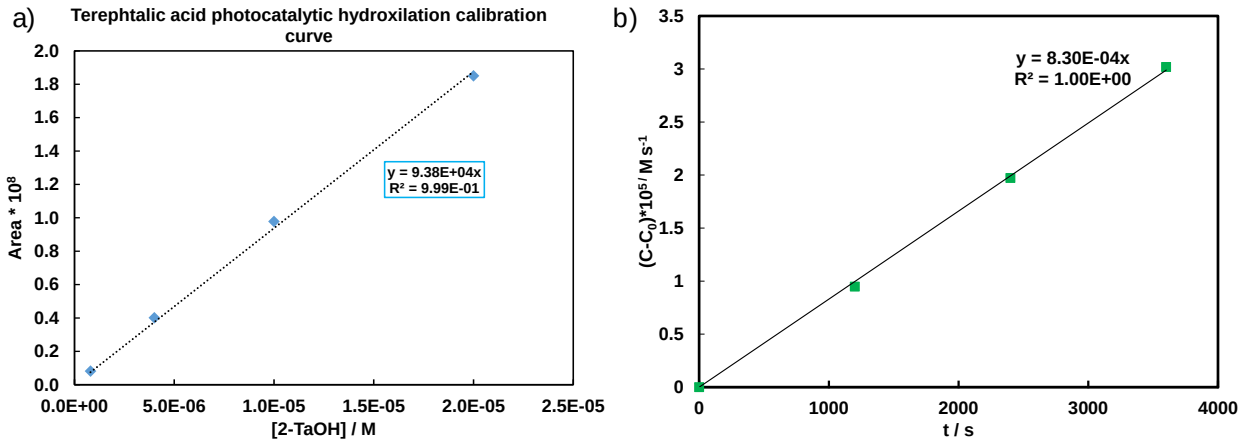

Figure 3.5.3: Calibration curve correlating the integrated emission intensity of 2-hydroxyterephthalic acid solutions of known 2-TaOH concentration (a); Example of a terephthalic acid hydroxylation photocatalytic run illustrating the linear production of 2-TaOH as a function of time (b).

3.6 References

1. Matthews, R. W. *Water Res.* **24**, 653–660 (1990).
2. Davydov, L. & Smirniotis, P. G. *J. Catal.* **191**, 105–115 (2000).
3. Dozzi, M. V., Livraghi, S., Giamello, E. & Selli, E. *Photochem. Photobiol. Sci.* **10**, 343 (2011).
4. Makhatova, A., Ulykbanova, G., Sadyk, S., Sarsenbay, K., Atabaev, T. S., Inglezakis, V. J. & Poulopoulos, S. G. *Sci. Rep.* **9**, 1–15 (2019).
5. Torun, M., Gültekin, Ö., Şolpan, D. & Güven, O. *Environ. Technol.* **36**, 970–982 (2015).
6. Ellwood, T., Živković, L. A., Denissenko, P., Abiev, R. S., Rebrov, E. V & Petkovska, M. *Processes* **9**, (2021).
7. Mrowetz, M. & Selli, E. *New J. Chem.* **30**, 108–114 (2006).
8. Carraway, E. R., Hoffman, A. J. & Hoffmann, M. R. *Environ. Sci. Technol.* **28**, 786–793 (1994).
9. Bielski, B. H. J. & Allen, A. O. *J. Phys. Chem.* **81**, 1048–1050 (1977).
10. Mrowetz, M. & Selli, E. *New J. Chem.* **30**, 108–114 (2006).
11. Mrowetz, M., Villa, A., Prati, L. & Selli, E. *Gold Bull.* **40**, 154–160 (2007).

12. Shiraishi, F., Nakasako, T. & Hua, Z. *J. Phys. Chem. A* **107**, 11072–11081 (2003).

13. Maurino, V., Minero, C., Mariella, G. & Pelizzetti, E. *Chem. Commun.* 2627–2629 (2005).

14. Hoffman, A. J., Carraway, E. R. & Hoffmann, M. R. *Environ. Sci. Technol.* **28**, 776–785 (1994).

15. Dozzi, M. V., Prati, L., Canton, P. & Selli, E. *Phys. Chem. Chem. Phys.* **11**, 7171–7180 (2009).

16. Minero, C., Mariella, G., Maurino, V. & Pelizzetti, E. *Langmuir* **16**, 2632–2641 (2000).

17. Weiher, N., Beesley, A. M., Tsapatsaris, N., Delannoy, L., Louis, C., Van Bokhoven, J. A. & Schroeder, S. L. M. *J. Am. Chem. Soc.* **129**, 2240–2241 (2007).

18. Dozzi, M. V., Marzorati, S., Longhi, M., Coduri, M., Artiglia, L. & Selli, E. *Appl. Catal. B Environ.* **186**, 157–165 (2016).

19. Dozzi, M. V., Ohtani, B. & Selli, E. *Phys. Chem. Chem. Phys.* **13**, 18217–18227 (2011).

20. Kanakaraju, D., Glass, B. D. & Oelgemöller, M. *Environ. Chem. Lett.* **12**, 27–47 (2014).

21. Han, F., Kambala, V. S. R., Srinivasan, M., Rajarathnam, D. & Naidu, R. *Appl. Catal. A Gen.* **359**, 25–40 (2009).

22. Weldegebrieal, G. K. *Inorg. Chem. Commun.* **120**, 108140 (2020).

23. Chan, S. H. S., Wu, T. Y., Juan, J. C. & Teh, C. Y. *J. Chem. Technol. Biotechnol.* **86**, 1130–1158 (2011).

24. Nuengmatcha, P., Chanthai, S., Mahachai, R. & Oh, W. C. *J. Environ. Chem. Eng.* **4**, 2170–2177 (2016).

25. Borhan, A. I., Samoila, P., Hulea, V., Iordan, A. R. & Palamaru, M. N. *J. Photochem. Photobiol. A Chem.* **279**, 17–23 (2014).

26. Spessato, L., Duarte, V. A., Viero, P., Zanella, H., Fonseca, J. M., Arroyo, P. A. & Almeida, V. C. *J. Hazard. Mater.* **411**, 125166 (2021).

27. Cheng, Y. Y. & Tsai, T. H. *J. Agric. Food Chem.* **65**, 1078–1085 (2017).

28. Dozzi, M. V., Montalbano, M., Marra, G., Mino, L. & Selli, E. *Mater. Today Chem.* **22**, 100624 (2021).

29. Palmer, C. D. & Wittbrodt, P. R. *Environ. Health Perspect.* **92**, 25–40 (1991).

30. Waterhouse, J. A. *Br. J. Cancer* **32**, 262 (1975).

31. Park, J. H. *Environ. Pollut.* **266**, 115073 (2020).

32. Sharma, P., Singh, S. P., Parakh, S. K. & Tong, Y. W. *Bioengineered* **13**, 4923–4938 (2022).

33. Bianchi, V., Zantedeschi, A., Montaldi, A. & Majone, F. *Toxicol. Lett.* **23**, 51–59 (1984).

34. Oliveira, H. *J. Bot.* **2012**, 1–8 (2012).

35. Gu, B. & Chen, J. *Geochim. Cosmochim. Acta* **67**, 3575–3582 (2003).

36. Testa, J. J., Grela, M. A. & Litter, M. I. *Environ. Sci. Technol.* **38**, 1589–1594 (2004).

37. Yang, J. K. & Lee, S. M. *Chemosphere* **63**, 1677–1684 (2006).

38. Wang, X., Pehkonen, S. O. & Ray, A. K. *Ind. Eng. Chem. Res.* **43**, 1665–1672 (2004).

39. Zhao, Z., An, H., Lin, J., Feng, M., Murugadoss, V., Ding, T., Liu, H., Shao, Q., Mai, X., Wang, N., Gu, H., Angaiah, S. & Guo, Z. *Chem. Rec.* **19**, 873–882 (2019).

40. Clesceri, L. S., Greenberg, A. E. & Eaton, A. D. *Standard Methods for the Examination of Water and Wastewater, 20th Ed. American Public Health Association, Washington, DC* (1998).

41. Pflaum, R. T. & Howick, L. C. *J. Am. Chem. Soc.* **78**, 4862–4866 (1956).

42. Yu, H., Li, Y., Xu, C., Jin, F., Ye, F. & Li, X. *Energy Storage Sav.* **1**, 53–69 (2022).

43. Liu, X., Bao, C., Zhu, Z., Zheng, H., Song, C. & Xu, Q. *Int. J. Hydrogen Energy* **46**, 26741–26756 (2021).

44. Ranjekar, A. M. & Yadav, G. D. *Ind. Eng. Chem. Res.* **60**, 89–113 (2021).

45. Al-Mazroai, L. S., Bowker, M., Davies, P., Dickinson, A., Greaves, J., James, D. & Millard, L. *Catal. Today* **122**, 46–50 (2007).

46. Chiarello, G. L., Aguirre, M. H. & Selli, E. *J. Catal.* **273**, 182–190 (2010).

47. Bernareggi, M., Dozzi, M. V., Bettini, L., Ferretti, A., Chiarello, G. L. & Selli, E. *Catalysts* **7**, 301 (2017).

48. Chiarello, G. L., Dozzi, M. V., Scavini, M., Grunwaldt, J. D. & Selli, E. *Appl. Catal. B Environ.* **160–161**, 144–151 (2014).

49. Chiarello, G. L., Forni, L. & Selli, E. *Catal. Today* **144**, 69–74 (2009).

50. Chiarello, G. L., Ferri, D. & Selli, E. *J. Catal.* **280**, 168–177 (2011).

51. Dozzi, M. V., Zuliani, A., Grigioni, I., Chiarello, G. L., Meda, L. & Selli, E. *Appl. Catal. A Gen.* **521**, 220–226 (2016).

52. Dozzi, M. V., Chiarello, G. L., Pedroni, M., Livraghi, S., Giamello, E. & Selli, E. *Appl. Catal. B Environ.* **209**, 417–428 (2017).

53. Chiarello, G. L., Dozzi, M. V., Scavini, M., Grunwaldt, J. D. & Selli, E. *Appl. Catal. B Environ.* **160–161**, 144–151 (2014).

54. Chiarello, G. L., Dozzi, M. V. & Selli, E. *J. energy Chem.* **26**, 250–258 (2017).

55. Xiao, Q. & Ouyang, L. *Chem. Eng. J.* **148**, 248–253 (2009).

56. O'Shea, K. E. & Cardona, C. *J. Photochem. Photobiol. A Chem.* **91**, 67–72 (1995).

57. Xiao, Q., Si, Z., Zhang, J., Xiao, C. & Tan, X. *J. Hazard. Mater.* **150**, 62–67 (2008).

58. Nosaka, Y. & Nosaka, A. Y. *Chem. Rev.* **117**, 11302–11336 (2017).

59. Xiang, Q., Yu, J. & Wong, P. K. *J. Colloid Interface Sci.* **357**, 163–167 (2011).

60. Barbieriková, Z., Dvoranová, D., Sofianou, M. V., Trapalis, C. & Brezová, V. *J. Catal.* **331**, 39–48 (2015).

61. Brezová, V., Šlebodová, A. & Staško, A. *Food Chem.* **114**, 859–868 (2009).

62. Tó, H. & Systems, O. A. 8977–8984 (2000).

63. Brezová, V., Dvoranová, D. & Staško, A. *Res. Chem. Intermed.* **33**, 251–268 (2007).

64. Ishibashi, K. I., Fujishima, A., Watanabe, T. & Hashimoto, K. *Electrochem. commun.* **2**, 207–210 (2000).

65. Yener, H. B., Yılmaz, M., Deliismail, Özkan, S. F. & Helvacı. *Sep. Purif. Technol.* **173**, 17–26 (2017).

66. Buck, C., Skillen, N., Robertson, J. & Robertson, P. K. J. *Chinese Chem. Lett.* **29**, 773–777 (2018).

67. Bubacz, K., Kusiak-Nejman, E., Tryba, B. & Morawski, A. W. *J. Photochem. Photobiol. A Chem.* **261**, 7–11 (2013).

68. Charbouillot, T., Brigante, M., Mailhot, G., Maddigapu, P. R., Minero, C. & Vione, D. *J. Photochem. Photobiol. A Chem.* **222**, 70–76 (2011).

69. Ahmed, A. Y., Kandiel, T. A., Oekermann, T. & Bahnemann, D. *J. Phys. Chem. Lett.* **2**, 2461–2465 (2011).

70. Nakamura, R. & Nakato, Y. *J. Am. Chem. Soc.* **126**, 1290–1298 (2004).

71. Nakabayashi, Y. & Nosaka, Y. *Phys. Chem. Chem. Phys.* **17**, 30570–30576 (2015).

72. Nagarajan, S., Skillen, N. C., Fina, F., Zhang, G., Randorn, C., Lawton, L. A., Irvine, J. T. S. & Robertson, P. K. J. *J. Photochem. Photobiol. A Chem.* **334**, 13–19 (2017).

73. Žerjav, G., Albreht, A., Vovk, I. & Pintar, A. *Appl. Catal. A Gen.* **598**, (2020).

74. Maisano, M., Dozzi, M. V., Coduri, M., Artiglia, L., Granozzi, G. & Selli, E. *ACS Appl. Mater. Interfaces* **8**, 9745–9754 (2016).

75. Ye, L., Mao, J., Liu, J., Jiang, Z., Peng, T. & Zan, L. *J. Mater. Chem. A* **1**, 10532–10537 (2013).

Chapter 4: Effect of N,F-Doping and Au Nanoparticles Deposition on the Photocatalytic Activity of TiO_2 Anatase Materials

4.1 Introduction

Over the past years, researchers worldwide have focused on developing methods and strategies aimed at boosting the photocatalytic performance of TiO_2. In fact, despite different materials and technologies have been proposed as alternative promising semiconductor photocatalysts,[1-3] titanium dioxide in powder form still represents nowadays the most widely employed, studied and cost-effective semiconductor photocatalyst for many photocatalytic applications.[4-7] Furthermore, the material is also particularly suited for large-scale usage and to produce patented commercial products.[8,9]

Among the possible semiconductor modification strategies, doping the bulk structure of titanium dioxide represents a valuable path possibly able to improve its visible light harvesting capability, as well as to decrease the fast recombination rate of photogenerated charge carriers, both representing the main drawbacks limiting its performance as a photocatalyst.[10-13] However, the optimal amount of dopant included in a semiconductor should be thoughtfully examined and evaluated, as the introduction of point defects associated to the introduction of extra-lattice species within the bulk structure of a semiconductor may result in favouring charge recombination rather than their desired separation, as an excessive amount of point defects may behave as undesired charge recombination centres.

Another strategy pursuable in combination with the usage of an optimal amount of doping in boosting the performance of anatase consists in modifying its surface with noble metal nanoparticles, resulting in the formation of a Schottky barrier at the metal-semiconductor interface.[14-16] Such heterostructure usually favours the separation of free charge carriers within the semiconductor thanks to the fast and efficient ability of noble metal nanoparticles (Au, Pt, Ag) to scavenge electrons in the semiconductor conduction band, with an overall limitation of their recombination with the holes photoproduced in the valence band.

Among various noble metals, Au nanoparticles have proven to behave in a unique and peculiar way when deposited on the surface of titanium dioxide. This is especially relevant when Au nanoparticles are compared to the Pt ones. For example, in the case of Pt-group noble metals a classical strong metal support interaction (SMSI), i.e. a phenomenon resulting in the encapsulation of noble metal nanoparticles by a titania overlayer, was observed as early as the late 1970s. Differently, a Au/TiO_2 SMSI was observed only in 2017 with the pioneering work of Tang et al., in which the authors succeeded not only in demonstrating the existence of such phenomena for Au nanoparticles on TiO_2, but also in evidencing the extremely marked stability of the resulting composite material towards CO oxidation.[17] More interestingly, when metallic nanoparticles of Au and Pt were deposited on a titanium dioxide surface enriched with oxygen vacancies through photodeposition, some very peculiar phenomena were reported. According to a 2007 study by Kydd et al.,[18] the electron portioning effect involved in the conventional photodeposition process causes Au nanoparticles to nucleate and grow on specific TiO_2 surface sites, characterized by high-electron density and so defective in terms of oxygen content. On the other hand, the adsorption behaviour of Pt ions and complexes from the solution onto the TiO_2 surface is different, which means that the density of nucleation sites for Pt nanoparticles may be dissimilar from those available for gold, i.e. resulting in a greater level of dispersion for Pt compared to Au nanoparticles for the same nominal metal loading. Later observations from scanning tunnelling microscopy[19] and Raman investigations[20] have shown that gold nanoclusters have a unique tendency to grow on electron-rich defective sites of TiO_2, specifically oxygen vacancies and edge sites, in contrast to Pt nanoparticles. The Raman investigation further revealed that only the deposition of gold nanoparticles caused a significant blue shift and broadening of TiO_2 Raman features, while this was not observed in the case of Pt nanoparticles deposition. These studies jointly suggest that one may expect stronger interaction between defective titania and gold instead than Pt nanoparticles.

In a paper published by our research group in 2018,[21] Dozzi et al. found that combining N,F-doping of titanium dioxide bulk structure with the surface photodeposition of noble metal nanoparticles produced a peculiar synergistic cooperation only between dopant-induced Ti^{3+} defective trap states and deposited Au nanoparticles, whereas no similar effects were attained in the presence of photodeposited Pt nanoparticles. In particular, not only the average size and distribution of deposited nanoparticles were heavily influenced by the amount of dopant included in the supports, but also the photoactivity of the material modified with the optimal dopant content benefitted more from the deposition of Au rather than Pt in both methanol photo-steam reforming and formic acid oxidation, despite of the lower work function of Au providing a lower Schottky barrier height compared to Pt. The following effect was ascribed to the possible presence

of preferential electron transfer channels occurring between photodeposited Au nanoparticles and dopant-induced trap states, which were absent in the case of photodeposited platinum.

Even more interestingly, the presence of such preferential electron exchange channels was also monitored and showcased through the photoluminescent properties of N,F-doped titanium dioxide upon noble metal nanoparticles deposition. In fact, both the photoluminescence (PL) intensity and temporal evolution of the PL signal of bare N,F-doped titanium dioxide resulted to be quenched upon metal nanoparticles deposition. However, such quenching effect resulted to be much more marked when the properly N,F doped material was paired with Au rather than Pt nanoparticles deposition. Such effect is a strong indication of the presence of a preferential and more efficient transfer of electrons trapped at dopant induced photoluminescent Ti^{3+} trap states[22] towards photodeposited Au nanoparticles.

However, the choice of the photodeposition method may have played a significant role in observing such cooperation between photoluminescent dopant induced Ti^{3+} trap states and Au nanoparticles. In fact, it is extensively reported in literature that the properties of Au-modified TiO_2 materials are heavily influenced by the method adopted for the deposition of metallic nanoparticles.[23-27] In particular, photodeposition represents a unique deposition technique since, by employing the intrinsic reducing power of the metal oxide semiconductor to trigger the nucleation and growth of the noble metal nanoparticles on the surface of the support, it allows for a preferential deposition of metals on those regions where photogenerated electrons can be more efficiently trapped.[28-31] In particular, the photodeposition technique may allow the preferential Au nanoparticles fixation in the proximity of dopant-induced photoluminescent trap states, which cannot be achieved by adopting a different and non-selective Au nanoparticles deposition technique.

In this context, the following chapter presents a systematic investigation on the effects possibly produced on either the photocatalytic activity (in different oxidation and reduction test reactions) and the photoluminescence properties of N,F-doped TiO_2 samples, by the use of a non-selective Au nanoparticles deposition method, i.e. deposition-precipitation (DP), in comparison to those deriving by adopting the selective photodeposition (P) method. In this way it should be possible to shed light on the importance played by the chosen noble metal nanoparticles deposition route in maximizing the photoefficiency of metal-modified and bulk doped titanium dioxide.

4.2 Experimental section

4.2.1 Synthesis of N,F-doped TiO_2 powders

The syntheses of TiO_2 N,F-doped powders were carried out as described in detail in section 2.1.1 (page 47). The obtained TiO_2 doped materials labelled as DX_Y, where X represents the nominal F/Ti molar percent ratio and Y refers to the calcination temperature in °C. The amount of NH_4F added during the synthesis of each material, as well as their calcination temperature, are reported in Table 4.2.1. Reference undoped materials prepared by the same synthetic route in the absence of NH_4F are named as D0_Y.

Table 4.2.1: NH_4F amounts and calcination temperature employed in the synthesis of the investigated samples.

Sample	Nominal Ti/F ratio	Ti amount / mol	F^- amount /mol	NH_4F mass / g	Calcination temperature
D0_500	-	0.0328	-	-	500 °C
D0_600	-	0.0328	-	-	600 °C
D0_700	-	0.0328	-	-	700 °C
D5_700	20	0.0328	0.0016	0.0607	700 °C
D18_700	5.56	0.0328	0.0059	0.2185	700 °C
D50_700	2	0.0328	0.0164	0.6068	700 °C
D80_700	1.25	0.0328	0.0262	0.9709	700 °C

4.2.2 Surface modification of doped TiO_2 powders

Two series of Au-modified photocatalysts with Au loading equal to 0.5 wt%, labelled as DX_Y_DP and DX_Y_P, were also prepared by modifying DX_Y materials using the deposition-precipitation (DP, as described in section 2.3.1, page 54) and the photodeposition (P, as described in section 2.4.1, page 56), respectively.

4.2.3 Materials characterization

The following techniques were employed for the characterization of the materials:

- X-Ray Powder Diffraction (XRPD), as described in section 2.5.1 (page 63)
- Specific surface area (SSA) measurement, as described in section 2.6.1 (page 69)
- UV-Visible DR Spectroscopy, as described in section 2.7.1 (page 72)
- ICP-OES analysis, as described in section 2.8.1 (page 74)
- HRTEM imaging, as described in section 2.9.1 (page 79)
- Time-Resolved Photoluminescence Spectroscopy, as described in section 2.10.1 (page 83)

4.2.4 Photocatalytic activity tests

4.2.5 Photocatalytic oxidation of formic acid

Formic acid photodegradation tests were performed according to a well-established procedure described in detail in section 3.1.3 (page 96).[22,27,32] Experimental runs were also performed with a photocatalyst concentration equal to 0.063 g dm^{-3}, in addition to the 0.1 g dm^{-3} concentration commonly employed throughout this thesis.

4.2.6 Photocatalytic Reduction of Cr(VI)

Photocatalytic Cr(VI) reduction runs were performed as described in detail in section 3.3.2 (page 102).[32,33]

4.3 Results and Discussion

4.3.1.1 Materials Characterization

Home-prepared N,F-doped titanium dioxide materials were fully characterized by means of the main physico-chemical characterization techniques. In particular, X-Ray powder diffraction analysis was carried out to monitor the phase composition of the materials, as well as to calculate the average size of anatase phase crystallites by using the Scherrer equation.

As shown in Figure 4.3.1, all XRPD patterns of doped samples are characterized by the presence of diffraction peaks originating from a single crystal phase easily attributable to pure anatase, excluding the presence of any appreciable amount of undesired rutile or brookite phases. These results are quantitatively confirmed by Rietveld analysis (Table 4.3.1). As expected from literature data,[22] the presence of bulk fluoride anions stabilizes the anatase phase at higher temperatures, inhibiting the anatase to rutile phase transition by hampering the condensation of spiral chains of rutile TiO_6 octahedra responsible for the phase transformation, usually occurring at temperatures above 600 °C. In this way it is thus possible to obtain full anatase powders with a higher degree of crystallinity without introducing impurities of less photocatalytically active phases such as rutile.

In the case of undoped samples, the calcination temperature plays a key role in determining the phase composition of the powders, as illustrated by an increased rutile content passing from 500 °C to 700° C calcination temperature. Due to the presence of undesired mixed phase composition of both D0_600 and D0_700 materials, the D0_500 specimen was preferred as a reference undoped material to be compared with the full-anatase doped titania powders. In fact, despite the different calcination temperature employed during the thermal treatment procedure,

maintaining the same crystal phase composition represents a vital parameter when comparing the effects deriving from the combination of noble metal nanoparticles deposition and bulk material doping. The introduction of an additional variable such as the presence of extra crystalline phases may get more difficult the interpretation of the photoactivity results attained with the metal-modified, N,F-doped TiO_2-based materials. Thus, reference undoped materials calcined above 500 °C will be only briefly discussed within this thesis and will not be considered as appropriate reference undoped materials to be compared with N,F-doped titania specimens.

By considering the trend exhibited by the FWHM of the XRPD anatase peaks of the investigated materials, we found a progressive anatase crystallites dimension increase with increasing the nominal dopant content of the TiO_2 materials. Furthermore, similar results were attained with increasing the calcination temperature due to the favored nanoparticles sintering at relatively high temperatures (Table 4.3.1).

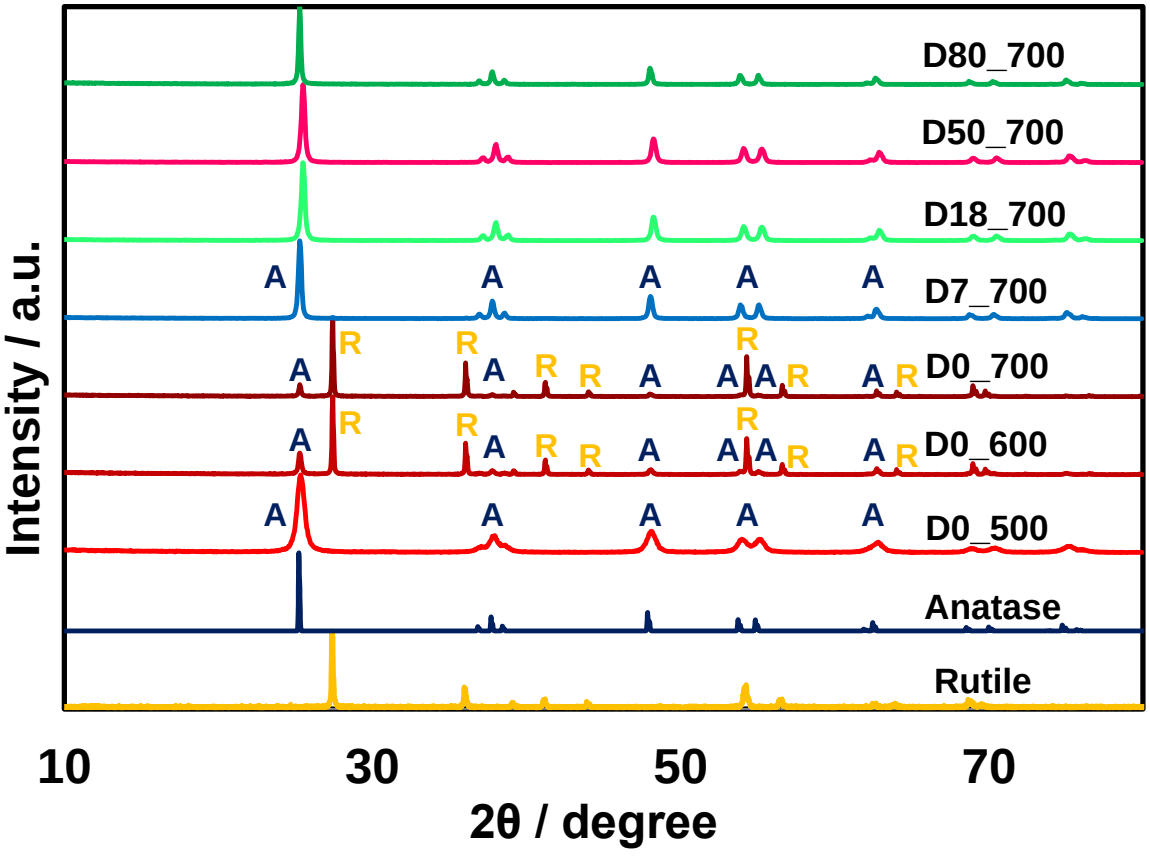

Figure 4.3.1: X-Ray Powder Diffraction patterns of TiO_2 powders obtained by adding different nominal amounts of NH_4F and calcined at different temperatures.

Table 4.3.1: Phase composition, crystallite size, cell parameters (for the anatase phase) and quality of the Rietveld refinement obtained from XRD Analysis. The anatase phase structure was always refined in the $I4_1/amd$ space group (number 141), while the rutile phase, when present, was refined in the $P4_2/mnm$ space group in each case (number 136).

Sample	Anatase content (%)	Rutile content (%)	d_A (nm)	a_A (nm)	c_A (nm)	R_p (%)
D0_500	99.6	0.4	14.8	0.3786	0.9507	7.49
D0_600	29.1	70.9	30.5	0.3876	0.9518	9.60
D0_700	15.5	84.5	37.3	0.3785	0.9518	9.72
D7_700	99	1	35.7	0.3784	0.9514	5.96
D18_700	100	0	39.0	0.3785	0.9512	6.01
D25_700	100	0	39.3	0.3784	0.9513	8.80
D50_700	100	0	42.5	0.3783	0.9514	7.80
D80_700	100	0	66.1	0.3786	0.9518	7.64

It is interesting to notice that, despite the introduction of a bulk dopant, the cell parameters of the anatase phase did not undergo any appreciable variation with increasing F/Ti nominal molar ratio. This result is consistent with the structural model of F-doped TiO_2 depicted by Czoska et al.,[34] in which fluorine doping results in the lattice substitution of O^{2-} ions by F^- ions, leading to the formation of bridging Ti-F-Ti bonds. As differences in lengths between Ti-F-Ti and Ti-O-Ti bonds are very small, the introduction of the dopant does not result in a significant variation of the lattice constants, and consequently the cell parameters are unchanged upon varying the dopant content. The lattice parameters of both phases remained unchanged also with increasing the calcination temperature, indicating that the microscopic structure of the TiO_6 octahedra has not been affected by the thermal treatment, which instead resulted to deeply affect the crystallite size and the crystallinity degree of the prepared samples.

Unfortunately, the calculation of the crystallite size for the rutile phase was impossible due to the poor fittings of the characteristic rutile peak profile by means of the Pseudo-Voigt function through the WinPLOTR software. This leads to data calculation of unreliable quality and were therefore not considered.

The specific surface area of the materials, evaluated according to the BET method, showed a progressive decrease with increasing the materials calcination temperature (Table 4.3.2), which is in line with the increased crystallite size attained at higher calcination temperature, as demonstrated by the XRPD analysis (Table 4.3.1). As a consequence, the reference undoped D0_500 material,

being calcined at 500 °C, is characterized by a much larger specific surface area (~ 60 $m^2 g^{-1}$) compared to N,F-doped TiO_2 powders, which instead have all been calcined at 700 °C. Regardless, all doped materials calcined at 700 °C exhibited very similar specific surface area (SSA) values (12-20 $m^2 g^{-1}$ range), i.e. perfectly consistent with those reported in literature for similar samples.[35]

Table 4.3.2: BET specific surface area of the bare N,F-doped TiO_2 powders.

Sample	Calcination temperature	Specific Surface Area ($m^2 g^{-1}$)
D0_500	500 °C	60
D7_700	700 °C	16
D18_700	700 °C	20
D50_700	700 °C	12
D80_700	700 °C	12

Normalized nitrogen physisorption isotherms (Figure 4.3.2) can be classified as type IVa according to the IUPAC classification, which are typical of mesoporous solids.[36] Hysteresis loops, instead, are of type H2, which are characteristic of a complex system of pores with a bottleneck-type geometry.[37] All the adsorption isotherms of samples prepared with a nominal F/Ti molar ratio higher than 7 did not show appreciable variation with the nominal dopant content. The shift of the hysteresis loop in the D0_500 sample, instead, could be ascribed to a closer packing of the anatase crystallites due to their smaller size, leading to the formation of tighter necks in the pores. In fact, as the analysed powders are not intrinsically porous, the origin of the hysteresis loops is attributed to the crystal packing of the nanoparticles. Such behaviour is also reflected in the analysis of the porosity variation in terms of volume as a function of the pore's diameter (Figure 4.3.3). In such analysis, all curves relative to doped samples show a similar behaviour, characterized by the presence of a maximum in the region of the micropores and in the range between 30-50 nm. For the D0_500 sample, instead, the maximum in the range between 2-5 nm is much more pronounced with respect to that shown by other samples, indicating a pore distribution mainly shifted towards relatively smaller micropores diameter, consistently with what observed through the adsorption/desorption isotherms measurements.

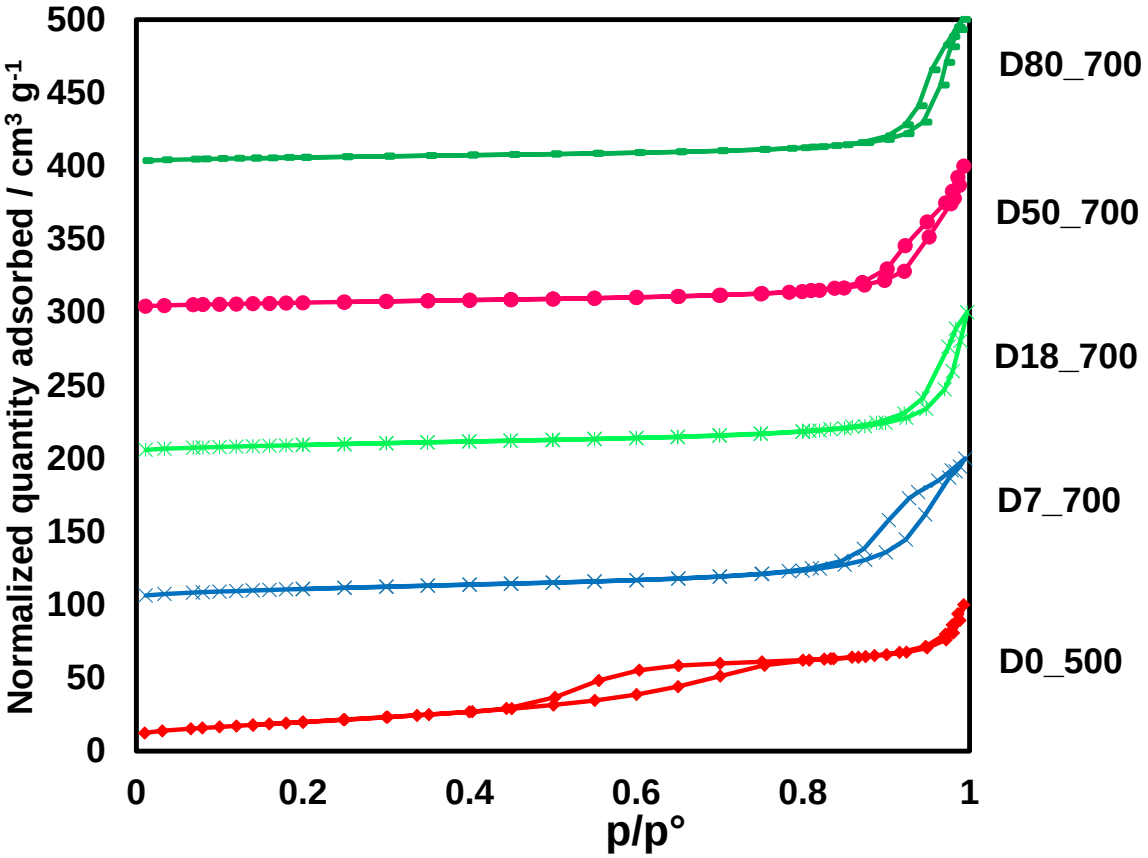

Figure 4.3.2: Nitrogen adsorption-desorption isotherms of NH_4F doped TiO_2 powders.

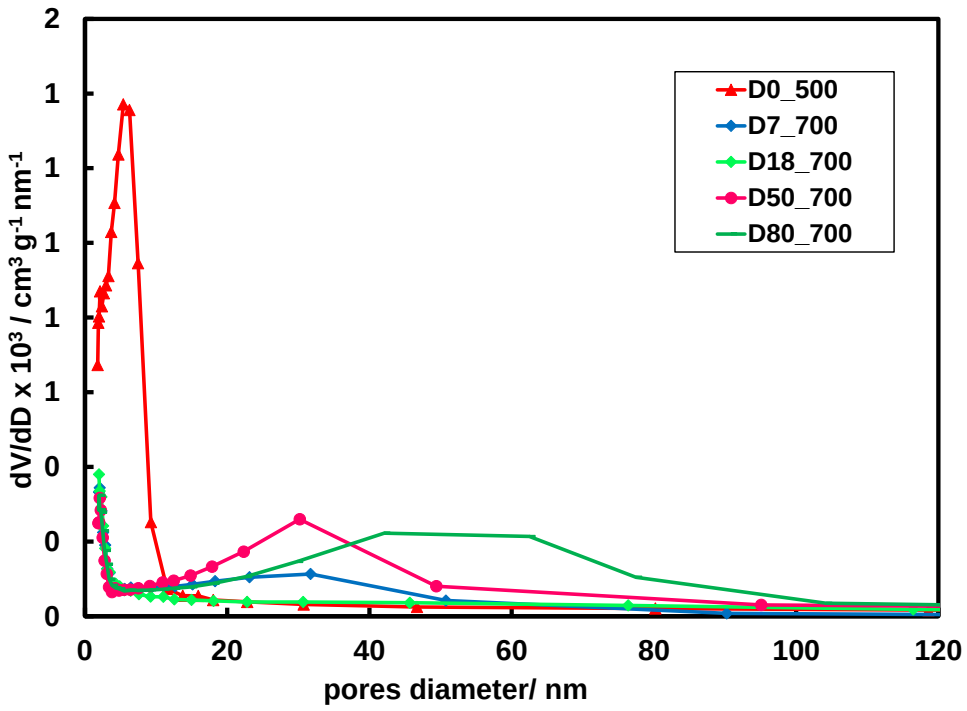

Figure 4.3.3: Variation of the porosity of the analysed samples in terms of volume as a function of the pore diameter.

The UV-Visible absorption spectra of metal-free N,F-doped titanium dioxide materials are characterized by the typical spectroscopic features of pure anatase, *i.e.,* little-to-no absorption for $\lambda > 400$ nm and a marked absorption for wavelengths below the ~400 nm absorption onset (Figure 4.3.4).[35,38] The same behavior was observed in the case of reference undoped D0-500 material, being also fully composed by anatase phase. Congruently with our previous investigations, the presence of rutile as majority phase in undoped samples calcined at temperatures above 500 °C leads to a bathochromic shift in the powders absorption edges, passing from ~ 380 nm (for full anatase samples) to ~ 410 nm in the case of materials mainly composed of rutile, as determined through the calculation of the numerical first derivative of the absorption spectra of the powders (Figure 4.3.5).[39] In fact, the position of the adsorption edges allows to qualitatively estimate the absorption band gap of the semiconductors prepared, being ~ 3.26 eV and ~ 3.06 eV for anatase and rutile phase, respectively, as confirmed by literature data.[40]

The total absence of any absorption component in the visible range demonstrates the absence of any residual carbonaceous species (from the synthesis precursors) and/or unexpected visible light absorbing impurities. Coherently with literature reports,[41,42] the absorption spectra of all doped samples do not show any peculiar difference, indicating that the introduction of the dopant did not substantially affect the visible light harvesting properties of the powders.

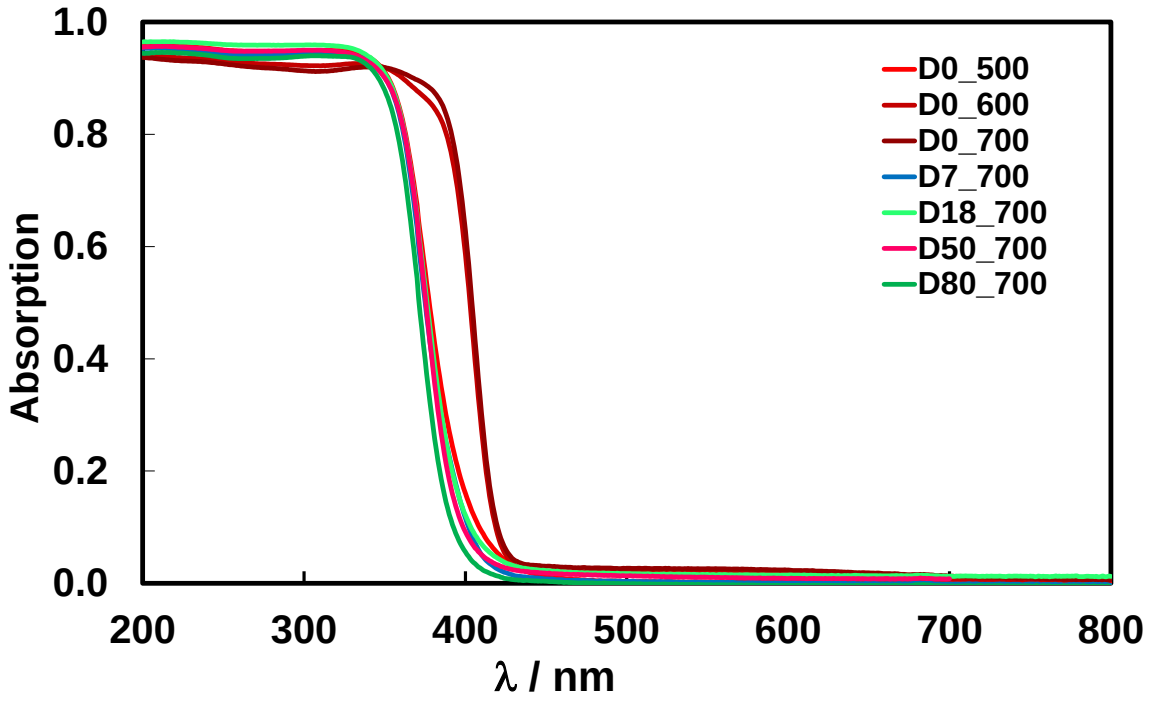

Figure 4.3.4: UV-Vis DRS absorption spectra of metal-free NH_4F-doped TiO_2 powders.

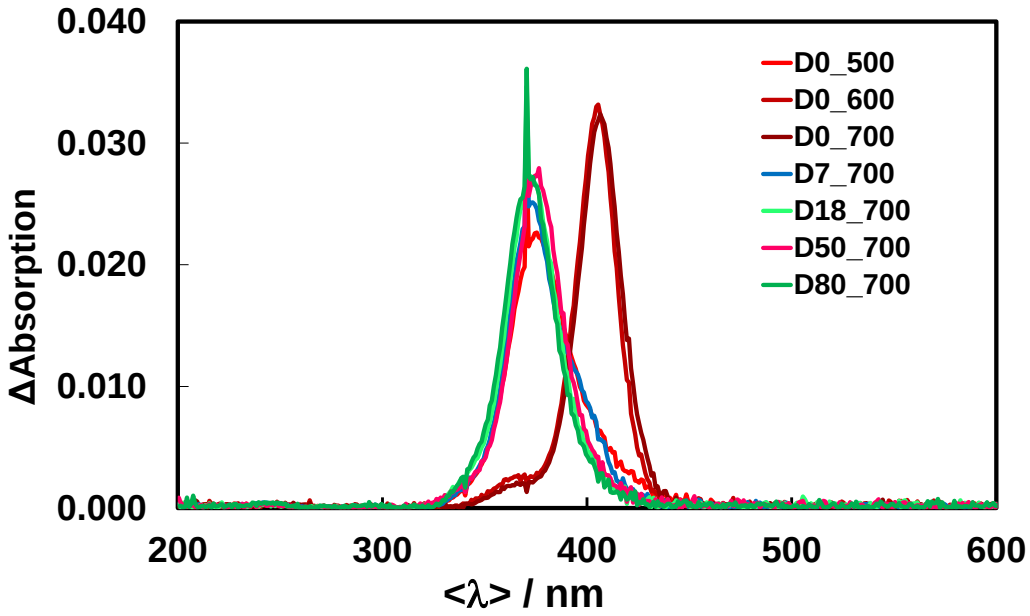

Figure 4.3.5: First derivative plot of the DRS absorption spectra of N,F-doped bare TiO_2 samples.

The UV-Vis absorption spectra of the doped TiO_2 powders modified with 0.5 wt.% of Au nanoparticles by means of the deposition-precipitation method are reported in Figure 4.3.6. The deposition of Au metal nanoparticles resulted in a chromatic shift of the powders, passing from brilliant white to deep purple. The UV-Vis absorption spectra show the typical localized surface plasmon resonance (LSPR) absorption of Au metal nanoparticles, causing the appearance of a very distinct absorption peak with a maximum in the region between 530-500 nm,[43] which is totally absent in the corresponding bare powders (Figure 4.3.4). This effect is at the origin of the above-mentioned chromatic shift of the metal oxides.

Intensity and position of the plasmonic band maximum absorption depends on the effective Au deposited content and on the average Au nanoparticles size distribution, respectively.[27] The slight shift of the plasmonic maximum absorption position indicates the presence of very slight differences in terms of Au NPs dimension deposited on differently doped samples. The D0_500 sample, instead, is characterized by a slight red shift in the position of the absorption maximum of the LSPR, possibly indicating the deposition of Au nanoparticles with sizes somewhat differing from those anchored on N,F-doped TiO_2 powders.[44]

The obtainment of pretty similar maximum intensities of Au plasmon absorption bands indirectly confirmed the deposition of comparable Au loading on N,F-doped materials. This can be better appreciated by comparing the absorption difference spectra, i.e., calculated by subtracting the spectrum of bare TiO_2 sample from that of the corresponding metal-containing one (Figure 4.3.7). As variations in the intensity of the absorption difference spectra in the visible region are

very small, we can conclude that similar amounts of noble metal nanoparticles have been loaded on the doped samples. The difference in terms of plasmonic band intensity exclusively attained with the D0_500 sample can be somehow attributed to different surface properties of the starting metal oxide due to the lower adopted calcination temperature. In fact, apart for the deposited metal amount, the intensity of the localized surface plasmon resonance phenomenon of Au nanoparticles may be also heavily affected by the chemical environment surrounding the noble metal nanoparticles themselves. Therefore, Au NPs supported on TiO_2 samples with different surface properties may be characterized by LSPR NPs with different shape and/or maximum wavelength position or intensity.[44]

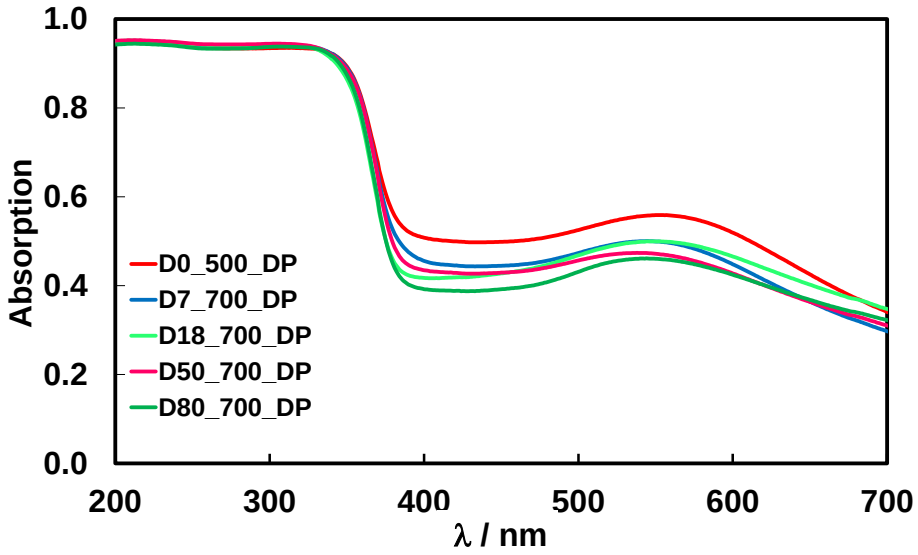

Figure 4.3.6: UV-Vis DRS spectra of selected differently doped TiO_2 powders modified with 0.5 wt.% Au surface metal nanoparticles by means of the deposition precipitation method.

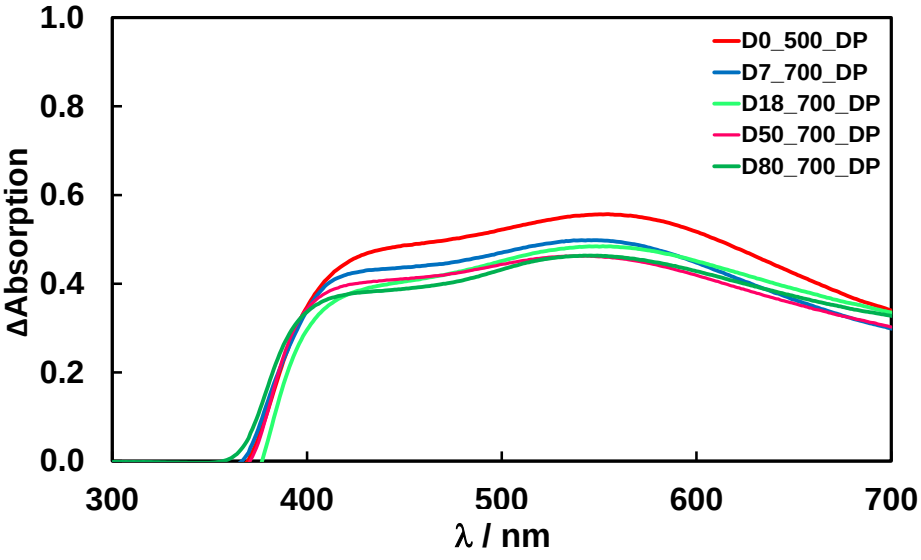

Figure 4.3.7: Absorption difference spectra of selected differently doped DP-modified TiO_2 powders.

The effects deriving from the use of a different noble metal nanoparticles deposition technique, i.e. photodeposition (P), were then evaluated by comparing the absorption spectra of P-modified materials with those of the materials modified through deposition-precipitation bearing the same amount of dopant content (Figure 4.3.8).

In the case of N,F-doped materials, except for the D7_700 sample, the absorption spectra of the Au-modified materials resulted to be very similar whether the DP or the P method was used to deposit the noble metal nanoparticles, possibly indicating the deposition of similar content of Au nanoparticles, also characterized by analogous average size and distribution (Figure 4.3.8 c-e). Differently, in the case of both reference undoped D0_500 and lowest doped D7_700 materials, significant differences in the absorption profiles are observable between Au-containing materials modified with the two different deposition techniques, possibly unveiling an effective role played by the adopted deposition route on the resultant physico-chemical properties of the anchored Au NPs (Figure 4.3.8 a-b).

Anyway, the actual loading of Au NPs, pretty close to the nominal 0.5 wt% value, has been confirmed through ICP-OES analysis for all prepared samples, regardless of the adopted deposition method employed and the N,F dopant amount introduced in the TiO_2 bulk structure (Table 4.3.3).

Table 4.3.3: ICP-OES analysis results evidencing the deposition of similar amounts of Au wt% among selected Au-modified materials regardless of the method employed for their deposition and the dopant content included within the TiO_2 samples.

Sample	Au content (wt%)
D0_500_DP	0.42(2)
D0_500_P	0.45(1)
D7_700_DP	0.46(2)
D7_700_P	0.50(2)
D80_700_P	0.45(2)

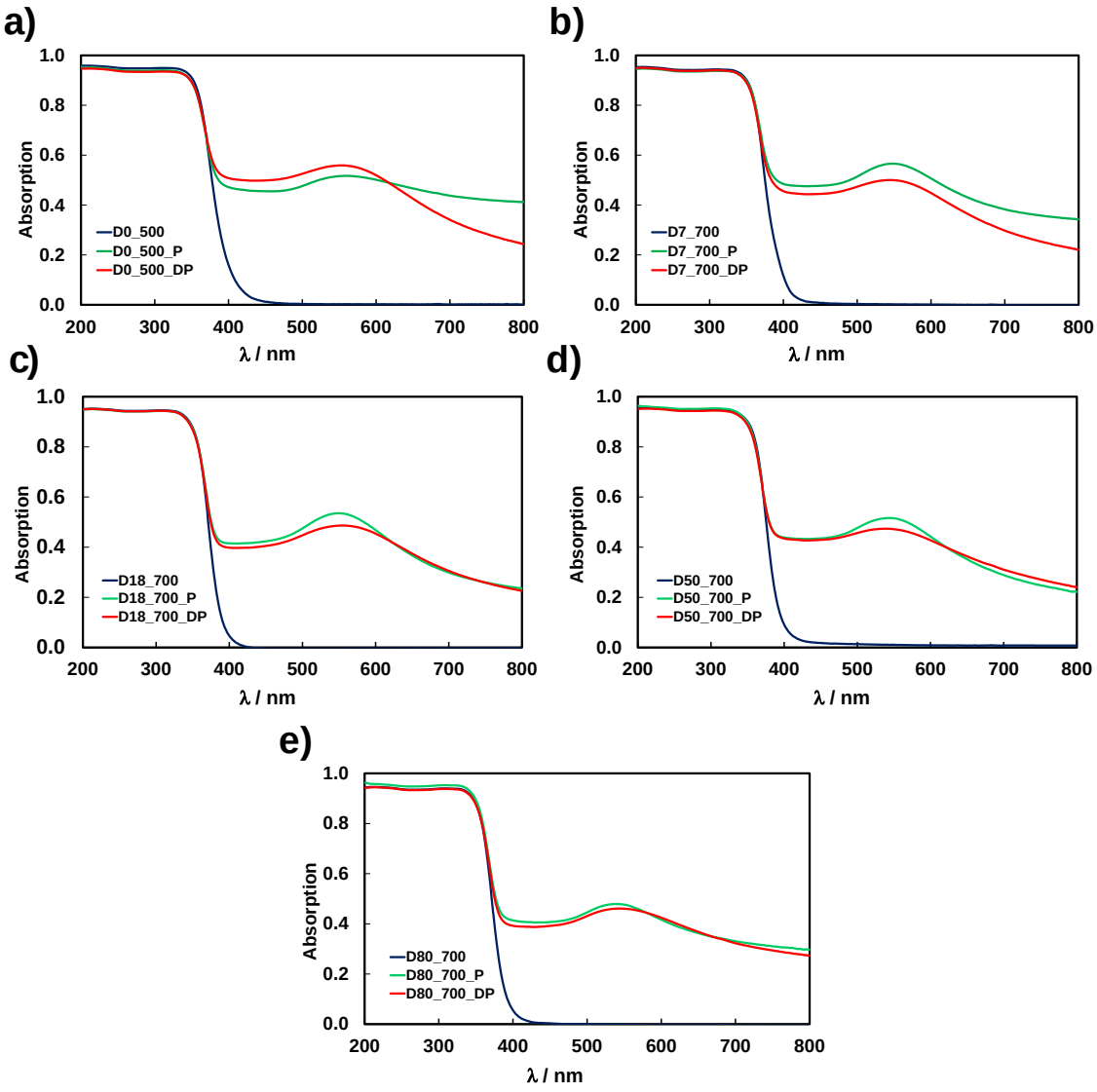

Figure 4.3.8: Absorption spectra of D0_500 (a), D7_700 (b), D18_700 (c), D50_700 (d), D80_700 (e) materials modified with 0.5 wt% of Au through the photodeposition (P, green curves) or the deposition-precipitation (DP, red curves) methods.

The actual deposition of noble metal nanoparticles over the surface of titanium dioxide materials was also confirmed through HR-TEM imaging, which clearly illustrates the deposition of finely dispersed and spherically shaped Au nanoparticles over the surface of all the investigated specimens (Figure 4.3.9 - Figure 4.3.11)

Figure 4.3.9 shows TEM images recorded on D0_500_DP. As can be seen, the powder is characterized by small, highly agglomerated spherical-shaped TiO_2 crystallites with average size of about 10-20 nm (Figure 4.3.9a). This result is consistent with the average crystallite size calculated by applying the Scherrer equation to XRPD analysis (Table 4.3.1). Interestingly, noble metal nanoparticles immediately appear to be highly diluted on the sample surface, especially when compared with images acquired for the DX_Y_DP series samples (Figure 4.3.10 and Figure

4.3.11). This may be ascribed to the relative higher SSA of D0_500 powder, compared DX_700 samples, thus leading to a relatively lower Au NPs surface concentration.

The lower Au surface concentration achieved with the D0_500_DP material may be at the origin of the different plasmon resonance absorption band intensity compared to that exhibited by other DX_Y_DP materials (Figure 4.3.6), regardless of the same Au nanoparticles loading, as evidenced by ICP-OES analysis reported in Table 4.3.3.

Unfortunately, TEM images of D0_500_P were characterized by a not sufficient amount of observable noble metal nanoparticles to perform a statistical investigation of the average size of the deposited nanoparticles, thus not allowing to ascertain if and how the lower calcination temperature of undoped TiO_2 influenced the properties of Au NPs deposited through the photodeposition method.

In line with the calculated average crystallites dimensions obtained through XRPD analysis (Table 4.3.1), TEM images of D18_700, D50_700 and D80_700 materials (Figure 4.3.9 - Figure 4.3.11) confirmed the presence of TiO_2 grains with ca. 40-50 nm mean diameter, being larger with respect to that attained in the case of the reference D0_500 sample. At the same time, due to their relatively lower SSA, all doped materials exhibited a higher Au NPs surface concentration compared to the undoped Au-modified D0_500 photocatalyst.

More importantly, thanks to TEM analysis we were also able to better evaluate the effective Au NPs size distribution by means of counting methods.

In particular, we observed that DP-modified materials exhibited a progressive Au NPs average size increase with increasing dopant amount included in the bulk structure of titanium dioxide (and thus with increasing the average size of TiO_2 nanoparticles, Table 4.3.1), i.e. passing from ca. 6 nm to ca. 13 nm for reference undoped D0_500_DP and highly doped D80_700_DP, respectively. Differently, the average size of Au nanoparticles deposited through the photoreduction method resulted to be independent of the relative dopant amount included within the TiO_2 powders. Thus, differently from the DP method, photodeposition allowed us to obtain noble metal nanoparticles with the same average size regardless of the intrinsic properties of the starting support. The uniformity in the average size of the photodeposited Au nanoparticles, however, was unexpected. In fact, a previous work on photodeposited Au nanoparticles on N,F-doped titania carried out in our research group[21] clearly illustrated that the average size of Au NPs deposited via photoreduction was indeed influenced by the dopant amount included within the support, with doped materials allowing for the photodeposition and growth of smaller nanoparticles compared

to reference undoped titanium dioxide. Such effect was ascribed to the influence of dopant-induced electron trap states on the nucleation and growth mechanism of Au NPs, which reasonably grew in the proximity of such electron trap states during photodeposition, and closely interacting with them. In contrast, in this case, we observed a uniformity in the average sizes of the photodeposited Au nanoparticles, regardless of the dopant content within the titanium dioxide structure. This possibly suggests that the nanoparticles in this study were not grown in close proximity to or closely interacting with electron trap states, as observed in the aforementioned research work.

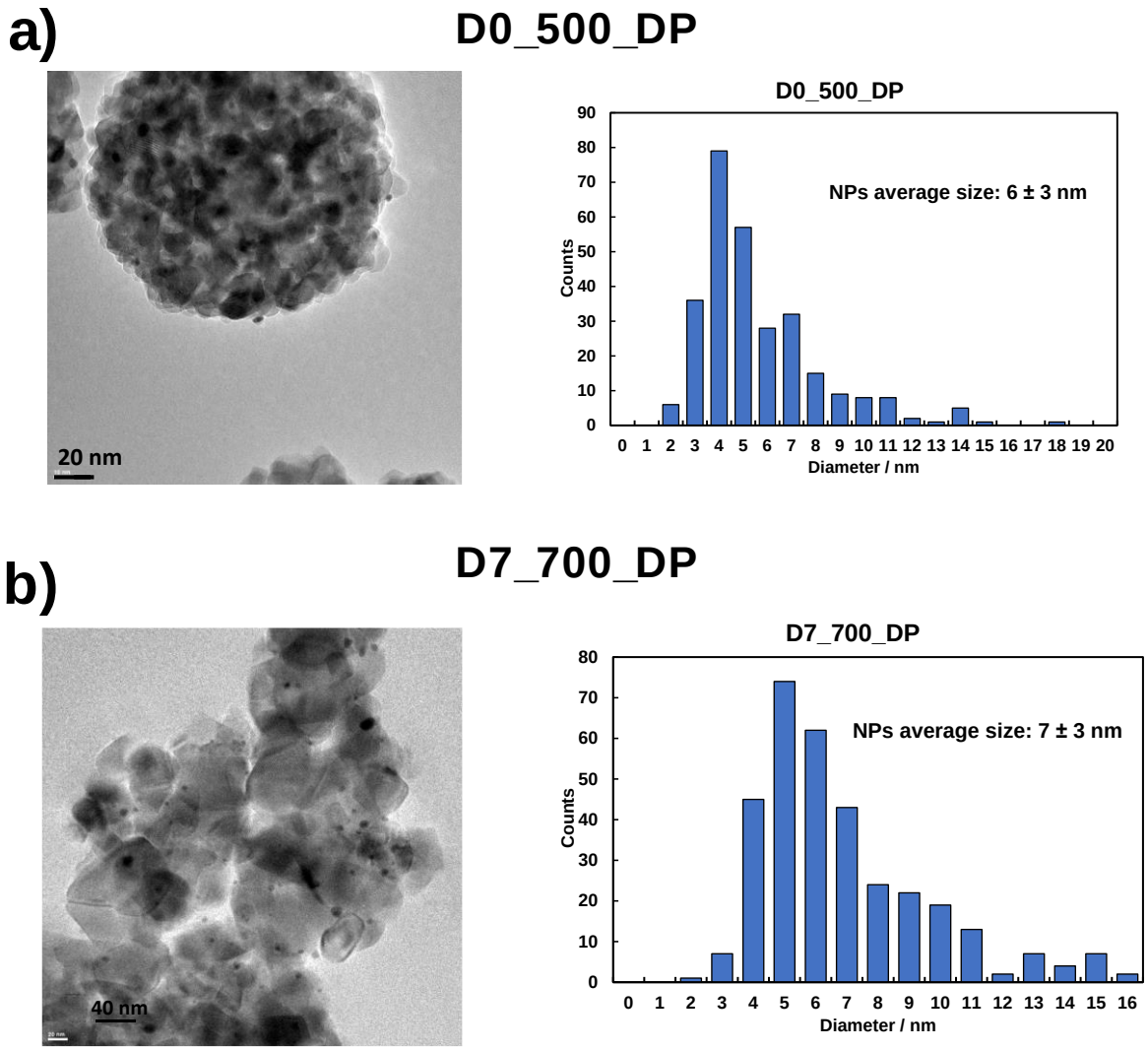

Figure 4.3.9: Transition Electron Microscopy imaging and Au nanoparticles diameter distribution of D0_500_DP (a) and D7_700_DP (b) materials. The total Au NPs counts ranged from 300 to 500 counts.

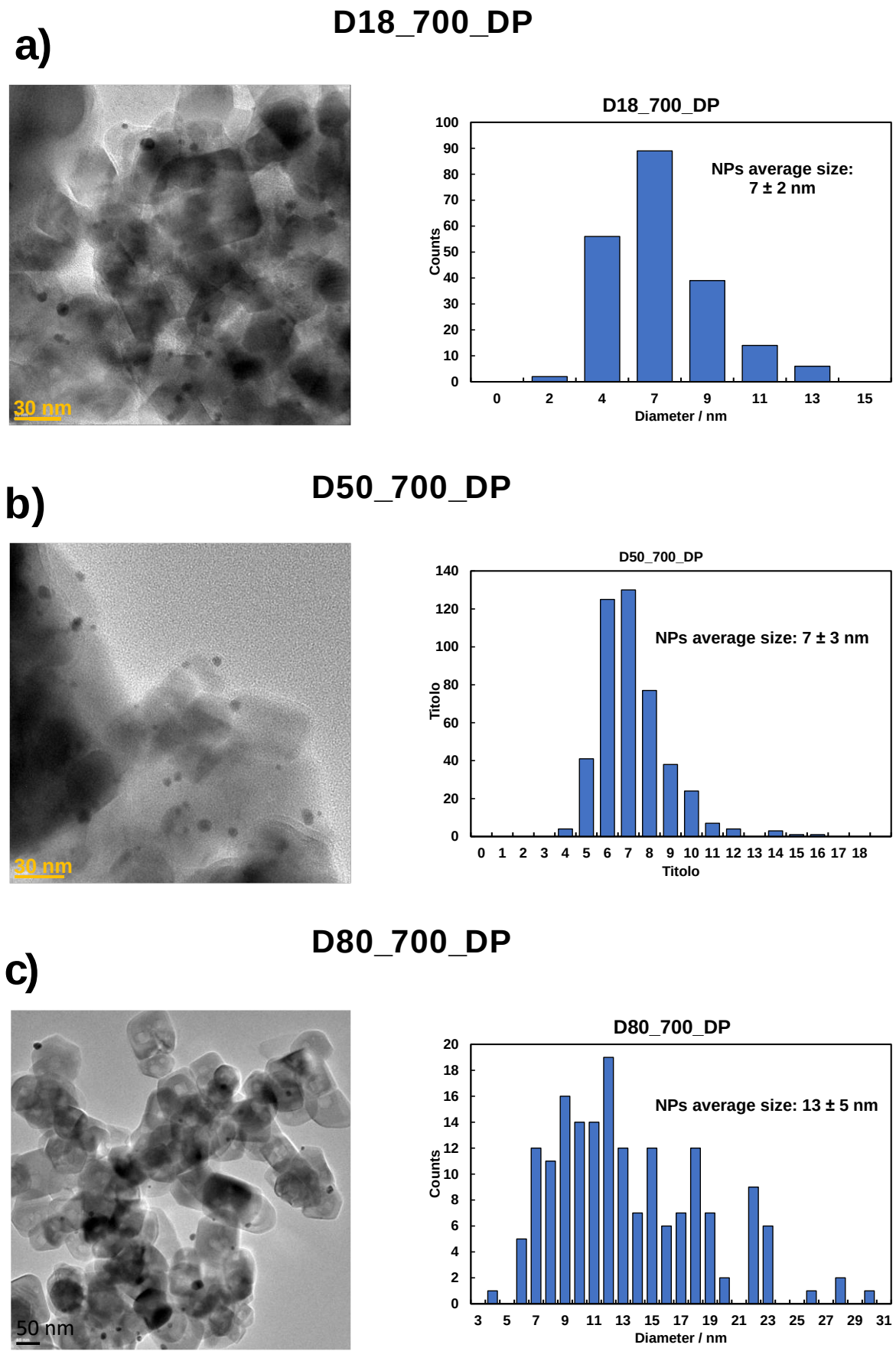

Figure 4.3.10: Transition Electron Microscopy imaging and Au nanoparticles diameter distribution of D18_700_DP (a), D50_700_DP (b) and D80_700_DP (c) materials. The total Au NPs counts ranged from 300 to 500 counts.

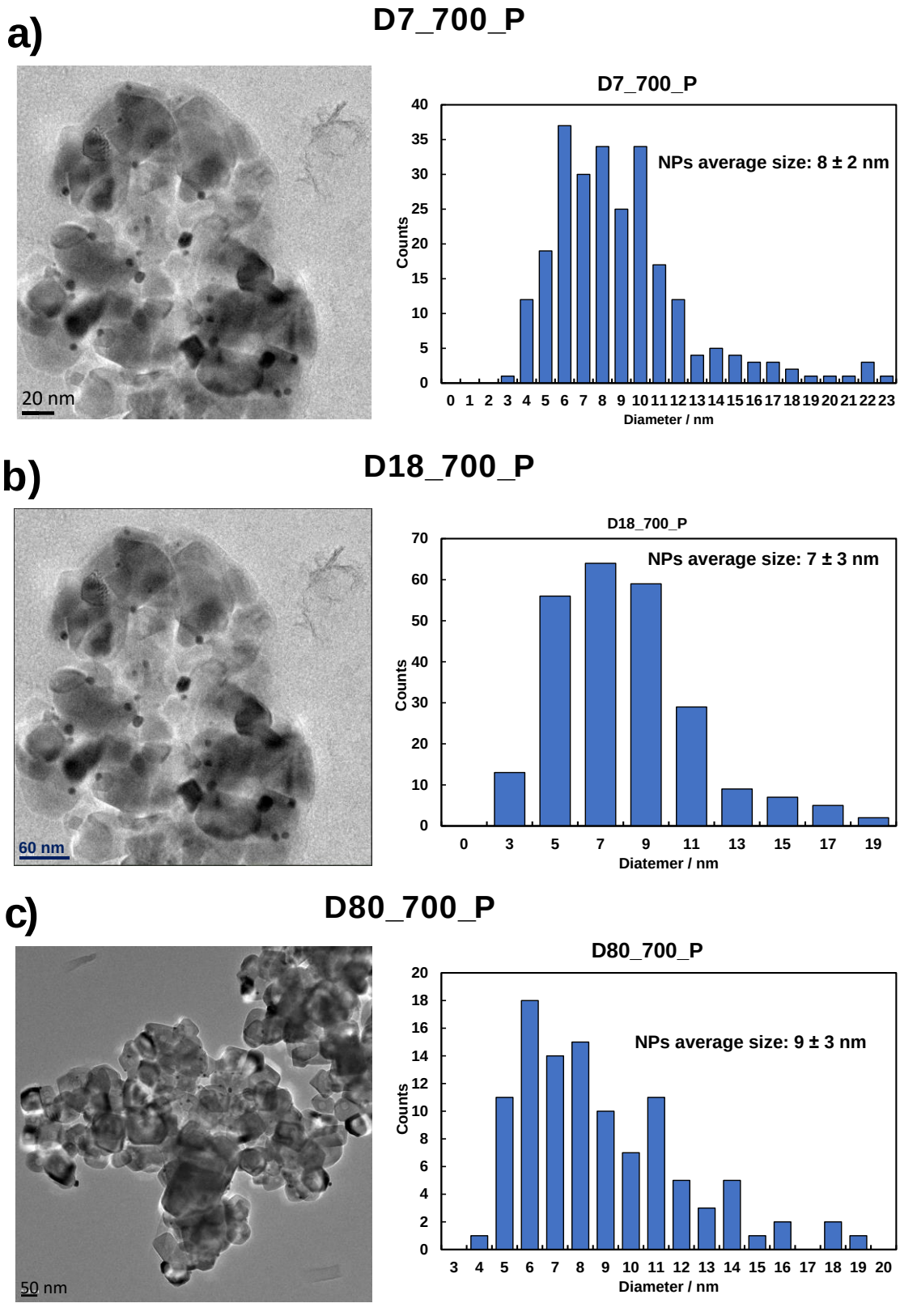

Figure 4.3.11: Transition Electron Microscopy imaging and Au nanoparticles diameter distribution of D7_700_P (a), D18_700_P (b) and D80_700_P (c) materials. The total Au NPs counts ranged from 300 to 500 counts.

4.3.2 Materials Photoactivity

4.3.2.1 Photocatalytic oxidation of Formic Acid

The photocatalytic activity of the materials was firstly screened in the photocatalytic oxidation of formic acid (FA), a test reaction chosen for its robustness and simplicity of the degradation path, occurring via a single-step direct oxidation only, with no formation of stable intermediates possibly interfering during the degradation run (more in-detail discussion on formic acid oxidation is provided in section 3.1, page 93). The photoactivity of the materials was firstly tested by employing a 0.1 g m^{-3} photocatalyst concentration and the zeroth-order rate constants (k_{For}) for the photocatalytic oxidation of formic acid attained under such experimental conditions with both metal-free and Au-containing samples are reported in Figure 4.3.12.

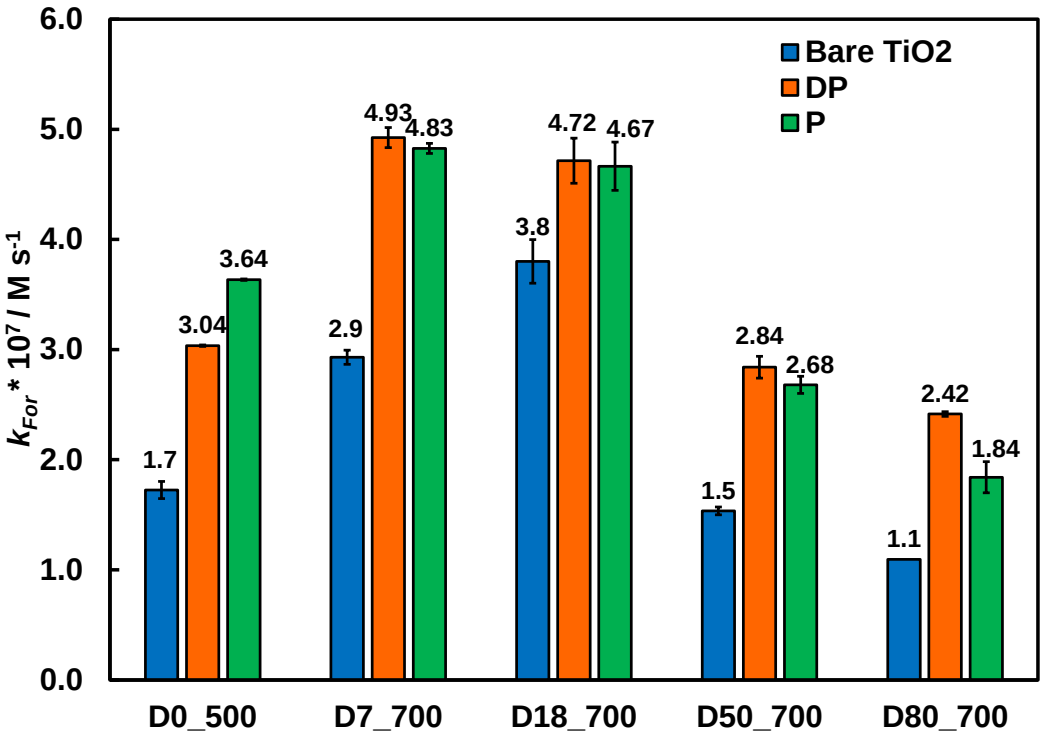

Figure 4.3.12: Pseudo-zero-order rate constants for photocatalytic oxidation of formic acid with differently N,F-doped TiO_2 powders calcined at 500 or 700 °C (blue bars) and their corresponding 0.5 wt% Au-modified materials prepared through the deposition-precipitation (orange bars) or the photoreduction (green bars) deposition routes. TiO_2 concentration: 0.1 g dm^{-3}.

A volcano shaped trend of the zeroth-order kinetic rate constant for the photocatalytic oxidation of formic acid is generally observed with increasing the nominal dopant content, with a photoactivity maximum for relatively low doped photocatalyst (ca. 5% of F/Ti molar ratio), as reported by previous works.[22] Though being perfectly in line with such expectation, in the present case the highest photoactivity in FA oxidation has been attained with the D18_700 sample, i.e. exhibiting a slightly larger amount of dopant source. This variation may be ascribed to the here

adopted harsher synthetic conditions, i.e. the higher vacuum applied in the solvent removal step of the sol-gel synthesis possibly resulting in a higher removal of fluoride anions from the liquid phase with a consequent lower dopants incorporation in the TiO_2 bulk structure compared to previous works. In fact, the sol-gel synthesis is well known to be very susceptible to even subtle changes applied to the solvent removal step such as an increase in the vacuum pressure, affecting the overall properties of the resulting materials (section 2.1, page 43).

Surely, the introduction of a relatively low dopant content (up to a nominal F/Ti ratio equal to 18%) resulted in producing TiO_2 materials with higher photoactivity compared to the reference undoped D0_500. Differently, a further increase of dopant content determined a systematic photoactivity decrease, with both D50_700 and D80_700 samples performing even worst then the undoped D0_500 material, possibly as a consequence of the introduction of an excess of defective sites within the TiO_2 structure. In fact, as previously reported, an optimal/moderate amount of defective Ti^{3+} states, accompanied by the N,F doping, may positively act in capturing electrons photopromoted to the TiO_2 conduction band, thus resulting in a net delay of electron-hole couples recombination, as demonstrated by an increase of the average lifetime of charge carriers photogenerated on doped TiO_2 systems compared to the undoped ones.[12]

The presence of an excess concentration of bulk defects may instead act as detrimental photogenerated charge recombination centers, with a consequent decrease of the overall photocatalytic reaction rate.[35] At the same time, a further increase of fluorine-containing dopant source employed during the synthesis could also result in a higher degree of substitution of surface hydroxyl groups by fluoride anions, which could eventually interfere with the adsorption of FA molecules on the photocatalyst surface with a consequent substrate photodegradation rate decrease, as the investigated reaction mainly proceeds via the direct interaction of adsorbed formic acid with holes photogenerated on the photocatalyst surface.[45]

Concerning the undoped D0_500 sample, we should correlate its quite satisfying FA mineralization photoactivity to the relatively high specific surface area (SSA), being ca. 4-5 times larger than that of all doped samples calcined at 700 °C (Table 4.3.2). In fact, a photocatalyst exposing a significantly higher specific surface area is expected to be intrinsically characterized by a larger number of active sites, able to adsorb larger amounts of substrates to be photocatalytically oxidized.

Indeed, the normalization of the kinetic rate constant with respect to the specific surface area of each photocatalyst may provide better insights on the effective/intrinsic role played by N,F

doping on overall TiO_2 photoactivity. The SSA-normalized FA oxidation rate constants attained with the investigated materials can be compared in Figure 4.3.13.

Interestingly, in this way we can observe that all doped TiO_2 materials outperform the undoped one, i.e. N,F-doping coupled with high calcination temperature possibly being beneficial in favoring TiO_2 charge carriers separation on the whole investigated dopant content range (7-80 at%)

At the same time, Au-containing D7_700 materials exhibited the highest SSA-normalized rate constants for the photocatalytic degradation of formic acid.

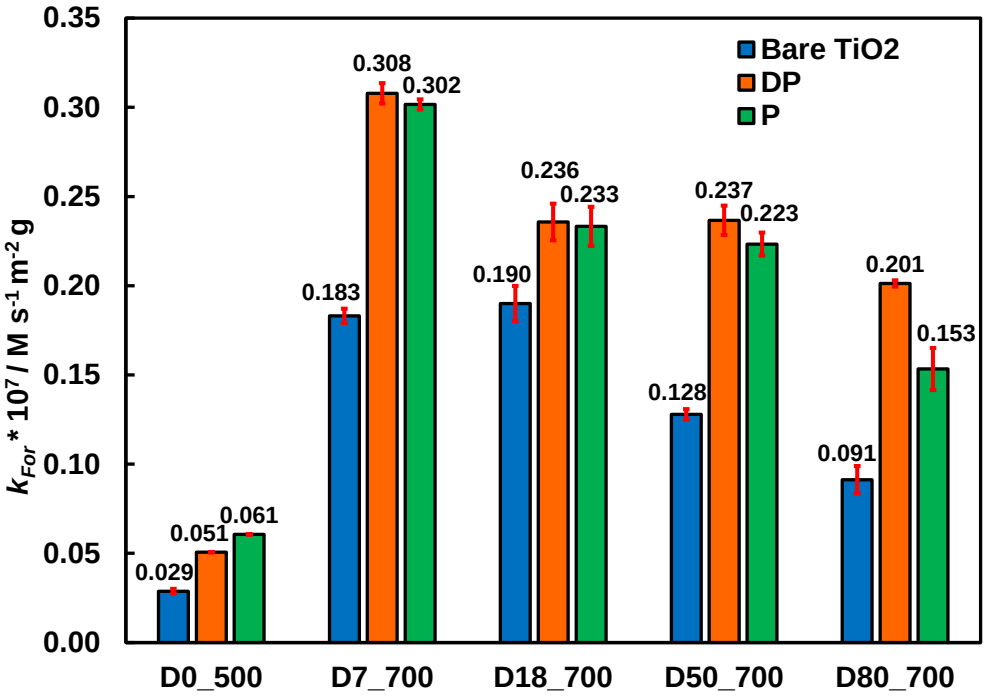

Figure 4.3.13: SSA normalized pseudo-zeroth order rate constants for formic acid photocatalytic oxidation with differently N,F-doped TiO_2 powders calcined at 500 or 700 °C (blue bars) and their corresponding 0.5 wt% Au-modified materials prepared through the deposition-precipitation (orange bare) or the photoreduction (green bars) deposition routes. TiO_2 concentration: 0.1 g dm^{-3}.

As expected, all Au-containing materials resulted to be more photoactive than the corresponding bare TiO_2. Nevertheless, apart from the heavily doped D80_700 material, which most benefitted from the use of the DP compared to the P method, no significant photoactivity differences were observed by changing the adopted Au NPs deposition methods.

This preliminary finding attained in the photocatalytic degradation of formic acid may indirectly suggest that no specific synergistic mechanism occur between Ti^{3+} states, introduced by N,F doping, and Au NPs, which are instead expected to be anchored in their proximity by means of the selective photodeposition (P) method.

Thus, we decided to search for alternative strategies aimed at probing if and how the use of different Au nanoparticles deposition methods (DP or P) may specifically affect the photoactivity of the resulting Au/TiO_2 composites.

We firstly decided to explore potential effects induced on photoactivity by lowering the photocatalyst content in suspension. In this way, we should expect that by diminishing the exposure of photocatalytic active sites (provided by a lower TiO_2 amount), the overall photoactivity rate may be mainly affected by intrinsic charge recombination phenomena instead of mass diffusion-related effects (possibly related to a non-sufficiently fast replenishment of the adsorbed substrate at the surface of the semiconductor photocatalyst under illumination conditions). In these new experimental conditions, we thus would try to better unveil potential photoactivity variations among the differently prepared Au-modified samples.

Therefore, we fixed the photocatalyst concentration at 0.063 g dm^{-3} and checked the photoactivity of formic acid degradation with both bare and Au-containing photocatalysts belonging to the D0_500, D7_700 and D_80_700 series samples. In this way we can monitor the Au deposition effects on photoactivity of undoped, slightly and heavily doped systems.

The so obtained and SSA-normalized zero-order rate constants for formic acid oxidation with the selected samples are reported in Figure 4.3.14. In particular, within each series sample, DP- and P- materials exhibited pretty similar rate constants of formic acid degradation. Thus, diluting the photocatalyst concentration did not allow to unveil any significant Au NPs deposition-induced effect on the materials photoactivity in the investigated test reaction.

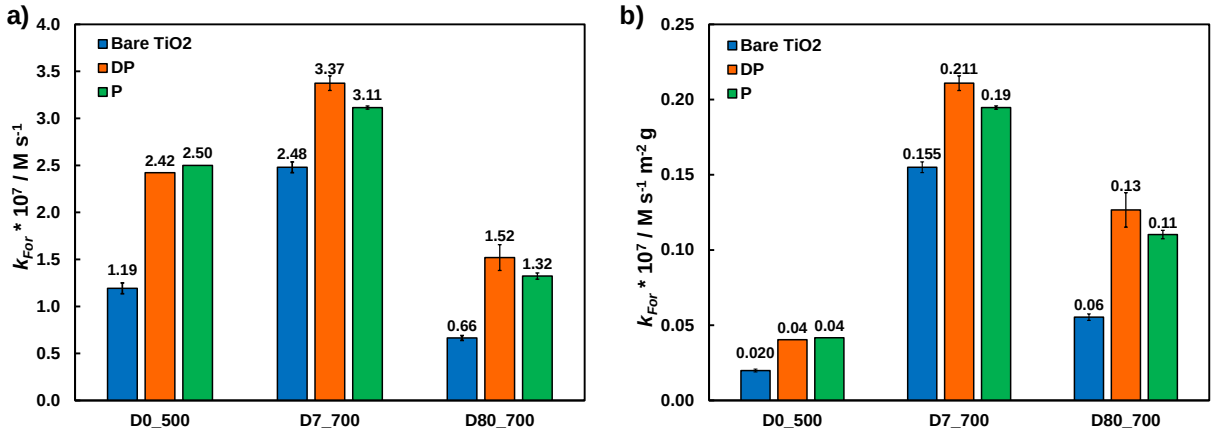

Figure 4.3.14: Formic acid photocatalytic oxidation pseudo-zeroth rate constants (a) and SSA normalized rate constants (b) of differently N,F-doped TiO_2 powders calcined at 500 or 700 °C (blue bars) and their corresponding 0.5 wt% Au-modified materials prepared through the deposition-precipitation (orange bars) or the photoreduction (green bars) deposition routes. TiO_2 concentration: 0.063 g dm^{-3}.

Next, we decided to investigate possible effects induced on N,F-doped TiO_2 properties by using a different light source during the Au NPs photodeposition route. In fact, the relatively low emission intensity in the highly energetic UV region provided by the OSRAM Power Ball lamp (employed for the preparation of P-modified materials as reported in section 2.4.1, page 56) may determine the generation of a relatively low extent of electron-hole pairs on TiO_2 surface, which may thus interfere on the effective fixation of Au NPs in the proximity of Ti^{3+} sites, generally acting as efficient Au NPs nucleation centers.

In particular, we decided to use a light source with a more intense UV emission (previously employed in our research group for similar experiments[42]) to modify the D7_700 sample, which is expected to be characterized by a more efficient charge carrier separation positively affecting the resultant Au NPs photodeposition on its surface.

The so-prepared specimen, labelled as UV_D7_700_P, was prepared by photodeposition starting from 10 a vol% methanol–water suspension containing 3 g dm^{-3} of D7_700 and the amount of NM precursor, $HAuCl_4$, necessary to obtain a fixed nominal metal loading of 0.5 wt%. Au(III) photoreduction to metallic nanoparticles on the oxide surface was achieved by irradiating the suspension for 2 h under nitrogen atmosphere with an immersion fluorescent, low pressure mercury arc lamp (Jelosil) emitting in the 300–400 nm range, with a maximum emission peak at 360 nm. UV_D7_700_P was recovered after at least three centrifugation and washing cycles with water, up to the complete removal of residual ions and organic precursors. Then, it was dried at 70 °C for one day and stored in the absence of light and humidity. Additional information on the properties of UV_D7_700_P are provided in the appendix section (page 160) of this chapter. In particular, the Au NPs deposited on UV_D7_700_P resulted to be very similar, either in content and size distribution, to those anchored onto the D7_700_P photocatalysts.

The photoactivity of UV_D7_700_P, was investigated in formic acid oxidation with a photocatalyst concentration equal to 0.063 g dm^{-3} and the resultant zero-order rate constant can be compared to those attained under the same experimental conditions by D7_700 and D7_700_P samples in Figure 4.3.15. Surprisingly, neither the use of a possibly more suitable light source during the Au NPs photodeposition route led to appreciable photoactivity improvements in formic acid oxidation attributable to peculiar interplays between TiO_2 structural defectivity and nucleation/fixation of Au nanoparticles.

Based on these results and by taking into account the main role played by noble metal nanoparticles in scavenging photogenerated electrons and thus to act as efficient co-catalyst species in reductive photocatalytic reaction, we supposed that the considered FA oxidation test reaction

may not be so suitable for our investigation purposes, so to unveil potential synergic effects occurring between Ti^{3+} defective states and selectively deposited Au NPs. Therefore, we decided to systematically study the activity of the home-made Au/TiO_2 samples on Cr(VI) photoreduction, i.e. a photocatalytic process mainly proceeding via a direct reductive pathway.

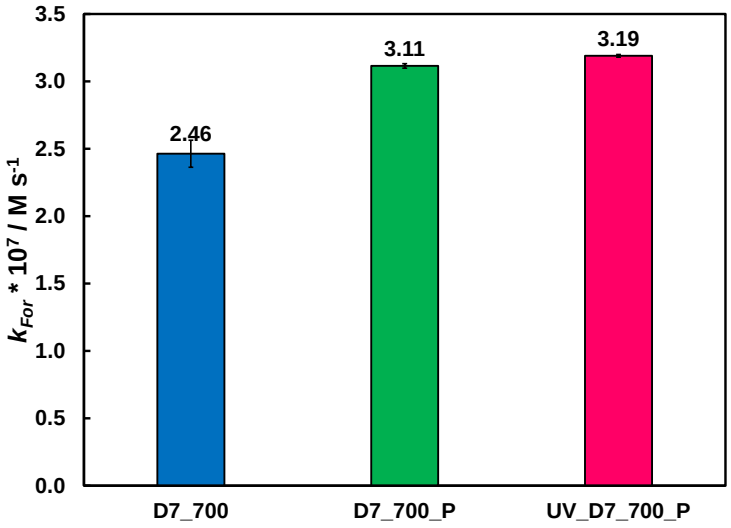

Figure 4.3.15: Photocatalytic formic acid oxidation rate constants for bare D7_700 N,F-doped titanium dioxide (blue bar) and D7_700 materials modified with 0.5 wt% of Au through photodeposition employing the OSRAM Power Ball light source (D7_700_P, green bar) and an alternative light source, mainly emitting in the UV component (pink bar, UV_D7_700_P).

4.3.2.2 Cr(VI) photocatalytic reduction

The photocatalytic activity of the materials has thus been checked also in the photocatalytic reduction of Cr(VI) ions at pH = 3.7, occurring according to a first-order rate law. In particular, the calculated specific surface area-normalized photocatalytic reaction rates, collected in Figure 4.3.16, evidence the typical bell-shaped trend, in line to what observed in the photocatalytic oxidation of formic acid. More interestingly, in this case, D7_700_P sample clearly exhibits an outstanding photoactivity.

Moreover, for the here investigated photoreduction test reaction, appreciable photoactivity differences are induced by either the adopted Au NPs deposition method and the relative TiO_2 dopant content. In fact, by considering the calculated photoactivity improvement ratios attained upon Au NPs deposition (Figure 4.3.17), while the undoped D0_500 sample exhibits similar k_{Au}/k for both DP and P methods, the Au NPs photodeposition route seemed to enable the relatively highest photoactivity increase (compared to the DP one) only in the case of the low doped D7 sample. By far greater photoactivity improvements have been attained upon Au NPs deposition for the D80 sample, especially by employing the DP technique.

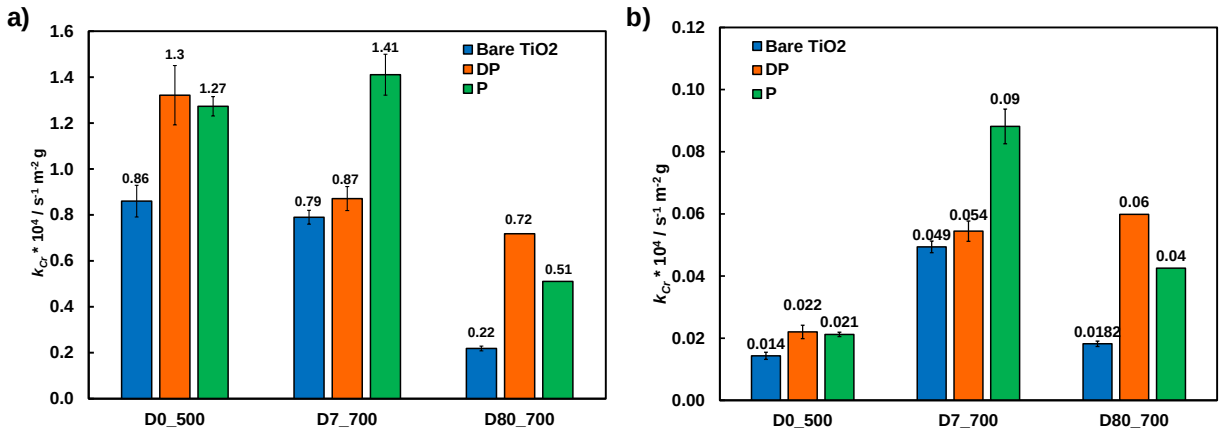

Figure 4.3.16: Cr(VI) photocatalytic reduction pseudo-first order rate constants (a) and SSA normalized rate constants (b) of differently N,F-doped TiO_2 powders calcined at 500 or 700 °C (blue bars) and their corresponding 0.5 wt% Au-modified materials prepared through the deposition-precipitation (orange bars) or the photoreduction (green bars) deposition routes.

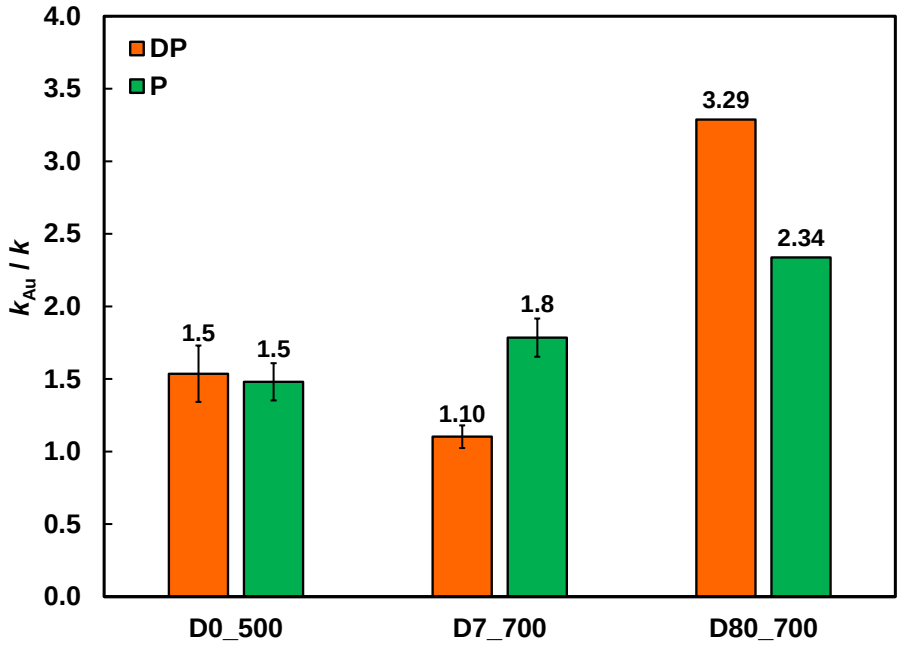

Figure 4.3.17: Photocatalytic activity improvement ratio of DP- (orange bars) and P- (green bars) Au-modified N,F-doped TiO_2 samples in the photocatalytic reduction of Cr(VI) ions.

The obtained results may unveil the presence of specific effects possibly occurring between the dopant induced defective TiO_2 structure and the adopted noble metal nanoparticles surface deposition. In particular, the photodeposition method seems to positively exploit the intrinsic defective structure of the D7 material, resulting in an excellent charge separation efficiency. Au NPs may thus selectively anchor on its surface and consequently open a new efficient electron transfer path from the TiO_2 defective trap states to the adsorbed dichromate ions undergoing reduction.

Differently, the D80 sample, showing a relatively poor charge separation ability, exhibits a relative more marked photoactivity increase only upon Au NPs deposition by means of the unspecific deposition-precipitation DP method (with a k_{Au}/k equal to ca. 3.3). Finally, the absence of defective trap states in reference undoped D0_500 did not produce any significant variation in the photoactivity improvement ratios attained with both DP or P methods, suggesting that specific/peculiar effects produced by Au NPs (photo)deposition may be mostly attained with TiO_2 materials clearly exhibiting a defective crystalline structure. It is important to note, moreover, that such preferential efficient electron transfer path have been observed only when the investigated test reaction proceeded through a reductive path, but not through an oxidative step, such as in the case of formic acid oxidation. Thus, the combination of Au NM NPs deposition through photoreduction and the intrinsic titanium dioxide bulk defectivity results to be most effective as a titanium dioxide photoefficiency improvement strategy when the materials are to be employed in photocatalytic processes mainly proceeding via a reductive reaction path.

To better understand the origin of the improved photoactivity of titanium dioxide upon introducing defective Ti^{3+} states within its electronic structure, as well as the different behavior upon the use of two different Au nanoparticles deposition techniques on the photoactivity attained for the Cr(VI) photocatalytic reduction with differently N,F-doped TiO_2 powders, we decided to investigate the photoluminescent properties of the prepared materials through photoluminescence spectroscopy analysis. Such technique, in fact, being able to provide useful information on the dynamics of radiative decay paths in photoexcited semiconductors,[46-51] may allow to gather information on the presence of specific electron transfer paths occurring between defective TiO_2 states and differently deposited Au metal nanoparticles, possibly significantly deepening the understanding of the photogenerated charge carriers dynamics of the prepared materials under illumination conditions.

4.3.3 Photoluminescence Spectroscopy Analysis

4.3.3.1 Investigation of the sample preparation method

Before acquiring photoluminescence (PL) spectroscopy data, preliminary studies aimed at understanding the optimal sample preparation route allowing to obtain the most reliable results were conducted. In fact, investigations on the photoluminescent properties of TiO_2 powders were previously performed in our research group by compressing the photocatalysts powders in the form of small, thin, circular pellets.[21,22] However, in the present work, such sample preparation technique led to unreliable results, especially concerning the reproducibility in terms of PL emission intensity. The homogeneity of the pellets originally prepared for a first set of

measurements was thus initially evaluated using a home-made microscopy imaging system held in Politecnico of Milano, in which macroscopic spots of the samples were excited using a 350 nm pulsed laser. This way, the overall photoluminescence intensity of the whole pellets (and not only isolated pellets spots with the laser beam size), can be macroscopically monitored. Unfortunately, this technique resulted to be not capable of detecting any major non-uniformity in the PL emission of the pellets due to the low emission intensity of the samples, requiring long exposure times for the acquisition of low PL emission intensity, especially in the case of Au-modified titanium dioxide (Figure 4.3.18).

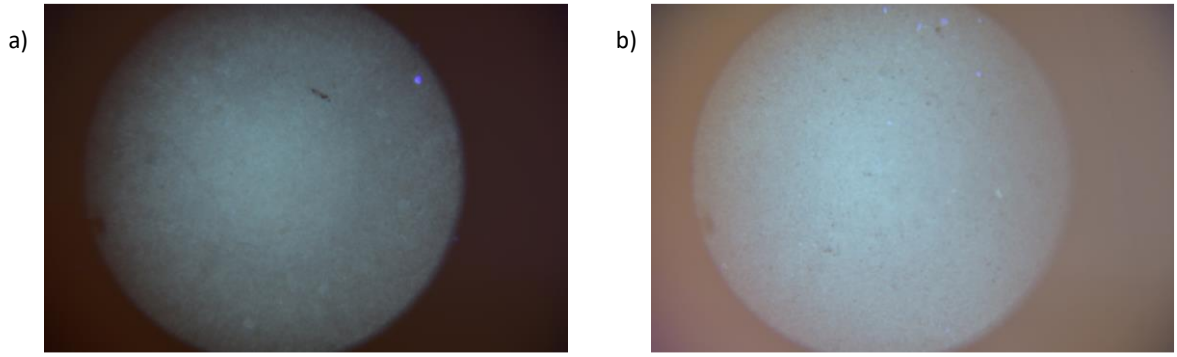

Figure 4.3.18: Fluorescence microscopy images of D7_700 (a) and D7_700_DP (b) samples. Brighter spots were attributed to emission deriving from the presence of adventitious impurities on the pellets.

Regardless, pellets of the metal-modified powders presented eye-detectable differently coloured regions, ranging from deep purple to light pink. In particular, the PL signal intensity was found to dramatically change by exciting the pellet in a relatively brighter or darker region through laser spot excitation (Figure 4.3.20 a). Differently, when the powders were directly deposited in home-made sample holders in the form of thick, dense films of the same height (analogous to the sample preparation technique commonly employed during XRPD or UV-Vis DRS analyses), the reproducibility in emission intensity resulted to be immensely improved, as illustrated by the astonishing reproducibility in PL emission intensity obtained when acquiring spectra in multiple randomly-chosen spots over the whole exposed surface of the sample holder (Figure 4.3.20 b). Thus, throughout this study, the previous pellet preparation route was discarded and all the PL spectroscopy analyses were carried out on powders directly placed in home-made sample holders, developed within this project (Figure 4.3.19).

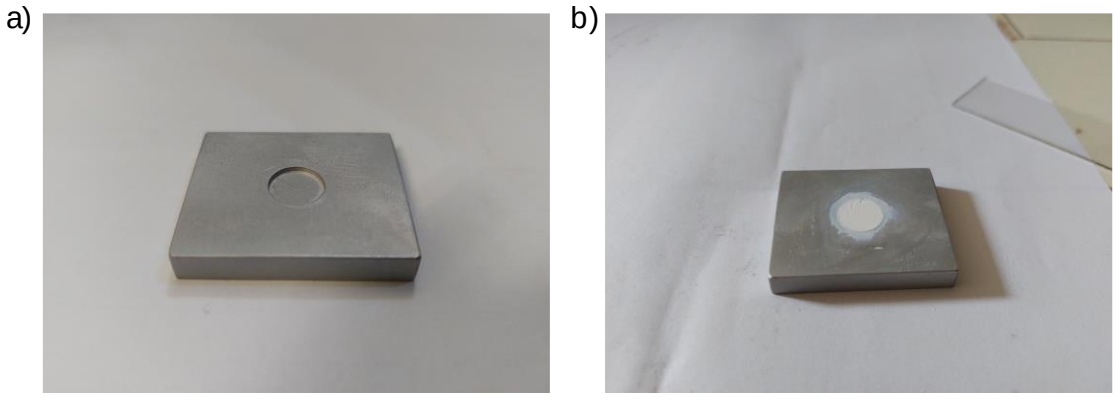

Figure 4.3.19: Picture of the empty (a) and filled (b) PL sample holder.

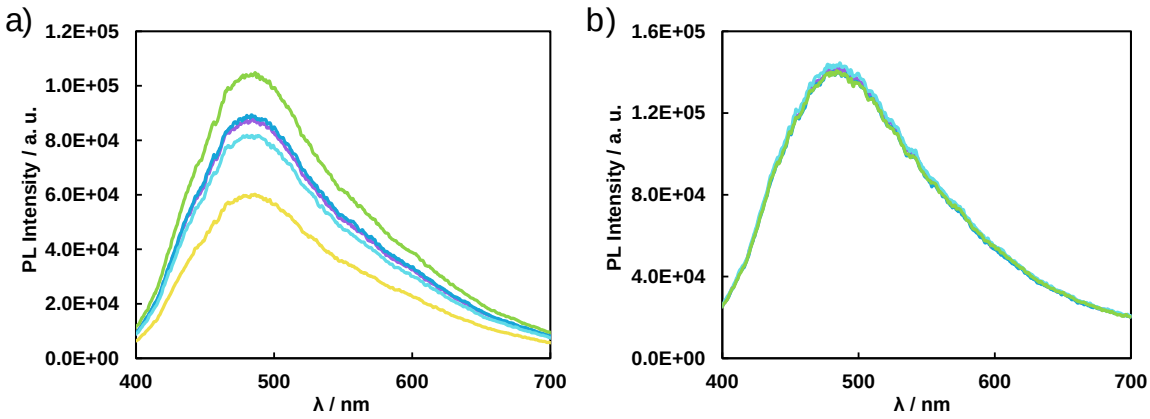

Figure 4.3.20: Intensity of photoluminescent emission of the D0_700_P sample acquired in a bright spot (green) and in a dark spot (yellow) of the pellet (a); Intensity of PL emission acquired in five different random spots of the same sample prepared in the form of a thick, dense film in the home-made sample holder (b).

4.3.3.2 Photoluminescence spectroscopy of N,F-doped metal-free TiO_2

Photoluminescence (PL) emission intensities under steady-state irradiation conditions obtained with the DX_Y series samples were firstly compared to observe if and how the powders radiative emission properties depend on the relative dopant amount included within the bulk structure of the metal oxide semiconductor.

As expected, the intensity of the PL signal resulted to be deeply affected by the amount of dopant included within the specimens (Figure 4.3.21a). In particular, remarkably high PL intensity has been observed in the case of the D7_700 sample, such emission profile becoming progressively less intense with increasing the dopant content. Most notably, the integrated area underneath the emission profiles trend as a function of the dopant content (Figure 4.3.21b) somewhat resembled that observed in the case of SSA normalized kinetic rate constants in both formic acid oxidation and Cr(VI) photocatalytic reduction (Figure 4.3.14, Figure 4.3.16), *i.e.*, the observed photoluminescent emission resulted to be beneficial for the photoactivity of the materials in both test reactions, with most emitting specimens characterized by the highest photoefficiency.

Moreover, the PL emission of doped samples always resulted to be much more intense compared to that of the undoped materials.

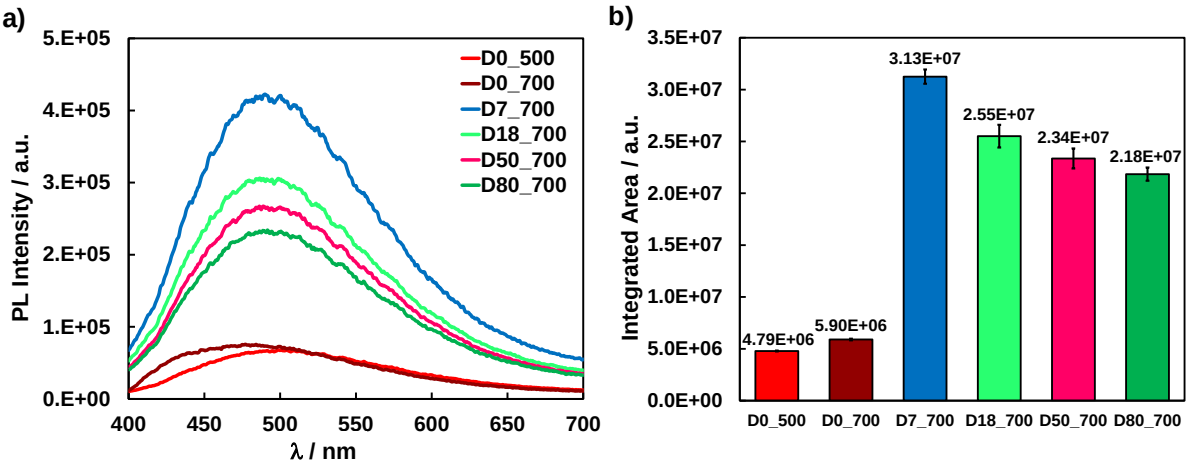

Figure 4.3.21: Steady-state photoluminescence emission spectra (a) and integrated intensity (b) of metal-free N,F-doped titanium dioxide materials.

The photoluminescent emission of N,F-doped anatase, which has already been extensively rationalized and explained by our research group for similar materials,[22] cannot be attributed to the the direct recombination of electrons photoexcited into the TiO_2 conduction band with holes photogenerated in TiO_2 valence band, such radiative emission being very weak at room temperature due to the indirect band gap nature of the TiO_2 semiconductor. As electronic transitions in indirect band gap semiconductors must respect the selection rule of momentum conservation, electronic excitations from the top of the valence band to the bottom of the conduction band in anatase must always be assisted by a phonon. It follows that since the intervention of a phonon in electronic transitions renders such band-edge emission orders of magnitude less efficient compared to direct band gap semiconductors,[52] the photon emission originating from the direct recombination of electrons from the conduction band of titanium dioxide with valence band holes is mostly of very weak intensity. Moreover, in the case of doped materials, the energetic positioning of the maximum PL emission intensity, located around 2.5 eV, is bathochromically shifted compared to the anatase band gap, usually located around 3.2 eV.[53] Thus, it is not energetically compatible with a direct band gap recombination emission.

On the other hand, relaxed selection rules for localized defect states permit the radiative recombination of trapped electrons and holes. The spectrum and intensity of PL signals are thus mainly related to the presence of surface traps induced by defective TiO_2 crystal structures.[22] Since the main effect of O^{2-} lattice substitution with fluoride anions is that of introducing Ti^{3+} defect states in the material,[34] an increase in the PL signal is thus obtained upon doping. Excessive

amounts of doping, however, could induce bulk charge carrier recombination before electrons can populate luminescent trap states at the surface of the material,[35] and therefore a reduction in the PL intensity is observed.

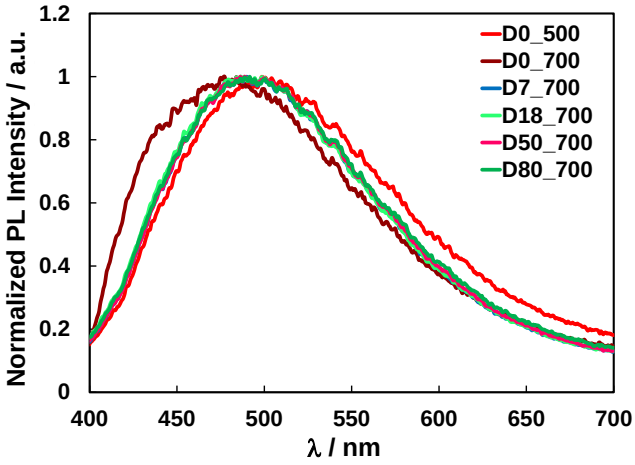

Figure 4.3.22: Normalized PL emission spectra of differently N,F-doped titanium dioxide samples.

Normalized PL spectra (Figure 4.3.22) illustrate that the emission profile of all samples is almost superimposable, indicating that the origin of the PL emission is similar for each doped metal oxide powder, except for the D0_700, exhibiting a slightly blue-shifted maximum of PL emission. This difference in the emission profile is easily accountable to its different phase composition, D0_700 being composed mainly of rutile, while all other samples are composed of pure anatase (Table 4.3.1).

For all investigated materials, the temporal evolution of the integrated intensity of PL emission between 450-550 nm was then gathered via Time-Resolved Photoluminescence Spectroscopy (TRPL) with pulsed laser excitation and the results obtained in terms of normalized intensity decay curves can be directly compared in Figure 4.3.23.

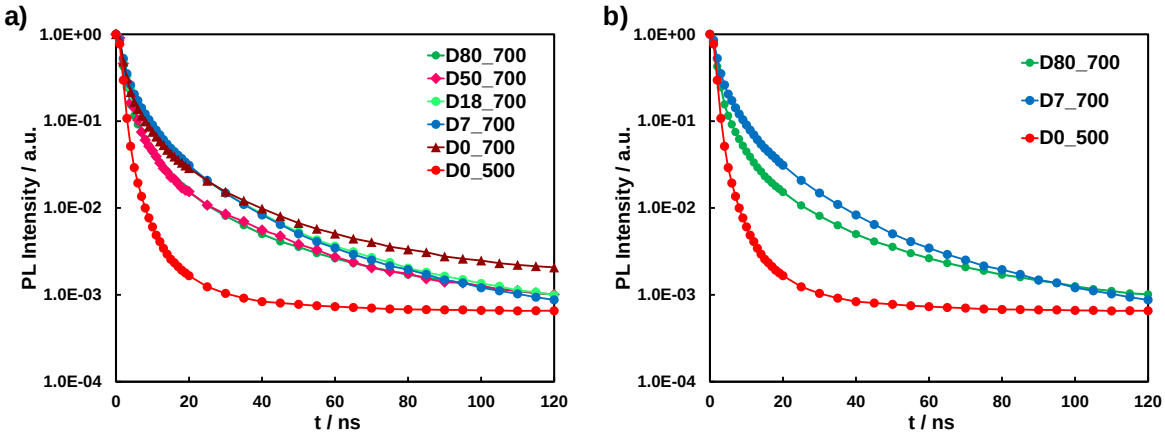

Figure 4.3.23: Temporal evolution of the integrated intensity of PL emission between 450-550 nm of differently N,F-doped titanium dioxide specimens (a). Temporal evolution of the integrated intensity of PL emission between 450-550 nm of selected mostly significant N,F-doped titanium dioxide specimens (b).

By looking at the decay curves, it is possible to notice at a first glance that the photoluminescence signal of the fully anatase composed reference undoped D0_500 is characterized not only by a much weaker photoluminescent emission under steady-state

conditions, but also by a much faster decay kinetics of the PL emission compared to all the N,F-doped materials. As in the case of steady state photoluminescent emission, the samples characterized by the most intense emission and better photoefficiency were also characterized by a longer lasting photoluminescent emission. In fact, the less doped and better performing D7_700 and D18_700 materials are characterized by the most intense and longer lasting photoluminescent emission, followed by the highly doped D50_700 and D80_700 samples, and then by the reference undoped D0_500 sample. Such trend becomes even clearer when considering the decay curves of the selected mostly relevant samples only (Figure 4.3.23b).

The behaviour of the reference undoped material calcined at 700 °C, D0_700, is quite peculiar, such material being characterized by the longest lasting PL emission despite its poor photoefficiency in formic acid oxidation and the low intensity of its photoluminescent emission. The difference in the behaviour of the temporal evolution of the PL emission compared to other DX_Y samples, however, can be easily attributed to its different phase composition, i.e., being the only sample characterized by a mixed anatase-rutile phase composition, mainly composed of rutile (Table 4.3.1). Such strikingly different behaviour in its PL emission further supports the previously mentioned consideration of the material being not suitable to be compared with N,F-doped materials as reference undoped titanium dioxide, as such strikingly marked difference in its phase composition deeply affects its overall properties to the point of making very difficult if not impossible to discern the effects of doping from those deriving from changes in phase composition.

Fitting the PL decay curves according to the following triexponential decay model:

$$F(t) = \sum_{i=1}^{3} A_i \tau_i e^{-t/\tau_i}(1 - e^{-W/\tau_i}) + W_{Offset}$$

allowed us to better appreciate the effects of N,F-doping on structural TiO_2 properties, which may significantly affect the resultant overall photocatalytic activity. In fact, through such fitting, we were able to quantitatively extrapolate the most relevant parameters of the photoluminescence decay kinetics, *i.e.*, the relative population of the i-th emitting state A_i and its average lifetime τ_i. As appreciable in Table 4.3.4, the introduction of the dopant within the bulk structure of titanium dioxide did not result in significantly changing the average lifetime of the emitting states, all samples being characterized by the presence of a fast emitting state of average lifetime τ_1 around 1 ns, an intermediate living state of average lifetime τ_2 around 6 ns and a longer emitting state with an average lifetime τ_3 of about 30 ns.

On the other hand, rather than increasing the average lifetime of the emitting states, N,F-doping seems to mainly affect the relative population A_i of such trap states within the TiO_2 bulk structure. In particular, the cumulative relative population of the longer lasting emitting states, determined as $A_2 + A_3$, significantly increases when passing from the reference undoped D0_500 material to the slightly doped D7_700 material, and then progressively decrease with increasing nominal dopant content. It follows that the employment of an optimal dopant content within the titanium dioxide structure favors an efficient transfer of photoexcited electrons towards long-lasting photoluminescent Ti^{3+} trap states, where they can be efficiently trapped, with a beneficial resultant charge carrier separation and overall photoefficiency improvement.

When an excessive doping amount is introduced, however, point defect recombination limits the efficiency of such charge transfer phenomena, thus reducing the relative population of long emitting states and decreasing the overall photoefficiency of the systems.

It is also important to note, that all doped samples are characterized by a much higher population of long emitting states compared to the reference undoped D0_500 material, whose photoluminescent emission is instead characterized by the total absence of the longer lasting A_3 component and by a very low relative population of the intermediate living A_2 component.

Table 4.3.4: TRPL decay kinetics parameters for metal-free N,F-doped titanium dioxide materials.

Sample	A_1 (%)	A_2 (%)	A_3 (%)	τ_1 (ns)	τ_2 (ns)	τ_3 (ns)	$A_2 + A_3$ (%)
D0_500	99.7(1)	0.3(1)	-	1.0(1)	6.5(1)	-	0.3(1)
D0_700	95.1(1)	4.6(2)	0.3(1)	1.2(1)	6.1(2)	36(4)	4.9(2)
D7_700	92(1)	7.8(1)	0.6(1)	1.3(1)	5.6(2)	23(2)	8.4(1)
D18_700	93(1)	6.3(2)	0.4(1)	1.3(1)	6.1(3)	28(3)	6.7(2)
D50_700	97.3(1)	2.9(3)	0.8(1)	1.1(1)	5.4(2)	26(1)	3.7(3)
D80_700	96.8(1)	3.1(1)	0.1(1)	1.2(1)	5.8(2)	27(6)	3.2(1)

4.3.3.3 Photoluminescence spectroscopy of metal-modified N,F-doped TiO_2

The influence of noble metal nanoparticles deposition on the photoluminescent properties of N,F-doped titanium dioxide was investigated at first by focusing on materials modified with 0.5 wt% of Au NPs deposited through the deposition-precipitation (DP) route.

As reported in a preliminary work published by our research group,[21] the deposition of Au nanoparticles on the TiO_2 surface determined a significant PL emission intensity decrease. In fact, the formation of a metal-semiconductor interface is always accompanied by a fast and efficient transfer of photoexcited electrons from the photocatalyst's surface towards the deposited noble metal nanoparticles.[54] Au deposition, thus, introduces an additional non-radiative decay path,

which causes a rapid depopulation of the luminescent Ti^{3+} states, with a consequent reduction of the materials PL emission intensity (Figure 4.3.24).

In order to investigate if and how the extent of the observed photoluminescent emission quenching may be influenced by the relative dopant content, for each material we calculated the ratio between the integrated area underneath the emission profile of the Au-modified powder and that acquired with the corresponding unmodified sample (defined as A_{Au}/A_{Bare}). The interest towards such parameter, here better represented in terms of the so-called photoluminescence *quenching degree* (QD), defined as $\mathrm{QD} = 1 - A_{Au}/A_{Bare}$, arises from the possibility of probing the eventual presence of preferential electron exchange channels originating upon a close, synergic interaction between dopant-induced photoluminescent states and deposited Au NPs. In particular, a higher quenching degree may be diagnostic of the presence of more efficient and beneficial transfer of photoexcited electrons from Ti^{3+} states to noble metal nanoparticles.

However, as illustrated in Figure 4.3.25, all DP-modified samples exhibited very similar photoluminescence quenching degrees, being almost independent of the dopant amount introduced within the TiO_2 powders. This behaviour can be possibly ascribed to the intrinsic non-selective nature of the employed DP surface modification method. In fact, since Au nanoparticles are randomly deposited via DP on the TiO_2 surface, it is reasonable to expect that the interaction between dopant induced Ti^{3+} species and deposited Au NPs resulted to be almost unchanged for all samples, regardless of the charge carrier separation properties of the starting bare TiO_2 materials. Therefore, PL experiments did not unveil any specific and/or preferential electron transfer paths between structural defective states and Au NPs deposited by means of the DP technique. Consequently, the obtainment of similar Ti^{3+} states depopulation degree due to the photoexcited electron transfer towards Au NPs may account for the similar PL quenching degree observed for the DX_Y_DP samples.

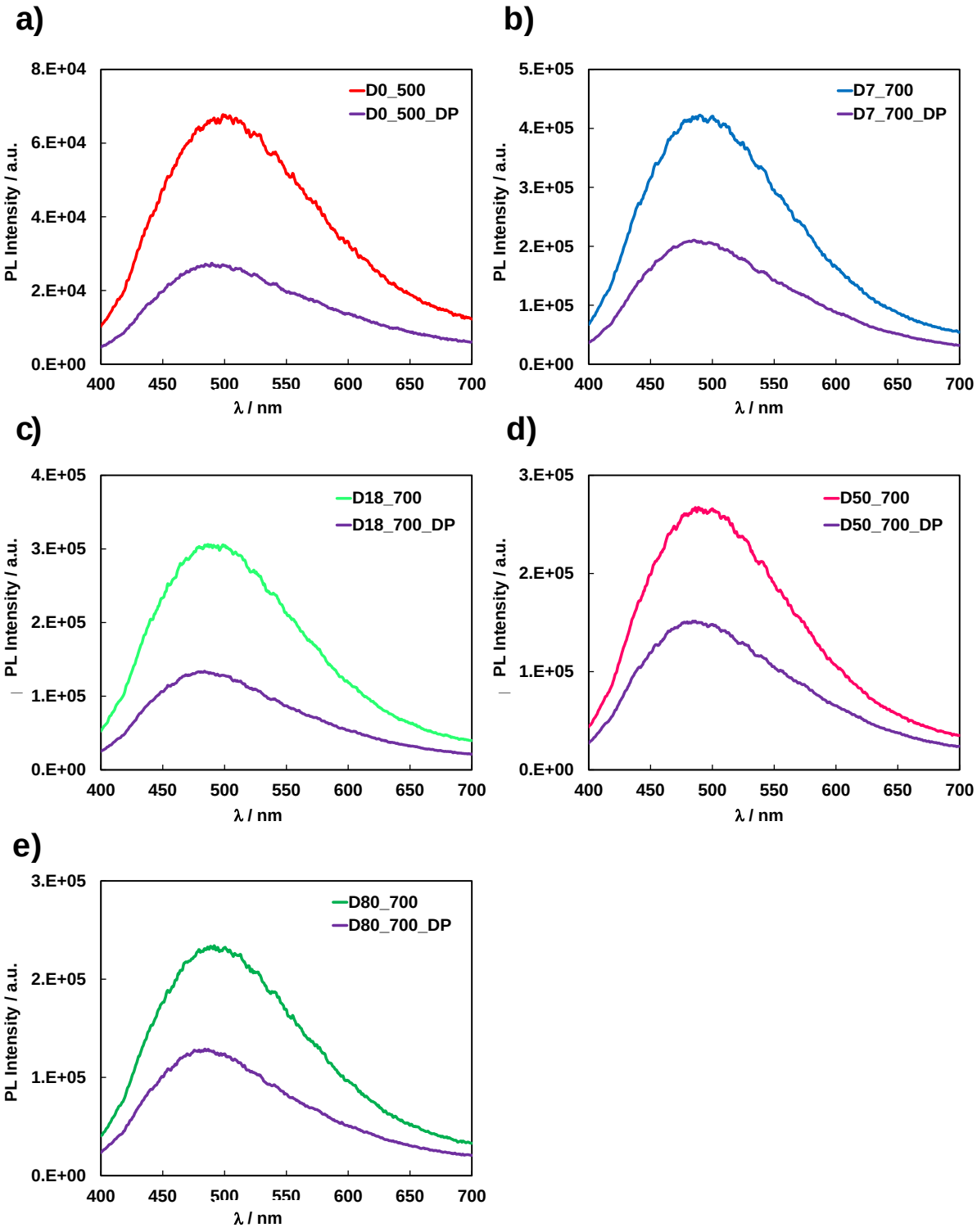

Figure 4.3.24: Comparison of the steady-state PL emission of bare and corresponding Au-modifed N,F-doped TiO_2 materials through the deposition-precipitation (DP) method.

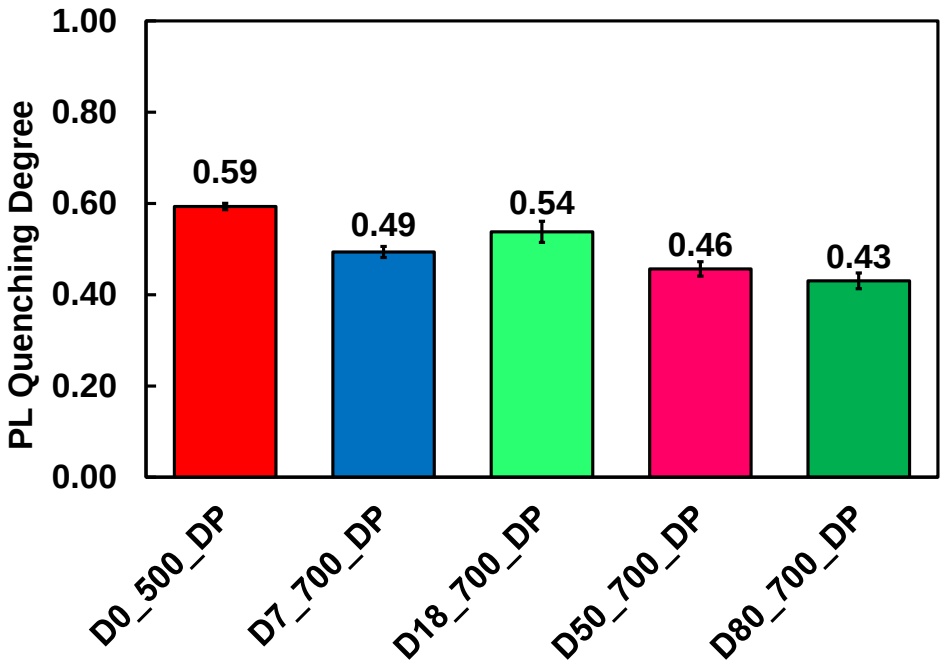

Figure 4.3.25: PL emission intensity quenching degree attained for differently N,F doped TiO_2 samples upon Au nanoparticles deposition through the deposition-precipitation (DP) method.

It is fundamental to note that, differently from what observed in terms of PL intensity quenching degree, the variation of the PL decay temporal profile attained with Au-containing samples seemed to be influenced by the relative doping amount introduced within the starting TiO_2 photocatalysts. In particular, the bare unmodified D7_700 material, characterized by a longer lasting PL emission, was also characterized by a more markedly sped-up decay kinetics upon deposition of Au metal nanoparticles (Figure 4.3.26).

In the light of the obtained results, it is likely that the presence of specific electron transfer channels between defective PL-emitting states and the deposited Au nanoparticles may possibly be better and/or exclusively unveiled by analysing the time evolution of the PL signal under pulsed laser excitation conditions.

Such effects, moreover, become even more evident when analyzing quantitatively the temporal evolution of the photoluminescence signal by fitting the decay curves acquired with the DP-modified materials according to the above-mentioned triexponential decay model, thus obtaining most relevant TRPL parameters, *i.e.*, the relative population of the i-th emitting state A_i and its average lifetime τ_i (Table 4.3.5).

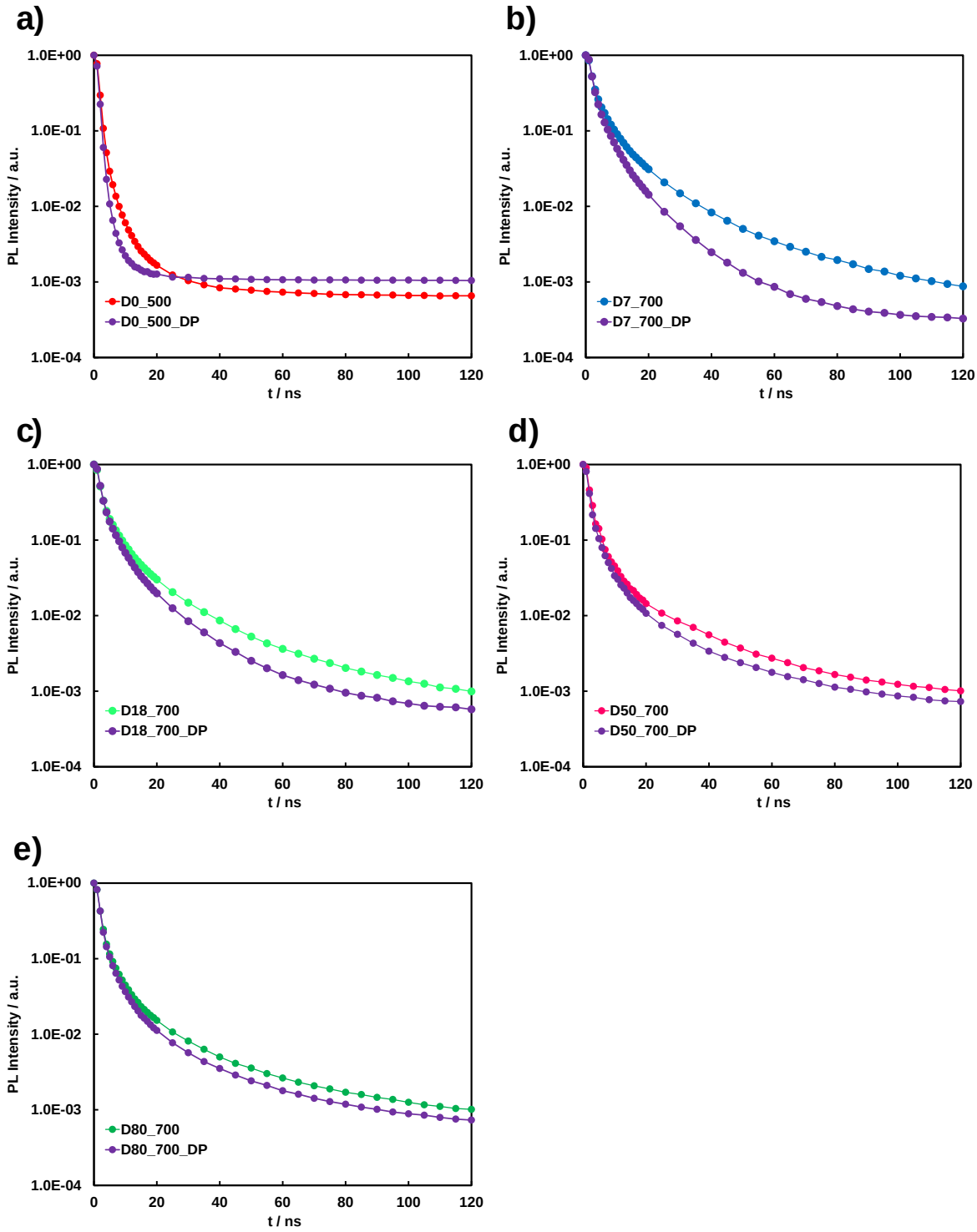

Figure 4.3.26: Temporal evolution of the PL emission intensity, integrated between 450-550 nm, of the bare and the corresponding N,F-doped TiO_2 samples Au-modified through the deposition-precipitation (DP) method.

Clearly, the faster decay rate of the PL emission intensity is represented by the total absence of the third, i.e. the longest emitting photoluminescent component, from the decay curves of all the DP-modified materials. Peculiarly, in the case of reference undoped D0_500, only the faster A_1 component is preserved upon noble metal nanoparticles deposition, i.e. the A_2 intermediate-lasting emitting component is also missing. Nevertheless, the addition of the noble metal

nanoparticles does not result in altering the average lifetime of the emitting states, which are very close to those observed in the case of bare N,F-doped titanium dioxide materials, but rather profoundly affects the relative population of such emitting states. This may be related to the fact that, upon irradiation, the photoexcited electrons, instead of being trapped at Ti^{3+} states, may be directly transferred towards deposited Au NPs, determining the complete or partial depopulation of the longer-lasting (A_3) and the intermediate-lasting (A_2) states, respectively.

Table 4.3.5: TRPL decay kinetics parameters calculated for the DP-modified N,F-doped TiO_2 materials.

Sample	A_1 (%)	A_2 (%)	A_3 (%)	τ_1 (ns)	τ_2 (ns)	τ_3 (ns)	$A_2 + A_3$ (%)
D0_500_DP	100	-	-	0.8	-	-	-
D7_700_DP	95.8	4.2	-	1.3	5.6	-	4.2
D18_700_DP	94.8	5.2	-	1.4	7.3	-	5.3
D50_700_DP	97.6	2.4	-	1.5	7.4	-	2.4
D80_700_DP	97.9	2.1	-	1.2	7.4	-	2.1

To better appreciate the effects of doping on the photoluminescent properties of DP-modified N,F-doped titanium dioxide materials, we compared the overall relative population of the longer-lasting emitting components $(A_2 + A_3)$ of the bare N,F-doped TiO_2 materials with those of the corresponding DP-modified specimens (Table 4.3.6). In particular, among the investigated materials, the D7_700 sample, characterized by the most intense and longer lasting PL emission, as well as the best SSA-normalized photoefficiency, exhibited the largest depopulation extent of the longer-lasting emitting states $(A_2 + A_3)$ upon Au NPs deposition. This could be an indication of a more efficient transfer of photopromoted electrons from photoluminescent trap states towards noble metal nanoparticles, occurring only with the best performing photocatalyst. Increasing the dopant amount within the titanium dioxide surface, instead, resulted in limiting such depopulation effect. A possible explanation for such behavior can be accounted to a decreased probability of electron transfer from Ti^{3+} states towards noble metal nanoparticles with increasing dopant content as a consequence of the lower population of long-lasting photoluminescent trap states within the titanium dioxide support deriving from the increased bulk charge recombination. As the initial population of longer lasting photoluminescent trap states is lowered, the electron transfer probability from such trap states towards noble metal nanoparticles is thus consequently reduced, leading to a lower extent of depopulation of the longer-lasting emitting states compared to D7_700.

Table 4.3.6: Relative population of the longer-lasting PL emitting states for bare, metal-free N,F-doped materials and DP-modified materials and their relative percent difference.

Sample	$A_2 + A_3$ (%) Bare	$A_2 + A_3$ (%) DP	Relative difference (%)
D0_500	0.3	-	-
D7_700	8.4	4.2	67
D18_700	6.7	5.3	25
D50_700	4.1	0.7	41
D80_700	3.2	2.1	44

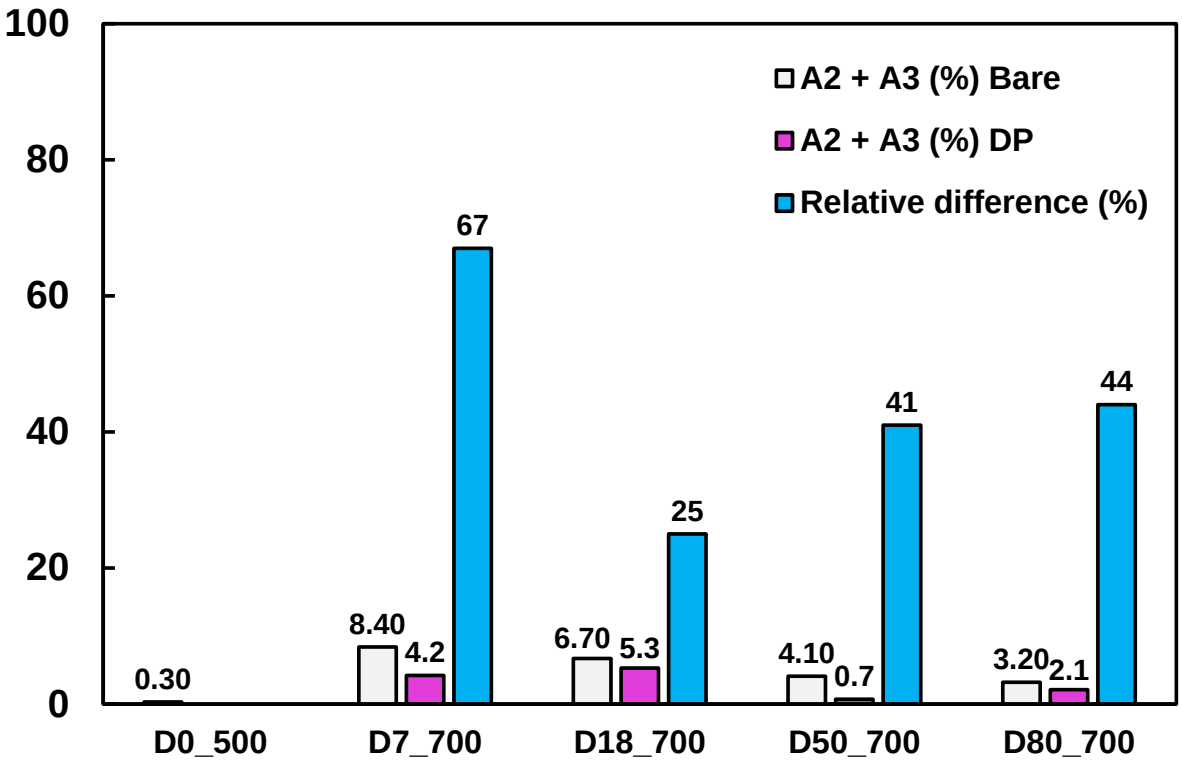

Figure 4.3.27: Relative population of the longer-lasting PL emitting states for bare, metal-free N,F-doped materials and DP-modified materials and their relative percent difference.

As demonstrated in a paper previously published by our research group, the evidence of a significant interaction between photodeposited Au NPs and electrons trapped at the defect sites in N,F-doped TiO_2 can be also testified by the relatively slight but peculiar change in spectral shape of the PL response, which was observed only in the case of Au NPs containing doped materials, but not in the case of the undoped sample.[21] In fact, the normalized PL spectrum of Au-modified doped system usually shows a remarkably lower emission in the 500−600 nm range compared to that of the corresponding bare sample, which perfectly matches the plasmonic absorption features of Au NPs. This effect was thus accounted to ability of Au NPs not only to efficiently scavenge electrons trapped at the TiO_2 defect sites, but also to (re)absorb PL photons with energy corresponding to their plasmonic resonance. To check if such effects could be also observed for the here investigated materials, the normalized PL spectra of the DX_Y_DP photocatalysts series

are compared to those of the corresponding DX_Y ones in Figure 4.3.28. We can clearly notice that there is no a systematic PL emission intensity lowering in the 500-600 nm range as a function of the materials dopant content. It is possible to observe only a slight spectra shape modification upon Au NPs deposition for the D18_700 and the D80_700 samples.

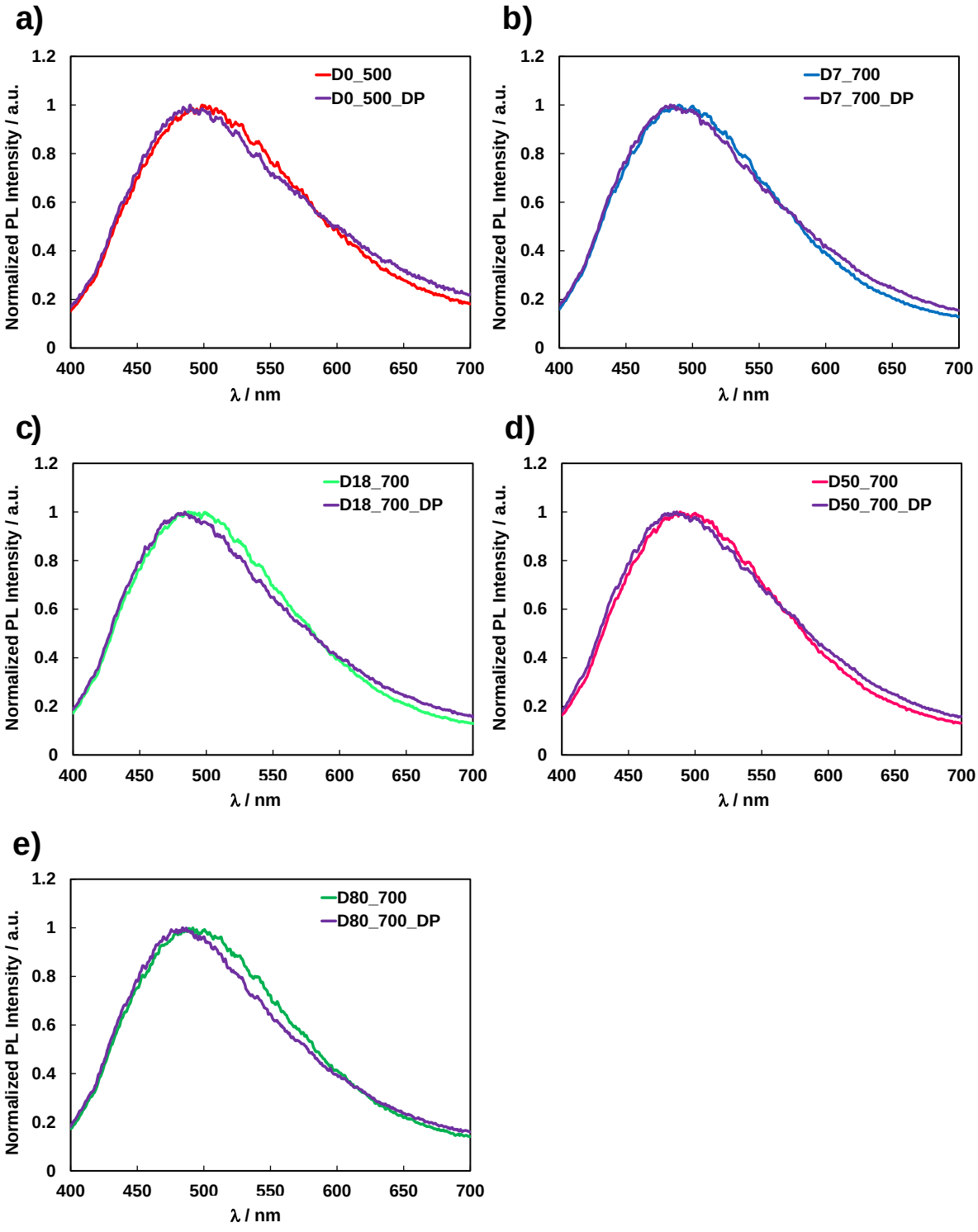

Figure 4.3.28: Intensity-normalized steady-state PL emission profiles of differently N,F-doped TiO_2 materials modified with 0.5 wt% of Au through the deposition-precipitation (DP) method.

The effects induced by the use of different Au nanoparticles deposition methods on the photoluminescence properties of differently N,F-doped TiO_2 materials were also investigated via TRPL. In doing so, we compared both the emission intensity under steady-state irradiation conditions and the temporal evolution of the photoluminescence signal of materials modified with 0.5 wt% of Au nanoparticles through deposition-precipitation (DP) or photoreduction (P) for selected materials with fixed dopant content (*i.e.*, the reference undoped D0_500 and the relatively less doped D7_700 and D18_700 materials). As appreciable in Figure 4.3.29, the deposition of Au nanoparticles always produced a PL emission intensity quenching. The extent of such quenching, as a function of the adopted deposition method, resulted to be dependent on the dopant amount of the starting TiO_2 sample. In particular, whereas for either the undoped D0_500 and the D18_700 materials the PL intensity has been mainly reduced upon Au NPs deposition through the DP method, Au modification by means of the photodeposition technique ensured a relatively larger PL quenching degree (compared to the DP route) only for the D7_700 material.

This could be an indirect indication of the presence of possible preferential electron exchange channels occurring among dopant-induced photoluminescent Ti^{3+} trap states and Au nanoparticles deposited through a selective deposition method, *i.e.*, photodeposition, only in the case of defective TiO_2 material containing an optimal dopant amount (that is, a nominal F/Ti molar ratio equal to 7%).

It is reasonable to suppose that only the D7_700 sample, being characterized by the most intense and longer lasting photoluminescent emission, underwent the preferential growth of Au nanoparticles in the proximity of photoluminescent Ti^{3+} trap states.[21] Thanks to such spatial proximity, only gained by applying the P method, the photodeposited Au NPs may thus more efficiently scavenge the photoexcited electrons trapped at the Ti^{3+} states, with a consequent more marked PL intensity quenching (exhibited by the D7_700_P sample). This phenomenon is instead not achieved with both D0_500 and D18_700 samples.

The temporal evolution of integrated PL intensity between 450 and 550 nm, however, revealed to be unable to probe significant differences in terms of either relative population of emitting states A_i or average lifetime τ_i induced by using different Au nanoparticle deposition techniques for any of the investigated material (Table 4.3.7). Observing such differences could be of fundamental importance when investigating the presence of preferential electron exchange channels between photoluminescent electron trap states and deposited noble metal nanoparticles as they represent strong evidence of the presence of the forehand mentioned synergic exchange mechanisms.

In the light of the experimental results previously obtained in both photoluminescent emission quenching and photoactivity of the powders in Cr(VI) photocatalytic reduction (Figure 4.3.16), the inability to probe significant differences either in terms of relative population of emitting states A_i or average lifetime τ_i induced by using different Au nanoparticle deposition techniques through TRPL measurements may most likely derive from the use of an inappropriate time resolution window (in the order of tenths of nanoseconds) employed to acquire the PL decay signals. In fact, synergistic electron exchange mechanisms between populated PL trap states and Au NPs may occur on a shorter time scale and might not be detected with the here employed experimental setup. A more suitable experimental setup for the detection of such fast electron exchange phenomena may require the use of a streak camera, as detection system, instead of the here employed CCD Camera, thus allowing to probe light emission phenomena up to the 1-10 ps time scale.

Table 4.3.7: TRPL decay kinetics parameters for N,F-doped titanium dioxide materials modified with 0.5 wt% of Au through the deposition-precipitation (DP) and photodeposition (P) technique.

Sample	A_1 (%)	A_2 (%)	A_3 (%)	τ_1 (ns)	τ_2 (ns)	τ_3 (ns)	$A_2 + A_3$ (%)
D0_500_DP	100	-	-	0.8	-	-	-
D0_500_P	100	-	-	0.9	-	-	-
D7_700_DP	95.8	4.2	-	1.3	5.6	-	4.2
D7_700_P	94.6	5.4	-	1.4	5.7	-	5.4
D18_700_DP	94.8	5.2	-	1.4	7.3	-	5.3
D18_700_P	95.7	4.3	-	1.4	7.4	-	4.3

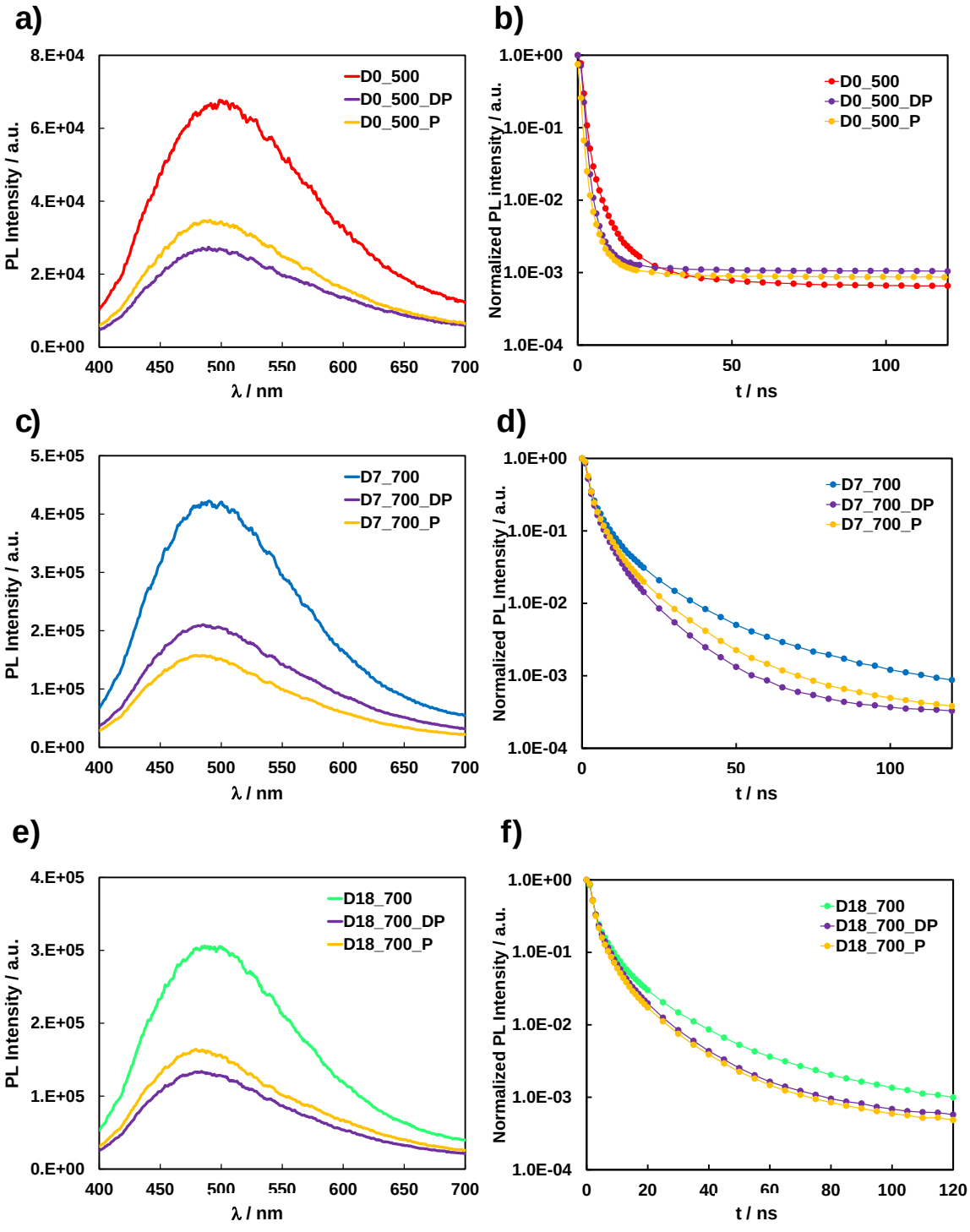

Figure 4.3.29: Steady-state PL emission spectra (a,c,e) and PL decay profiles (b,d,f) of selected N,F-doped TiO_2 materials, also further modified with 0.5 wt% of Au NPS by means of the DP and P methods.

4.4 References

1. Spasiano, D., Marotta, R., Malato, S., Fernandez-Ibañez, P. & Di Somma, I. *Appl. Catal. B Environ.* **170–171**, 90–123 (2015).

2. Ren, H., Koshy, P., Chen, W. F., Qi, S. & Sorrell, C. C. *J. Hazard. Mater.* **325**, 340–366 (2017).

3. Tong, H., Ouyang, S., Bi, Y., Umezawa, N., Oshikiri, M. & Ye, J. *Adv. Mater.* **24**, 229–251 (2012).

4. Magalhães, P., Andrade, L., Nunes, O. C. & Mendes, A. *Rev. Adv. Mater. Sci.* **51**, 91–129 (2017).

5. Dal Santo, V. & Naldoni, A. *Catalysts* **8**, 10–13 (2018).

6. Haider, A. J., Jameel, Z. N. & Al-Hussaini, I. H. M. *Energy Procedia* **157**, 17–29 (2019).

7. Benedix, R., Dehn, F., Quaas, J. & Orgass, M. *Lacer* **5**, 157–168 (2000).

8. Paz, Y. *Appl. Catal. B Environ.* **99**, 448–460 (2010).

9. Muscetta, M. & Russo, D. *Catalysts* **11**, 1–26 (2021).

10. Yu, J. C., Yu, J., Ho, W., Jiang, Z. & Zhang, L. *Chem. Mater.* **14**, 3808–3816 (2002).

11. Yang, Y., Ye, K., Cao, D., Gao, P., Qiu, M., Liu, L. & Yang, P. *ACS Appl. Mater. Interfaces* **10**, 19633–19638 (2018).

12. Dozzi, M. V. & Selli, E. *J. Photochem. Photobiol. C Photochem. Rev.* **14**, 13–28 (2013).

13. Karakitsou, K. E. & Verykios, X. E. *J. Phys. Chem.* **97**, 1184–1189 (1993).

14. Hope, G. A. & Bard, A. J. *J. Phys. Chem.* **87**, 1979–1984 (1983).

15. Xue, H., Chen, W., Liu, C., Kong, X., Qu, P., Liu, Z., Zhou, J., Shen, L., Zhong, Z. & Ruan, S. *3rd IEEE Int. Conf. Nano/Micro Eng. Mol. Syst. NEMS* 108–111 (2008).

16. Cheng, L., Zhang, D., Liao, Y., Li, F., Zhang, H. & Xiang, Q. *J. Colloid Interface Sci.* **555**, 94–103 (2019).

17. Tang, H., Su, Y., Zhang, B., Lee, A. F., Isaacs, M. A., Wilson, K., Li, L., Ren, Y., Huang, J., Haruta, M., Qiao, B., Liu, X., Jin, C., Su, D., Wang, J. & Zhang, T. *Sci. Adv.* **3**, 1–9 (2017).

18. Kydd, R., Chiang, K., Scott, J. & Amal, R. *Photochem. Photobiol. Sci.* **6**, 829–832 (2007).

19. Gong, X. Q., Selloni, A., Dulub, O., Jacobson, P. & Diebold, U. *J. Am. Chem. Soc.* **130**, 370–381 (2008).

20. Melvin, A. A., Illath, K., Das, T., Raja, T., Bhattacharyya, S. & Gopinath, C. S. *Nanoscale* **7**,

13477–13488 (2015).

21. Dozzi, M. V., Candeo, A., Marra, G., D'Andrea, C., Valentini, G. & Selli, E. *J. Phys. Chem. C* **122**, 14326–14335 (2018).

22. Dozzi, M. V., D'Andrea, C., Ohtani, B., Valentini, G. & Selli, E. *J. Phys. Chem. C* **117**, 25586–25595 (2013).

23. Prati, L. & Villa, A. *Catalysts* **2**, 24–37 (2011).

24. Dimitratos, N., Villa, A., Bianchi, C. L., Prati, L. & Makkee, M. *Appl. Catal. A Gen.* **311**, 185–192 (2006).

25. Compagnoni, M., Villa, A., Bahdori, E., Morgan, D. J., Prati, L., Dimitratos, N., Rossetti, I. & Ramis, G. *Catalysts* **8**, (2018).

26. Dimitratos, N., Villa, A., Prati, L., Hammond, C., Chan-Thaw, C. E., Cookson, J. & Bishop, P. T. *Appl. Catal. A Gen.* **514**, 267–275 (2016).

27. Dozzi, M. V., Prati, L., Canton, P. & Selli, E. *Phys. Chem. Chem. Phys.* **11**, 7171–7180 (2009).

28. Wenderich, K. & Mul, G. *Chem. Rev.* **116**, 14587–14619 (2016).

29. Zeng, Y., Wang, Y., Meng, Y., Song, F., Zhang, S. & Zhong, Q. *Chem. Phys. Lett.* **730**, 95–99 (2019).

30. Meng, A., Zhang, L., Cheng, B. & Yu, J. *Adv. Mater.* **31**, 1807660 (2019).

31. Hu, X., Lu, S., Tian, J., Wei, N., Song, X., Wang, X. & Cui, H. *Appl. Catal. B Environ.* **241**, 329–337 (2019).

32. Dozzi, M. V., Montalbano, M., Marra, G., Mino, L. & Selli, E. *Mater. Today Chem.* **22**, 100624 (2021).

33. Dozzi, M. V., Saccomanni, A. & Selli, E. *J. Hazard. Mater.* **221–22**, 188–195 (2012).

34. Czoska, A. M., Livraghi, S., Chiesa, M., Giamello, E., Agnoli, S., Granozzi, G., Finazzi, E., Di Valentiny, C. & Pacchioni, G. *J. Phys. Chem. C* **112**, 8951–8956 (2008).

35. Dozzi, M. V., Ohtani, B. & Selli, E. *Phys. Chem. Chem. Phys.* **13**, 18217–18227 (2011).

36. Thommes, M., Kaneko, K., Neimark, A. V., Olivier, J. P., Rodriguez-Reinoso, F., Rouquerol, J. & Sing, K. S. W. *Pure Appl. Chem.* **87**, 1051–1069 (2015).

37. Thommes, M. *Chemie-Ingenieur-Technik* **82**, 1059–1073 (2010).

38. Maisano, M., Dozzi, M. V. & Selli, E. *J. Photochem. Photobiol. C Photochem. Rev.* **28**, 29–43 (2016).

39. Zolt, K., Eniko, E. A., Klarka, H., Tamas, G., Baia, L., Gabor, V., Zsuzsanna, L. & Pap, Z. *Molecules* **25**, 4842 (2020).

40. Scanlon, D. O., Dunnill, C. W., Buckeridge, J., Shevlin, S. A., Logsdail, A. J., Woodley, S. M., Catlow, C. R. A., Powell, M. J., Palgrave, R. G., Parkin, I. P., Watson, G. W., Keal, T. W., Sherwood, P., Walsh, A. & Sokol, A. A. *Nat. Mater.* **12**, 798–801 (2013).

41. Dozzi, M. V., Artiglia, L., Granozzi, G., Ohtani, B. & Selli, E. *J. Phys. Chem. C* **118**, 25579−25589 (2014).

42. Dozzi, M. V., Saccomanni, A., Altomare, M. & Selli, E. *Photochem. Photobiol. Sci.* **12**, 595–601 (2013).

43. Kamat, P. V. *J. Phys. Chem. B* **106**, 7729–7744 (2002).

44. Link, S. & El-Sayed, M. A. *J. Phys. Chem. B* **103**, 8410–8426 (1999).

45. Mrowetz, M. & Selli, E. *New J. Chem.* **30**, 108–114 (2006).

46. Dozzi, M. V. & Selli, E. *Catalysts* **3**, 455–485 (2013).

47. Wakabayashi, K., Yamaguchi, Y., Sekiya, T. & Kurita, S. *J. Lumin.* **112**, 50–53 (2005).

48. Iijima, K., Goto, M., Enomoto, S., Kunugita, H., Ema, K., Tsukamoto, M., Ichikawa, N. & Sakama, H. *J. Lumin.* **128**, 911–913 (2008).

49. Wang, X., Feng, Z., Shi, J., Jia, G., Shen, S., Zhou, J. & Li, C. *Phys. Chem. Chem. Phys.* **12**, 7083 (2010).

50. Fessi, N., Nsib, M. F., Chevalier, Y., Guillard, C., Dappozze, F., Houas, A., Palmisano, L. & Parrino, F. *Langmuir* **36**, 13545–13554 (2020).

51. Fessi, N., Nsib, M. F., Cardenas, L., Guillard, C., Dappozze, F., Houas, A., Parrino, F., Palmisano, L., Ledoux, G., Amans, D. & Chevalier, Y. *J. Phys. Chem. C* **124**, 11456–11468 (2020).

52. Prasankumar, R. P. & Taylor, A. J. *Optical Techniques for Solid-State Materials Characterization*. (CRC Press, 2012).

53. Shen, S., Wang, X., Chen, T., Feng, Z. & Li, C. *J. Phys. Chem. C* **118**, 12661–12668 (2014).

54. Zhang, Z. & Yates, J. T. *Chem. Rev.* **112**, 5520–5551 (2012).

4.5 Appendix

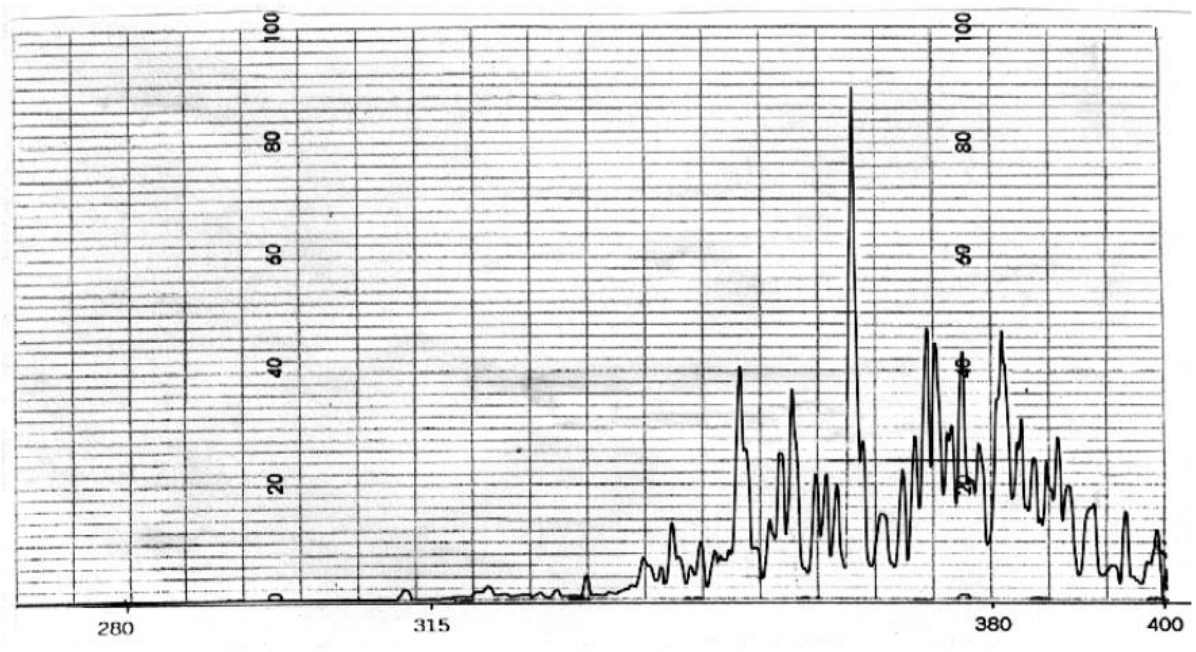

Figure A1: Emission spectrum of the immersion fluorescent, low pressure mercury arc lamp (Jelosil), emitting in the 300–400 nm range, employed for the deposition of Au nanoparticles on the UV_D7_700_P surface through the photodeposition technique.

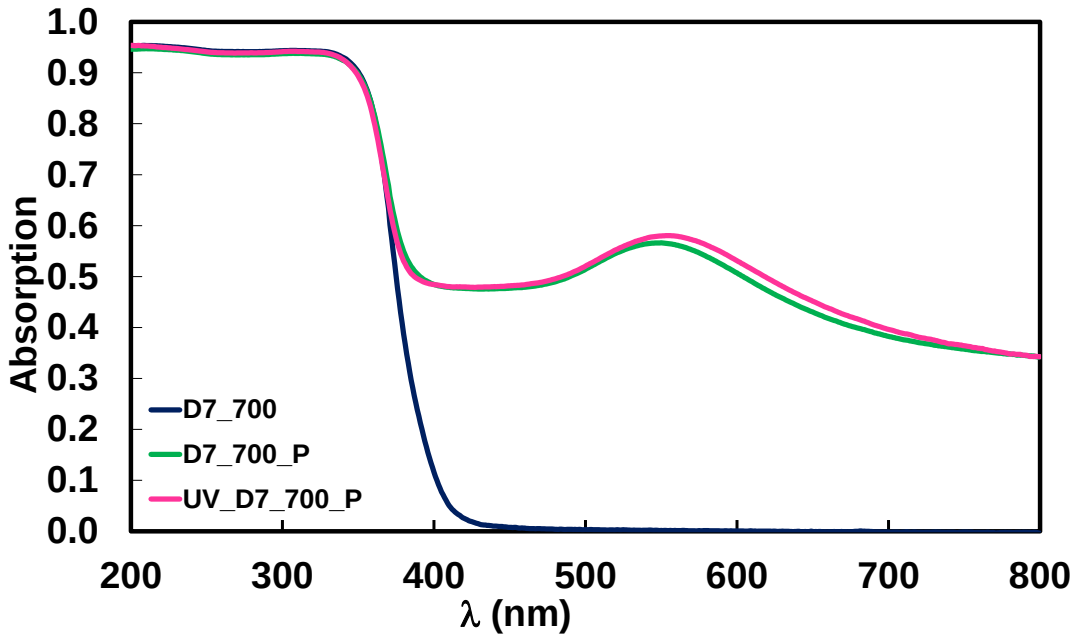

Figure A2: Absorption spectra of D7_700 (blue curve), D7_700_P (green curve) and UV_D7_700_P (purple curve) samples

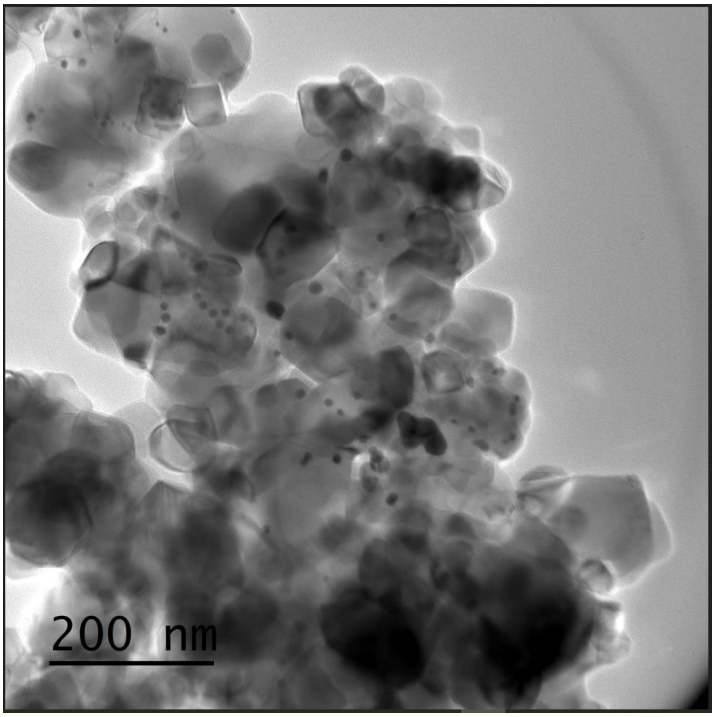

Figure A3: Selected TEM image of Au-modified UV_D7_700_P material.

[This page intentionally left blank]

Chapter 5: Effects of *In-Situ* Surface Fluorination on the Photocatalytic Activity of Differently Shaped TiO_2 Materials

5.1 Introduction

The design and synthesis of cost effective, efficient, and scalable TiO_2-based materials able to convert light into chemical energy through photocatalytic processes is a key challenge for a sustainable energy economy. A wide variety of synthetic routes has been developed to prepare TiO_2 in different forms and shapes, with different surface area and porosity,[1-3] and to improve its photocatalytic activity, either by enhancing light absorption[4-7] or by improving the separation of photoproduced charge couples.[8-10]

In particular, shape-controlled anatase TiO_2 has been prepared mainly by adding capping agents during the synthesis, which may preferentially stabilize the {001} facets during the crystal growth, with the production of nanocrystals with a plate-like shape (Figure 5.1.1).[11-14] Such facets, though thermodynamically less stable, are expected to be more reactive with respect to the dominant {101} ones, mainly due to a high density and a very strained configuration of surface undercoordinated Ti atoms. Moreover, by tailoring the truncation degree of anatase crystals, the overall photoactivity may be further increased as a direct consequence of the selective migration of photogenerated holes towards the {001} facets and of photopromoted electrons to the {101} ones.[15]

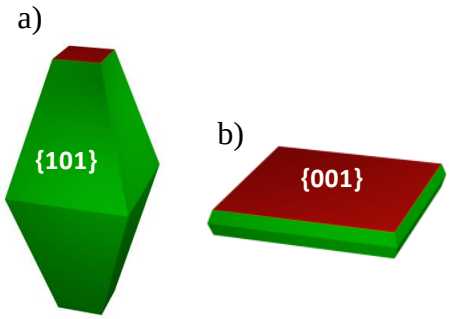

Figure 5.1.1: Equilibrium crystal shape (a) and platelet-like morphology of anatase crystal with the indication of the types of exposed facets (b).

At the same time, another strategy that may be pursued to improve the photocatalytic performance of TiO_2 consists in the *in-situ* surface fluorination,[16-19] implying a simple ligand exchange reaction between fluoride anions and surface hydroxyl groups (at acidic pH):

$$\equiv Ti - OH + F^- \rightarrow \equiv Ti - F + OH^- \qquad (5.1.1)$$

This method was found to induce different effects on photocatalysis, depending not only on the main degradation paths of different substrates,[20] but also on the surface area and phase composition of TiO_2.[21]

On the other hand, fluoride anions are often used as capping agents in the synthesis of shape controlled anatase[22-28] and the effects on photoactivity arising from residual surface fluorination are very difficult to distinguish from those deriving from the morphology of such materials. Indeed, plate-like materials are usually synthesized in the presence of a higher fluoride ions concentration with respect to spherically shaped TiO_2 materials.[13,15,29] The different amount of residual adsorbed fluoride anions for the two morphologies does not allow to appreciate if the effects on photoactivity induced by surface fluorination may synergistically cooperate with morphology control in boosting the photoactivity of TiO_2-based materials.[15]

In this framework we investigated the effects that TiO_2 surface fluorination has on photocatalytic oxidation and reduction reactions in relation to the amount of exposed anatase {001} facets. Fluorine-free TiO_2 materials with different morphologies were obtained through post-synthesis washing to efficiently remove the capping agent. Such materials were eventually successively *in-situ* re-fluorinated. Under such conditions the home-made photocatalysts were systematically tested in formic acid photo oxidation, Rhodamine B photobleaching and Cr(VI) photoreduction, proceeding through completely different mechanistic routes.[30-32] These model test reactions find an important application of photocatalysis as innovative and clean/environmentally friendly technology for industrial wastewaters decontamination.[33-38] In fact, hexavalent Cr(VI) ions, notoriously toxic and carcinogenic[39] and generally released in effluents by various industrial activities (*e.g.* electroplating, leather tanning, textile production, steel fabrication), can be efficiently converted by photocatalytic reduction on semiconductors into Cr(III) species, exhibiting lower toxicity and mobility in the environment.[40] At the same time, the demand for Rhodamine B (RhB) conversion into harmless chemicals has also started growing in the recent years, due to the increased use of xanthene-derived dyes in food, paper, textile and leather industry. The undesired presence of RhB (Figure 5.1.2) in waters and food represents a serious threat for the human health due to the dye ability of causing injury to human skin, eyes, respiratory system as well as being

potentially carcinogenic and neurotoxic.[41,42] Rhodamine B decomposition is thus highly required also to gain a sustainable recycling of industrial wastewaters.

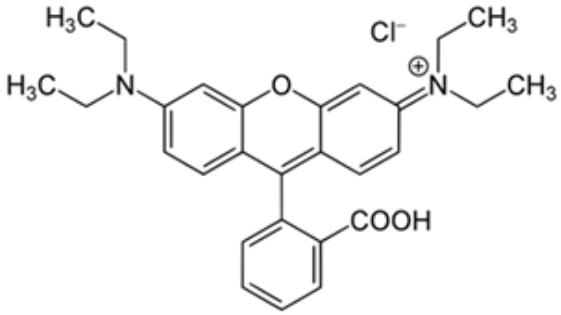

Figure 5.1.2: Rhodamine B (RhB).

5.2 Experimental section

5.2.1 Photocatalyst preparation

Differently shaped TiO_2 samples, characterized by a pseudo-spherical shape or a nanosheet structure, were prepared through the hydrothermal route as described in section 2.2.1 (page 51). The so-obtained washed samples were labelled as HT_X_NaOH.

5.2.2 Photocatalyst characterization

The following techniques were employed for the characterization of the materials:

- X-Ray Powder Diffraction (XRPD), as described in section 2.5.1 (page 63)
- Specific surface area (SSA) measurement, as described in section 2.6.1 (page 69)
- UV-Visible DR Spectroscopy, as described in section 2.7.1 (page 72)
- ICP-OES analysis, as described in section 2.8.1 (page 74)
- HRTEM imaging, as described in section 2.9.1 (page 79)

Additionally, Thermogravimetric Analysis (TGA) was carried out on a Mettler-Toledo TGA/DSC 2 STARe system. Thermograms were recorded in the 30-800 °C temperature range, with a heating ramp of 10 °C min^{-1} under a 50 cm^3 min^{-1} air flux.

X-Ray photoemission spectra (XPS) were recorded on a M-Probe apparatus, Surface Science Instruments, equipped with an Al-K_α monochromatic radiation X-Ray source (1486.6 eV photon energy). XPS surveys were recorded in a binding energy range from 1000 to 0 eV and peak shift correction was applied using the adventitious carbon C1s signal at 284.6 eV as internal reference.

For Fourier-transform infrared (FT-IR) spectroscopy measurements the samples were pressed in self-supporting pellets ("optical density" of ca. 10 mg·cm^{-2}) and placed in quartz cells equipped with KBr windows designed to carry out spectroscopic analysis in controlled atmosphere. The thermal treatments at increasing temperatures (150, 300 and 500 °C) were performed for 90 min

under dynamic vacuum (residual pressure < 1×10^{-4} mbar). At the end of each treatment step, the samples were contacted with O_2 at 10 mbar to restore the stoichiometry of the TiO_2. The spectra were obtained using a Bruker Equinox 55 spectrometer with a resolution of 2 cm^{-1} and averaging 64 scans. The optical density of the pellets was employed to normalize all acquired spectra.

5.2.3 Photocatalytic oxidation of formic acid

Formic acid photodegradation tests were performed according to a well-established procedure described in detail in section 3.1.3 (page 96).[43-45] The photocatalyst concentration was set to 0.17 g dm^{-3}, differently from the 0.1 g dm^{-3} concentration reported in the general description of the experimental procedure.

5.2.4 Photocatalytic activity in the absence or upon *in-situ* addition of fluorides

The photocatalytic activity of home-made samples was tested in aqueous suspensions, employing the dye Rhodamine B (RhB) or dichromate ($Cr_2O_7^{2-}$) ions as organic or inorganic degradation substrates, respectively. The photostability of both substrates in aqueous solution was preliminarily verified under the adopted irradiation conditions.

All photocatalytic degradation runs were performed under atmospheric conditions using the setup and experimental procedure described in detail in section 3.2.2 (page 99) for RhB photodegradation and section 3.3.2 (page 102) for Cr(VI) photoreduction.

5.2.5 Substrates adsorption measurements on TiO_2 and fluorinated TiO_2

Aiming at investigating the substrates affinity for the different photocatalysts, adsorption tests were performed at pH 3.7, both in the presence and in the absence of NaF, under the same experimental conditions adopted during the photocatalytic runs, except for the amount of TiO_2, which was fixed at 1.0 g L^{-1}. The suspensions were kept under stirring in the dark and samples were withdrawn after 15 min, 60 min and 180 min, centrifuged and analyzed for determining the Cr(VI) and/or RhB residual amount in the supernatant. Adsorption equilibrium was attained in 15-30 min, though the adsorption data after 3 h-long equilibration were considered as most reliable, as in previous studies.[46]

5.3 Results and Discussion

5.3.1 Materials Characterization

XRPD diffractograms of all samples of the HT_X series were recorded to investigate both phase composition and morphology of the materials. As shown in Figure 5.3.1, all diffraction patterns perfectly matched those of pure anatase.

Quantitative phase analysis (Table 5.3.1), performed through Rietveld refinement,[47] showed that rutile or brookite was non-detectable, nor appreciable presence of other phases such as $TiOF_2$ was observed, indicating that the samples were composed of pure anatase independently of the amount of fluorine employed during the synthesis. With increasing fluorine content the width of reflections with ($l > h,k$) broadened, accompanied by a shrinking of the peaks characterized by a strong h component, in the 35-50° 2θ range, indicating a change in crystal growth along specific crystallographic directions.[29]

Table 5.3.1: Average nanoparticles thickness and width, percentage of {001} facets exposure, BET specific surface area (SSA) and residual carbonaceous content detected by TGA analysis of the synthesized pure anatase materials.

Sample	thickness / nm	width / nm	{001} (%)	SSA (m^2 g^{-1})	Total carbon loss (%)
HT_0	21.4(4)	14.6(2)	7.2(6)	93(1)	4
HT_0.1	17.2(3)	16.8(3)	14.8(8)	78(1)	5
HT_1	7.8(2)	39(1)	67(2)	84(4)	6
HT_0.1_NaOH	18.5(8)	16.5(7)	14.0(2)	82(2)	5
HT_1_NaOH	8.2(2)	38(1)	65(1)	82(7)	5

The nanoparticles size and the relative amount of exposed {001} facets in the different samples, calculated by applying a Rietveld-based XRPD approach,[48] are collected in Table 5.3.1. The so obtained values clearly demonstrate that the anatase {001} facets percentage increased by increasing the HF amount during the synthesis, *i.e.,* passing from *ca.* 15% for HT_0.1 to 65% for HT_1.

The latter sample incontrovertibly consisted of plate-like nanocrystals, as confirmed by the HR-TEM images reported in Figure 5.3.5a,b. In line with previous findings,[29] the plate-like crystals of HT_1 appeared piled up face-to-face, one above the other, thus minimizing the total surface energy.[28,49] On the contrary, the casual distribution of particles displayed by HT_0.1 aggregates (Figure 5.3.5b) is coherent with an isotropic shape of crystals (Figure 5.3.5a).

At the same time, HR-TEM images further confirmed both crystal thickness and width values of platelet-like HT_1 nanoparticles, calculated from XRPD data,[48] corresponding to *ca.* 8 and 40 nm, respectively (Table 5.3.1). More interestingly, the capping agent removal procedure did not significantly alter the percentage of exposed {001} facets in any of the investigated materials (Table 5.3.1), the specific TiO_2 crystal shape being entirely preserved even after the samples washing (Figure 5.3.5c-f).

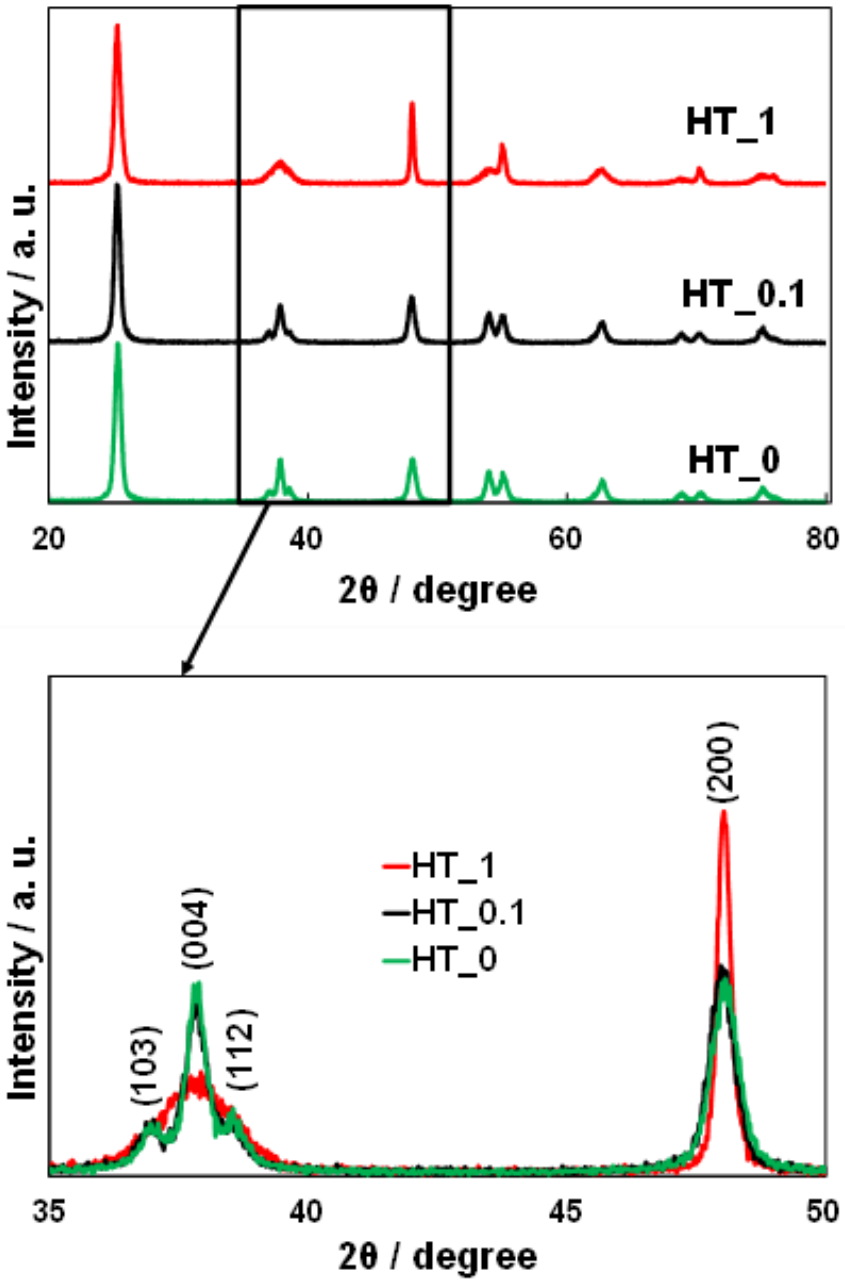

Figure 5.3.1: XRPD patterns of samples of the HT_X series evidencing (103), (004), (112), and (200) anatase reflections.

BET analysis confirmed similar SSA in the 82-93 m^2 g^{-1} range for both HT_X and HT_X_NaOH series samples, except for reference HT_0, synthesized in the absence of fluoride anions, having a slightly higher SSA (Table 5.3.1). Moreover, no significant variation in SSA was observed upon washing. Thus, the photocatalytic activities of the materials can be directly compared, all of them having the same SSA.

Congruently with our previous findings,[29] BET adsorption/desorption isotherms can be classified as of type IV, according to IUPAC classification (Figure 5.3.2).[50] The observed porosity originating hysteresis loops is to be attributed to the packing of the crystallites rather than to an actual porosity of the material, as anatase is not inherently porous.[51] However, increasing the

amount of nominal F/Ti ratio employed during the synthesis of the materials results in a shift from H2-type pores, associated to "ink bottle" pores typically formed due to packing of sphere-like particles, towards H3-type pores, which are instead usually observed due to the packing of plate-like particles forming slit-shaped pores. This finding is in line with both XRD and HR-TEM measurements, further confirming the morphological evolution of the materials, undoubtedly passing from pseudo-spheres to a nanosheets shape.

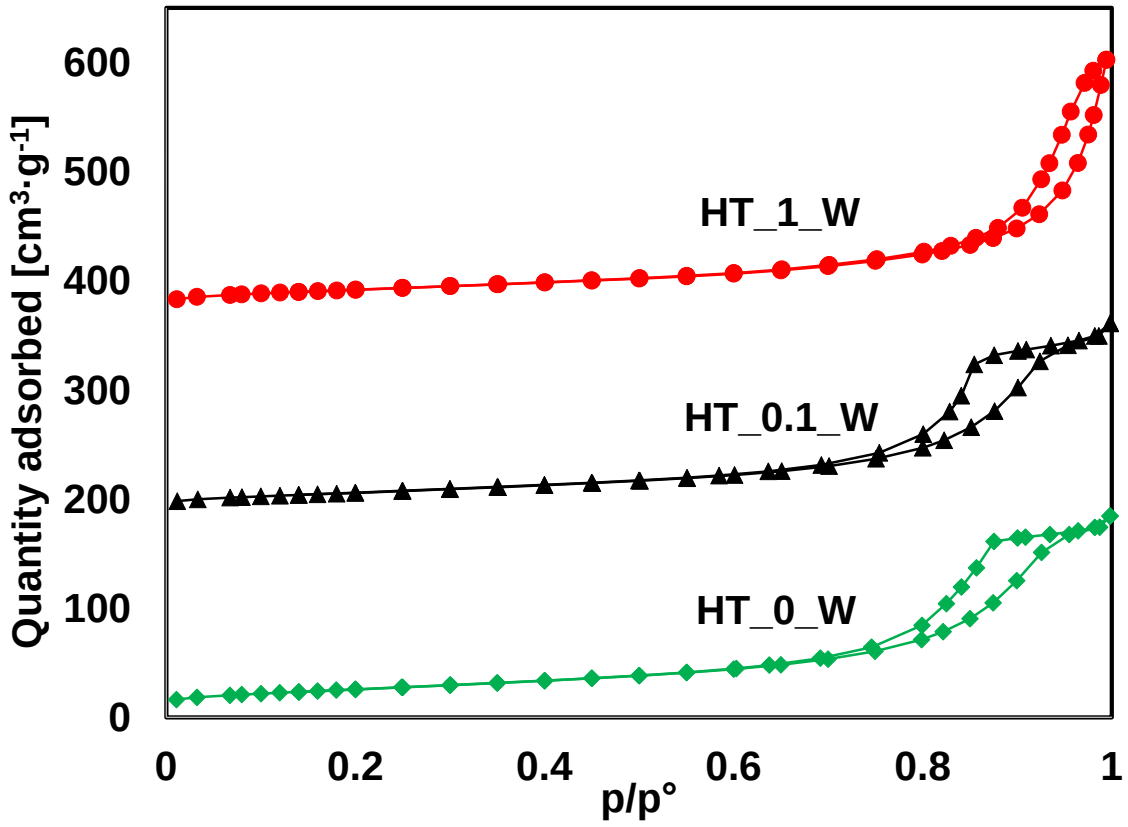

Figure 5.3.2: BET adsorption-desorption isotherms of samples of the HT_X_W series.

Diffuse Reflectance UV-Vis absorption spectra of the investigated samples are characterized by a very marked absorption onset for $\lambda < 400$ nm, similar to that of pure anatase (Figure 5.3.3). The absorption onset was found to be independent of the F/Ti ratio employed during the synthesis, *i.e.,* it is unaffected by the relative amount of exposed crystal facets (inset of Figure 5.3.3). In the literature the anatase band gap has been reported to be red-,[52-54] blue-[29,55] shifted or unmodified[56,57] by an increase in the {001} facets content. Moreover, the washing procedure did not produce any absorption edge variation for any of the prepared samples, thus resulting in an overall preservation of the original optical properties also upon the application of the here adopted fluorine removal treatment (Figure 5.3.3).

UV-vis absorption spectra did not evidence the presence of any residual carbonaceous impurity adsorbed on the materials surface (which are generally known to cause the appearance of

continuous absorption in the visible region of TiO_2 in full DR spectra),[58] in line with the finding that pretty similar percentages of total mass losses were obtained by thermogravimetric analysis (TGA) of all samples (Table 5.3.1).

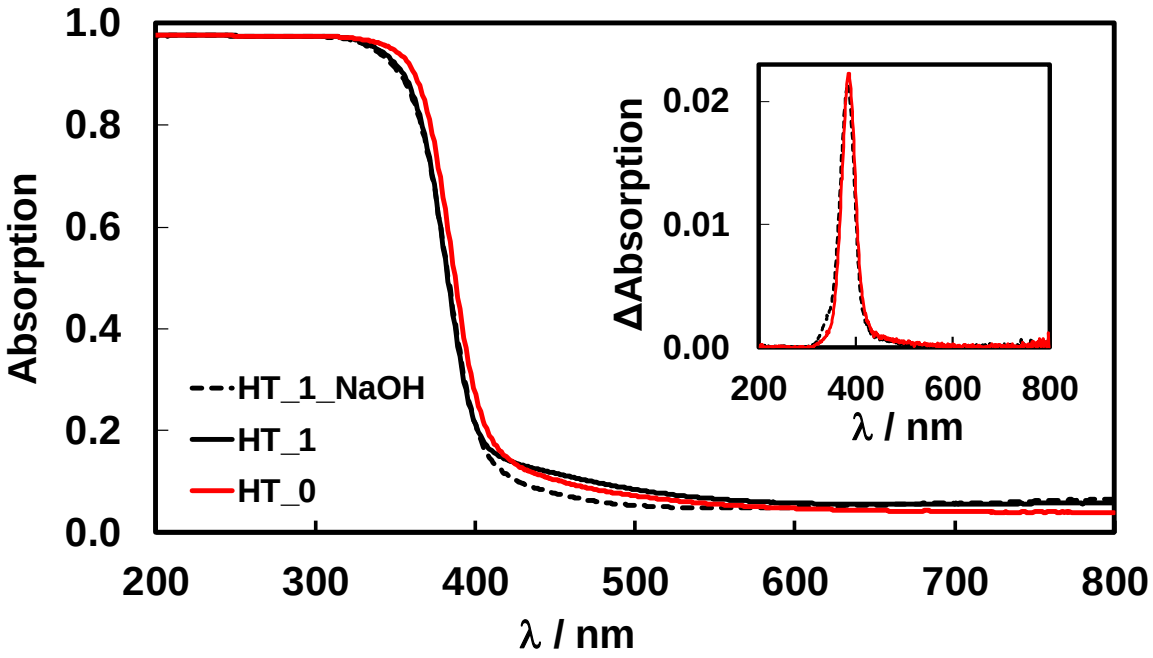

Figure 5.3.3: Absorption spectra of HT_X and HT_X_NaOH series samples. Inset: DRS spectra numerical first derivative of HT_X_NaOH samples highlights invariance of the absorption band edge with titania morphology.

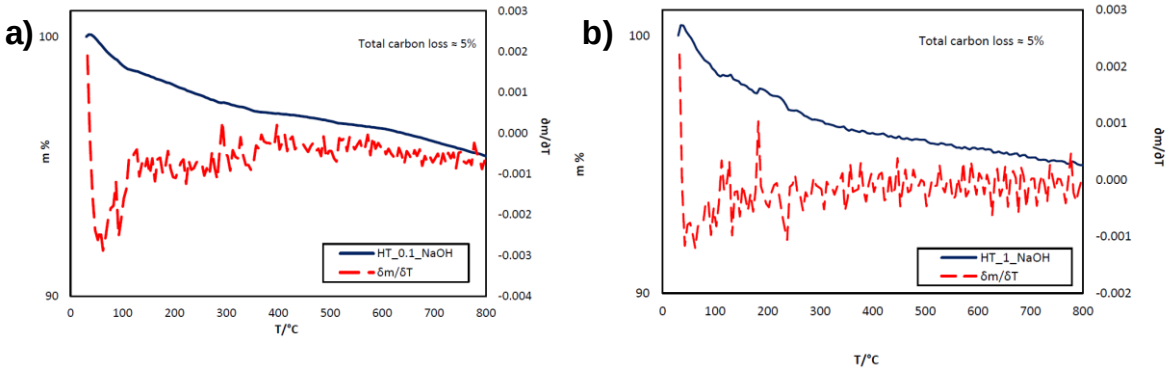

Figure 5.3.4: Example TGA analysis of HT_0.1_NaOH (a) and HT_1_NaOH (b) indicating similar percent carbon loss among the synthesized materials.

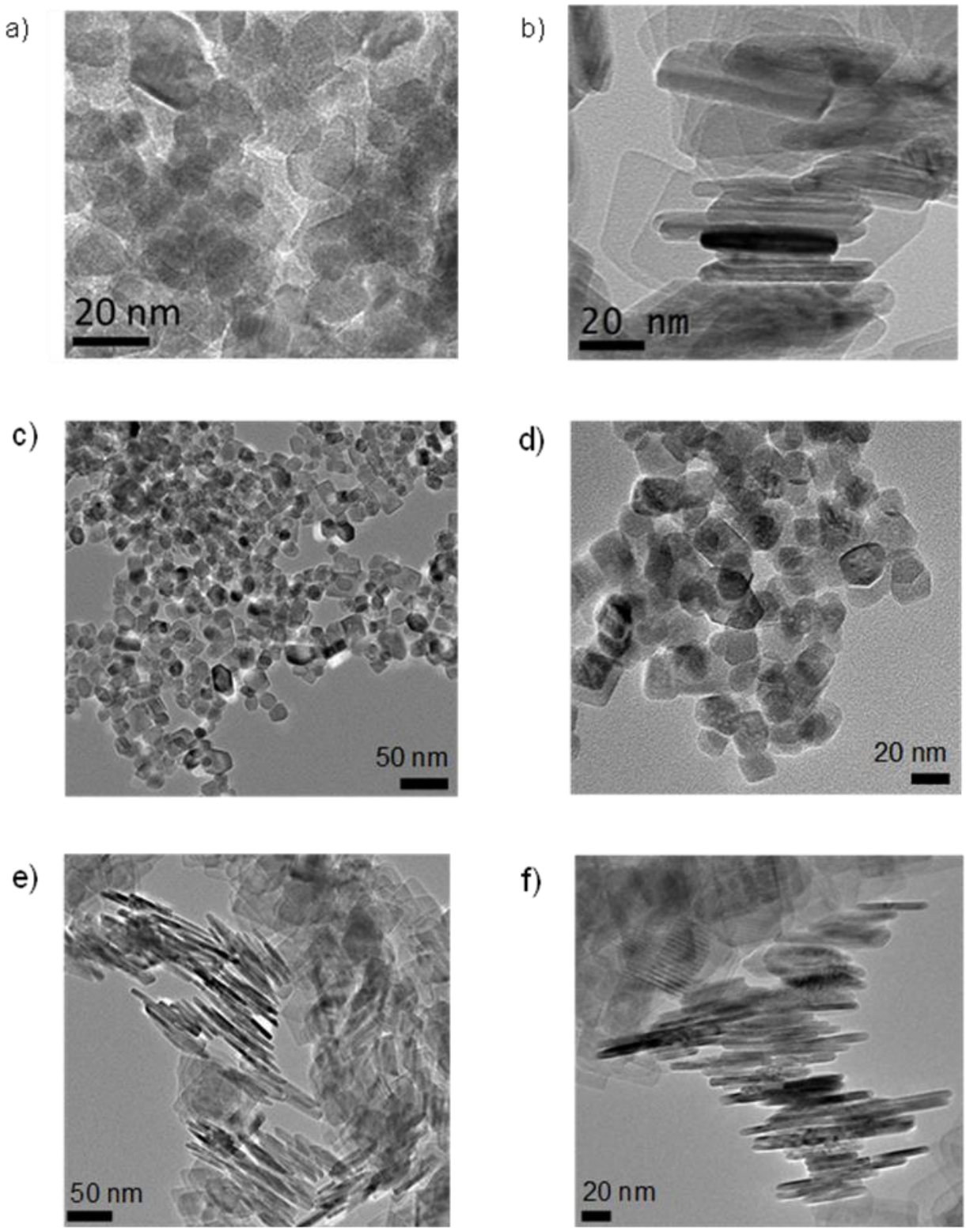

Figure 5.3.5: HRTEM images of HT_0.1 (a), HT_1 (b), HT_0.1_NaOH (c, d) and HT_1_NaOH (e, f).

The surface chemical composition of the home-made samples was assessed *via* XPS analysis (Figure 5.3.6).

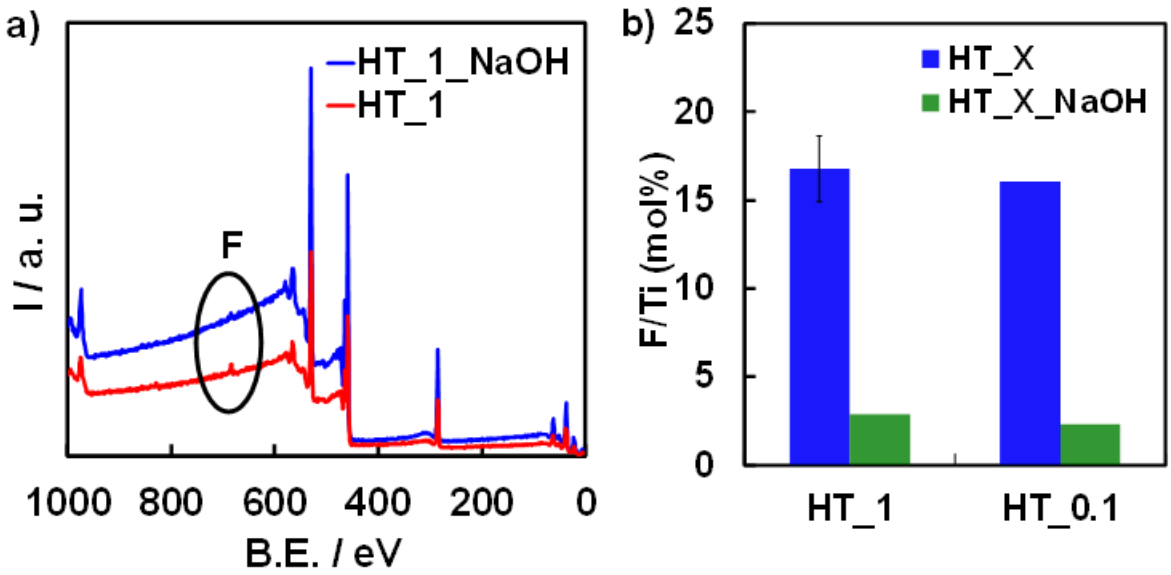

Figure 5.3.6: XPS survey spectra (a) and quantitative surface F/Ti molar percentages obtained for the HT_X and HT_X_NaOH samples (b). As highlighted in panel (a) the surface fluoride ions signal is located at 684 eV.

Titanium, carbon, and oxygen were identified in XPS spectra by the signals binding energies (BE) at *ca.* 458.8 eV (Ti 2p), 531 eV (O 1s) and 284.5 eV (C 1s), respectively. Spectra of HT_1 and HT_0.1 also show a small peak at binding energy 684 eV,[59,60] attributed to F1s, indicating the residual presence of fluoride anions on the surface of the original materials. No XPS signal at 688 eV, assigned to substitutional F ions in the TiO_2 lattice, was detected, possibly always being below the detection limit of the XPS technique.[29,61]

As reported in Figure 5.3.6b, quantitative XPS analysis demonstrated the effective (though not complete) removal of the residual F capping agent from HT_1 and HT_0.1 by the here applied post-synthesis washing procedure. In fact, the overall surface F/Ti ratios passed from *ca.* 16% to *ca.* 2% in the washed samples.

5.3.2 Photocatalytic degradation of formic acid

Formic acid degradation was firstly chosen as a model test reaction to investigate the photocatalytic activity of differently shaped titanium dioxide materials. The photoactivity of the materials, compared in terms of pseudo-zeroth order kinetic rate constants k_{For} (Figure 5.3.7), highlight that shifting the anatase morphology towards nanosheet-shaped crystallites results in slightly worsening the photoefficiency of the semiconductor photocatalyst for both surface fluorinated and washed materials. More surprisingly, cleaning the surface of titanium dioxide from surface fluoride anions through NaOH washing did not result in any change in the photoactivity of the materials. Negligible effects on photoactivity induced by the removal of surface fluoride

anions through washing procedures in the photocatalytic degradation of formic acid on anatase have been systematically reported in the literature and consistently observed in our research group.[29,62] However, these results are rather surprising since, as surface adsorbed fluoride anions are well-known to prevent the adsorption of formic acid very efficiently on the surface of titanium dioxide,[63,64] an improvement of the photocatalytic activity of the materials should be naturally expected upon fluoride removal, the adsorption of formic acid on anatase being mandatory for its photocatalytic degradation.[64]

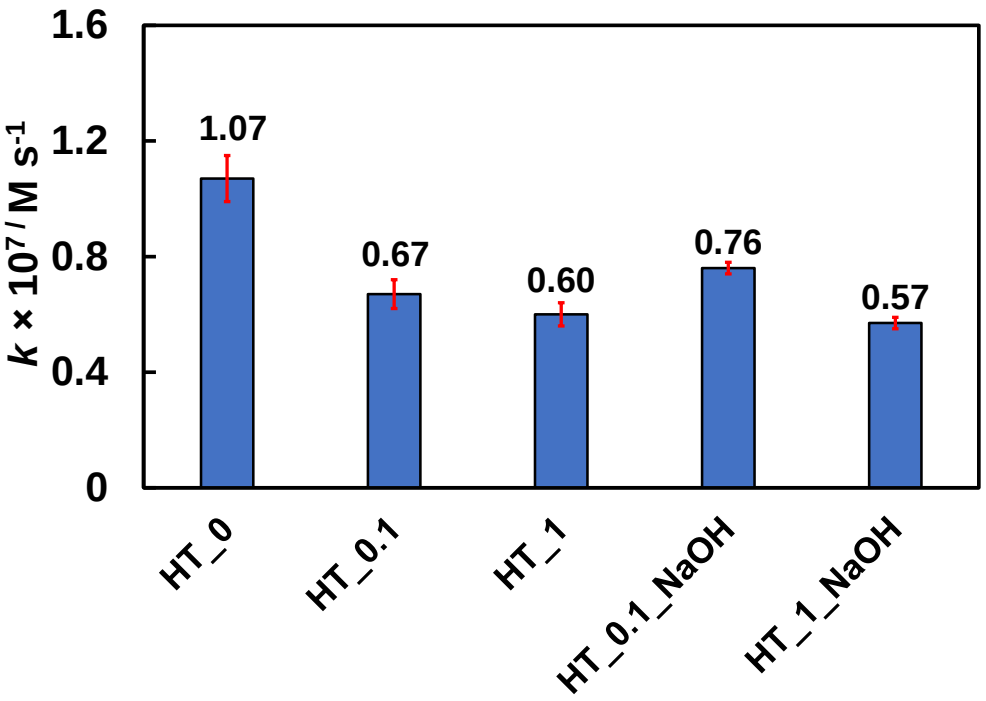

Figure 5.3.7: Pseudo-zeroth order rate constants of formic acid photodegradation obtained with the HT_X and HT_X_W series photocatalysts.

Previous investigations in our research group highlighted that, differently from washing with NaOH, calcining platelet-like materials at 500 °C, despite provoking a *ca.* doubled percentage (101) facets exposure due to nanoparticles sintering driven by minimization of surface energy, provoked a large improvement of the photocatalytic activity of the materials, with calcined platelet-like materials bearing a much higher photocatalytic activity than pseudo-spherically shaped mainly exposing (101) facets.[29] Thus, a higher exposure of (001) facets is indeed beneficial in the photocatalytic degradation of the formic acid. These results suggest that fluoride anions adsorbed on (001) facets could possibly prevent the adsorption of formic acid so efficiently that even the small amount of fluoride anions residual after the washing procedure with NaOH (Figure 5.3.6) could highly restrain the adsorption of the substrate on such facets, thus hindering any possible beneficial effect deriving from a higher exposure of more reactive (001) facets, in spite of the

surface removal treatment. On the other hand, high temperature calcination, leading to the complete removal of fluoride anions, allows to fully reveal the beneficial effect of (001) facets in the here investigated test reaction. It should be noted, however, that in the case of calcined materials it is very difficult to ascertain the origin of the photoactivity improvement observed after the thermal treatment to remove fluoride anions, as several properties of the material may be affected by heat treatment, such morphology changes.

5.3.3 Cr(VI) adsorption and photocatalytic reduction

The effects induced on Cr(VI) adsorption on the investigated samples by the *in-situ* surface fluorination and by the TiO_2 morphology can be appreciated in Figure 5.3.8, reporting the relative percent amounts of Cr(VI) adsorbed on HT_0.1_NaOH and HT_1_NaOH, both in the absence (blue) and in the presence (yellow) of fluoride ions at pH 3.7.

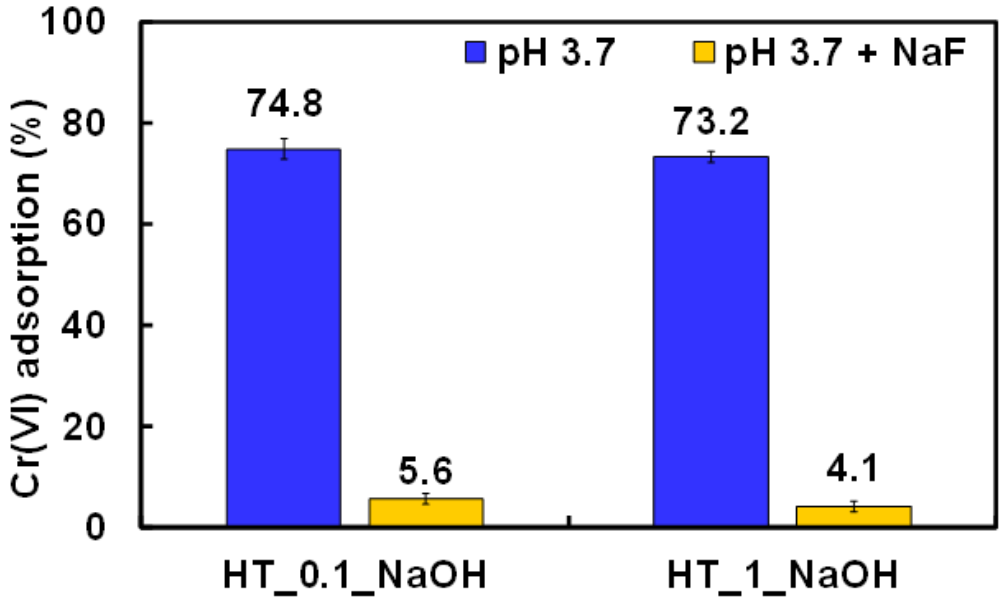

Figure 5.3.8: Percent amount of adsorbed Cr(VI) onto HT_0.1_NaOH and HT_1_NaOH after 180 min stirring in the dark at pH 3.7 in the absence of fluoride ions (blue) and under in-situ fluorinated conditions with a F/Ti ratio equal to 0.1 at the same pH (yellow).

The adsorption of dichromate species is strongly hampered upon *in-situ* surface fluorination on both materials, even for the relatively low F/Ti molar ratio here employed (corresponding to 0.1). In fact, in the absence of fluoride anions, the surface of titanium dioxide is rich in surface bound terminal $\equiv Ti-OH$ groups, which play a key role in ensuring dichromate adsorption on TiO_2 by means of surface complexation.[65] Moreover, at pH 3.7, the titanium dioxide surface is expected to be positively charged, this pH being below the zero charge (pH_{pzc}) of TiO_2, generally located for TiO_2-based materials at pH 5.6.[66] These combined effects of course allow for a fast and significant (almost quantitative) adsorption of negatively charged $Cr_2O_7^{2-}$ anions on the TiO_2

surface.[30,67] Differently, *in-situ* fluorination implies the formation of stable $\equiv Ti - F$ termination on the TiO_2 surface, with a consequent shift of the surface charge towards more negative values, which hinders the dichromate anions adsorption on the surface of titanium dioxide,[68] as evidenced in Figure 5.3.8.

In the absence of light, both HT_0.1_NaOH and HT_1_NaOH samples are equally able to adsorb dichromate ions. So, the relative percent amounts of the inorganic anionic species adsorbed on the investigated TiO_2 photocatalysts seems not to be affected by the relative {001} facets exposure, either in the absence or in the presence of *in-situ* added fluoride ions.

The activity of the here investigated TiO_2 samples in Cr(VI) photocatalytic reduction can be compared in terms of first order rate constants, measured either in aqueous suspensions at pH 3.7 (k_{ac}) and at pH 3.7 in the presence of fluoride anions (*in-situ* fluorinated surface, k_F), as shown in Figure 5.3.9.

Firstly, among the HT_X_NaOH samples, *i.e.,* showing different relative percentages of clean {001} facets, the plate-like material is by far the best photocatalyst, with an activity double to that of commercial benchmark P25 TiO_2 (for which $k_{ac} = 3.3 \cdot 10^{-4}$ s^{-1}).

Interestingly, the outstanding photoactivity attained by increasing the percentage of exposed {001} TiO_2 facets, the k_{ac} attained with HT_1_NaOH being three-times greater than that obtained with HT_0.1_NaOH, cannot be explained by taking into account the similar dichromate anions adsorption under dark conditions on the platelet-like and the spherical-shaped washed samples (Figure 5.3.8). Such a significant photoactivity improvement should result from multiple positive effects related to the titania crystal morphology.

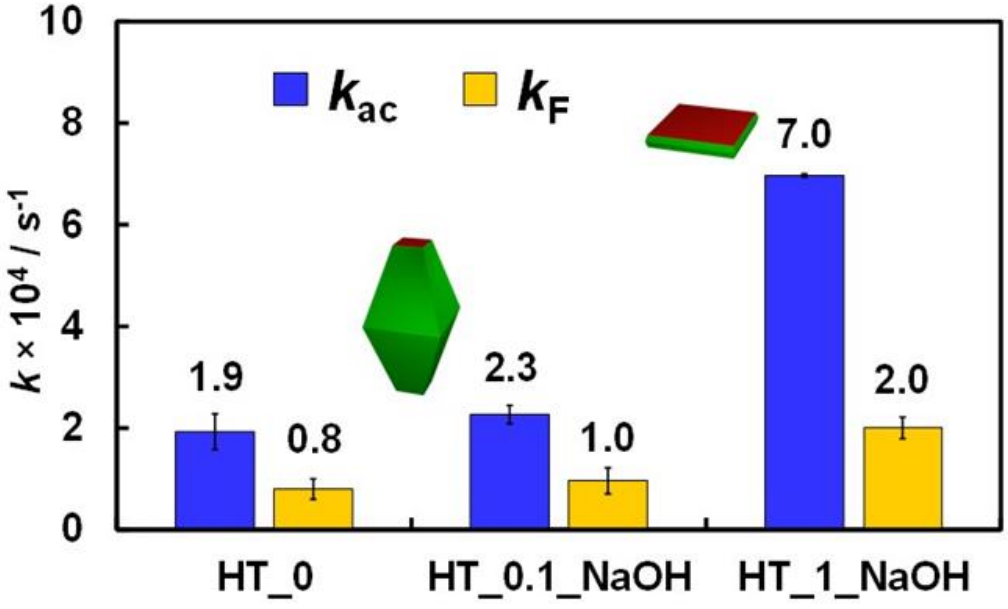

Figure 5.3.9: First order rate constants of Cr(VI) photoreduction at pH 3.7 (k_{ac}, in blue) and upon in-situ fluorination at the same pH (k_F, in yellow).

In fact, a significant enhancement in the effective photogenerated charge carrier separation may be attained with increasing the {001} facets exposure in TiO_2, leading to platelet-like better performing materials.[57,69-71] Interestingly, anatase crystals with different co-exposed facets can be envisaged forming 'surface heterojunctions',[57,62,69] with the selective migration of photogenerated holes and electrons towards {001} and {101} facets, respectively, being driven by the minimization of their respective energies. In particular, an optimal percent mixture of different anatase facets might have positive effects in electron-hole pair separation, as in mixed anatase-rutile systems.[72] Of course, the optimal percent amount of exposed {001} facets in anatase materials, ensuring the highest photoactivity, depends on the relative rates of the two simultaneous (reduction and oxidation) semi-reactions involved in the overall investigated photocatalytic process, the best charge carrier separation being generally gained for anatase samples with ca. 50-60% of {001} facets content. Interestingly, He *et al.*[22] reported a maximum photoactivity in Cr(VI) reduction for TiO_2 materials showing a 72% amount of {001} facets, which is comparable to the {001} facets exposure of the here investigated best performing HT_1_NaOH sample. This confirms that a balanced exposure of {001} and {101} facets is needed to achieve an optimal distribution of electrons and holes between them, possibly depending on the peculiar investigated substrate-sensitive process.[57]

In addition, the overall efficiency of photocatalytic processes is generally affected by the extent and mode of substrate adsorption, which may also depend on the type of crystal facets predominantly exposed by the anatase photocatalyst, since facets differ in their surface atomic structure.[73,74]

In the specific case of Cr(VI) photocatalytic reduction, {001} facets, displaying 100% unsaturated surface Ti-5c and undercoordinated O-2c atoms, tend to favour the dissociative adsorption/chemisorption of water (or methanol) molecules, accompanied by the formation of terminal Ti−OH species,[75,76] possibly in a larger extent under irradiation conditions. Such TiO_2 surface bound -OH moieties may thus behave as crucial adsorption sites for promoting fast and efficient dichromate anions adsorption,[30,65] resulting in their faster conversion to Cr(III) through their direct interaction with electrons photopromoted in the TiO_2 conduction band.[67] The presence of a relatively high amount of {001} facets may be necessary in order to promote the overall water oxidation semi-reaction, with a consequent beneficial effect also on the simultaneous photocatalytic Cr(VI) photocatalytic reduction process.

The combination of both electronic and adsorption effects, therefore, may lead to higher rates of dichromate photoreduction on the {001}-facet enriched TiO_2 material, highlighting a TiO_2 facet-dependent photoactivity in the photocatalytic degradation of Cr(VI).

Regardless of the specific TiO_2 morphology, *in-situ* surface fluorination of washed samples leads to a conspicuous (*ca.* 60-70%) photoactivity decrease, most probably consequent to a dramatically reduced adsorption of negatively charged $Cr_2O_7^{2-}$ ions (Figure 5.3.9). This confirms the major role played by the specific substrate-TiO_2 interactions on the overall efficiency of Cr(VI) photocatalytic reduction. However, the photoactivity decrease, though clearly evident, is not as strong as the *ca.* 90% substrate adsorption inhibition effect induced by *in-situ* fluorination (Figure 5.3.8). This finding is in line with a previous research carried out by Ku *et al.,*[30] in which the pH effect on the photocatalytic reduction of Cr(VI) was found to have a trend different than the Cr(VI) adsorption capability on the TiO_2 surface. Thus, dichromate anions adsorption on TiO_2 does not represent the only parameter determining the rate of Cr(VI) photoreduction, the overall photocatalytic process being also affected by the photogenerated electrons transfer towards dichromate anions, occurring after the adsorption step.

5.3.4 Rhodamine B adsorption and photocatalytic oxidation

Figure 5.3.10 shows the relative percent amounts of RhB adsorbed on the pseudo-spherical and platelet-like shaped materials (*i.e.,* HT_0.1_NaOH and HT_1_NaOH, respectively) in adsorption tests performed at pH 3.7 (blue) and at this pH in the presence of fluoride anions, with a F/Ti ratio corresponding to 2 (yellow).

The adsorption of the cationic dye on the TiO_2 surface at pH 3.7 is rather poor and further inhibited by *in-situ* TiO_2 fluorination, most likely due to alterations of the adsorption equilibrium at the water-TiO_2 interface induced upon substitution of $\equiv Ti-OH$ terminal groups with $\equiv Ti-F$ moieties, in line with previous findings achieved with other organic dyes.[64,77] The adsorption of the organic substrate seems to be slightly hindered by a platelet-like TiO_2 morphology and this effect is maintained upon *in-situ* fluorination of the TiO_2 surface. In fact, as evidenced in Figure 5.3.10, the relative percent amounts of adsorbed RhB decreased by *ca.* 76% and 66%, upon fluoride ions addition, for HT_1_NaOH and HT_0.1_NaOH, respectively. This finding may indirectly suggest a more extensive {001} surface coverage with fluorinated sites, accompanied by a more marked inhibition of RhB surface adsorption.

Firstly, in order to check that RhB photobleaching occurs thorough the photocatalytic path (and not through self-degradation), the photostability of Rhodamine B was confirmed by 6-hours long experiments at pH 3.7, both in the absence and in the presence of fluoride anions, under the here adopted irradiation conditions.

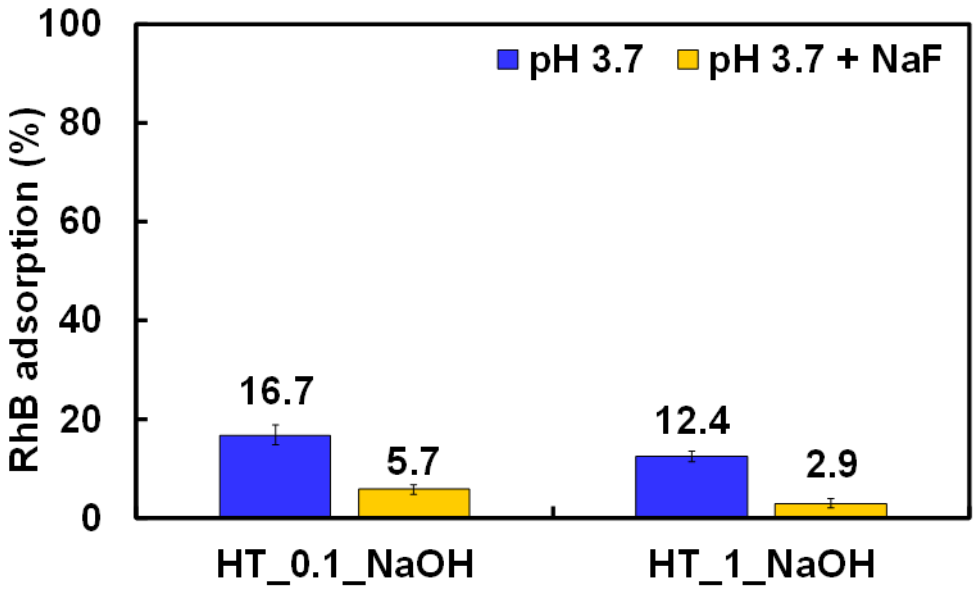

Figure 5.3.10: Percent amounts of adsorbed RhB on HT_0.1_NaOH and HT_1_NaOH after 180 min stirring in the dark in the absence of fluoride at acidic pH (blue) and at acidic pH in the presence of a F/Ti ratio in aqueous suspension equal to 2 (yellow).

The photocatalytic degradation of Rhodamine B always occurred according to a first-order kinetics. The intensity of the RhB maximum absorption at 553 nm always gradually decreased during the degradation runs, with a very limited hypsochromic shift in the absorption spectrum, without the appearance of any other absorption features (Figure 5.3.11a). This excludes the formation of high concentration of light absorbing species during the runs. Consequently, the absorbance values at 553 nm can be taken as only due to RhB absorption.

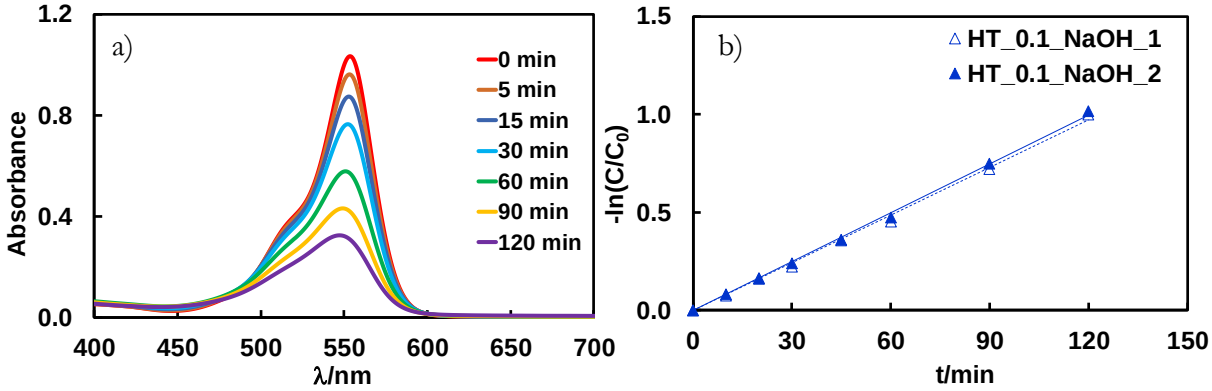

Figure 5.3.11: RhB absorption spectra recorded during its photocatalytic degradation in aqueous suspension at pH 3.7 on HT_0.1_NaOH (a) and data elaboration according to first order plots obtained in two runs under identical conditions (b).

This finding, in line the literature data,[31,78,79] supports the idea that the RhB oxidative degradation mainly proceeds through the cleavage of the RhB chromophore group, which may occur 1) via the direct interaction of RhB molecules with positive valence band holes (h_{VB}^{+}) photogenerated on the semiconductor surface, or 2) through the indirect $^{\bullet}OH$ radicals-mediated degradation mechanism.

The photoactivity trend of the home-made photocatalysts in RhB bleaching is shown in Figure 5.3.12, in terms of first order rate constants, determined in aqueous suspensions at natural pH (k_{nat}), or measured at pH 3.7 in the absence (k_{ac}) or in the presence of fluoride ions (*in-situ* fluorinated surface, k_F). The photoefficiency shown by the plate-like sample at natural or acidic pH is quite similar to that attained with samples mainly exposing {101} facets. Thus, the specific TiO_2 morphology does not significantly affect RhB photodegradation, at difference with respect to Cr(VI) photoreduction. Moreover, while lowering the pH has a negligible effect on the reaction rate, the *in-situ* fluorination is beneficial, although it hinders RhB surface adsorption.

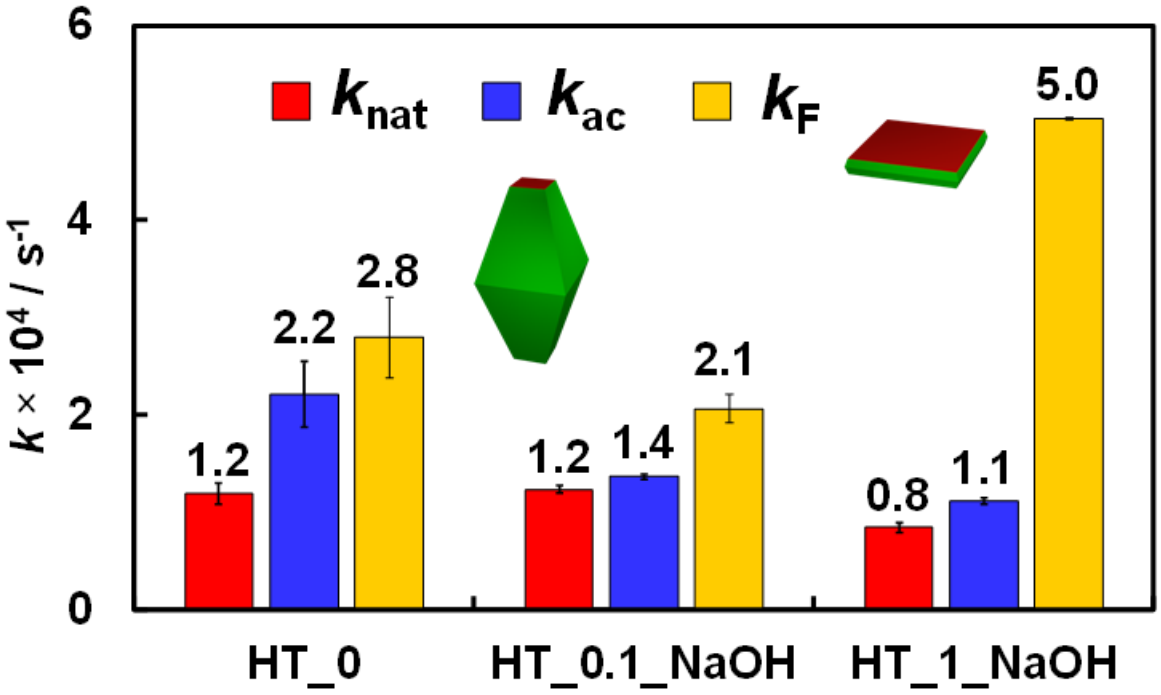

Figure 5.3.12: First-order rate constants of RhB photodegradation for the HT series samples in the absence of fluorides at natural pH (red, k_{nat}), at acidic pH (blue, k_{ac}) or at acidic pH in the presence of a F/Ti ratio equal to 2 (yellow, k_F).

Due to the relatively poor RhB adsorption on the investigated materials surface, it is likely to expect that, differently from Cr(VI) photoreduction, a direct reaction mechanism occurring between the positive valence band holes (h_{VB}^+) photogenerated on the photocatalyst surface and the adsorbed substrate molecules cannot be envisaged as the main RhB photobleaching path. The interaction of the dye molecules with hydroxyl radicals, formed upon h_{VB}^+-induced oxidation of water molecules, may play a more important role on the overall photocatalytic degradation mechanism of the organic substrate, especially in the case of *in-situ* fluorinated TiO_2 materials, for which the RhB surface adsorption capability resulted to be extremely hindered (Figure 5.3.10).

In this context, an increase in RhB degradation rate upon TiO_2 surface fluorination can only be explained by considering an enhanced photoproduction of $^{\bullet}OH$ radicals, which may attack RhB molecules, thus promoting their photodegradation.[31,32,80] In fact, fluoride ions substituting for TiO_2

surface –OH groups inhibit surface trapping of photogenerated holes as ≡Ti-O˙ species, through the following reaction:

$$\equiv \mathrm{Ti} - \mathrm{OH} + \mathrm{h}_{vb}^{+} \rightarrow \equiv \mathrm{Ti} - \mathrm{O}^{\bullet} + \mathrm{H}^{+} \qquad (5.3.1)$$

At the same time, by considering that $\equiv \mathrm{Ti} - \mathrm{F}$ species are stable and cannot be oxidized by valence band holes even at the here employed acidic pH,[64] surface –F ions favour the desorption of photogenerated active species, *i.e.*, ˙OH free radicals, which can thus accumulate in the aqueous phase[81] as follows:

$$\equiv \mathrm{Ti} - \mathrm{F} + \mathrm{h}_{vb}^{+} + \mathrm{H_2O} \rightarrow \equiv \mathrm{Ti} - \mathrm{F} + \mathrm{HO}^{\bullet} + \mathrm{H}^{+} \qquad (5.3.2)$$

In particular, an outstanding photoactivity increase is observed upon surface fluorination of the {001}-facet enriched HT_1_NaOH sample, with a k_F/k_{ac} ratio of 4.52 (Table 5.3.2). Thus, a synergistic effect induced by the plate-like anatase TiO_2 morphology and its *in-situ* surface fluorination is clearly outlined in RhB degradation. Moreover, as reported in Table 5.3.2, similar k_F/k_{ac} ratios were obtained for both HT_1_NaOH and HT_1, which were significantly higher than the k_F/k_{ac} ratios obtained for the HT_0.1_NaOH and HT_0.1. This provides a further confirmation of the here unveiled synergistic effect.

In particular, the absence of any significant morphology-dependent RhB adsorption effect on fluorinated TiO_2 surfaces suggests that such rate increase is related to the intrinsic ability of F-{001} facets of boosting ˙OH radical mediated oxidation paths, possibly due to an improved charge carriers separation. A cooperative contribution in improving the separation of photogenerated charge carriers upon fluorination of {001}-facet enriched materials may be at the origin of the here observed morphology-dependent synergistic effect, as previously reported by Chen *et al.* for the gas phase photocatalytic oxidation of ammonia.[82] The spontaneous tendency of photogenerated holes to migrate towards {001} facets[57,69,70] is amplified by the electric-field effect induced by fluorination,[83] promoting holes attraction towards {001} facets (present in larger extent) and photogenerated electrons repulsion from {101} facets, with a consequent overall beneficial increase of photogenerated charge carriers separation.

Moreover, the beneficial effect of surface fluorination on the photoactivity of plate-like TiO_2 in RhB degradation may originate from the presence of specific surface defects and/or the enhanced initial exposure of surface OH groups[75] (due to favored water molecules dissociation), leading to a higher surface density of fluorinated sites, which are involved in the production and accumulation of reactive ˙OH radicals, as discussed above.

Table 5.3.2: Ratios between the rate constants of RhB photodegradation performed under different experimental conditions.

Sample	k_{ac} / k_{nat}	k_F / k_{ac}
HT_0	1.86 ± 0.33	1.26 ± 0.27
HT_0.1_NaOH	1.11 ± 0.04	1.51 ± 0.11
HT_1_NaOH	1.33 ± 0.09	4.52 ± 0.15
HT_0.1	1.41 ± 0.10	1.42 ± 0.22
HT_1	1.22 ± 0.12	4.94 ± 0.02

FT-IR spectroscopy was employed to get better insight at the molecular level into the differences in surface hydration and hydroxylation between HT_0.1_NaOH and HT_1_NaOH. From the black spectra in Figure 5.3.13, obtained after outgassing at room temperature, we observe that both samples show an evident band at 1620 cm^{-1}, ascribed to $\delta(H_2O)$, bending mode of adsorbed water.[75] The H_2O molecules are not isolated, but are interacting via hydrogen bonds as testified by the intense and broad ν(OH) band in the 3600-3000 cm^{-1} range.[84] In this spectral region also the IR signals of OH groups are present, but to properly investigate them it is necessary to remove molecular water by outgassing at increasing temperatures. Heating at 150 °C (blue curves in Figure 5.3.13) considerably decreases the intensity of the $\delta(H_2O)$ band, which finally disappears at 300 °C (grey curves in Figure 5.3.13), molecular water being completely removed from both samples by outgassing at such temperature. Interestingly, from the grey spectra in the ν(OH) spectral region, we note that HT_0.1_NaOH shows only some weak and sharp components at $\nu \geq 3600$ cm^{-1} due to few isolated OH groups.[76,85] Conversely, HT_1_NaOH still exhibits a broad and quite intense band in the 3600-3000 cm^{-1} range, arising from a significant number of hydroxyl groups still present on the {001} facets, which are expected to strongly adsorb water in a dissociative way.[49,86] Finally, outgassing at 500 °C (red curves in Figure 5.3.13) nearly completely removes the OH groups from both samples.

The IR results thus confirm that plate-like TiO_2 shows a considerably higher concentration of OH groups that can be fluorinated and lead to a significantly enhanced production of hydroxyl radicals, which are considered the main oxygen reactive species involved in the photocatalytic oxidation of Rhodamine B molecules.

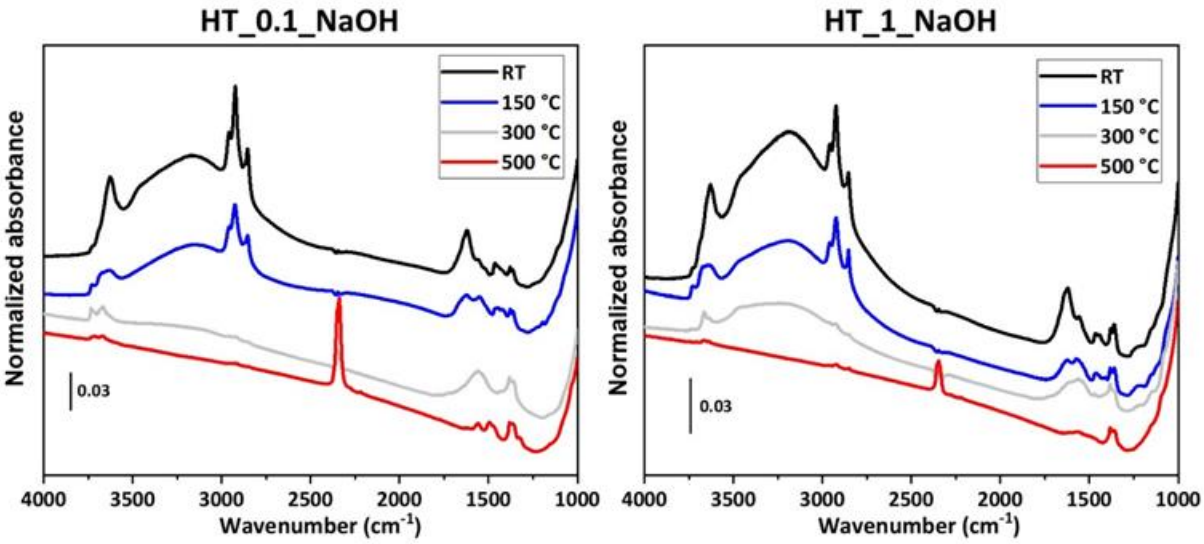

Figure 5.3.13: FT-IR spectra of the HT_0.1_NaOH and HT_1_NaOH samples outgassed for 1 hour at increasing temperatures: room temperature (black curve), 150 °C (blue curve), 300 °C (grey curve) and 500 °C (red curve).

5.4 References

1. Zhou, X., Liu, N. & Schmuki, P. *ACS Catal.* **7**, 3210–3235 (2017).
2. Wang, S., Ding, Z., Chang, X., Xu, J. & Wang, D.-H. *Catalysts* **10**, 1–38 (2020).
3. Gao, M., Zhu, L., Ong, W. L., Wang, J. & Ho, G. W. *Catal. Sci. Technol.* **5**, 4703–4726 (2015).
4. Patil, S. B., Basavarajappa, P. S., Ganganagappa, N., Jyothi, M. S., Raghu, A. V. & Reddy, K. R. *Int. J. Hydrogen Energy* **44**, 13022–13039 (2019).
5. Mittal, A., Mari, B., Sharma, S., Kumari, V., Maken, S., Kumari, K. & Kumar, N. *J. Mater. Sci. Mater. Electron.* **30**, 3186–3207 (2019).
6. Truppi, A., Petronella, F., Placido, T., Striccoli, M., Agostiano, A., Curri, M. L. & Comparelli, R. *Catalysts* **7**, 100 (2017).
7. Bera, S., Won, D. Il, Rawal, S. B., Kang, H. J. & Lee, W. I. *Catal. Today* **335**, 3–19 (2019).
8. Xu, H., Ouyang, S., Liu, L., Reunchan, P., Umezawa, N. & Ye, J. *J. Mater. Chem. A* **2**, 12642–12661 (2014).
9. Li, G. & Gray, K. A. *Chem. Phys.* **339**, 173–187 (2007).
10. Kumar, S. G. & Rao, K. S. R. K. *Appl. Surf. Sci.* **391**, 124–148 (2017).
11. Liu, G., Yu, J. C., Lu, G. Q. & Cheng, H. M. *Chem. Commun.* **47**, 6763–6783 (2011).

12. Ong, W. J., Tan, L. L., Chai, S. P., Yong, S. T. & Mohamed, A. R. *Nanoscale* **6**, 1946–2008 (2014).

13. Dozzi, M. V. & Selli, E. *Catalysts* **3**, 455–485 (2013).

14. Wang, K., Janczarek, M., Wei, Z., Raja-Mogan, T., Endo-Kimura, M., Khedr, T. M., Ohtani, B. & Kowalska, E. *Catalysts* **9**, 1054–1/30 (2019).

15. Maisano, M., Dozzi, M. V. & Selli, E. *J. Photochem. Photobiol. C Photochem. Rev.* **28**, 29–43 (2016).

16. Lv, K., Li, X., Deng, K., Sun, J., Li, X. & Li, M. *Appl. Catal. B Environ.* **95**, 383–392 (2010).

17. Choi, W. *Catal. Surv. from Asia* **10**, 16–28 (2006).

18. Minero, C., Mariella, G., Maurino, V. & Pelizzetti, E. *Langmuir* **16**, 2632–2641 (2000).

19. Kim, J., Choi, W. & Park, H. *Res. Chem. Intermed.* **36**, 127–140 (2010).

20. Mrowetz, M. & Selli, E. *New J. Chem.* **30**, 108–114 (2006).

21. Dozzi, M. V. & Selli, E. *Catal. Today* **206**, 26–31 (2013).

22. He, Z., Cai, Q., Wu, M., Shi, Y., Fang, H., Li, L., Chen, J., Chen, J. & Song, S. *Ind. Eng. Chem. Res.* **52**, 9556–9565 (2013).

23. Li, X., Zhu, J. & Li, H. *Catal. Commun.* **24**, 20–24 (2012).

24. He, Z., Jiang, L., Wang, D., Qiu, J., Chen, J. & Song, S. *Ind. Eng. Chem. Res.* **54**, 808–818 (2015).

25. Wu, H., Ma, J., Li, Y., Zhang, C. & He, H. *Appl. Catal. B Environ.* **152–153**, 82–87 (2014).

26. Mikrut, P., Kobielusz, M. & Macyk, W. *Electrochim. Acta* **310**, 256–265 (2019).

27. Xiang, Q., Lv, K. & Yu, J. *Appl. Catal. B Environ.* **96**, 557–564 (2010).

28. Lv, K., Xiang, Q. & Yu, J. *Appl. Catal. B Environ.* **104**, 275–281 (2011).

29. Maisano, M., Dozzi, M. V., Coduri, M., Artiglia, L., Granozzi, G. & Selli, E. *ACS Appl. Mater. Interfaces* **8**, 9745–9754 (2016).

30. Ku, Y. & Jung, I. L. *Water Res.* **35**, 135–142 (2001).

31. Qu, P., Zhao, J., Shen, T. & Hidaka, H. *J. Mol. Catal. A Chem.* **129**, 257–268 (1998).

32. Qi, L., Yu, J. & Jaroniec, M. *Adsorption* **19**, 557–561 (2013).

33. Ke, J., Adnan Younis, M., Kong, Y., Zhou, H., Liu, J., Lei, L. & Hou, Y. *Nano-Micro Lett.* **10**, 1–27 (2018).

34. Park, H., Park, Y., Kim, W. & Choi, W. *J. Photochem. Photobiol. C Photochem. Rev.* **15**, 1–20 (2013).

35. Chiu, Y. H., Chang, T. F. M., Chen, C. Y., Sone, M. & Hsu, Y. J. *Catalysts* **9**, 430–1/32 (2019).

36. Dozzi, M. V., Saccomanni, A. & Selli, E. *J. Hazard. Mater.* **221–22**, 188–195 (2012).

37. Li, Y. X., Wang, X., Wang, C. C., Fu, H., Liu, Y., Wang, P. & Zhao, C. *J. Hazard. Mater.* **399**, 123085 (2020).

38. Li, Y. X., Fu, H., Wang, P., Zhao, C., Liu, W. & Wang, C. C. *Environ. Pollut.* **256**, 113417 (2020).

39. Palmer, C. D. & Wittbrodt, P. R. *Environ. Health Perspect.* **92**, 25–40 (1991).

40. Bianchi, V., Zantedeschi, A., Montaldi, A. & Majone, F. *Toxicol. Lett.* **23**, 51–59 (1984).

41. Cheng, Y. Y. & Tsai, T. H. *J. Agric. Food Chem.* **65**, 1078–1085 (2017).

42. Spessato, L., Duarte, V. A., Viero, P., Zanella, H., Fonseca, J. M., Arroyo, P. A. & Almeida, V. C. *J. Hazard. Mater.* **411**, 125166 (2021).

43. Dozzi, M. V., Prati, L., Canton, P. & Selli, E. *Phys. Chem. Chem. Phys.* **11**, 7171–7180 (2009).

44. Dozzi, M. V., D'Andrea, C., Ohtani, B., Valentini, G. & Selli, E. *J. Phys. Chem. C* **117**, 25586–25595 (2013).

45. Dozzi, M. V., Montalbano, M., Marra, G., Mino, L. & Selli, E. *Mater. Today Chem.* **22**, 100624 (2021).

46. Bernardini, C., Cappelletti, G., Dozzi, M. V. & Selli, E. *J. Photochem. Photobiol. A Chem.* **211**, 185–192 (2010).

47. Rietveld, H. M. *J. Appl. Crystallogr.* **2**, 65–71 (1969).

48. Coduri, M., Maisano, M., Dozzi, M. V. & Selli, E. *Zeitschrift fur Phys. Chemie* **230**, 1233–1248 (2016).

49. Mino, L., Pellegrino, F., Rades, S., Radnik, J., Hodoroaba, V. D., Spoto, G., Maurino, V. &

Martra, G. *ACS Appl. Nano Mater.* **1**, 5355–5365 (2018).

50. Thommes, M., Kaneko, K., Neimark, A. V., Olivier, J. P., Rodriguez-Reinoso, F., Rouquerol, J. & Sing, K. S. W. *Pure Appl. Chem.* **87**, 1051–1069 (2015).

51. Yu, J., Qi, L. & Jaroniec, M. *J. Phys. Chem. C* **114**, 13118–13125 (2010).

52. Ye, L., Mao, J., Liu, J., Jiang, Z., Peng, T. & Zan, L. *J. Mater. Chem. A* **1**, 10532–10537 (2013).

53. Liu, L., Liu, Z., Liu, A., Gu, X., Ge, C., Gao, F. & Dong, L. *ChemSusChem* **7**, 618–626 (2014).

54. Li, T., Tian, B., Zhang, J., Dong, R., Wang, T. & Yang, F. *Ind. Eng. Chem. Res.* **52**, 6704–6712 (2013).

55. Luan, Y., Jing, L., Xie, Y., Sun, X., Feng, Y. & Fu, H. *ACS Catal.* **3**, 1378–1385 (2013).

56. Li, C., Koenigsmann, C., Ding, W., Rudshteyn, B., Yang, K. R., Regan, K. P., Konezny, S. J., Batista, V. S., Brudvig, G. W., Schmuttenmaer, C. A. & Kim, J.-H. *J. Am. Chem. Soc.* **137**, 1520–1529 (2015).

57. Yu, J., Low, J., Xiao, W., Zhou, P. & Jaroniec, M. *J. Am. Chem. Soc.* **136**, 8839–8842 (2014).

58. Bernareggi, M., Dozzi, M. V., Bettini, L., Ferretti, A., Chiarello, G. & Selli, E. *Catalysts* **7**, 301–314 (2017).

59. Wu, G., Wang, J., Thomas, D. F. & Chen, A. *Langmuir* **24**, 3503–3509 (2008).

60. Yu, J. C., Yu, J., Ho, W., Jiang, Z. & Zhang, L. *Chem. Mater.* **14**, 3808–3816 (2002).

61. Dozzi, M. V., Artiglia, L., Granozzi, G., Ohtani, B. & Selli, E. *J. Phys. Chem. C* **118**, 25579−25589 (2014).

62. Pellegrino, F., Sordello, F., Mino, L., Minero, C., Hodoroaba, V. D., Martra, G. & Maurino, V. *ACS Catal.* **9**, 6692–6697 (2019).

63. Monllor-Satoca, D., Lana-Villarreal, T. & Gómez, R. *Langmuir* **27**, 15312–15321 (2011).

64. Mrowetz, M. & Selli, E. *New J. Chem.* **30**, 108–114 (2006).

65. Weng, C. H., Wang, J. H. & Huang, C. P. *Water Sci. Technol.* **35**, (1997).

66. Kosmulski, M. *Adv. Colloid Interface Sci.* **99**, 255–264 (2002).

67. Asuha, S., Zhou, X. G. & Zhao, S. *J. Hazard. Mater.* **181**, 204–210 (2010).

68. Park, H. & Choi, W. *J. Phys. Chem. B* **108**, 4086–4093 (2004).

69. Di Liberto, G., Tosoni, S. & Pacchioni, G. *J. Phys. Chem. Lett.* **10**, 2372–2377 (2019).

70. Ohno, T., Sarukawa, K. & Matsumura, M. *New J. Chem.* **26**, 1167–1170 (2002).

71. Zheng, Z., Huang, B., Lu, J., Qin, X., Zhang, X. & Dai, Y. *Chem. Eur. J.* **17**, 15032–15038 (2011).

72. Deák, P., Aradi, B. & Frauenheim, T. *J. Phys. Chem. C* **115**, 3443–3446 (2011).

73. Lazzeri, M., Vittadini, A. & Selloni, A. **63**, 1–9 (2001).

74. Zhou, P., Zhang, H., Ji, H., Ma, W., Chen, C. & Zhao, J. *Chem. Commun.* **53**, 787–790 (2017).

75. Arrouvel, C., Digne, M., Breysse, M., Toulhoat, H. & Raybaud, P. *J. Catal.* **222**, 152–166 (2004).

76. Mino, L., Morales-García, Á., Bromley, S. T. & Illas, F. *Nanoscale* **13**, 6577–6585 (2021).

77. Park, H. & Choi, W. *J. Phys. Chem. B* **108**, 4086–4093 (2004).

78. Wang, Q., Chen, C., Zhao, D., Wanhong, M. & Zhao, J. *Langmuir* **24**, 7338–7345 (2008).

79. Yao, C., Wang, X., Zhao, W., Li, T., He, Y., Ran, X. & Guo, L. *J. Alloys Compd.* **846**, 156335–1/9 (2020).

80. Hu, Y., Li, D., Wang, H., Zeng, G., Li, X. & Shao, Y. *J. Mol. Catal. A Chem.* **408**, 172–178 (2015).

81. Mrowetz, M. & Selli, E. *Phys. Chem. Chem. Phys.* **7**, 1100–1102 (2005).

82. Chen, M., Ma, J., Zhang, B., He, G., Li, Y., Zhang, C. & He, H. *Appl. Catal. B Environ.* **207**, 397–403 (2017).

83. Sheng, H., Li, Q., Ma, W., Ji, H., Chen, C. & Zhao, J. *Appl. Catal. B Environ.* **138–139**, 212–218 (2013).

84. Mino, L., Negri, C., Santalucia, R., Cerrato, G., Spoto, G. & Martra, G. *Molecules* **25**, 4605 (2020).

85. Mahdavi-Shakib, A., Arce-Ramos, J. M., Austin, R. N., Schwartz, T. J., Grabow, L. C. & Frederick, B. G. *J. Phys. Chem. C* **123**, 24533–24548 (2019).

86. Sun, C., Liu, L. M., Selloni, A., Lu, G. Q. & Smith, S. C. *J. Mater. Chem.* **20**, 10319–10334 (2010

Chapter 6: Effects of Au nanoparticles deposition and *in-situ* Surface Fluorination on the Photocatalytic Activity of Differently Shaped TiO_2 Materials

6.1 Introduction

Photocatalysis appears as a promising technology able to provide answers for the need of a sustainable and greener society due to the possibility to remediate wastewater and air from harmful polluting chemicals in an environmentally friendly and sustainable fashion.[1-8] Moreover, the quest for sustainable energy solutions has driven researchers to explore alternative energy sources such as the conversion of light into chemical energy through photocatalytic processes.[9-13] One of the key challenges in this field is the development of cost-effective and scalable materials. Among these, TiO_2-based materials are particularly attractive for photocatalytic applications due to their many advantageous properties such as versatility, low costs, chemical stability, or non-toxicity.[14-17]

In the recent years, many resources have been expended searching for strategies to overcome the main shortcomings of the transition metal oxide in photocatalysis, *i.e.*, the fast recombination of its photoexcited charge carriers and the need of irradiating the material with highly energetic UV radiation. As a result, in recent years, shape-controlled anatase TiO_2 has emerged as a promising candidate for improving the photoactivity of the metal oxide semiconductor in a wide variety of processes.[18-23] By preferentially stabilizing {001} facets during crystal growth, plate-like nanocrystals can be produced, which are expected to be more reactive than the dominant {101} facets.

At the same time, another possible strategy pursuable to improve the photoactivity of titanium dioxide-based materials in photocatalysis is represented by the modification of its surface with noble metal nanoparticles.[24-30] In fact, metal-semiconductor heterojunctions are particularly attractive in semiconductor science since the equilibration of the Fermi level among the two phases results in the generation of a Schottky barrier, *i.e.*, a potential energy barrier causing the trapping of electrons within the nanoparticle, possibly improving the charge separation of the materials. In

addition, *in-situ* surface fluorination has been proposed as a strategy capable of enhancing the photocatalytic performance of TiO_2, especially in the case of hydroxy radical-mediated degradation paths.[31-34]

The effects on TiO_2 photoactivity induced by both the modification strategies are rather far from trivial and has been found to depend not only on the properties of the specific titanium dioxide support (*e.g.*, its phase composition, extent of surface exposure, or its specific morphology),[35-38] but also on the specific investigated test reaction. For example, we have recently found that whereas the *in-situ* TiO_2 surface fluorination is beneficial for rhodamine B photocatalytic oxidation, especially when applied to nanosheet-shaped materials, the photoactivity of the metal oxide semiconductor drastically dropped upon fluorination in both Cr(VI) photocatalytic reduction and formic acid oxidation.[39] Several other studies have also reported that the specific effects induced by TiO_2 surface fluorination need to be evaluated on the basis of either the specific test reaction and the physico-chemical properties of the employed titanium dioxide material.[35,37,40,41]

The effects on photoactivity deriving from the deposition of noble metal nanoparticles have also been reported to depend on several factors including (but not limited to) the phase composition of the TiO_2 support, the presence of specific surface defects interacting with noble metal nanoparticles, the specific investigated test reaction and the technique employed for the deposition of the nanoparticles.[42-46] Yet, literature reports aimed at systematically investigating the effects played by different metal nanoparticles deposition methods on the photoactivity of differently shaped titanium dioxide materials are still lacking, especially for what concerns the role played by the specific photocatalytic process on potential photoactivity-related effects induced by combining metal nanoparticles deposition and *in-situ* surface fluorination.

In this scenario, the following chapter of this PhD thesis presents a systematic study concerning the role played by Au nanoparticles deposition on the TiO_2 surface on either photocatalytic oxidation and reduction reactions, with a particular focus on: i) the influence of the specific TiO_2 morphology; ii) the use of different Au nanoparticles deposition methods and iii) the potential benefits of coupling surface Au nanoparticles deposition with *in-situ* TiO_2 surface fluorination. The aim is that of providing useful information for preparing better performing titanium-dioxide based composite materials, specifically designed and optimized for a peculiar photocatalytic application.

6.2 Experimental section

6.2.1 Materials preparation

Differently shaped titanium dioxide powders have been prepared according to a slightly modified version of the well-established hydrothermal process described in detail in section 2.2.1 (page 51). In the process, different amounts of concentrated hydrofluoric acid, used as capping agent able to preferentially stabilize {001} surfaces and favoring their exposure, were added to a fixed quantity of titanium isopropoxide in a Teflon liner. The obtained suspension has been then left under stirring in the dark for 15 min and transferred to a stainless-steel autoclave to be heated at 180 °C in an electric oven for 24 hours. The resulting bluish paste has been recovered and washed several times with milli-Q water until the fluoride anion concentration in the supernatant was below 5 ppm (detected through ionic chromatography, Metrohm 761 Compact IC equipped with Metrosep A Supp 4/6 Guard anion column and conductivity detector). Powders were then suspended in 250 cm^3 of 0.1 M NaOH at 60 °C for 1 hour, to be then left under stirring in the dark at room temperature for 12 hours.[47] Solid particles were separated from the sodium hydroxide solution via centrifugation, washed several times with milli-Q water until neutrality of the supernatant was obtained and dried in an electric oven at 70 °C overnight. A fine powder was lastly obtained via grinding in an agate mortar. Samples showing pseudo-spherical morphology were characterized by a F/Ti molar ratio of 0.1 (HT_0.1 series), while materials with a platelet-like morphology, with preponderant exposure of {001} facets, were prepared with an F/Ti ratio of 1.0 (HT_1 series). In order to obtain enough photocatalytic powder for Au NPs deposition, three batches for each sample series were prepared and labeled as HT_0.1_B, with B referring to the batch number, going from 1 to 3. Each batch was modified with a different amount of Au NPs, namely 0.3 wt% (batch 1), 0.5 wt% (batch 2), and 1.0 wt% (batch 3), employing the DP[48] (as described in section 2.3.1, page 54) or P[45] (as described in section 2.4.1, page 56) deposition technique. The resulting samples were indicated as %_HT_X_T, where % represents the Au/TiO_2 weight percentage, X indicates the nominal F/Ti molar ratio employed in the hydrothermal synthesis, while T refers to the adopted deposition technique (DP or P).

6.2.2 Materials characterization

The following techniques were employed for the characterization of the materials:

- X-Ray Powder Diffraction (XRPD), as described in section 2.5.1 (page 63)
- Specific surface area (SSA) measurement, as described in section 2.6.1 (page 69)
- UV-Visible DR Spectroscopy, as described in section 2.7.1 (page 72)
- ICP-OES analysis, as described in section 2.8.1 (page 74)

- HRTEM imaging, as described in section 2.9.1 (page 79)

6.2.3 Photocatalytic activity tests

6.2.3.1 Photocatalytic oxidation of formic acid

Formic acid photodegradation tests were performed according to a well-established procedure described in detail in section 3.1 (page 93).[39,46,50] The photocatalyst concentration was set to 0.17 g dm^{-3}, differently from the 0.1 g dm^{-3} concentration reported in the general description of the experimental procedure.

6.2.3.2 Photocatalytic oxidation of Rhodamine B and Cr(VI) photoreduction

The photocatalytic activity of home-made samples was tested in aqueous suspensions, employing the dye Rhodamine B (RhB) or dichromate ($Cr_2O_7^{2-}$) ions as organic or inorganic degradation substrates, respectively. The photostability of both substrates in aqueous solution was preliminarily verified under the adopted irradiation conditions.

All photocatalytic degradation runs were performed under atmospheric conditions using the setup and experimental procedure described in detail in section 3.2 (page 98) for RhB degradation and section 3.3 (page 101) for Cr(VI) reduction.

6.2.3.3 Photocatalytic hydroxylation of terephthalic Acid

The photocatalytic hydroxylation of terephthalic acid (TA) was performed using the experimental setup and procedure described in detail in section 3.5 (page 107).

6.2.3.4 Hydrogen production by photo-steam reforming of methanol

The photocatalytic activity in hydrogen production from methanol photo-steam reforming was tested using the experimental setup and procedure described in detail in section 3.4 (page 103).

6.3 Results and Discussion

6.3.1 Materials Characterization

Phase composition, as well as morphology of all the synthesized samples, were analyzed via X-Ray Powder Diffraction (XRPD). In all cases, the diffraction patterns of the prepared materials always matched those of pure anatase, with clear indication of the absence of characteristic peaks of other phases, which could be present under the here employed synthetic conditions of titanium dioxide, such as rutile or $TiOF_2$.[51] Moreover, in the case of Au modified materials, the absence of any Au characteristic diffraction peak indicates the deposition of finely dispersed noble metal nanoparticles on the photocatalyst surface, with an average size small enough not to be detected

through XRPD, thus possibly excluding the presence of clustered Au NPs. As observed in our previous works,[39,45,51] the diffraction patterns of all prepared materials are characterized by a broadening of reflections with ($l > h,k$) with increasing nominal F/Ti ratio employed during the materials' hydrothermal treatment, accompanied by a shrinking of the peaks with a strong h component in the 35-50° 2ϑ range, highlighting the morphological evolution of the synthesized materials, passing from a pseudo-spherical shape to a sheet-like morphology (see Figure 6.3.1).

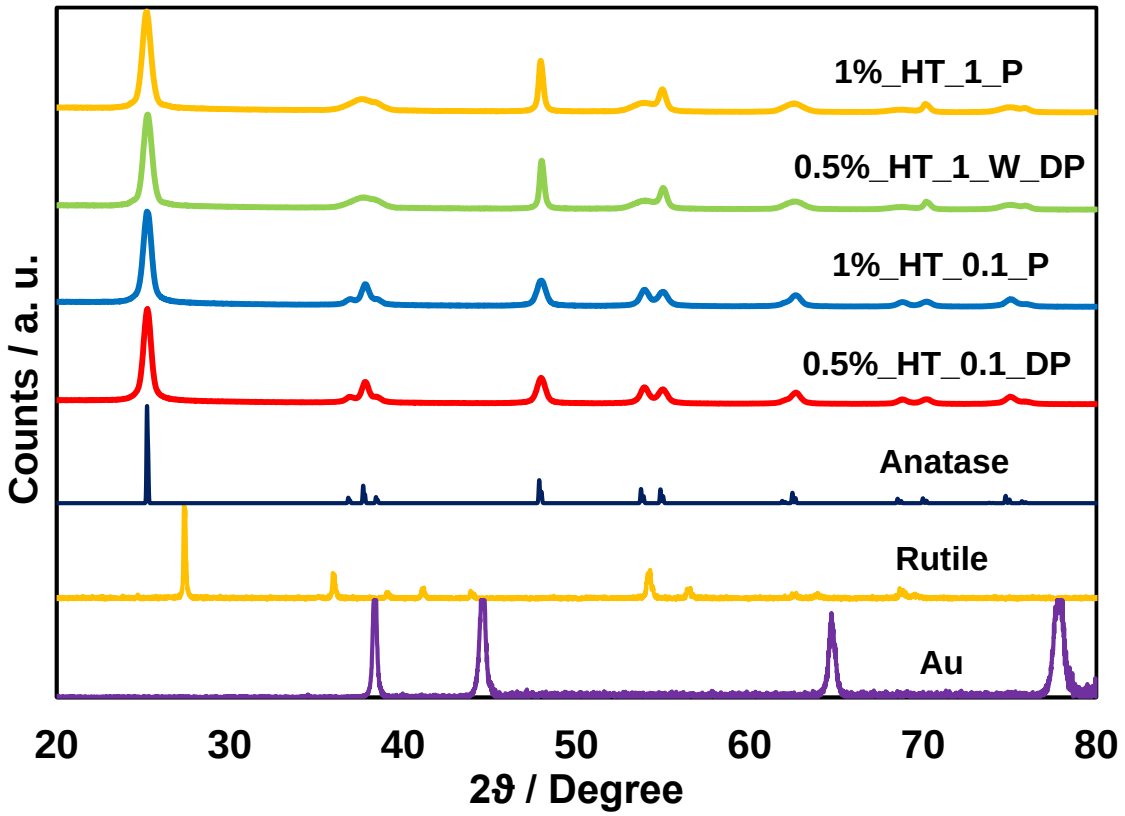

Figure 6.3.1: X-Ray powder diffraction pattern of selected Au-containing 0.5%_HT_0.1_DP (red), 1%_HT_0.1_P (blue), 0.5%_HT_1_DP (green) and 1%_HT_1_P (yellow) samples. XRPD diffractograms referring to pure TiO_2 anatase, TiO_2 rutile and metallic Au are reported for comparison.

Crystallite dimensions along specific crystallographic directions (representing the thickness t and the width w of the crystallites), as well as the relative exposure percentage of {001} surfaces in differently shaped materials, were calculated through a Scherrer equation-based approach[52] and are reported in Table 6.3.1. In line with our previous findings,[39,51] increasing the nominal F/Ti ratio resulted in an increase in the width of the crystallites accompanied by a decrease in their thicknesses, with a consequent drastic increase in the percentage of {001} facets exposed, passing from *ca.* 15% to *ca.* 65% for all the synthesized materials.

Table 6.3.1: Average nanoparticles thickness, width, percentage of {001} facets exposure and BET specific surface area (SSA) of the synthesized pure anatase materials.

Sample	Thickness (t) / nm	Width (w) / nm	{001} (%)	SSA (m^2 g^{-1})
HT_0.1_1	14.80(6)	13.91(3)	**16**	83(3)
HT_0.1_2	18.54(8)	16.47(7)	**14**	81(3)
HT_0.1_3	14.04(4)	14.30(4)	**18**	85(3)
HT_1_1	7.63(2)	37.36(3)	**67**	86(3)
HT_1_2	7.91(2)	37.73(3)	**66**	80(3)
HT_1_3	7.65(1)	36.95(4)	**66**	85(3)

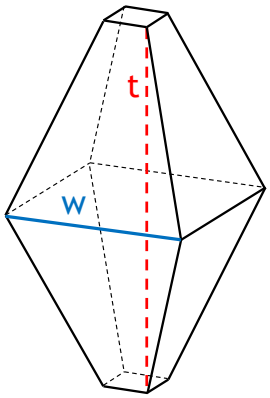

The specific surface area (SSA) of synthesized materials, analyzed via the BET method, resulted to be independent of morphology, thus allowing to directly compare differences in photoactivity of the samples without discrepancies in surface exposure affecting the relative performance of the materials. Moreover, the SSA of the powders also resulted to be unaffected by the deposition of Au NPs. Similarly to our previous findings and observations,[51] BET adsorption/desorption isotherms of all materials can be classified as of type IV, according to IUPAC classification (Figure 6.3.2).[53] The observed porosity originating hysteresis loops is to be attributed to the packing of the crystallites rather than to an actual porosity of the material, as anatase is not inherently porous.[54] However, increasing the amount of nominal F/Ti ratio employed during the synthesis of the materials results in a shift from H2-type pores, associated to "ink bottle" pores typically formed due to packing of sphere-like particles, towards H3-type pores, which are instead usually observed due to the packing of plate-like particles forming slit-shaped pores. This finding, in line with both XRD and HR-TEM measurements (see below), further confirmed the morphological evolution of the prepared materials, undoubtedly passing from pseudo-spheres to nanosheet shaped crystallites.

UV-Visible absorption spectra of pristine TiO_2 materials are characterized by the typical spectroscopic features of pure titanium dioxide, *i.e.,* little-to-no absorption for $\lambda > 400$ nm and a marked absorption at wavelengths below the ~400 nm absorption onset.[55,56] Materials bearing a pseudo-spherical morphology were always characterized by the presence of a small continuous absorption component in the visible region of the spectra, and by a slight bathochromic shift in the position of the absorption edge compared to nanosheet-shaped materials (Figure 6.3.3a,b), although unvaried[57,58] and hypsochromically shifted[51,59] absorption edges have also been previously reported in literature (Figure 6.3.3). In line with these finding, all HT_0.1 samples show a pale grey colour compared to HT_1 materials, which are rather brilliant white (the typical colour of titanium

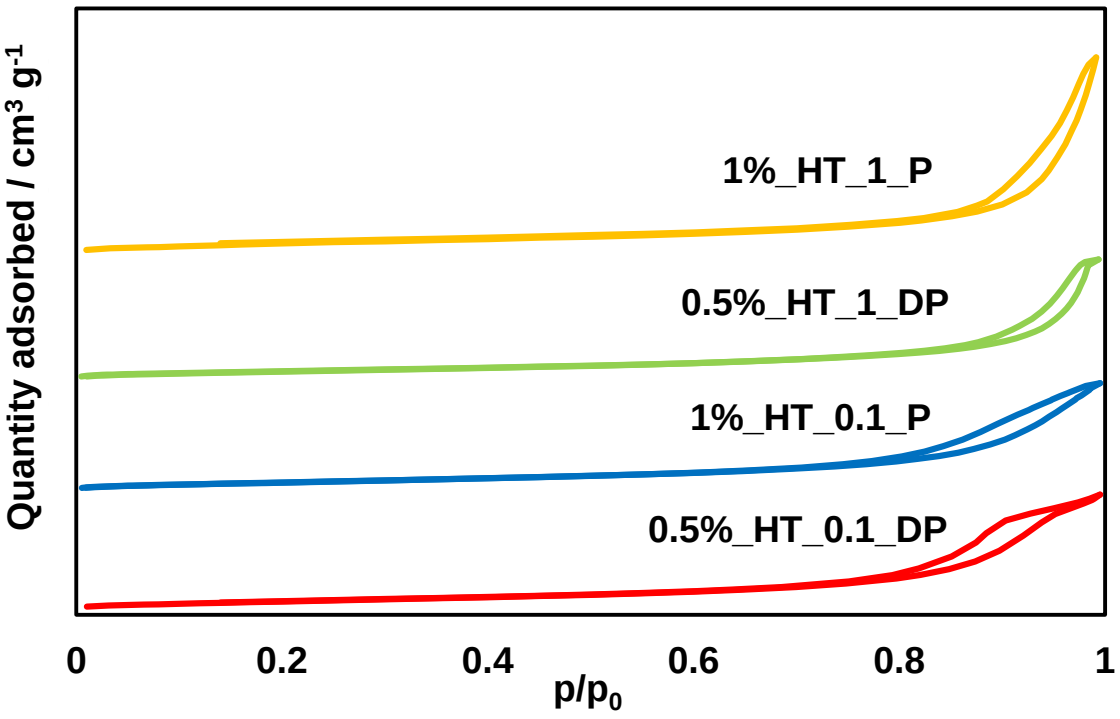

Figure 6.3.2: BET adsorption isotherms of selected Au-containing 0.5%_HT_0.1_DP (red), 1%_HT_0.1_P (blue), 0.5%_HT_1_DP (green) and 1%_HT_1_P (yellow) samples.

dioxide). However, the origin of this absorption is nontrivial. In fact, such absorption cannot be attributed to a greater amount of residual carbon species from the synthesis adsorbed on the surface of HT_0.1 samples, as thermogravimetric analyses (TGA) performed in our previous works (Figure 5.3.4, page 170) on identically synthesized materials showed that the residual adsorbed carbon is the same among all synthesized materials, regardless of their morphology.[60] Currently, we hypothesize such absorption to be most likely related to the presence of a higher amount of inserted fluorine atoms within the bulk structure of HT_0.1 materials compared to HT_1 materials, such atoms being capable to generate localized electrons in the t_{2g} orbitals of Ti cations without forming oxygen vacancies.[61] Such centres may represent occupied electronic states located close in energy to anatase TiO_2 CB, thus allowing electronic transitions in the 400-800 nm range. However, such statement should be considered only as an hypothesis, requiring a more in-depth investigation to be verified.

The deposition of Au metal nanoparticles on the surface of titanium dioxide led to the appearance of the typical localized surface plasmon resonance (LSPR) absorption band in the absorption spectra of all metal modified materials, with its characteristic peak centered around 550 nm,[42,62,63] as also evidenced by the chromatic shift in the color of the powders, passing from brilliant white to deep purple (Figure 6.3.3). Materials modified with 0.3 and 0.5 wt% of Au were characterized by a similar intensity, absorption profile and maximum positioning of the plasmonic

absorption band (further evidenced by the here reported absorption difference spectra, *i.e.,* obtained by subtracting the absorption spectra of the bare materials from those of the corresponding metal-modified sample, Figure 6.3.3) regardless of the support morphology or the method chosen for the nanoparticles deposition, possibly indicating the growth of noble metal nanoparticles with similar average size, distribution, in similar amount on the surface of the supports.[46,64] Differently, materials modified with 1% of Au show markedly differing absorption intensities in the plasmonic region, possibly indicating a non-quantitative deposition of the metal nanoparticles over the surface of the transition metal oxide for materials prepared with the deposition-precipitation technique under the here employed experimental conditions. These data highlight the incomplete anchoring of the metal nanoparticles at the relatively high loading degree of a cocatalyst deposited by means of the DP method only. In fact, the photodeposition method allowed to obtain a quantitative deposition of the cocatalyst regardless of the employed nominal loading. This conclusion is also supported by the experimental observation of the supernatant of the suspension turning to a very dark brownish-to-black color upon addition of $NaBH_4$ to the separated liquid portion present in the synthesis' slurry. This procedure was systematically employed during the preparation of each Au-containing material as a double-check test for investigating if non-adsorbed metal cations were left in the supernatant of the slurry. Such phenomenon, observed only in the case of 1%_HT_X_DP materials, very likely originates from the formation of unsupported metal nanoparticles in solution. For such reason, materials modified with 1 wt% of Au prepared through the DP method were excluded from further discussion and/or characterization and photoactivity tests.

The actual quantitative Au wt% loading value was obtained by means of ICP-OES analysis (Table 6.3.2), which proved loading of noble metal values very close to the nominal ones. Most importantly, samples with the same nominal ratio appear to be modified with very similar weight percentages of gold, confirming the deposition of comparable amounts of metal nanoparticles for all materials modified with the same nominal gold content. An exception is represented by the two samples modified with 1 wt% of Au, for which the percentage of Au loading significantly differs between them, as previously highlighted through DRS data (Figure 6.3.3).

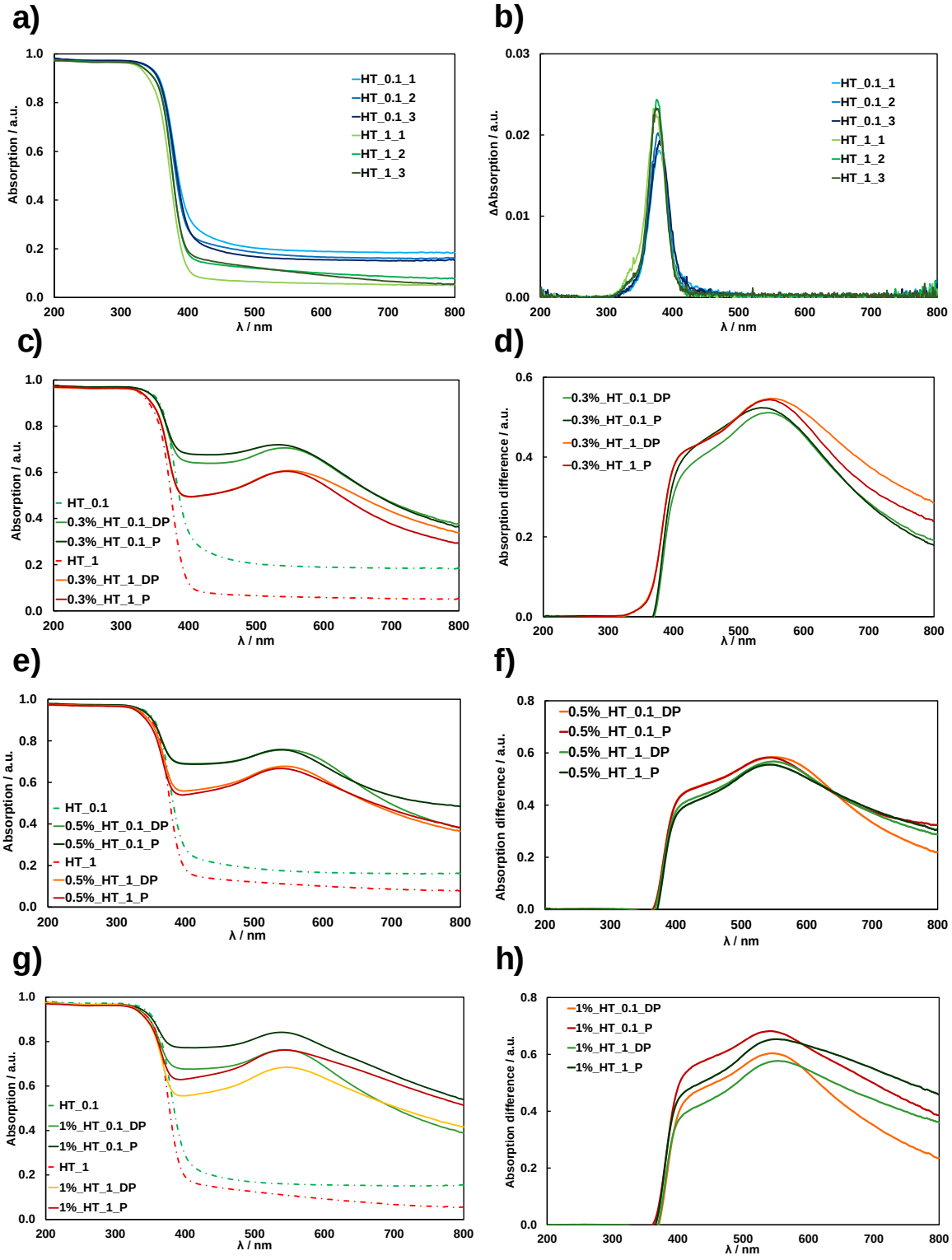

Figure 6.3.3: UV-Vis DRS absorption spectra of differently shaped titanium dioxide materials (a) modified with 0.3 wt% (c), 0.5 wt% (e) and 1 wt% (g) of Au nanoparticles and their corresponding absorption difference spectra (d, f, h); first order derivative absorption spectra of differently shaped titanium dioxide materials, illustrating no significant shift of the absorption edge with increasing truncation degree of the materials (b).

The morphological evolution of the materials, passing from a pseudo-spherical to a platelet-like shape, was undoubtedly confirmed via HR-TEM imaging (Figure 6.3.4), which shows TiO_2 crystallites with thicknesses and widths comparable with those calculated via powder diffraction analysis (Table 6.3.1). Congruently with our previous findings, TiO_2 nanosheets tend to pile in a face-to-face configuration to minimize their surface energy, whereas randomly aggregated nanoparticles were instead observed for HT_0.1 materials.[39,65,66]

Table 6.3.2: Au wt.% deposited on differently shaped titanium dioxide anatase materials obtained via ICP-OES analysis.

Sample	Au wt%
0.3%_HT_0.1_DP	0.30(2)
0.3%_HT_0.1_P	0.29(2)
0.3%_HT_1_P	0.28(2)
0.5%_HT_0.1_DP	0.49(3)
0.5%_HT_1_DP	0.50(3)
0.5%_HT_1_P	0.48(3)
1%_HT_0.1_P	1.04(1)
1%_HT_1_P	0.97(1)

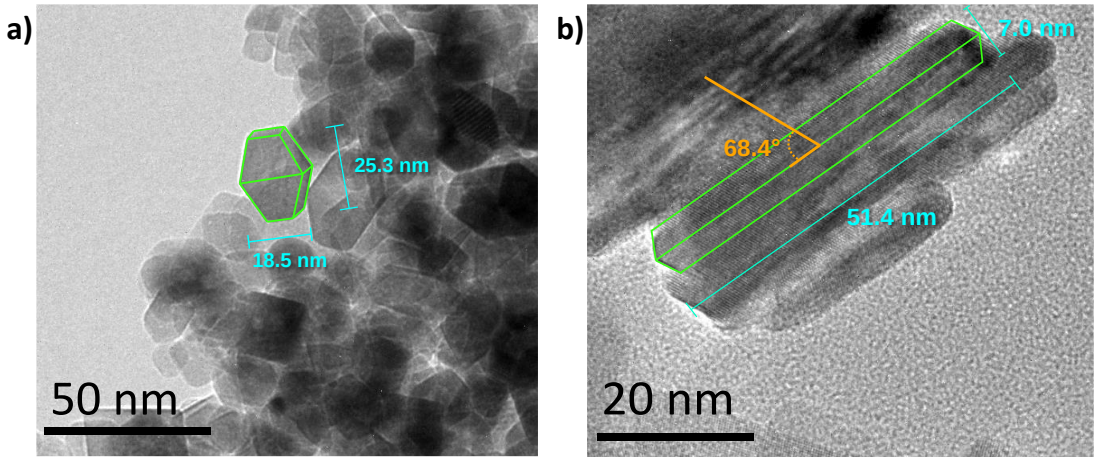

Figure 6.3.4: HR-TEM images highlighting the morphology of HT_0.1 (a) and HT_1 (b) materials. Incident angle between diffraction planes illustrated in (b) is perfectly compatible with the theoretical value calculated between {001} and {101} planes in anatase (68.7°).

HR-TEM images of Au-modified powders (Figure 6.3.5 - Figure 6.3.7) allowed us not only to confirm the actual deposition of metallic gold NPs on the TiO_2 surface, but also to study their average size and distribution. Finely dispersed, spherically shaped Au NPs were, in fact, deposited on the surface of the investigated materials regardless of the method chosen for their modification, the morphology of TiO_2 or the amount of deposited Au. Congruently with literature reported data, the distribution of the deposited Au NPs diameters always behaved according to slightly positively skewed lognormal distributions,[67-69] as confirmed by the non-rejection of the null hypothesis for the Kolmogorov-Smirnov test ($\alpha = 0.05$).[70] In all cases, Au nanoparticles with similar average sizes

and variance were deposited on the surface of the photocatalysts, with mean diameters in the 6-10 nm range, regardless of the morphology of the support, the Au wt.% loading or the technique employed for its deposition.

For neither adopted methods (DP or P) a preferential deposition of noble metal nanoparticles on either {001} or {101} facet was observed from TEM images, being very difficult to discern on which crystal facets the metal particles are deposited on (see below). In fact, while in the case of DP-modified materials a random, non-selective nor preferential deposition of finely dispersed noble metal nanoparticles is expected to be obtained, when the photodeposition (P) method is used, a preferential deposition of Au nanoparticles over {101} surfaces can possibly be obtained, as a consequence of the expected preferential migration of electrons towards such facets. However, the characterization techniques employed during this PhD work were unable to clarify if Au NPs may be preferentially loaded on specific TiO_2 crystalline facets as a function of the adopted deposition method (P nor the DP).

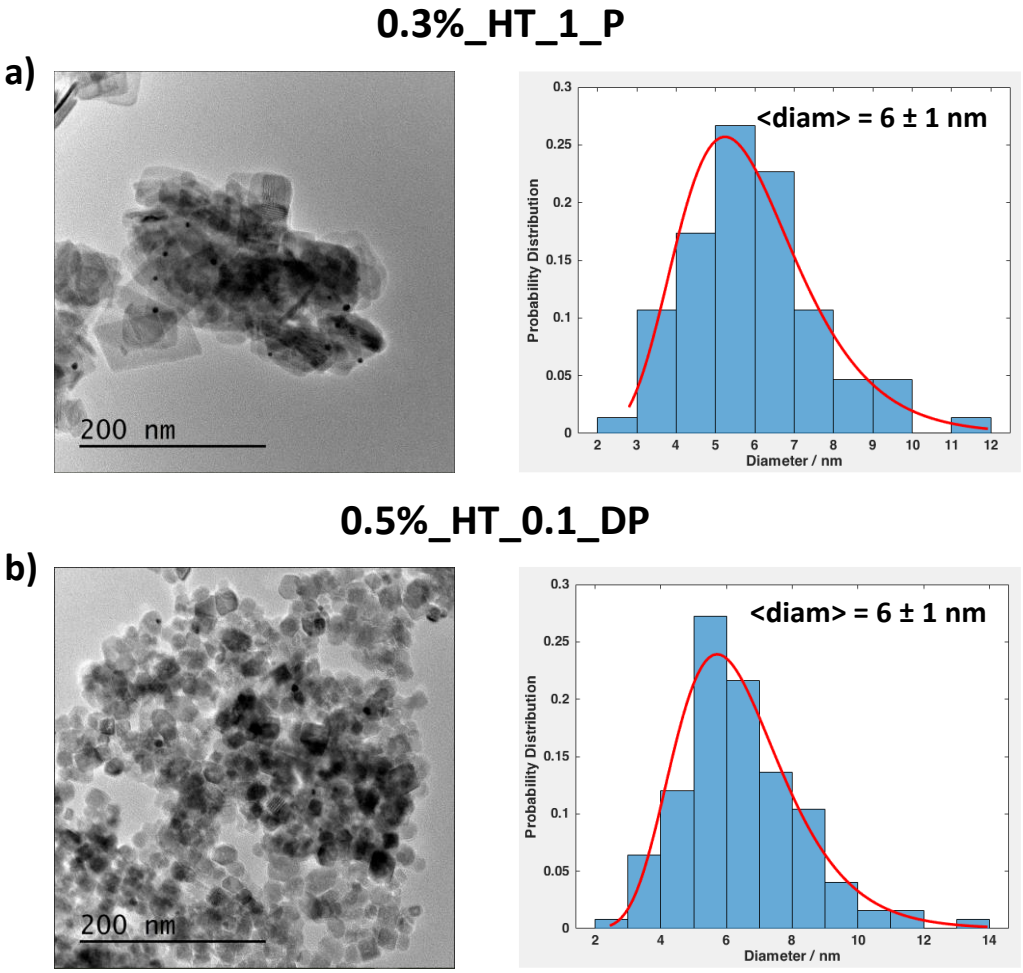

Figure 6.3.5: Transmission Electron Microscopy images and corresponding Au nanoparticles diameter distributions of differently shaped titanium dioxide materials modified with different amounts of noble metal nanoparticles by means of the DP and P technique. The total Au NPs counts ranged from 100 to 200 counts.

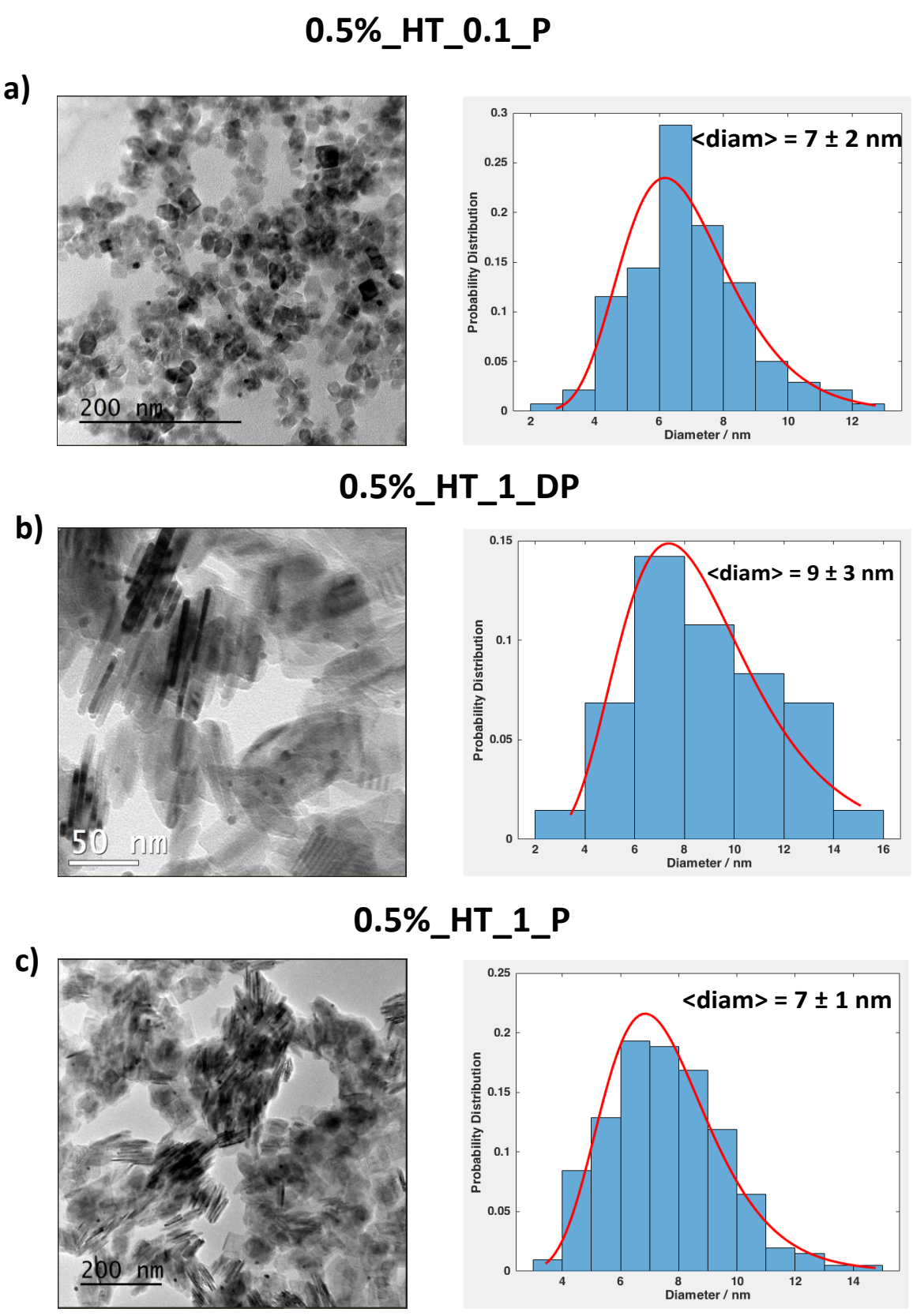

Figure 6.3.6: Transmission Electron Microscopy images and corresponding Au nanoparticles diameter distributions of differently shaped titanium dioxide materials modified with different amounts of noble metal nanoparticles by means of the DP and P technique. The total Au NPs counts ranged from 100 to 200 counts.

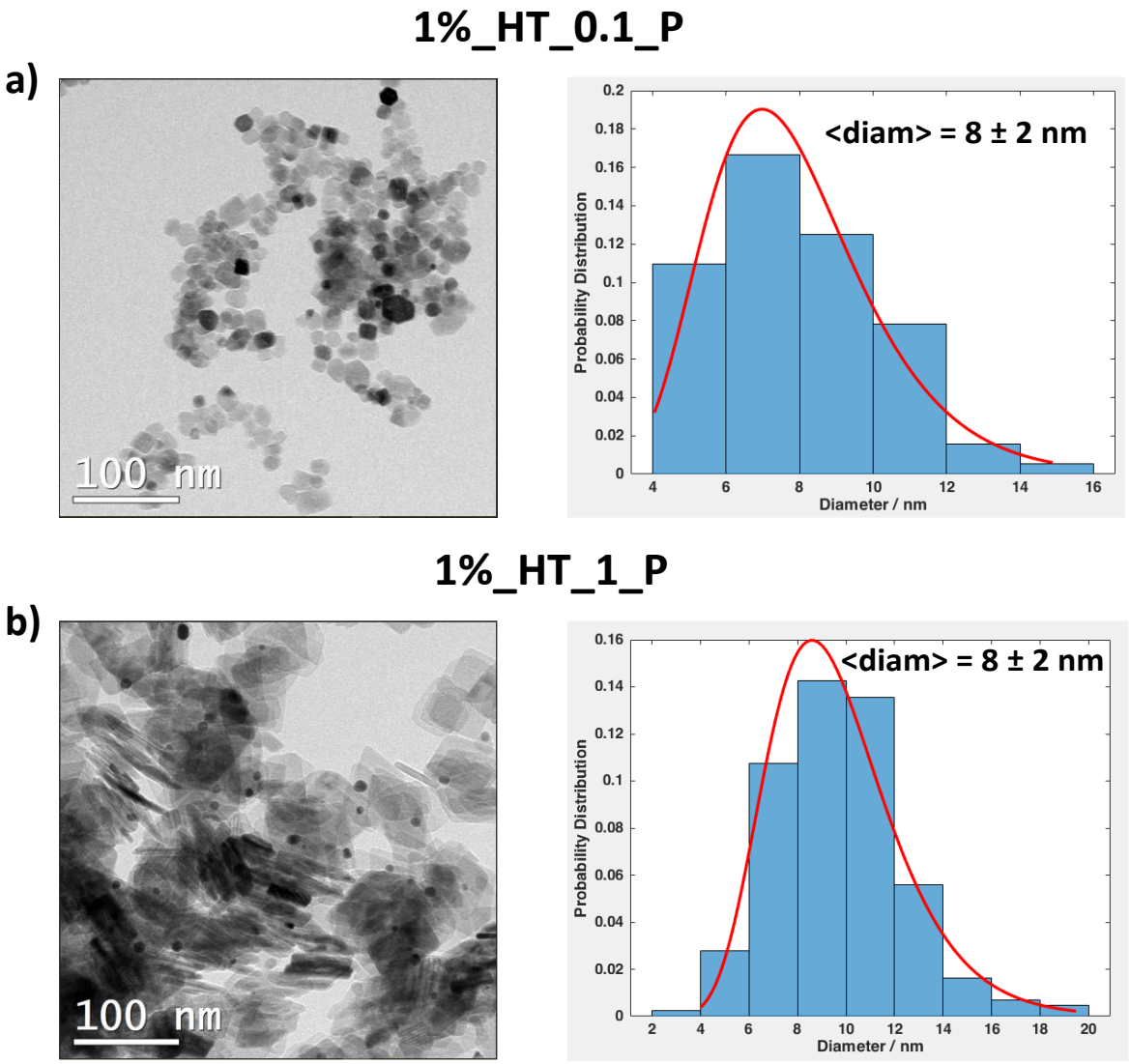

Figure 6.3.7: Transmission Electron Microscopy images and corresponding Au nanoparticles diameter distributions of differently shaped titanium dioxide materials modified with different amounts of noble metal nanoparticles by means of the DP and P technique. The total Au NPs counts ranged from 100 to 200 counts.

6.3.2 Photocatalytic activity

6.3.2.1 Photocatalytic oxidation of formic acid

The photocatalytic activity of the synthesized samples was tested in the photocatalytic oxidation of formic acid, reporting experimental results in terms of first order rate constants k_{For} (Figure 6.3.8). Differently from our previous investigations, samples bearing a sheet-like shape showed a slightly higher formic acid conversion compared to pseudo-spherically shaped materials. In this case, prepared materials were able to exhibit the expected improved photoefficiency attributable to the interplay between {101} and {001} facets which, differing in the location of their band edges, may cause the preferential migration of electrons and holes towards such facets, respectively. The coexistence of different facets in a more favorable {001}/{101} ratio in platelet-like materials may lead to the here observed improved photocatalytic activity as a consequence of

an improved charge separation (Chapter 5). Different batches of prepared samples showed slightly different photoactivity results, i.e. HT_0.1_3 and HT_1_3 samples bearing a higher photocatalytic activity with respect to the other corresponding batches. Such behavior is not surprising and can be attributed to the difficulty in producing reproducible inorganic materials through the hydrothermal method. However, the photoactivity trend is retained, the platelet like material always performing better than the corresponding pseudo-spherically shaped one, as confirmed by the calculated average rate constants, reported in Figure 6.3.8b.

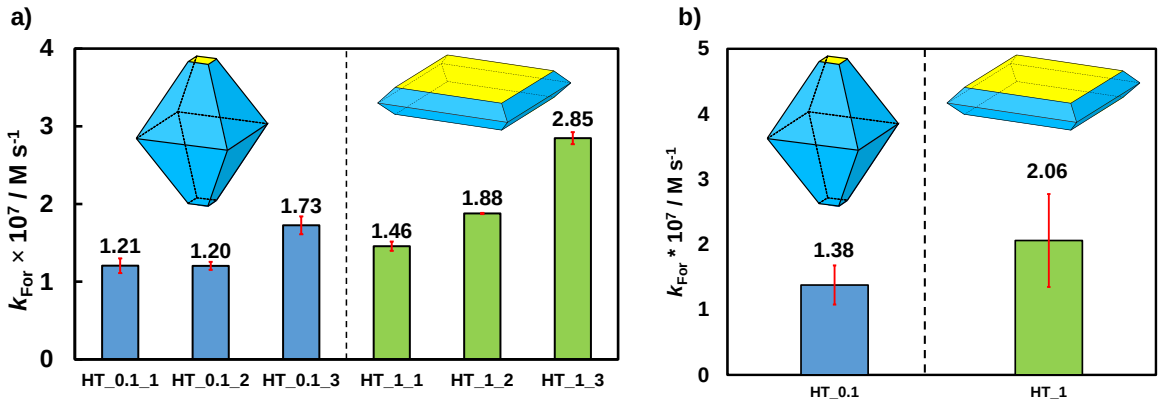

Figure 6.3.8: Formic acid photocatalytic oxidation rate constants (a) and their average value (b) for metal free, differently shaped HT_0.1 (pseudo-sphere) and HT_1 (nanosheet shaped) material.

The effects produced on TiO_2 photoactivity upon Au NPs deposition resulted to be strictly dependent on the specific morphology of TiO_2. In fact, in the case of pseudo-spherically shaped materials, the deposition of Au NPs always guaranteed beneficial effects, as evidenced by the photocatalytic activity improvement ratio upon metal deposition (calculated as the ratio between the zeroth-order rate constant of the metal modified materials and the corresponding bare, unmodified titanium dioxide) $k_{Au}/k_{For} > 1$. Differently nanosheet-shaped materials underwent a photoactivity decrease upon Au NPs surface deposition ($k_{Au}/k_{For} < 1$). Such effect resulted also to be independent on the technique used for the deposition of the nanoparticles and of the Au amount (Figure 6.3.9d).

The following results highlight that, despite the better charge separation and photocatalytic activity offered by the nanosheet morphology, in the case of metal-modified samples only materials bearing a pseudo-spherical shape were able to positively utilize the electron trapping effect offered by the Schottky barrier formed upon Au deposition. Indeed, in the case of pseudo-spherically shaped materials, the modification with Au metal nanoparticles has been reported to consistently result in a photoactivity improvement in formic acid oxidation.[46,49] Thus, a detrimental effect on photoactivity in the case of metal modified nanosheet-shaped materials appears quite unusual and

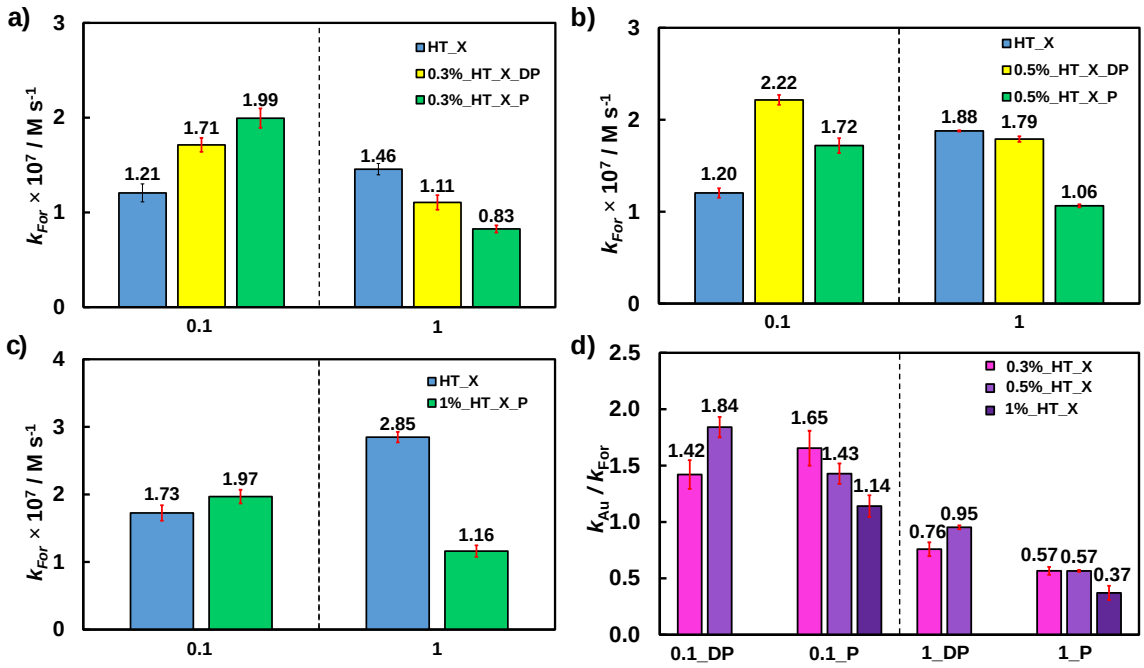

Figure 6.3.9: Photocatalytic rate constants in formic acid photocatalytic degradation for samples of the HT_X series modified with 0.3 wt% (a), 0.5 wt% (b) and 1 wt% (c) of Au nanoparticles with the DP or P method (yellow and green bars, respectively). Photoactivity of the corresponding bare materials are reported in blue colour; d) Photocatalytic activity improvement ratio upon Au NPs deposition on samples of the HT_X series in the photocatalytic degradation of formic acid.

should be strictly related to morphology-dependent interactions occurring between deposited Au nanoparticles and titanium dioxide. Such interaction can be rationalized by considering that if noble metal nanoparticles are mainly deposited on the most abundant {101} facets, as in the case of HT_0.1 materials, they may be able to efficiently scavenge the photoexcited electrons, which may tend to preferentially migrate towards such facets (as a consequence of the expected different CB and VB redox potentials location of different crystal TiO_2 facets), thus improving the overall materials' charge separation ability. On the opposite side, if noble metal nanoparticles are mainly deposited on {001} surfaces (being the most exposed facets in titanium dioxide nanosheets), the preferential migration of photogenerated holes towards {001} facets may be hindered by the presence on such facets of deposited Au nanoparticles, which, acting as electron scavengers, may instead promote the undesired charge carriers recombination, with a consequent drop in photoefficiency. Moreover, by considering the redox potential of the Au^0/Au^+ couple (1.68 V vs NHE), Au NPs may be partially oxidized to Au^+ species by the holes photogenerated on the TiO_2 surface and spontaneously migrating towards the {001} facets. As a consequence, the VB holes are less available to directly interact with the organic substrate molecules,[46] while Au^+ species may further act as undesired charge carriers recombination centres (see below).

With the exception of the HT_0.1 material modified with 0.3 wt% of Au, all materials modified with the deposition-precipitation technique resulted to be better performing than the corresponding materials modified through photodeposition. As illustrated from the analysis of the distributions of the average size of the deposited nanoparticles, however, such an effect cannot be ascribed to significant differences in the average size of the deposited nanoparticles, as they are characterized by very similar values regardless of the employed deposition technique. However, as suggested by literature reports on photodeposited Au nanoparticles,[43] the photodeposition method may result in the deposition of partially oxidized, yet not fully reduced Au nanoparticles, whereas instead the chemical reduction step of the deposition-precipitation technique ensures the deposition of fully reduced metallic Au nanoparticles, thus leading to the here observed better performance of DP-modified materials due to their better charge separation capability.

Generally, 0.5 wt% of Au resulted to be the optimal metal loading, able to best improve the photoactivity of the metal-modified materials. Increasing the gold content to 1 wt% resulted in severely dampening the performances of the materials with respect to both 0.3 wt% and 0.5 wt% Au loadings, most likely due to a light-shielding effect played by such high co-catalyst loading, possibly hindering light absorption by TiO_2.

Regardless, the TiO_2 specific morphology appears to be of fundamental importance in designing efficient metal/semiconductor composite materials for formic acid oxidation. In fact, while the combination of pseudo-spherically shaped titanium dioxide with Au NPs deposition seems to be a good strategy for improving the overall photocatalysts performance, the opposite effect is attained for nanosheet-shaped materials, for which the photoactivity is systematically hindered upon noble metal nanoparticles deposition. Thus, they do not represent suitable supports for Au/anatase composite materials for formic acid oxidation. On the other hand, in the case of metal-free TiO_2 samples, the material's performance is rather improved passing from a pseudo-spherical shape to a nanosheet structure.

6.3.2.2 Photocatalytic degradation of rhodamine B: effects of *in-situ* surface fluorination

In order to investigate the effects of *in-situ* surface fluorination, further combined with titanium dioxide morphology and Au NPs deposition, the photocatalytic activity of selected synthesized samples was tested in the photocatalytic degradation of rhodamine B under acidic conditions (pH = 3.7) and under *in-situ* fluorinated conditions at the same pH. In particular, metal-free materials have been firstly tested under such experimental conditions.

The rate constants of RhB photodegradation attained with bare HT_X series samples in the absence of fluoride ions at acidic pH (k_{Ac}) or at acidic pH upon *in-situ* fluoride addition (k_F) are reported in Figure 6.3.10. In line with our previous investigations (section 5.3.4, page 177),[39] the photoefficiency shown by the plate-like sample at natural or acidic pH are quite similar to those attained with the sample mainly exposing {101} facets, *i.e.,* the specific TiO_2 morphology does not significantly affect RhB photodegradation. Moreover, while lowering the pH has a negligible effect on the reaction rate, the *in-situ* fluorination is beneficial, although it hinders RhB surface adsorption. The *in-situ* surface fluorination determines a beneficial RhB oxidation rate increase for all investigated samples. By considering that RhB adsorption is inhibited on F-TiO_2, such an increase in RhB degradation rate constants upon TiO_2 surface fluorination can only be explained by considering an enhanced photoproduction of $^{\bullet}OH$ radicals, which may indirectly attack RhB molecules, thus promoting their photodegradation. In fact, fluoride ions, substituting for TiO_2 surface -OH groups, inhibit surface trapping of photogenerated holes as $\equiv$Ti-O$^{\bullet}$ species and favour the desorption of photogenerated active species (*i.e.,* $^{\bullet}OH$ free radicals) from the surface of titanium dioxide as follows:[35,37,39]

$$\equiv Ti - F + h^{+}_{VB} + H_2O \rightarrow \equiv Ti - F + {}^{\bullet}OH + H^{+}$$

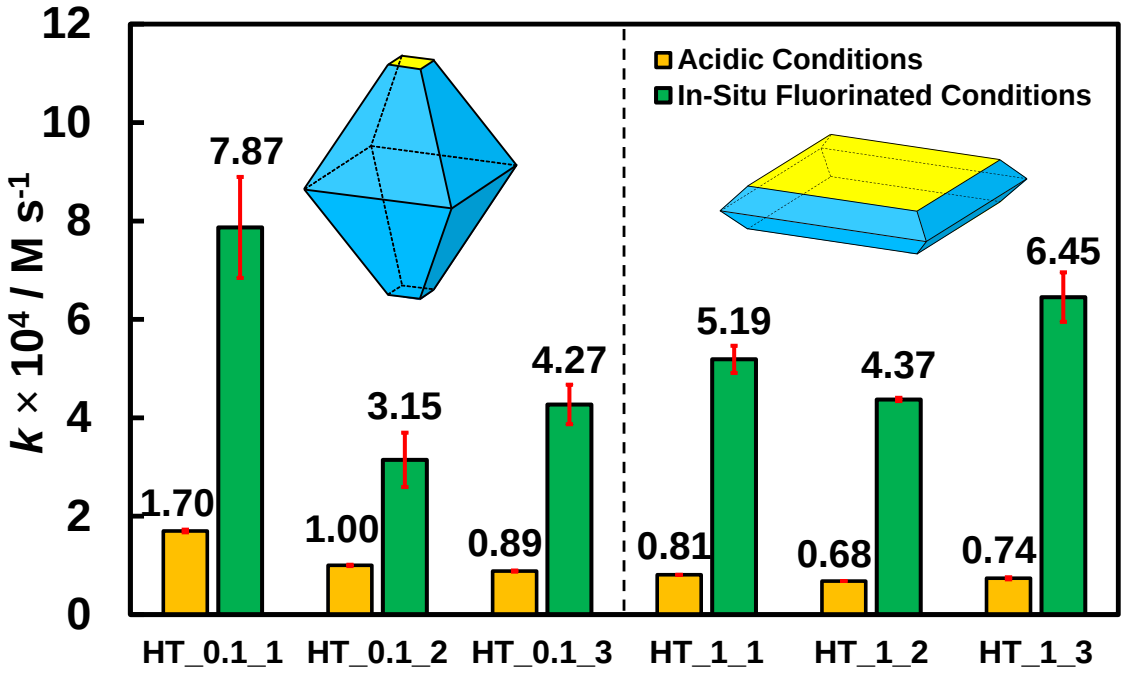

Figure 6.3.10: pseudo-first order kinetic rate constants for RhB photodegradation with bare TiO_2 samples obtained in the absence of fluorides at acidic pH (orange bars) or at acidic pH upon in-situ TiO_2 surface fluorination with a F/Ti ratio equal to 2 (green bars).

To provide an accurate picture of the phenomenon occurring during the photocatalytic degradation of Rhodamine B over titanium dioxide and properly rationalize the obtained experimental results, we decided to investigate the most-likely degradation mechanism of the cationic dye under the here-employed experimental conditions, with the purpose of further supporting the idea that an increased production of $HO^{\bullet}$ radicals is responsible for the photoactivity increase under *in-situ* fluorinated conditions. In fact, under UV-light irradiation and air atmosphere (the conditions of our experimental results), Rhodamine B can be mainly degraded by means of two different degradation paths,[71,72] *i.e.*, a photo-assisted path and an indirect oxidation path.

In the photo-assisted degradation mechanism, an electronically excited Rhodamine B molecule adsorbed on the surface of titanium dioxide injects an electron in the conduction band of the metal oxide semiconductor, causing the generation of electronically unstable $RhB^{+\bullet}$ species, which rapidly degrade through de-ethylation of the N-ethyl moiety of the cationic dye. As the main chromophore structure of the cationic dye is preserved through this degradation path, the photo-assisted path causes the accumulation in solution of the N-deethylated Rhodamine B-derived species which are absorb visible light, leading to a hypsochromic shift of the absorption maximum in the absorption spectra, becoming more and more prevalent as RhB is further degraded.

In the indirect oxidation path, instead, the dye is indirectly attacked by $HO^{\bullet}$ radicals produced via photocatalytic oxidation of water molecules or via degradation of $HOO^{\bullet}$ radicals produced via reduction of dissolved oxygen at the surface of the semiconductor photocatalyst. However, we were able to exclude a significant contribution from the photo-assisted mechanism to the overall Rhodamine B photocatalytic degradation considering that no Rhodamine B degradation was observed when irradiating the slurries in the same experimental setup in the presence of a filter cutting off all incident radiation of wavelength lower than 420 nm. Under such conditions, titanium dioxide cannot be electronically excited since it absorbs light of wavelength lower than 400 nm. However, since Rhodamine B absorbs light in the 450-600 nm range, the electronic excitation of the cationic dye is still possible, and so it can degrade itself through the photo-assisted mechanism but not through $HO^{\bullet}$ radicals attacks, as the indirect oxidation mechanism is completely turned off. Under such experimental conditions, Rhodamine B proved to remain almost completely undegraded even after 18 hours of irradiation (~ 5% conversion), proving that the dye is not degraded through the photo-assisted path. Moreover, only moderate hypsochromic shifts of the absorption maximum of Rhodamine B have been observed. The photoactivity increase attained upon *in-situ* TiO_2 surface fluorination despite a significant reduction in the adsorption ability of

the dye over titanium dioxide led us to conclude that RhB degradation mainly occurs due to the dye interaction with reactive oxygen species (ROS) formed in solution as a consequence of either the photocatalytic oxidation of water molecules or the reduction of adsorbed dissolved oxygen at the TiO_2 surface.

To better understand the effects induced on RhB degradation by the *in-situ* surface fluorination of differently shaped TiO_2 samples, the ratios between the rate constants obtained under such experimental conditions (k_F/k_{Ac}) were calculated and are reported in Figure 6.3.11.

Importantly, an outstanding photoactivity increase can be observed upon *in-situ* surface fluorination of the platelet like HT_1 sample, in line with the previously observed clear synergistic effect induced by the plate-like anatase TiO_2 morphology and its *in-situ* surface fluorination. In fact, surface fluorine atoms on {001} exposed facets tend to attract photoproduced holes since they form a negative electric field on the TiO_2 surface, further promoting electron – hole separation.[39]

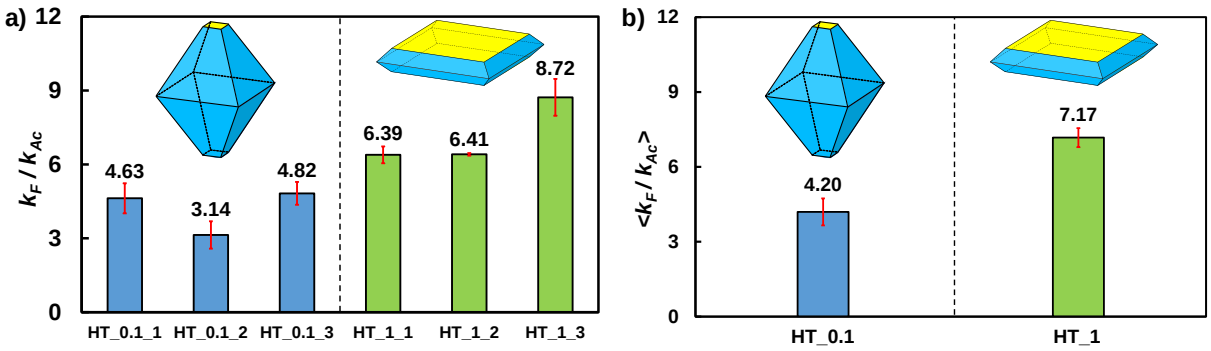

Figure 6.3.11: Photocatalytic activity improvement ratio k_F/k_{Ac} upon in situ TiO_2 surface fluorination of differently shaped titanium dioxide materials (a) and their average values (b).

Consequently, valence band holes, which are not able to oxidize the F^- anion because of the high oxidation potential of the $F^{\bullet}/F^-$ couple (3.6 V), directly react with water molecules at the interface producing relatively larger amounts of hydroxyl radicals responsible for RhB molecules oxidation. Differently, photopromoted electrons are repelled from fluorinated {101} surfaces and pulled towards {001} facets, where holes tend to preferentially migrate, thus favouring electron – hole recombination (Figure 6.3.12). Moreover, the remarkable beneficial effect of surface fluorination on the photoactivity of platelet-like TiO_2 in RhB degradation may originate from the presence of specific surface defects and/or the enhanced exposure of surface –OH groups, possibly allowing a higher surface density of fluorinated sites, in line with the findings previously discussed in Chapter 5.[39]

Considering the outstanding positive effects induced by combining *in-situ* surface fluorination with nanosheet TiO_2 morphology, we decided to explore the possibility of further increasing the photoactivity of nanosheet-shaped fluorinated TiO_2 in rhodamine B degradation by also coupling such structural and surface modification strategies with the surface deposition of Au nanoparticles which, by acting as electron scavenging species, may further promote charge separation within the composite materials, resulting in high-performing photocatalyst for Rhodamine B photocatalytic degradation.

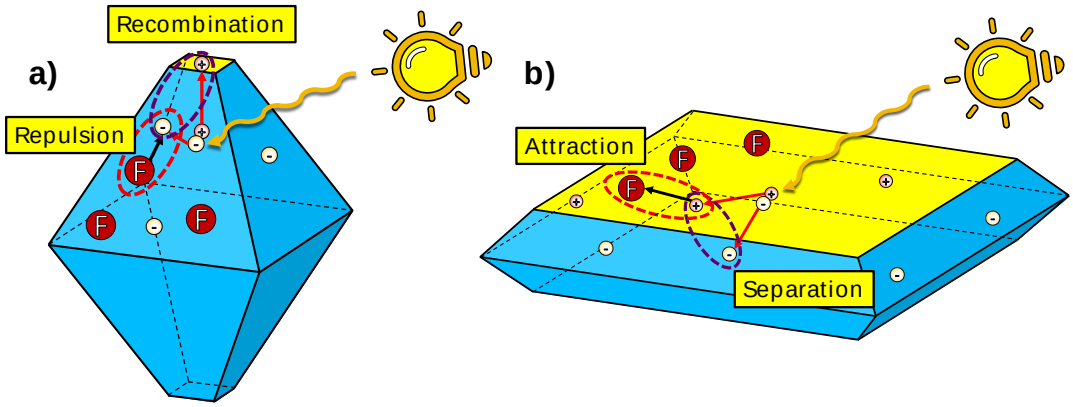

Figure 6.3.12: Schematic illustration of the likelihood of charges migration on fluorinated {001} (a) and {101} (b) facets of anatase TiO_2.

6.3.2.3 Photocatalytic degradation of rhodamine B: effects of *in-situ* surface fluorination and Au nanoparticles deposition

The photocatalytic activity of the metal modified materials in the photocatalytic oxidation of Rhodamine B was firstly evaluated under acidic condition at pH = 3.7. In such experimental conditions, the deposition of noble metal nanoparticles only resulted in moderate photoactivity improvements, if not even in a photoactivity suppression of the metal oxides with respect to the bare, unmodified titanium dioxide materials (Figure 6.3.13). This behaviour can be easily rationalized considering that under the here employed experimental conditions, in the absence of surface fluorination, photogenerated holes trapped at the semiconductor surface can oxidize Au nanoparticles before reacting with adsorbed RhB molecules. Positively charged metal nanoparticles, then, act as recombination centres with photopromoted electrons, thus favouring their recombination rather than promoting charge separation, which is essential to promote RhB degradation.[46]

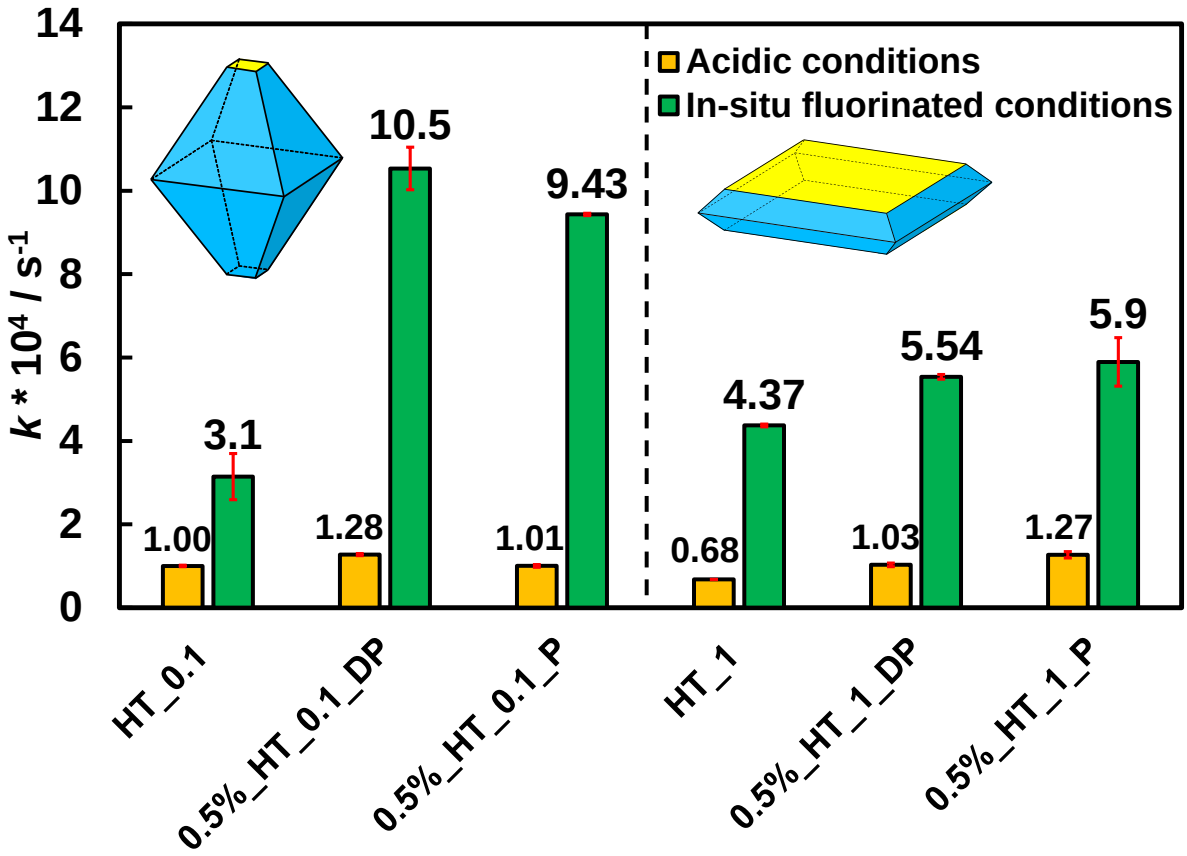

Figure 6.3.13: Pseudo-first order rate constants of rhodamine B photocatalytic degradation under acidic (green bars) and in-situ fluorinated conditions (blue bars) with materials of the HT_X series modified with 0.5 wt% of Au with the DP or P technique, compared to their corresponding bare metal-free materials.

In-situ surface fluorination generally allowed to appreciate the effects of metal NPs modification on the photoactivity of differently shaped titanium dioxide materials, since surface fluorination prevents the oxidation of Au nanoparticles by both inhibiting the trapping of photogenerated holes at the surface of the metal oxide semiconductor photocatalyst, and favouring the fast desorption from the surface of titanium dioxide of oxygen reactive species, which may also oxidize the noble metal nanoparticles.[35,37]

To evaluate the effects induced on photoactivity by *in-situ* surface fluorination of Au-containing TiO_2 samples with different morphology, the ratios between RhB degradation rate constant obtained at pH 3.7 in the presence of added fluoride (k_F) and that achieved at acidic pH in the absence of fluoride ions, k_F/k_{Ac}, was calculated for each Au/HT_X sample (Figure 6.3.14).

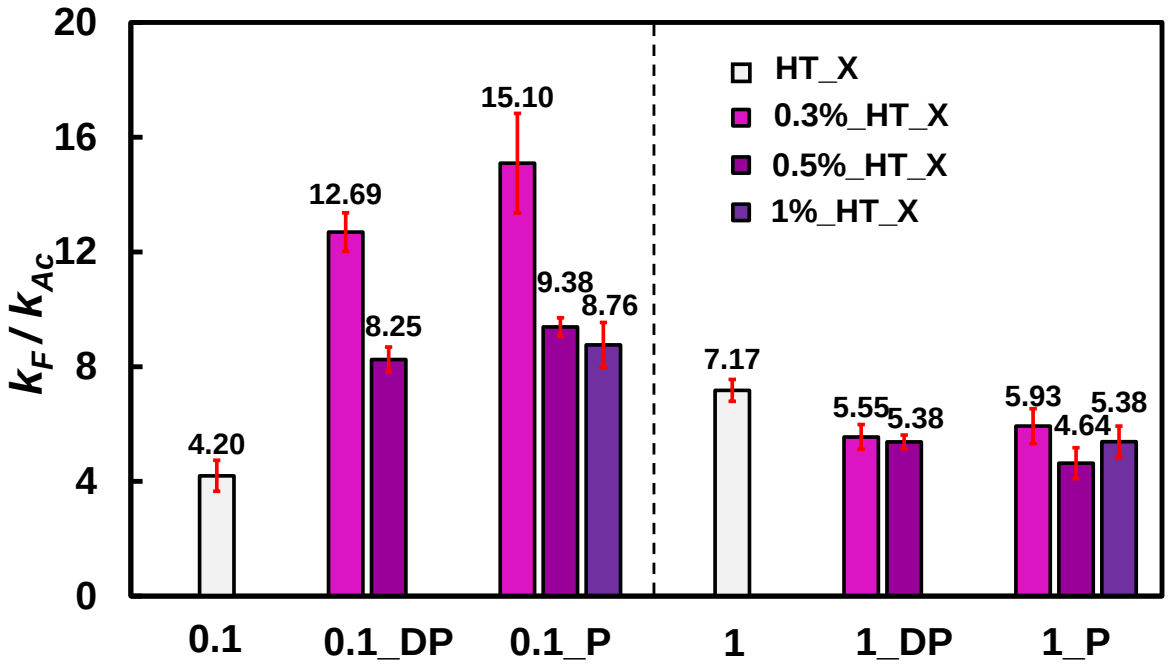

Figure 6.3.14: Photocatalytic activity ratio upon in-situ surface fluorination for differently shaped titanium dioxide materials modified with Au NPs by the deposition-precipitation (DP) or the photodeposition (P) method.

For any of the investigated materials in any of the experimental conditions (*i.e.*, under acidic or under *in-situ* fluorinated conditions), Rhodamine B did not undergo degradation when a 420 nm cut off filter was applied, indicating that also in the case of Au-modified materials a photo-assisted degradation path did not contribute to the overall observed photocatalytic degradation of the cationic dye.

The efficacy of *in-situ* surface fluorination of Au-modified materials on the photocatalytic degradation of Rhodamine B also resulted to be heavily dependent on the specific TiO_2 morphology. In fact, the photoactivity increase gained by Au-containing samples upon *in-situ* surface fluorination at acidic pH resulted significantly more marked compared to that achieved with the corresponding bare materials only for the Au/HT_0.1 series (having a pseudo-spherical morphology), independently of the adopted Au NPs deposition technique, with a 0.3 wt% Au content leading to the highest k_F/k_{Ac} ratio value. Surprisingly, the intriguing synergistic effect induced on RhB degradation by the platelet-like anatase TiO_2 morphology and its *in-situ* surface fluorination is completely suppressed upon Au NPs deposition, as illustrated by the k_F/k_{Ac} values obtained for all Au/HT_1 samples, which are significantly lower than those achieved with the corresponding bare HT_1 photocatalyst (for which the average value is 7.17, Figure 6.3.14).

The obtained results may be explained by considering that noble metal nanoparticles deposition could result in depleting the number of hydroxyl groups available on the photocatalysts surface for the ligand exchange reaction with the fluoride anions, necessary for the *in-situ* TiO_2 surface fluorination, being already occupied in anchoring Au NPs. On platelet-like materials, the deposition of metal nanoparticles on {001} surfaces may thus inhibit the fluorination of such facets, thus hampering the synergy between platelet-shaped materials and *in-situ* surface fluorination observed for metal-free specimens. On the other hand, Au NPs inhibiting surface fluorination on {101} surfaces could be beneficial for pseudo-spherically shaped materials, since surface fluorination on such facets is detrimental due to the interaction between the negative electric field generated by surface fluorides and photopromoted electrons there migrating, which are repelled and pulled towards {001} surfaces, where they can recombine with photogenerated holes.[73] Au loadings higher than 0.3 wt%, however, may start inhibiting the beneficial fluorination of less abundant {001} facets of pseudo-spherically shaped materials too, thus leading to the observed fluorination efficiency drop with increasing co-catalyst content.

Concerning the effects induced on RhB photocatalytic degradation by the presence of Au NPs on differently shaped anatase TiO_2 under *in-situ* acidic fluorination conditions, we calculated the ratios between the RhB degradation rate constants obtained upon *in-situ* fluoride addition with each Au-modified Y%_HT_X_T sample (k_{Au_F}) and that achieved under the same experimental conditions with the corresponding naked HT_X sample (k_F). The so obtained k_{Au_F}/k_F values can be compared in Figure 6.3.15. Clearly, Au deposition produces a significant increase in RhB degradation rate under fluorinated conditions only for samples mainly exposing {101} facets, the highest k_{Au_F}/k_F ratios being achieved with samples containing 0.5 wt.% of Au, corresponding to the optimal noble metal content. Differently, coupling the TiO_2 platelet-like morphology with Au NPs did not substantially alter the original photoefficiency of {001} facet-enriched samples, as shown by the k_{Au_F}/k_F ratios close to 1 obtained with the gold-containing HT_1 series.

Again, the effects induced by loading metal nanoparticles onto *in-situ* fluorinated titanium dioxide clearly are heavily dependent on the specific morphology of the titanium dioxide support. In fact, differently from bare materials, for which the use of nanosheet-shaped titanium dioxide results in significantly improving the photocatalytic activity of the metal oxide photocatalyst in degrading Rhodamine B under *in-situ* fluorinated conditions, with an outstanding synergistic cooperation between morphology control and surface fluorination, pseudo-spherically shaped materials resulted to be the ideal supports for noble metal nanoparticles deposition, allowing to fully exploit the improved charge separation offered by the formation of the Schottky barrier under *in-situ* surface fluorination. These results are in line with those of formic acid oxidation, in which

nanosheet shaped materials also resulted to be less suitable supports for noble metal nanoparticles deposition compared to the pseudo-spherically shaped ones.

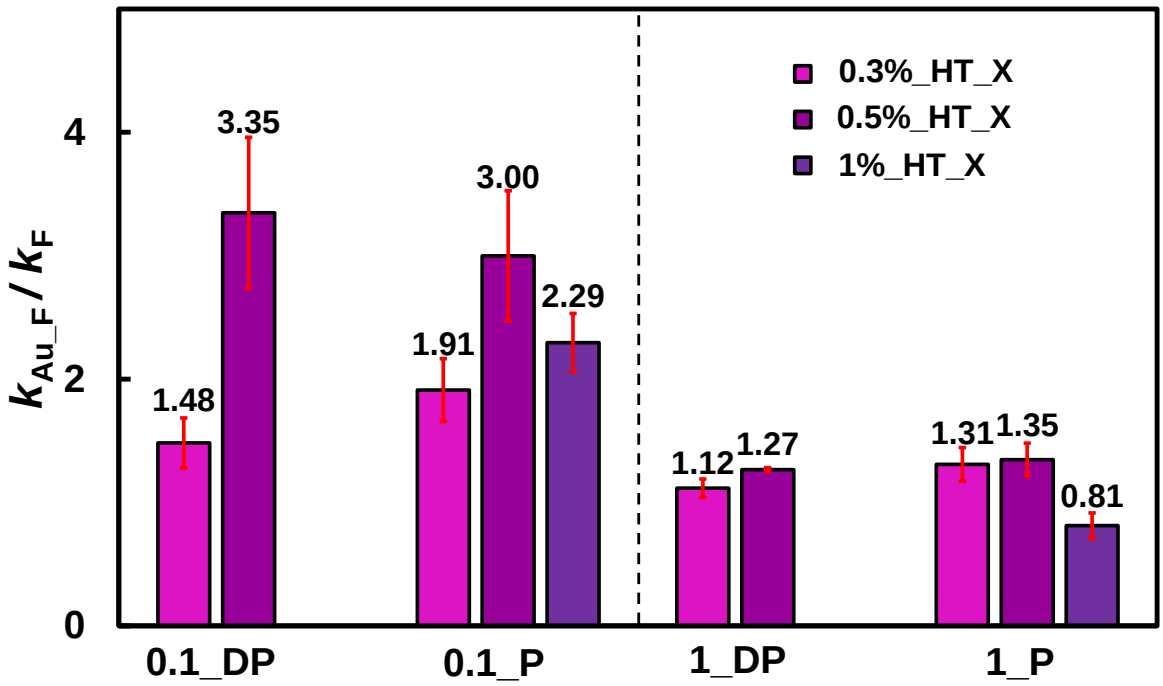

Figure 6.3.15: Photocatalytic activity ratio upon metal deposition for in-situ fluorinated differently shaped titanium dioxide materials modified with the deposition-precipitation (DP) or photodeposition (P) method.

The obtained results allowed us to hypothesize a mechanism able to rationalize the observed photocatalytic activities trend based on the likelihood migration of photogenerated charge carriers on differently shaped, *in-situ* fluorinated, metal modified titanium dioxide materials (Figure 6.3.16).

In fact, in the case of Au/HT_0.1_T samples, Au NPs, being mainly loaded on {101} facets, may rapidly and efficiently scavenge photoexcited electrons (Figure 6.3.16b), which already tend to selectively migrate to such crystalline facets (Figure 6.3.16a). The very efficient electron scavenging ability of Au nanoparticles results in suppressing the undesired electron repulsion effect deriving from the presence of the negatively charged electric field originated by the presence of fluorine atoms adsorbed on {101} facets. In the absence of Au nanoparticles, this causes the repulsion and migration of electrons towards {001} facets, where the proximity with holes already there migrating promotes their undesired recombination (Figure 6.3.16a). Therefore, the deposition of Au nanoparticles on the main-exposed {101} facets on pseudo-spherically shaped titanium dioxide confer a more efficient charge carriers separation, accompanied by a favoured RhB degradation by means of $^{\bullet}OH$ radicals, which can be thus proficiently photoproduced on F-{001} facets.

Differently, in the case of platelet-like photocatalysts, an effective charge separation may instead be limited by the presence of gold NPs deposited on the {001} prevailing facets which, by acting as electron scavenging species, promote instead an undesired electron-hole recombination by withdrawing electrons towards the same crystal facets where holes are already preferentially there migrating (Figure 6.3.16d). This results in an enhanced charge recombination and a lower photoefficiency in the investigated reaction. Moreover, Au NPs deposited on {001} facets may also be oxidized by photogenerated holes there migrating before reacting with water molecules at the semiconductor surface.[46] Such phenomena result in limiting the production of HO• radicals not only by subtracting photogenerated positively charged carriers, which react with NM NPs rather than with water, but also because the oxidation of the noble metal nanoparticles results in the generation of a partial positive charge within them. Such positive charge may then react with the electrons photopromoted in the TiO_2 CB which, while still being scavenged by Au nanoparticles, recombine within the noble metal, compensating the positive charge generated by the oxidative action of the photogenerated holes and restoring their metallic state. However, a fraction of photopromoted electrons is therefore not transferred to oxygen adsorbed at the semiconductor surface, but rather recombine with the positive charge within the noble metal nanoparticles, thus resulting in a net abatement of the HO• radicals production rate.

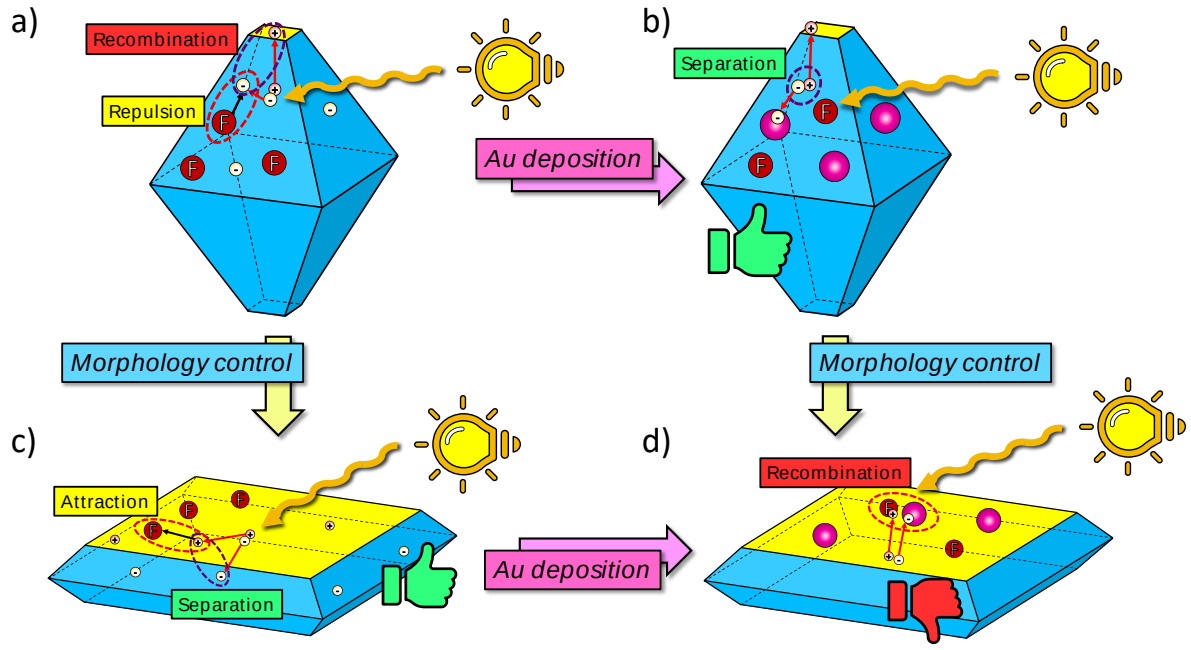

Figure 6.3.16: Schematic representation of the effects induced by combining Au NPs deposition and in-situ surface fluorination of anatase TiO_2 with different morphology.

Therefore, the original idea of boosting the photoactivity of *in-situ* surface fluorinated anatase by means of Au nanoparticles deposition resulted to be successful only for pseudo-spherically shaped anatase, but not for nanosheet-shaped TiO_2 crystallites, exhibiting instead a synergistic effects between morphology and *in-situ* surface fluorination for bare materials, i.e. in the absence of Au NPs deposition.

6.3.2.4 Photocatalytic hydroxylation of terephthalic acid

With the purpose of investigating the relative ability of differently shaped, metal modified titanium dioxide materials in producing reactive hydroxyl radical species in solution, the efficiency of the materials in the photocatalytic hydroxylation of terephthalic acid was investigated. In fact, terephthalic acid represents a largely employed substrate for monitoring the relative ability of different photocatalysts in producing $HO^{\bullet}$ radicals, since its reaction with such species results in the formation of the photoluminescent 2-hydroxyterephthalic acid, which can be only produced through an indirect radical attack by means of $HO^{\bullet}$ radicals in solution and whose concentration can be selectively monitored via spectrofluorimetric analysis (section 3.5, page 107).[74,75]

Unfortunately, the main drawback of using terephthalic acid as photocatalytic substrate is represented by its very low solubility in acidic or neutral solutions, meaning that photocatalytic tests can only be performed at alkaline pH (in our case, pH = 11). Under such pH conditions, however, it is not possible to investigate the photoactivity of the prepared materials under *in-situ* fluorinated conditions since surface fluorination is not preserved with such a high concentration of HO^{-} species in solution, since they will substitute surface ≡Ti-F moieties with ≡Ti-OH groups in a thermodynamically favoured ligand exchange reaction.

Photocatalytic 2-hydroxyterephthalic acid production rate constants for differently shaped, metal modified titanium dioxide materials at pH = 11 were recorded and reported in Figure 6.3.17.

Clearly, in the case of bare, metal free titanium dioxide materials, passing from a pseudo-spherical morphology to nanosheet-shaped materials resulted in an improvement of the 2-hydrotherephthalic production rate, thus confirming the beneficial effect played by a higher exposure of {001} facets in boosting the production of $HO^{\bullet}$ radicals in solution even in the absence of surface fluorinated conditions. The following observation allowed us to further confirm the origin of the increased photoactivity in the case of rhodamine B photocatalytic degradation under *in-situ* fluorinated conditions, although the differences in $HO^{\bullet}$ radicals production resulted to be even more marked in such case, due to the synergistic cooperation of the intrinsically improved $HO^{\bullet}$ radicals production ability over {001} facets and their surface fluorination, both

contributing in massively boosting the production of reactive oxygen species in solution, responsible for the degradation of Rhodamine B. In the absence of *in-situ* surface fluorination, i.e., under acidic conditions at pH = 3.7, however, significant photoactivity differences in rhodamine B photodegradation were not observed passing from a pseudo-spherical shape to a nanosheet morphology, most likely due to the poor photoactivity of the materials in degrading the cationic dye under the chosen experimental conditions not allowing to fully appreciate their different capability in producing HO• radicals. By these means, 2-hydroxytherephthalic acid production proved to be a better tool for discerning the relative ability of differently shaped metal-free titanium dioxide materials in producing ROS in solution in the absence of TiO_2 surface fluorination.

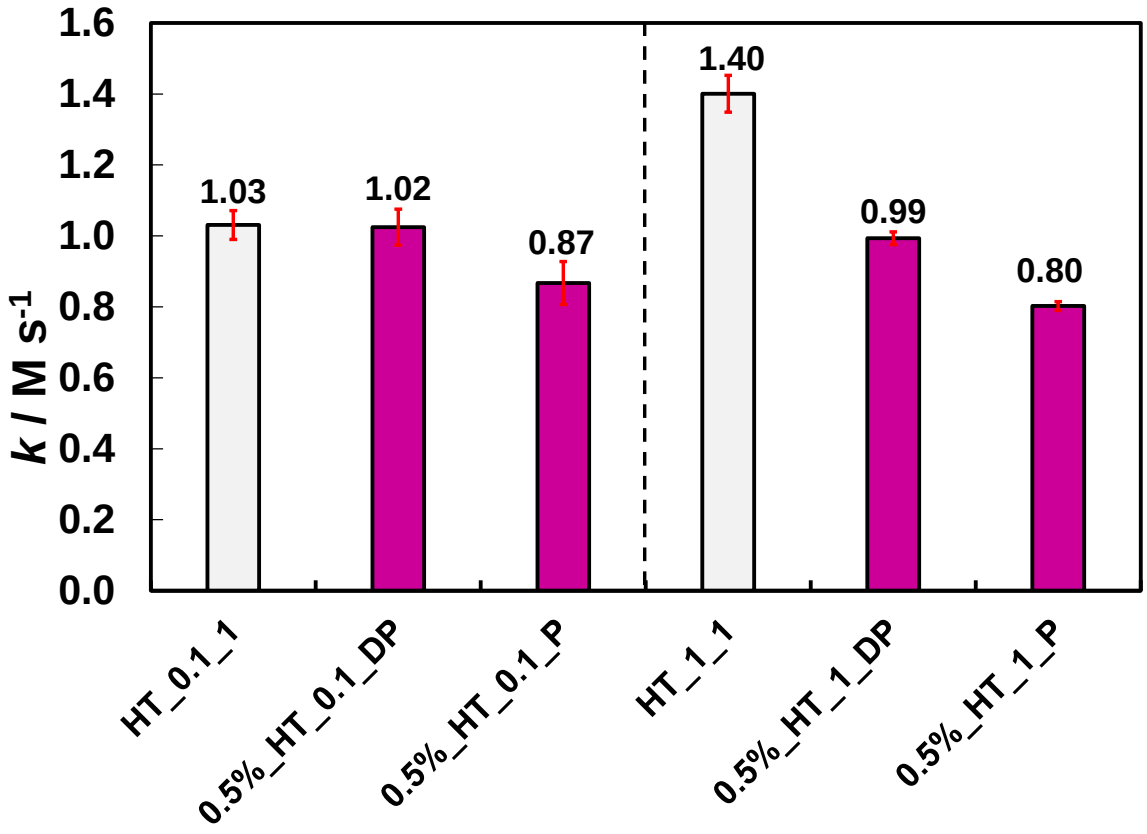

Figure 6.3.17: 2-Hydroxyterephthalic acid photocatalytic production rate constants for differently shaped TiO_2 materials modified with 0.5 wt% of Au nanoparticles via the DP or the P method.

The deposition of Au NPs, however, resulted to suppress the 2-hydroxyterephthalic acid production rate for all synthesized materials, except for the pseudo-spherically shaped 0.5%_HT_0.1_DP, whose photoactivity resulted to be unchanged respect to that of the corresponding HT_0.1 sample. This result can be rationalized considering that, similarly to the photocatalytic degradation of rhodamine B under acidic conditions, in the absence of *in-situ* TiO_2 surface fluorination, the photoproduced HO• radicals may be involved in oxidizing the deposited Au NPs instead of reacting with terephthalic acid molecules. Partially oxidized Au nanoparticles,

then, can act as recombination centres for photoexcited electrons. Therefore, the average lifetime of electron-hole pairs is decreased,[46] with a consequent inhibition of the overall photoactivity of the Au-containing materials with respect to their bare, unmodified titanium dioxide supports.

Such effect, however, resulted to be more marked for nanosheet-shaped materials, indicating that the deposition of noble-metal nanoparticles on {001} surfaces is particularly detrimental for their $HO^{\bullet}$ radicals production capability. In fact, if noble metal nanoparticles are deposited on {001} surfaces, the preferential migration of holes towards such facets results in oxidizing noble metal nanoparticles there deposited more efficiently than if they were deposited on {101} surfaces (as in the case of pseudo-spherically shaped HT_0.1 materials). This appears in line with the case of the photocatalytic degradation of rhodamine B under *in-situ* fluorinated conditions, for which the deposition of noble metal nanoparticles also resulted more efficient on pseudo-spherically shaped materials compared to platelet-like materials, due to the detrimental interaction occurring between the preferential migration of holes on {001} surface and the Au nanoparticles there deposited (Figure 6.3.12). However, under *in-situ* fluorinated conditions the oxidation of the noble-metal nanoparticles is likely limited by the presence of surface fluorine, and thus the photoactivity of the composite material is still improved upon metal modification (Figure 6.3.15).

Independently on the morphology of the support, materials prepared with the photodeposition method resulted to suppress the photoactivity of the titanium dioxide composite material by a larger extent compared to materials prepared through the deposition-precipitation route. As previous discussed, such an effect cannot be ascribed to significant differences in the average size of the deposited nanoparticles, as they are characterized by very similar values regardless of the deposition technique. However, as suggested by literature reports on differently reduced Au nanoparticles,[43] the photodeposition method may lead to the production of partially oxidated, yet not fully reduced Au nanoparticles, whereas the chemical reduction step of deposition-precipitation ensures the deposition of fully reduced metallic Au nanoparticles. Thus, a fraction of photopromoted electrons will be transferred to the metal nanoparticles to neutralize their partial positive charge, and thus a smaller amount of photopromoted electrons is available to transfer photopromoted electrons towards adsorbed molecular dioxygen compared to materials prepared through DP.

Thus, photocatalytic production of 2-hydroxyterephthalic acid allowed us to better unravel the effects on photoactivity deriving from morphology control and Au nanoparticles deposition on differently shaped titanium dioxide nanoparticles. In particular, the test reaction resulted to usefully highlight an improved $HO^{\bullet}$ radical production on mainly {001}-exposing materials, as well as

further confirms the presence of a detrimental interaction occurring when gold nanoparticles are mainly deposited on {001} rather than on {101} facets.

6.3.2.5 Photocatalytic reduction of Cr(VI)

Cr(VI) photocatalytic reduction, an environmentally-relevant test reaction, was chosen as a model reaction to check the effects of morphology control and Au nanoparticles deposition on photocatalytic processes occurring through a reductive reaction path.

The effects of Au nanoparticles deposition on the photocatalytic activity of differently shaped titanium dioxide materials for Cr(VI) to Cr(III) photoreduction at pH = 3.7 can be appreciated in Figure 6.3.18 in terms of first-order rate constants k_{Cr}. We did not investigate the effects of *in-situ* surface fluorination for this test reaction, as fluorination of the titanium dioxide surface results in severely hampering dichromate anion adsorption, resulting in significantly dampening the performance of the materials. In fact, surface adsorption is a mandatory requirement for the conversion of Cr(VI) to Cr(III) via photocatalytic processes. Moreover, it almost entirely conceals any morphology related photocatalytic effect.[39,76,77]

Congruently with our previous findings (Figure 5.3.9, page 175), an increase in the truncation degree of the truncated square bipyramidal crystallites (typical of HT_0.1 materials) resulted in massively boosting the performance of titanium dioxide anatase with an almost threefold photoactivity improvement, with plate-like shaped TiO_2 materials (HT_1) even outperforming reference benchmark P25 material. Thus, we were able to confirm the positive effects on the photocatalytic reduction of Cr(VI) induced by the use of a platelet-like morphology (section 5.3.3).[39]

The photocatalytic activity of the materials was either unaffected or only slightly improved by the deposition of the noble metal nanoparticles on the photocatalysts surface, with a maximum ~20% increase of the photocatalytic rate constant k_{Cr} in the case of platelet-like materials modified with 0.5 wt% of Au. Instead, spherical-shaped materials mostly retained the intrinsic photoactivity properties induced by the modification of their morphology upon Au NPs deposition. Such effects, moreover, resulted to be independent of the method chosen for the deposition of the noble metal nanoparticles on the photocatalyst surface. Similar findings have been previously reported in literature. For example, Dozzi et al. found that positive effects on the photocatalytic reduction of Cr(VI) induced by the noble metal nanoparticles deposition over P25 derived from modifications of the structure of the titanium dioxide support occurring during the metal nanoparticles deposition procedure rather than to an improvement deriving from the deposition of the noble metal nanoparticles themselves.[78] In their study regarding Au nanoparticles deposited

on mesoporous titania, Li et al. also reported that the photoactivity of titanium dioxide remained practically unchanged in Cr(VI) photoreduction upon noble metal nanoparticles deposition.[79] Such an effect, moreover, has also been reported in the case of Pt-modified titanium dioxide, i.e. such phenomenon was also observed for metals different than gold.[80] Moreover, all mentioned studies reported that the photoactivity of titanium dioxide-based materials improved in the presence of hole scavenging species, being oxidized more easily than water. Yet, even in the presence of organic sacrificial agents, the presence of noble metal nanoparticles did not improve the photoactivity of the composite materials with respect to their bare, unmodified titanium dioxide support.

The obtained results indicate that in the case of Cr(VI) photocatalytic reduction the anodic half reaction, *i.e.* in our case water oxidation, represents a kinetic bottleneck limiting the overall efficiency of the photocatalytic process.[81] Instead, due to the close interaction occurring between Cr(VI) anions chemisorbed at the titanium dioxide surface at the here employed pH, electrons photopromoted to the conduction band of titanium dioxide (or trapped in Au nanoparticles in the case of metal modified materials) are likely to be very fast and efficiently transferred to the transition metal cations.[82] Thus, the introduction of a reduction cocatalyst such as noble metal nanoparticles, improving the photocatalytic activity of semiconductor materials in reduction-limited photocatalytic paths, has little-to-no influence on the overall photocatalytic activity of the composite systems in Cr(VI) reduction. Eventual positive beneficial charge separation effects on photoactivity due to the formation of a Schottky barrier, eventually also capable of prolonging the average lifetime of photogenerated holes, play little role in this test reaction, as electrons are readily withdrawn from noble metal nanoparticles. Thus, the observed rate constants are rather a consequence of the phenomena occurring in the oxidation component of the process. Similar considerations have also been proposed in literature.[80]

In conclusion, noble metal nanoparticles deposition does not represent a pursuable strategy to improve the photoactivity of titanium dioxide-based materials in Cr(VI) photocatalytic reduction. On the other hand, improving the oxidation ability of titanium dioxide, *e.g.*, through deposition of an oxidation cocatalyst, addition of sacrificial hole-scavenging species or, most importantly, use of metal-free nanosheet-shaped anatase, represents winning alternatives to improve the photoactivity of the metal oxide semiconductor.

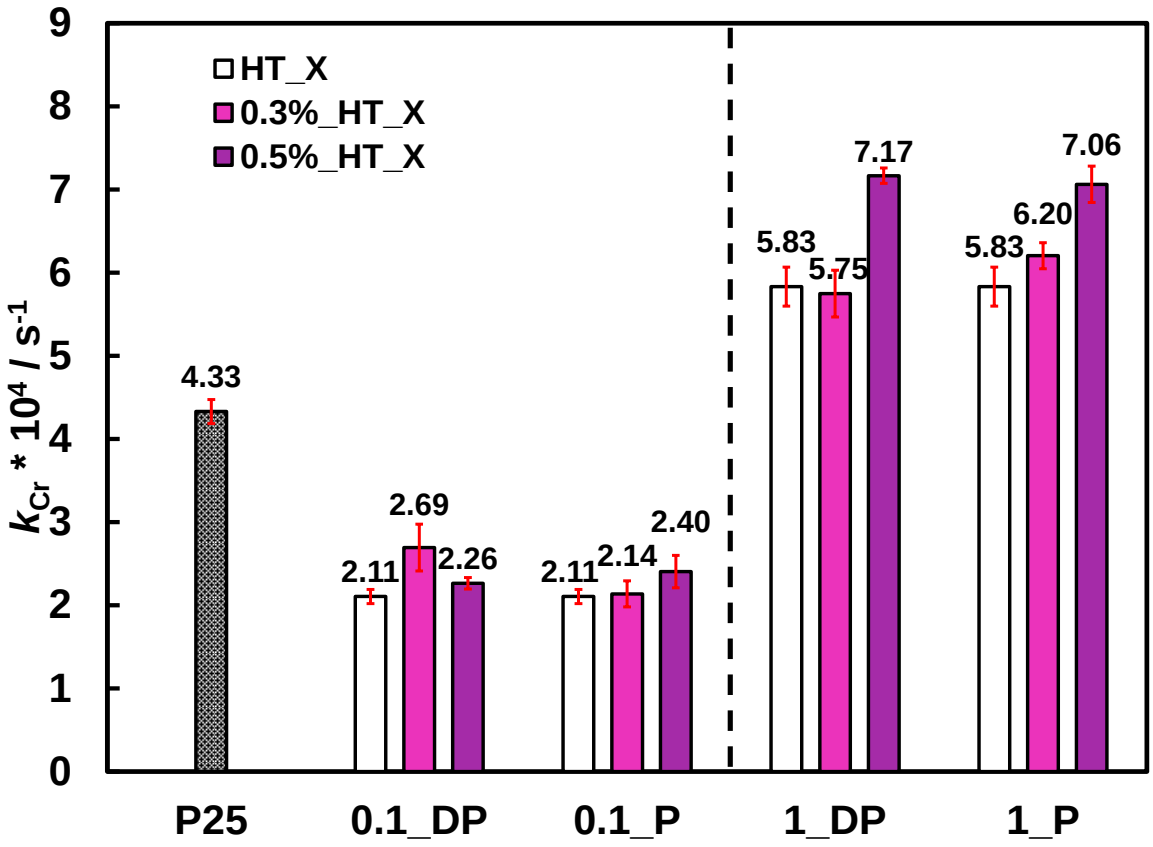

Figure 6.3.18: Pseudo first-order kinetic rate constants of Au-modified HT_X_Y samples in the photocatalytic reduction of Cr(VI) at pH = 3.7.

The results obtained through this PhD project allowed us to shed light and further confirm the origin of the outstanding beneficial effects induced by morphology control in Cr(VI) photoreduction. In fact, a higher exposure of {001} facets is indeed beneficial for this test reaction. In fact, as illustrated by the improved 2-hydroxyl radical production rate by means of nanosheet-shaped materials (Figure 6.3.17), their improved ability to oxidize water compared to {101} surfaces, due a higher concentration of undercoordinated Ti 5c sites and to a higher density of photogenerated holes preferentially migrating there, allows to better overcome the main kinetic bottleneck of Cr(VI) photocatalytic reduction. Thus, crystal facets engineering titanium dioxide represents a great strategy for improving the photoefficiency of the metal oxide semiconductor in Cr(VI) wastewater remediation.

6.3.2.6 Hydrogen production by photo-steam reforming of methanol

In the photocatalytic steam reforming reaction, hydrogen production is paralleled by methanol oxidation up to CO_2 through the formation of formaldehyde and formic acid as intermediate species; carbon monoxide and other minor side products are also produced. In all photocatalytic tests H_2, CO_2 and CO evolution occurred at constant rate under full lamp irradiation, as in previous studies. Some examples of photocatalytic hydrogen production rate vs. irradiation time are

reported in Figure 6.3.19b. The average rate of H_2 production attained with the here investigated photocatalysts are compared in Figure 6.3.19a, while the selectivity distribution to the main reaction products can be found in Figure 6.3.20.

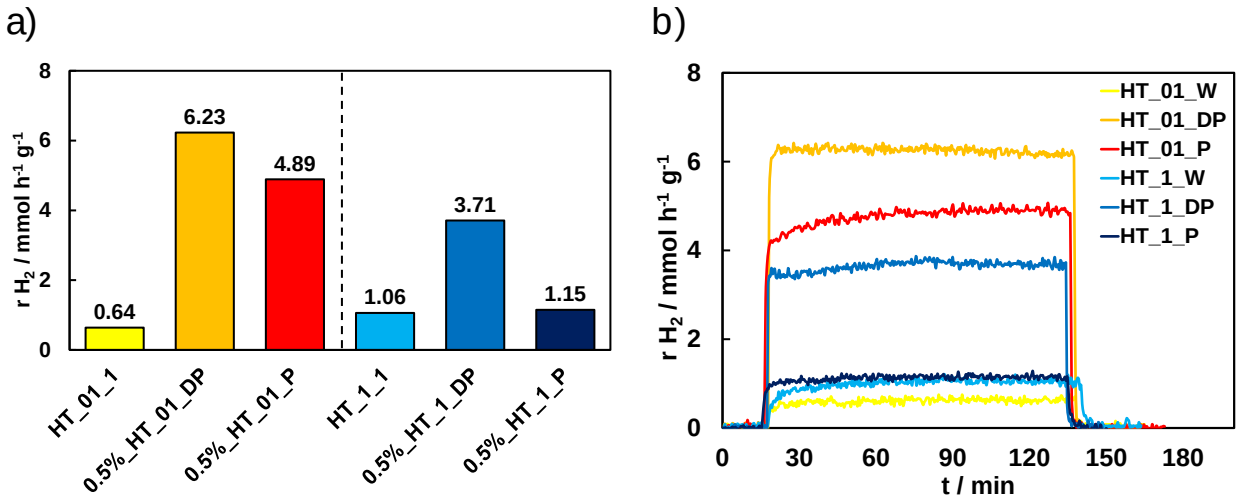

Figure 6.3.19: Average rates of H_2 production (a) and their evolution as a function of time (b) attained with differently shaped TiO_2 materials modified with 0.5 wt.% of Au NPs by means of the deposition-precipitation (DP) and photodeposition (P) methods.

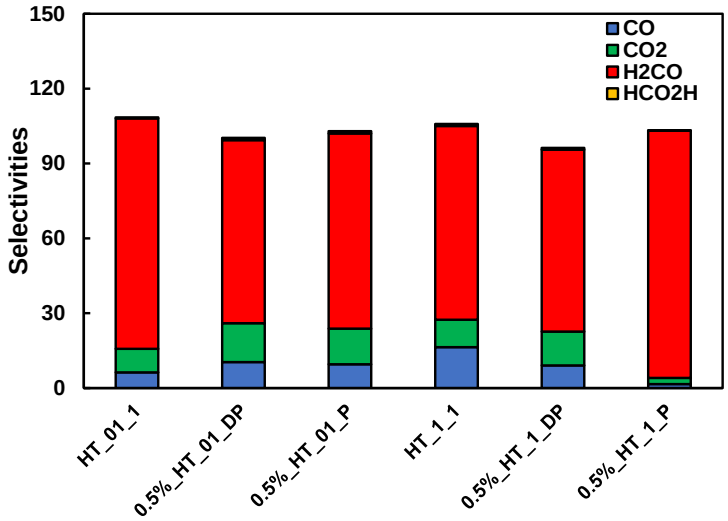

Figure 6.3.20: Percent selectivities to the main products attained with the investigated photocatalysts during methanol photocatalytic steam reforming.

We can observe that:

- in line with our expectations, the Au-modified samples show an increased ability in producing H_2 upon UV-vis light irradiation. This may be related to an enhanced separation of photogenerated charge carries promoted by the electrons scavenging properties of the noble metals NPs.

- Noble metal nanoparticles deposition, differently from our other investigated reduction test reaction, *i.e.*, the photocatalytic reduction of Cr(VI), resulted in always improving the photoactivity of the prepared materials in hydrogen evolution from methanol photo-steam reforming. In fact, due to the presence of methanol, acting as an efficient hole scavenger species, the here investigated reduction reaction is not limited by the anodic oxidation process. Thus, the improved charge separation and reduction ability offered by the presence of Au NPs results beneficial for the overall photoactivity of metal-modified materials;
- Interestingly, the HT_0.1 series samples behave more efficiently than platelet-like TiO_2 materials. Possibly, the larger exposure of {101} facets, i.e. acting as reduction sites, may guarantee a larger avaiability of reduction centers to promote H_2 evolution. Similar considerations have also been recently reported by Mino et al. in hydrogen reduction from formic acid photoreforming employing differently shaped platinized titanium dioxide,[83] relating the higher reactivity of pseudo-spherically shaped materials to a higher reductive capability of {101} facets.
- also in this test reaction Au NPs deposition on TiO_2 surface by DP seemed to guarantee the best photoefficiency. Again, a possibly incomplete reduction of the noble metal nanoparticles attained through the photodeposition method could limit the performance of materials modified through such technique compared to deposition-precipitation.[43] The photodeposition method did not induce any peculiar or beneficial effect with respect to the traditional DP technique.
- Noble metal nanoparticles deposition resulted to be particularly efficient on pseudo-spherically shaped materials, whereas in the case of nanosheet-shaped materials the photoactivity increase was more moderate, if not only slightly improved (as in the case of 0.5%_HT_1_P). These results are coherent with all the other test reactions in the absence of surface fluorination, i.*e.*, the deposition of Au nanoparticles is not ideal on materials mainly exposing {001} facets, as the preferential migration of holes towards such facets may result in Au NPs oxidation. If noble metal nanoparticles are mainly deposited on {101} facets, as in the case of pseudo-spherically shaped materials, the effects of preferential electron migration towards either such facets and the noble metal nanoparticles there deposited cooperate in improving the overall charge carrier separation in the metal-semiconductor composite material. Particularly inefficient was the combination of photodeposition and nanosheet-shaped TiO_2 materials, in which the incomplete reduction of the metal nanoparticles and their concurrent oxidation by means

of photogenerated holes prevent the electron transfer from the noble metal nanoparticles to the adsorbed protons to an extent by which negligible effects on photoactivity are observed upon noble metal nanoparticles deposition.

- Au-modified materials did not exhibit substantial variation in the selectivity distribution to the main products of methanol photo steam reforming with respect to the corresponding bare TiO_2. All the investigated photocatalysts mainly stabilize the production of formaldehyde; none of the investigated material seems to allow the complete methanol photomineralization to CO_2.

6.4 References

1. Hoffmann, M. R., Martin, S. T., Choi, W. & Bahnemann, D. W. *Chem. Rev.* **95**, 69–96 (1995).

2. Umar, M. & Aziz, H. A. in *Photocatalytic Degradation of Organic Pollutants in Water.*, Ch. 8 (2013).

3. Mahlambi, M. M., Ngila, C. J. & Mamba, B. B. *J. Nanomater.* **2015**, 1-29 (2015).

4. Vikrant, K., Park, C. M., Kim, K.-H., Kumar, S. & Jeon, E.-C. *J. Photochem. Photobiol. C: Photochem. Rev.* **41**, 100316 (2019).

5. Hu, G., Yang, J., Duan, X., Farnood, R., Yang, C., Yang, J., Liu, W. & Liu, Q. *J. Chem. Eng.* **417**, 129209 (2021).

6. Li, Z., Wang, S., Wu, J. & Zhou, W. *Renewable and Sustainable Energy Rev.* **156**, 111980 (2022).

7. Escobedo, S. & Lasa, H. de. *Catalysts* **10**, (2020).

8. Madkhali, N., Prasad, C., Malkappa, K., Choi, H. Y., Govinda, V., Bahadur, I. & Abumousa, R. A. *Results in Engineering* **17**, 100920 (2023).

9. Wang, X., Maeda, K., Thomas, A., Takanabe, K., Xin, G., Carlsson, J. M., Domen, K. & Antonietti, M. *Nat. Mater.* **8**, 76–80 (2009).

10. Kudo, A. *Pure Appl. Chem.* **79**, 1917–1927 (2007).

11. Leung, D. Y. C., Fu, X., Wang, C., Ni, M., Leung, M. K. H., Wang, X. & Fu, X. *ChemSusChem* **3**, 681–694 (2010).

12. Hisatomi, T. & Domen, K. *Nat. Catal.* **2**, 387–399 (2019).

13. Zhang, K. & Guo, L. *Catal. Sci. Technol.* **3**, 1672–1690 (2013).

14. Fujishima, A., Rao, T. N. & Tryk, D. A. *J. Photochem. Photobiol. C: Photochem. Rev.* **1**, 1–21 (2000).

15. Haider, A. J., Jameel, Z. N. & Al-Hussaini, I. H. M. *Energy Procedia* **157**, 17–29 (2019).

16. Gopinath, K. P., Madhav, N. V., Krishnan, A., Malolan, R. & Rangarajan, G. *J. Environ. Manage.* **270**, 110906 (2020).

17. Irshad, M. A., Nawaz, R., ur Rehman, M. Z., Adrees, M., Rizwan, M., Ali, S., Ahmad, S. & Tasleem, S. *Ecotoxicol. Environ. Saf.* **212**, 111978 (2021).

18. Liu, S., Yu, J. & Jaroniec, M. *Chem. Mater.* **23**, 4085–4093 (2011).

19. Lu, Y., Zang, Y., Zhang, H., Zhang, Y., Wang, G. & Zhao, H. *Science Bulletin* **61**, 1003–1012 (2016).

20. Dozzi, M. V. & Selli, E. *Catalysts* **3**, 455–485 (2013).

21. Wen, C. Z., Jiang, H. B., Qiao, S. Z., Yang, H. G. & Lu, G. Q. M. *J. Mater. Chem.* **21**, 7052–7061 (2011).

22. Liu, J., Olds, D., Peng, R., Yu, L., Foo, G. S., Qian, S., Keum, J., Guiton, B. S., Wu, Z. & Page, K. *Chem. Mater.* **29**, 5591–5604 (2017).

23. Li, M., Chen, Y., Li, W., Li, X., Tian, H., Wei, X., Ren, Z. & Han, G. *Small* **13**, 1604115 (2017).

24. Bowker, M., O'Rourke, C. & Mills, A. *Top. Curr. Chem.* **380**, 17 (2022).

25. Chiarello, G. L., Dozzi, M. V. & Selli, E. *J. Energy Chem.* **26**, 250–258 (2017).

26. Meng, A., Zhang, L., Cheng, B. & Yu, J. *Adv. Mater.* **31**, 1807660 (2019).

27. Humayun, M., Raziq, F., Khan, A. & Luo, W. *Green Chem. Lett. Rev.* **11**, 86–102 (2018).

28. Tada, H., Kiyonaga, T. & Naya, S. *Chem. Soc. Rev.* **38**, 1849–1858 (2009).

29. Kumar, A., Choudhary, P., Kumar, A., Camargo, P. H. C. & Krishnan, V. *Small* **18**, 2101638 (2022).

30. Li, X., Yu, J., Jaroniec, M. & Chen, X. *Chem. Rev.* **119**, 3962–4179 (2019).

31. Hu, W., Wen, Z., Yu, X., Qian, P., Lian, W., Li, X., Shang, Y., Wu, X., Chen, T. & Lu, Y. *Adv. Sci.* **8**, 2004662 (2021).

32. Li, J., Wu, X. & Liu, S. *Acta Phys.-Chim. Sin.* **37**, 2009038 (2021).

33. Monllor-Satoca, D., Lana-Villarreal, T. & Gómez, R. *Langmuir* **27**, 15312–15321 (2011).

34. Liu, S., Yu, J., Cheng, B. & Jaroniec, M. *Adv. Colloid Interface Sci.* **173**, 35–53 (2012).

35. Mrowetz, M. & Selli, E. *Phys. Chem. Chem. Phys.* **7**, 1100–1102 (2005).

36. Park, H. & Choi, W. *J. Phys. Chem. B* **108**, 4086–4093 (2004).

37. Mrowetz, M. & Selli, E. *New J. Chem.* **30**, 108–114 (2006).

38. Dozzi, M. V. & Selli, E. *Catalysts* **3**, 455–485 (2013).

39. Dozzi, M. V., Montalbano, M., Marra, G., Mino, L. & Selli, E. *Mater. Today Chem.* **22**, 100624 (2021).

40. Dozzi, M. V. & Selli, E. *Catal. Today* **206**, 26–31 (2013).

41. Dozzi, M. V., Chiarello, G. L. & Selli, E. *J. Adv. Oxid. Technol.* **13**, 305–312 (2010).

42. Dozzi, M. V., Candeo, A., Marra, G., D'Andrea, C., Valentini, G. & Selli, E. *J. Phys. Chem. C* **122**, 14326–14335 (2018).

43. Meire, M., Tack, P., De Keukeleere, K., Balcaen, L., Pollefeyt, G., Vanhaecke, F., Vincze, L., Van Der Voort, P., Van Driessche, I. & Lommens, P. *Spectrochim. Acta B: At. Spectrosc.* **110**, 45–50 (2015).

44. Dozzi, M. V. & Selli, E. *J. Adv. Oxid. Technol.* **19**, 16–19 (2016).

45. Dozzi, M. V., Saccomanni, A., Altomare, M. & Selli, E. *Photochem. Photobiol. Sci.* **12**, 595–601 (2013).

46. Dozzi, M. V., Prati, L., Canton, P. & Selli, E. *Phys. Chem. Chem. Phys.* **11**, 7171–7180 (2009).

47. Wu, H., Ma, J., Li, Y., Zhang, C. & He, H. *Appl. Catal. B* **152–153**, 82–87 (2014).

48. Zanella, R., Giorgio, S., Henry, C. R. & Louis, C. *J. Phys. Chem. B* **106**, 7634–7642 (2002).

49. Dozzi, M. V., Saccomanni, A., Altomare, M. & Selli, E. *Photochem. Photobiol. Sci.* **12**, 595–601 (2013).

50. Dozzi, M. V., D'Andrea, C., Ohtani, B., Valentini, G. & Selli, E. *J. Phys. Chem. C* **117**, 25586–25595 (2013).

51. Maisano, M., Dozzi, M. V., Coduri, M., Artiglia, L., Granozzi, G. & Selli, E. *ACS Appl. Mater. Interfaces* **8**, 9745–9754 (2016).

52. Coduri, M., Maisano, M., Dozzi, M. V. & Selli, E. *Z. Phys. Chem.* **230**, 1233–1248 (2016).

53. Thommes, M., Kaneko, K., Neimark, A. V., Olivier, J. P., Rodriguez-Reinoso, F., Rouquerol, J. & Sing, K. S. W. *Pure Appl. Chem.* **87**, 1051–1069 (2015).

54. Yu, J., Qi, L. & Jaroniec, M. *J. Phys. Chem. C* **114**, 13118–13125 (2010).

55. Dozzi, M. V., Ohtani, B. & Selli, E. *Phys. Chem. Chem. Phys.* **13**, 18217–18227 (2011).

56. Maisano, M., Dozzi, M. V. & Selli, E. *J. Photochem. Photobiol. C: Photochem. Rev.* **28**, 29–43 (2016).

57. Li, C., Koenigsmann, C., Ding, W., Rudshteyn, B., Yang, K. R., Regan, K. P., Konezny, S. J., Batista, V. S., Brudvig, G. W., Schmuttenmaer, C. A. & Kim, J. H. *J. Am. Chem. Soc.* **137**, 1520–1529 (2015).

58. Yu, J., Low, J., Xiao, W., Zhou, P. & Jaroniec, M. *J. Am. Chem. Soc.* **136**, 8839–8842 (2014).

59. Luan, Y., Jing, L., Xie, Y., Sun, X., Feng, Y. & Fu, H. *ACS Catal.* **3**, 1378–1385 (2013).

60. Scaltrini, A. *M.Sc. Thesis in Chemical Sciences* (Università degli Studi di Milano).

61. Pellegrino, F., Morra, E., Mino, L., Martra, G., Chiesa, M. & Maurino, V. *J. Phys. Chem. C* **124**, 3141–3149 (2020).

62. Long, J., Chang, H., Gu, Q., Xu, J., Fan, L., Wang, S., Zhou, Y., Wei, W., Huang, L., Wang, X., Liu, P. & Huang, W. *Energy Environ. Sci.* **7**, 973–977 (2014).

63. Tanaka, A., Hashimoto, K. & Kominami, H. *Chem. Comm.* **53**, 4759–4762 (2017).

64. Kowalska, E., Mahaney, O. O. P., Abe, R. & Ohtani, B. *Phys. Chem. Chem. Phys.* **12**, 2344–2355 (2010).

65. Lv, K., Li, X., Deng, K., Sun, J., Li, X. & Li, M. *Appl. Catal. B: Environ.* **95**, 383–392 (2010).

66. Mino, L., Pellegrino, F., Rades, S., Radnik, J., Hodoroaba, V. D., Spoto, G., Maurino, V. & Martra, G. *ACS Appl. Nano Mater.* **1**, 5355–5365 (2018).

67. Calla, J. T., Bore, M. T., Datye, A. K. & Davis, R. J. *J. Catal.* **238**, 458–467 (2006).

68. Dimitratos, N., Villa, A., Prati, L., Hammond, C., Chan-Thaw, C. E., Cookson, J. & Bishop, P. T. *Appl. Catal. A-Gen.* **514**, 267–275 (2016).

69. Compagnoni, M., Villa, A., Bahdori, E., Morgan, D. J., Prati, L., Dimitratos, N., Rossetti, I. & Ramis, G. *Catalysts* **8**, 623 (2018).

70. Massey, F. J. *J. Am. Stat. Assoc.* **46**, 68–78 (1951).

71. Qu, P., Zhao, J., Shen, T. & Hidaka, H. *J. Mol. Catal. A Chem.* **129**, 257–268 (1998).

72. Yao, C., Wang, X., Zhao, W., Li, T., He, Y., Ran, X. & Guo, L. *J. Alloys. Compd.* **846**, 156335 (2020).

73. Chen, M., Ma, J., Zhang, B., He, G., Li, Y., Zhang, C. & He, H. *Appl. Catal. B, Environ.* **207**, 397–403 (2017).

74. Bubacz, K., Kusiak-Nejman, E., Tryba, B. & Morawski, A. W. *J. Photochem. Photobiol. A: Chem.* **261**, 7–11 (2013).

75. Žerjav, G., Albreht, A., Vovk, I. & Pintar, A. *Appl. Catal. A: Gen.* **598**, (2020).

76. Mohapatra, P., Samantaray, S. K. & Parida, K. *J. Photochem. Photobiol. A: Chem.* **170**, 189–1 94 (2005).

77. Zhao, Z., An, H., Lin, J., Feng, M., Murugadoss, V., Ding, T., Liu, H., Shao, Q., Mai, X., Wang, N., Gu, H., Angaiah, S. & Guo, Z. *Chem. Rec.* **19**, 873–882 (2019).

78. Dozzi, M. V., Saccomanni, A. & Selli, E. *J. Hazard. Mater.* **221–22**, 188–195 (2012).

79. Li, H., Bian, Z., Zhu, J., Huo, Y., Li, H. & Lu, Y. *J. Am. Chem. Soc.* **129**, 4538–4539 (2007).

80. Siemon, U., Bahnemann, D., Testa, J. J., Rodríguez, D., Litter, M. I. & Bruno, N. *J. Photochem. Photobiol. A: Chem.* **148**, 247–255 (2002).

81. Litter, M. I. *Appl. Catal. B: Env.* **23**, 89–114 (1999).

82. Navío, J. A., Colón, G., Trillas, M., Peral, J., Domènech, X., Testa, J. J., Padrón, J., Rodŕguez, D. & Litter, M. I. *Appl. Catal. B: Env.* **16**, 187–196 (1998).

83. Pellegrino, F., Sordello, F., Mino, L., Minero, C., Hodoroaba, V. D., Martra, G. & Maurino, V. *ACS Catal.* **9**, 6692–6697 (2019).

Chapter 7: Conclusions and perspectives

The present PhD thesis aimed at systematically evaluating the combined effects produced on titanium dioxide photoactivity induced by noble metal nanoparticles deposition and *in-situ* fluorination as a function of the adopted deposition technique, the presence of bulk doping with N,F elements and/or the semiconductor morphology. The choice of both the employed semiconductor photocatalyst (TiO_2) and strategies explored for improving its photoefficiency in a plethora of photocatalytic processes are detailed in Chapter 1, which describes the main characteristics of titanium dioxide as a semiconductor photocatalyst (such as its chemical stability and the ability to promote a wide range of photocatalytic processes),[1,2] as well as the effects induced by the above-mentioned modification strategies on the physico-chemical properties of the metal-oxide semiconductor. By using different experimental techniques and methods, described in detail in Chapter 2 and Chapter 3, home-made titanium-dioxide based materials were synthesized, fully characterized, and compared in their efficiency in promoting both photo-oxidation and photoreduction test reactions, aiming at identifying if and how the combination of multiple titanium dioxide modification strategies could lead to better performing photocatalysts for specific applications. Moreover, this thesis aimed at providing further insight into the intrinsic features and the dynamics of photogenerated and photopromoted charge carriers of titanium dioxide-based composite materials under illumination conditions.

During my studies, I focused my attention on exploring modification strategies all aimed at hindering the high recombination rate of photoexcited charge carriers in titanium dioxide, representing its main deactivation path which greatly limits the probability of their transfer towards the substrate-semiconductor interface, and thus the overall photoefficiency of the metal oxide semiconductor.

Chapter 4 - Effect of N,F-Doping and Au Nanoparticles Deposition on the Photocatalytic Activity of TiO_2 Anatase Materials

The first set of modification strategies which I explored consisted in the combination of N,F bulk doping with Au nanoparticles deposition. The interest towards these modifications strategies derives from their ability to improve charge carrier separation within titanium dioxide either

through introduction of photoluminescent Ti^{3+} intra-band gap trap states,[3,4] as in the case of N,F doping, or by forming a Schottky barrier at the metal-semiconductor interface, as provided by the deposition of Au NPs.[5] Combining both modifications appear as a promising strategy possibly able to significantly boost the photoefficiency of titanium dioxide, since dopant-induced Ti^{3+} states and deposited Au nanoparticles can potentially synergistically cooperate in improving charge separation in titanium dioxide. In fact, electrons photopromoted towards the conduction band of titanium dioxide can be firstly captured in Ti^{3+} states, to be then efficiently transferred to deposited Au NPs.[6] As the chosen Au NPs deposition method may significantly influence the efficacy of such cooperative mechanism,[7,8] I decided to focus my attention on studying the effects deriving from the use of two different deposition methods, i.e. deposition-precipitation[9] and photoreduction,[10] on the photocatalytic properties of N,F-doped Au modified TiO_2.

N,F-doped titanium dioxide materials with different dopant content were thus prepared via sol-gel synthesis and modified with 0.5 wt% of Au nanoparticles using the aforementioned deposition techniques. Then, prepared materials were fully characterized by means of the main physico-chemical characterization techniques. In particular, structural and morphological characterization techniques allowed us to confirm the obtainment of fully-anatase composed materials, whereas the successful deposition of Au metal NPs on the surface of TiO_2 has been confirmed by the appearance of the typical Au surface plasmon resonance (SPR) absorption band, with its characteristic maximum absorption located at 553 nm. Furthermore, HR-TEM imaging confirmed the deposition of finely dispersed spherically-shaped Au nanoparticles with average diameter of 6 – 10 nm.

The photocatalytic activity of the synthesized materials has been firstly checked in the photocatalytic oxidation of formic acid, in which a typical bell-shaped trend with increasing dopant content was observed. As expected, all Au-modified materials exhibited a photoactivity higher than their corresponding bare samples, although no significant difference in materials' photoactivity was observed whether the DP or P method was employed to deposit NM NPs.

Differently, when the materials were tested in Cr(VI) photoreduction, appreciable photoactivity differences were induced by either the adopted Au NPs deposition method and the relative TiO_2 dopant content. In particular, in this case the lowest doped titania modified through Au NPs photodeposition exhibits an outstanding photoactivity, possibly unveiling the presence of specific interactions between the dopant induced defective TiO_2 structure and the Au NPs selectively deposited by the P method, further improving the charge carrier separation ability of doped semiconductors. Au NPs may selectively anchor on TiO_2 surface and open a new efficient

electron transfer path from the TiO_2 defective trap states to the adsorbed dichromate ions undergoing reduction. In contrast, the highest doped material, with a relatively poor charge separation ability, exhibits a more marked photoactivity increase only upon Au NPs deposition by means of the unspecific DP method.

To gain insight on the presence of possible cooperative mechanisms between Ti^{3+} photoluminescent trap states and the deposited Au NPs, possibly dependent on the adopted Au deposition route, I decided to study the materials through Time-Resolved Photoluminescence Spectroscopy (TRPL).

As previously observed by our research group,[4] the pristine low doped material was characterized by the most intense and longer lasting PL emission, followed by the highly doped and the reference undoped materials respectively, according to a trend resembling that of their photocatalytic activity in both the investigated test reactions.

The PL emission spectra recorded with NM-modified materials were characterized by a quenched emission intensity with respect to those of the corresponding unmodified materials. Also, the PL time decay profiles were faster as a consequence of the emptying of the PL trap states provided by the deposited NM NPs, i.e. acting as electrons scavenger species.[6] However, differences in PL decay lifetimes and/or populations of emitting states between DP- and P-modified materials, which could be a strong indication of the presence of cooperative mechanism between PL trap states and differently deposited Au NPs, could not be clearly observed for any of the investigated samples.

This finding may derive from the use of an inappropriate time resolution window (in the order of tenths of nanoseconds) to acquire the PL decay signals. In fact, synergistic electron exchange mechanisms between populated PL trap states and Au NPs may occur on a shorter time scale and might not be detected with the here employed experimental setup, mainly probing in the ns time scale.

Through this work, we were able to effectively evaluate the effects induced on titania photoactivity upon combining N,F doping with the deposition of Au NPs in both an oxidation and a reduction test reaction. Moreover, we were able to study how both N,F-doping and Au nanoparticles deposition affected the photoluminescent properties of titanium dioxide in terms of both emission intensity and PL signals decay kinetics. Further studies based on this work can be tackled in the future by deepening the knowledge on the TRPL properties of Au-modified N,F doped TiO_2 through measurements with a faster detecting TRPL experimental setup, potentially

allowing to better probe ultrafast (in the ps/fs temporal resolution scale) electron exchange phenomena occurring between dopant induced photoluminescence trap states and deposited Au NPs.

Chapter 5 - Effects of In-Situ Surface Fluorination on the Photocatalytic Activity of Differently Shaped TiO_2 Materials

Chapter 5 deals with investigating a second set of modification strategies consisting in the combination of morphology control with *in-situ* TiO_2 surface fluorination. In particular, through the present study we shed light on the combined effects of surface fluorination and morphology control in reduction and oxidation photocatalytic test reactions.

In doing so, morphology-controlled titanium dioxide materials were prepared by hydrothermal synthesis, using titanium isopropoxide as Ti precursor and fluoride ions (HF) as capping agent, able to stabilize {001} facets with respect to {101} ones. Two samples series, obtained in the presence of different nominal molar F/Ti ratios, were prepared, and systematically investigated. Samples showing pseudo-spherical morphology were characterized by a F/Ti molar ratio of 0.1 (HT_0.1 series), while materials with a platelet-like morphology, with preponderant exposure of {001} facets, were prepared with an F/Ti ratio of 1.0. The samples were then washed with aqueous NaOH solutions to remove residual fluorine used in the synthesis. All materials were fully characterized by physico-chemical characterization techniques. In particular, the phase composition was examined by X-ray powder diffraction (XRPD) as a function of the F/Ti ratio. All samples consisted of pure anatase and the relative percentage of {001} facets was calculated by the Scherrer method. The materials produced with a larger amount of capping agent in the hydrothermal synthesis (HT_1 series) exhibited a greater percent amount (*ca.* 68%) of exposed {001} facets, confirmed by TEM images.

The photoactivity of the materials was then screened in three different test reactions, i.e., Cr(VI) photoreduction, formic acid photo-oxidation and rhodamine B photobleaching. In particular, Cr(VI) photocatalytic reduction resulted to be strongly favoured by a large exposure of anatase {001} facets, with the best performing material having a platelet-like morphology. This is possibly due to an improved charge separation arising from an optimal mixture of co-exposed facets, which favours the selective migration of photogenerated holes and electrons towards {001} and {101} facets, respectively. *In-situ* surface re-fluorination of the materials, however, leads to a morphology independent photoactivity decrease, consequent to the reduced ability of the

fluorinated oxide to bind dichromate anions, a key step required for their direct reduction by conduction band electrons.

Concerning oxidative photocatalytic processes, the photoactivity of the specimens was tested in two test reactions, *i.e.*, formic acid and rhodamine B photodegradation, proceeding either through a direct or an indirect reaction path, respectively. In particular, whereas for formic acid oxidation the photoactivity of the powders was only slightly affected by a change in the morphology of titania, a strong synergistic shape-dependent photoactivity effect between platelet-like anatase TiO_2 morphology and surface fluorination is clearly outlined in RhB photodegradation, with an outstanding photoactivity increase observed only upon fluorination of the {001}-facet enriched material. This may result from an overall increased charge carriers separation combined with the higher amount of surface -OH groups in the platelet-like TiO_2 that can be fluorinated to generate F-{001} facets, which may considerably boost $^{\bullet}OH$ radical mediated oxidation paths. The here unveiled role played by morphology and surface fluorination on the photoactivity of shape-controlled TiO_2 materials may pave the way for designing highly performant TiO_2-based materials to be employed in efficient photocatalytic detoxification processes.

The results contained in this chapter have been reported in the paper entitled "Effects of anatase TiO_2 morphology and surface fluorination on environmentally relevant photocatalytic reduction and oxidation reactions" by M.V. Dozzi, M. Montalbano, G. Marra, L. Mino, E. Selli, published in Materials Today Chemistry 22 (2021) 100624. DOI: 10.1016/j.mtchem.2021.100624.

Chapter 6 - Effects of Au nanoparticles deposition and in-situ Surface Fluorination on the Photocatalytic Activity of Differently Shaped TiO_2 Materials

Chapter 6 presents a systematic study aimed at shedding light on the effects induced on photoactivity by Au nanoparticles deposition on differently shaped titanium dioxide anatase, eventually under *in-situ* fluorinated conditions. In particular, the effects induced by different techniques adopted to deposit Au NPs on TiO_2 surface were investigated, as well as those provoked by the *in-situ* addition of fluoride ions, in order to highlight possible synergistic effects on TiO_2 photoactivity induced by coupling surface fluorination, specific morphology and deposited NM NPs.

In doing so, differently shaped titanium dioxide materials were prepared using a properly optimized version of the synthetic procedure reported in Chapter 5 which, by skipping an unnecessary intermediate drying and grinding step, allowed to speed up the overall material

preparation procedure. Portion of the prepared titania powders were then modified with Au NPs by DP[9] or P[10] methods, according to the procedures described in Chapter 4.

All synthesized materials were systematically tested in different photocatalytic reactions, proceeding through different reaction paths, and fully characterized by physico-chemical characterization techniques. In particular, the phase composition was examined by X-ray powder diffraction (XRPD) as a function of the F/Ti ratio. All samples consisted of pure anatase and the relative percentage of {001} facets was calculated by applying the Scherrer method. The materials produced with a larger amount of capping agent in the hydrothermal synthesis (HT_1 series) exhibited a greater percent amount (*ca.* 68%) of exposed {001} facets. The diffuse reflectance spectra of the Au/TiO_2 systems showed the typical localized surface plasmonic band, with an absorption maximum around 550 nm. TEM images confirmed the morphological differences highlighted by XRPD analysis for the two TiO_2 HT_X series, while the Au NPs size distributions indicate that the Au-modified samples exhibit very small (*ca.* 6 nm) and similar gold NPs size, regardless of the Au nominal content and the adopted deposition technique. The actual Au percent weight deposited on selected samples was also determined by ICP-OES analysis.

Formic acid photocatalytic degradation

The performance of the synthesized materials was firstly screened in formic photocatalytic degradation. In particular, we observed that Au NPs deposition on TiO_2 is beneficial in FA degradation only in the case of {101} facet-dominated (and thus, pseudo-spherically shaped) materials. Moreover, the photoactivity of nanosheet shaped material modified through photodeposition decreased upon Au NPs deposition. Indeed, in the case of a pseudo-spherical morphology, Au NPs are expected to be mainly deposited on the most abundant {101} facets and may effectively contribute in scavenging photoexcited electrons, which, according to literature,[11,12] tend to migrate to such crystalline facets. This results in an overall increase of FA photocatalytic degradation rate.

Differently, in the case of platelet-like photocatalysts, the selective migration of valence band holes towards the prevailing {001} facets could be hindered by the presence of Au NPs deposited on such facets, which, acting as electron scavengers, may promote charge carriers recombination, with a consequent overall photoefficiency decrease. Furthermore, by considering the reduction potential of the Au^+/Au^0 couple (1.68 V vs. NHE), the holes photogenerated on the TiO_2 surface and migrating towards the {001} facets, instead of directly interacting with the organic substrate molecules, may partially oxidize Au NPs to Au^+ species, which then act as recombination centres of photoproduced charge carriers.[7]

Rhodamine B photocatalytic degradation: effects of in-situ TiO_2 surface fluorination and Au deposition

The photoactivity of the materials was then tested in rhodamine B photobleaching under acidic conditions (pH = 3.7) and under *in-situ* fluorinated conditions at the same pH. We found that the whereas the morphology of TiO_2 did not significantly influence the photodegradation of the dye at acidic pH, *in-situ* TiO_2 fluorination instead produced a significant photoactivity increase, which is particularly marked for platelet-like materials. By considering that RhB adsorption is inhibited on fluorinated TiO_2, regardless of the TiO_2 morphology, the increase in RhB degradation rate upon TiO_2 surface fluorination can only be due to an enhanced photoproduction of $^{\bullet}OH$ radicals, which may attack RhB molecules and promote their photodegradation.[11]

Differently, the photoactivity increase gained by Au-containing samples upon *in-situ* fluorination is significantly more marked compared to that achieved with the corresponding bare materials only for samples having a pseudo-spherical morphology, independently of the adopted Au NPs deposition technique. So, in the presence of Au NPs on the TiO_2 surface the intriguing synergistic effect in RhB degradation induced by the platelet-like anatase TiO_2 morphology and its *in-situ* surface fluorination is suppressed. This may be related to a lower extent of fluorination of Au/TiO_2 with respect to bare TiO_2.

Concerning the effects induced by Au NPs deposition on differently shaped *in-situ* fluorinated anatase TiO_2, we observed that Au deposition produced a significant increase of RhB degradation rate under fluorinated conditions only for samples mainly exposing {101} facets, the highest improvement obtained for photocatalysts containing 0.5 wt% Au, corresponding to the optimal NM content. Differently, coupling TiO_2 platelet-like morphology with Au NPs did not substantially alter the original photoefficiency of {001} facet-enriched samples. Thus, the selective migration of photogenerated holes towards {001} facets may be limited by the presence of gold NPs (deposited on such prevailing facets) which, behaving as electron scavengers, may promote electron-hole recombination, resulting in a lower photocatalytic activity in RhB degradation.

Photocatalytic hydroxylation of terephthalic acid

The efficiency of the materials in the photocatalytic hydroxylation of terephthalic acid was investigated with the purpose of studying the relative ability of differently shaped, metal modified titanium dioxide materials in producing reactive hydroxy radical species in solution. In particular, we observed that in the case of bare, metal free titanium dioxide materials, passing from a pseudo-spherical morphology to nanosheet-shaped materials resulted in an improvement of the 2-Hydrotherephtalic production rate, thus confirming the beneficial effect played by a higher exposure of {001} facets in boosting the production of $HO^{\bullet}$ radicals in solution, even in the

absence of surface fluorinated conditions. The deposition of noble metal nanoparticles, however, resulted to suppress the 2-hydroxyterephtalic acid production rate for all synthesized materials, possibly due to the oxidation of noble metal nanoparticles by either holes trapped at the semiconductor surface or by produced $HO^{\bullet}$ which, in the absence of surface fluorine, can oxidize noble metal nanoparticles before reacting with terephthalic acid.

Photocatalytic production of 2-hydroxyterephtalic acid, thus, allowed us to better unravel the effects on photoactivity deriving from morphology control and Au nanoparticles deposition on differently shaped titanium dioxide nanoparticles. In particular, the test reaction resulted to usefully highlight an improved $HO^{\bullet}$ radical production by means of mainly {001}-exposing materials, as well as further confirming the detrimental interaction occurring when gold nanoparticles are deposited on {001} surfaces rather than {101} facets.

Photocatalytic reduction of Cr(VI)

The photoactivity of the materials was then tested in the Cr(VI) to Cr(III) photocatalytic reduction at pH 3.7, in which we observed that increasing the truncation degree of TiO_2 nanoparticles dramatically boosted the anatase performance. This may be ascribed to an improved charge separation arising from an optimal mixture of co-exposed facets, favoring the selective migration of photogenerated holes and electrons towards {001} and {101} facets, respectively. Differently, the photocatalytic activity of the materials was either unaffected or only slightly improved upon Au NPs deposition on their surface, with a maximum ca. 20% increase in the case of platelet-like materials with 0.5 wt% Au, independently of the adopted DP or P deposition method. The strong adsorption of Cr(VI) anions on the TiO_2 surface may favor a fast and efficient transfer of photoexcited electrons towards the transition metal ions, which can be further increased by the presence of a co-catalyst, such as Au NPs[13] However, in Cr(VI) photoreduction the anodic half reaction (i.e., water oxidation) may represent the kinetic bottleneck limiting the overall efficiency of the photocatalytic process.[14] Therefore, the introduction of a reduction co-catalyst, such as NM NPs, may have little-to-no influence on the photoactivity of TiO_2-based materials, independently of their morphology.

Hydrogen production via methanol photo-steam reforming

The photoactivity of differently shaped Au modified titanium dioxide materials was finally tested in hydrogen production via methanol photo-steam reforming. We found that the photocatalytic activity of the materials greatly benefitted from the combination of pseudo-spherically shaped titanium dioxide materials with the deposition of Au nanoparticles, whereas the photoactivity improvement was more limited when NM NPs were deposited on {001}-facets

dominated materials. Possibly, the larger exposure of {101} facets, *i.e.* acting as reduction sites, may guarantee a larger avaiability of reduction centers to promote H_2 evolution.

Through this work, we shed light on the combined effects of Au NPs deposition with differently shaped titanium dioxide, eventually under *in-situ* fluorinated conditions, in a plethora of different photocatalytic oxidation and reduction test reaction. The obtained photoactivity results in the investigated test reactions, moreover, allowed us to hypothesize a reaction mechanism based on charge migration in differently shaped Au/TiO_2 composite materials able to rationalize the effects on photoactivity induced upon coupling Au NPs deposition with differently shaped TiO_2 materials, also under *in-situ* fluorinated conditions. Further studies based on this work can be tackled in the future by exploring the effects induced by the deposition of different noble metals other than gold, or deepening the knowledge on charge carrier dynamics under irradiation conditions in differently shaped NM-modified TiO_2 by performing time-resolved optical characterizations such as TRPL or transient absorption analyses measurements.

References

1. Fujishima, A., Rao, T. N. & Tryk, D. A. *J. Photochem. Photobiol. C: Photochem. Rev.* **1**, 1–21 (2000).

2. Hoffmann, M. R., Martin, S. T., Choi, W. & Bahnemann, D. W. *Chem. Rev.* **95**, 69–96 (1995).

3. Dozzi, M. V., Ohtani, B. & Selli, E. *Phys. Chem. Chem. Phys.* **13**, 18217–18227 (2011).

4. Dozzi, M. V., D'Andrea, C., Ohtani, B., Valentini, G. & Selli, E. *J. Phys. Chem. C* **117**, 25586–25595 (2013).

5. Dozzi, M. V., Saccomanni, A., Altomare, M. & Selli, E. *Photochem. Photobiol. Sci.* **12**, 595–601 (2013).

6. Dozzi, M. V., Candeo, A., Marra, G., D'Andrea, C., Valentini, G. & Selli, E. *J. Phys. Chem. C* **122**, 14326–14335 (2018).

7. Dozzi, M. V., Prati, L., Canton, P. & Selli, E. *Phys. Chem. Chem. Phys.* **11**, 7171–7180 (2009).

8. Prati, L. & Villa, A. *Catalysts* **2**, 24–37 (2011).

9. Zanella, R., Giorgio, S., Henry, C. R. & Louis, C. *J. Phys. Chem. B* **106**, 7634–7642 (2002).

10. Wenderich, K. & Mul, G. *Chem. Rev.* **116**, 14587–14619 (2016).

11. Dozzi, M. V, Montalbano, M., Marra, G., Mino, L. & Selli, E. *Mater. Today Chem.* **22**, 100624 (2021).

12. Chen, M., Ma, J., Zhang, B., He, G., Li, Y., Zhang, C. & He, H. *Appl. Catal. B: Env.* **207**, 397–403 (2017).

13. Navó, J. A., Colón, G., Trillas, M., Peral, J., Domènech, X., Testa, J. J., Padrón, J., Rodŕguez, D. & Litter, M. I. *Appl. Catal. B: Env.* **16**, 187–196 (1998).

14. Litter, M. I. *Appl. Catal. B: Env.* **23**, 89–114 (1999).

List of scientific contributions

Publications

M. V. Dozzi, M. Montalbano, G. Marra, L. Mino, E. Selli, "Effects of anatase TiO_2 morphology and surface fluorination on environmentally relevant photocatalytic reduction and oxidation reactions", *Mater. Today Chem.* **22**, 100624 (2021).

Communications (poster and oral)

Montalbano, M.; Dozzi, M. V.; Marra, G.; Selli, E. "Combining Morphology, Surface Fluorination and Au Nanoparticles Deposition on TiO_2: Effects on Rhodamine B Photodegradation" SPEA 11 -Turin, Italy, June 6-10, 2022. *Flash oral presentation*.

Montalbano, M.; Dozzi, M. V.; Selli, E. "Combining Morphology, Surface Fluorination and Au Nanoparticles Deposition on TiO_2: Effects on Rhodamine B Photodegradation", Giornate Italiane di Fotochimica organizzate dal Gruppo Italiano di Fotochimica – Online congress, 23-23 September 2021. *Oral presentation*.

Montalbano, M.; Dozzi, M. V.; Marra, G.; Selli, E. "Combining Morphology, Surface Fluorination and Au Nanoparticles Deposition on TiO_2: Effects on Rhodamine B Photodegradation", XXVII Congresso Nazionale della Società Chimica Italiana 2021 – Online congress, 14-23 September 2021. *Oral presentation*.

Acknowledgements

First and foremost, I am extremely grateful to my supervisor, Prof. Maria Vittoria Dozzi, for her always present guide, continuous support, and immense patience during my PhD study. Her profound knowledge and plentiful experience have encouraged me in all the time of my academic research and daily life. I will preciously lifelong cherish all the teachings you provided me over the course of this journey.

I would also like to express my deepest gratitude to Prof. Elena Selli for providing me with support, dedication, and for always being a reference point for my scientific formation during my PhD.

The work of Dr. Gianluigi Marra of Istituto ENI Donegani on TEM imaging is gratefully acknowledged.

Great thanks also to Nicolò Lo Presti and Andrea Zecchinelli, first for being brilliant, proactive, eager-to-learn students, and second for being some of the most trustworthy and easy-going colleagues I've ever had. The experimental work you both provided has been of immense importance for composing this PhD thesis.

Heartfelt thanks go to all the people of the Unimi Photocatalysis Group, with a special mention to Annalisa, Ivan, and Gian Luca. Thanks for the morning coffees, the friendship, and the great talks we've had almost every single day for years.

I must express my very profound gratitude to my dad Giuseppe (Vecchio!), my mom Anna and my brother Luigi for providing me with unfailing support and continuous encouragement throughout my years of study and through the process of researching and writing this thesis. This accomplishment would not have been possible without you. Thanks for your presence and for being a point of reference I can always rely on in my life.

I would also like to thank "I Consumatori di Follia", my very closest fellows Marli, Samu "MBB", Pol Bre, Puddu, Verza, Mastro, for providing me with endless laughs, emotional support, and having to listen to my whines when I had troubles during this PhD. Some of them (especially Marli) even had to act as unpaid proof-readers, having to help me out with better language solutions, or had to emergency-fix my windows installation just right before the submission of this thesis (Puddu). Thank you all, folks!

Sincere thanks also to all the dear friends from the Labirinto community, especially Luchino, Punzi, Elia, Roby, Tommy, Frizzo, Ciccius, Anacleto, Zanga and Pizza. Thanks for the laughs and the good company.

And last but not least, my most dear and sincere thanks go my significant other, Elena, for being the unique, special person she is every single day. Thanks for providing me with invaluable support, and for always making me feel like I'm the most important and desired person on this planet. Thanks for fulfilling my life with endless sweetness and love.